NONLINEAR ANALYSIS OF MILLIMETER AND SUB-MILLIMETER WAVE SOURCES SUCH AS CERENKOV MASERS, OROTRONS, AND UBITRONS
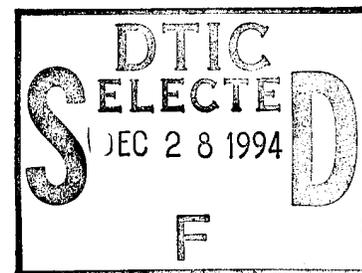
SAIC FINAL REPORT No. SAIC-94/1150

Submitted to:

Vacuum Electronics Branch, Code 6840
Electronics Science and Technology Division
Naval Research Laboratory
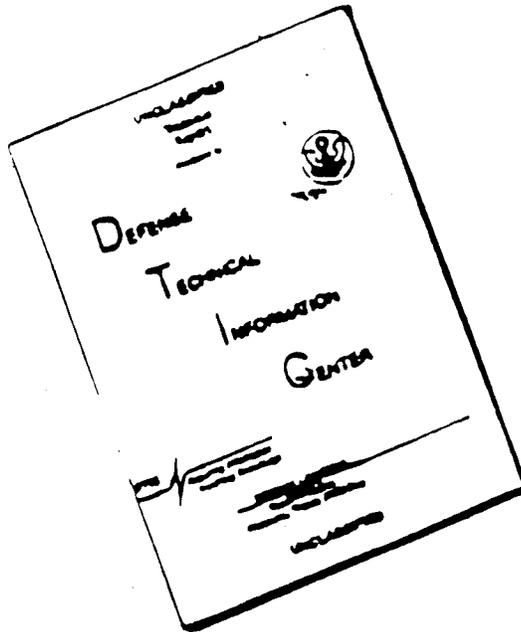Washington, D.C. 20375

Submitted by:

Applied Physics Operation
Science Applications International Corporation
1710 Goodridge Drive
McLean, VA 22102
(703) 734-5840

October 1994

19941219 114

DISCLAIMER NOTICE

THIS DOCUMENT IS BEST QUALITY AVAILABLE. THE COPY FURNISHED TO DTIC CONTAINED A SIGNIFICANT NUMBER OF PAGES WHICH DO NOT REPRODUCE LEGIBLY.

CONTENTS

I. INTRODUCTION

The research performed on this contract covers a broad range of topics related to coherent radiation sources. In general, the research can be divided into two broad categories: theoretical research into innovative concepts in the physics of ubitrons (or free-electron lasers), and in the application of this theory to the support of the experimental ubitron program in the Vacuum Electronics Branch of the Electronics Science and Technology Division at the Naval Research Laboratory (NRL). The work on this program was conducted by the Principal Investigator, Dr. H.P. Freund at a level of effort of 1 Manyear per calendar year during the contract period.

The general theory research covers a wide range of topics of interest. Linearized analyses of the ubitron/free-electron laser (FEL) have been performed to study (1) thermal effects on the gain in both planar and helical wiggler geometries in ubitrons, and (2) the relationship between the variation in the relative phase and optical guiding. Nonlinear analyses have been conducted for a wide variety of configurations and purposes. These can be roughly categorized as studies of: (1) the effect of wiggler imperfections on ubitron operation, (2) space-charge effects in ubitrons, (3) slow-wave ubitrons, (4) tunability of tapered wiggler configurations in ubitrons, (5) a high-efficiency collective FEL experiment using a helical wiggler and an anti-parallel axial guide magnetic field, (6) the inclusion of a model of self-electric and -magnetic fields in the nonlinear simulations of ubitrons, (7) a high power Cerenkov maser, and (8) the analysis of the Coaxial Hybrid Iron (CHI) wiggler.

The theory support for the ubitron program in Code 6840 covers two distinct experiments. The first experiment is that of a fundamental harmonic ubitron using a helical wiggler and an axial guide. Extensive theoretical capability to analyze this configuration has been developed over the course of this and preceding contacts with Code 6840 at NRL, and the simulation codes developed were employed to analyze the results of this experiment. Gratifyingly, good agreement has been found between the experiment and the theory. The second experiment employs a planar wiggler and operated at higher harmonics of the resonance frequency. Once again, good agreement has been found between simulation and the experiment.

The organization of this final report is as follows. A description of the general theory developed under the contract is given in Section. II. This will be divided into six sub-sections corresponding to each of the categories listed above. A discussion of the theoretical support provided for the ubitron experiments is given in Section III. A summary is given in Section IV. The text of the report will not be very detailed in that figures and drawings illustrating the results of the work will not be given in the body of the report. These are shown instead in the papers published during the contract period, and copies of all papers published in refereed journals for this research is given in Appendices following the text of the report.

II. GENERAL THEORY

A detailed description of the general theory will not be given here since this is contained within the papers in the Appendices. Instead, only a general overview of the principal results will be presented. To this end a brief discussion of the methodology used in nonlinear analyses is in order.

The nonlinear techniques used in this research program are based upon slow-time-scale analyses of the resonant interaction between the electron beam and the radiation field

in a variety of waveguide structures. For example, the vacuum TE modes in a cylindrical or coaxial waveguide can be expressed in the form

$$\delta\mathbf{A}(\mathbf{x},t) = \sum_{l=0,n=1}^{\infty} \delta A_{lm}(z) \left[\frac{l}{\kappa_{lm}r} Z_l(\kappa_{lm}r)\,\hat{\mathbf{e}}_r \sin\alpha_{lm} + Z_l'(\kappa_{lm}r)\,\hat{\mathbf{e}}_\theta \cos\alpha_{lm} \right] ,$$

where $\delta\mathbf{A}(\mathbf{x},t)$ denotes the vector potential,

$$\alpha_{lm} \equiv \int_0^z dz'\,k_{lm}(z') + l\theta - \omega t ,$$

denotes the phase corresponding to wavenumber k_{lm} and angular frequency ω, and κ_{lm} is the cutoff wavenumber of the mode. Observe that the amplitude $\delta A_{lm}(z)$ and wavenumber of each mode is assumed to vary slowly in z with respect to the wavelength of the mode. The cutoff wavenumbers are given by the dispersion equation $J_l'(\kappa_{lm}R_g) = 0$ for a cylindrical waveguide of radius R_g, and by $J_l'(\kappa_{lm}a)Y_l'(\kappa_{lm}b) = J_l'(\kappa_{lm}b)Y_l'(\kappa_{lm}a)$ for a coaxial waveguide of inner and outer radii a and b respectively. The polarization vector is given by $Z_l(\kappa_{lm}r) = J_l(\kappa_{lm}r)$ for a cylindrical waveguide, and $Z_l(\kappa_{lm}r) = J_l(\kappa_{lm}r) + \Delta_{lm}Y_l(\kappa_{lm}r)$ for a coaxial waveguide where $\Delta_{lm} \equiv -J_l'(\kappa_{lm}b)/Y_l'(\kappa_{lm}b)$.

The dynamical equations for each mode is found by substitution of the above-mentioned representation for the field into Maxwell's equations and (1) orthogonalizing in the transverse coordinates, and (2) averaging over a wave period. The results can be compactly written in the form

$$\left[\frac{d^2}{dz^2} + \left(\frac{\omega^2}{c^2} - k_{lm}^2 - \kappa_{lm}^2 \right) \right] \delta A_{lm} = \frac{\omega_b^2}{c^2} S_{lm}^{(1)} ,$$

and

$$2k_{lm}^{1/2} \frac{d}{dz}\left(k_{lm}^{1/2}\delta A_{lm} \right) = \frac{\omega_b^2}{c^2} S_{lm}^{(2)} ,$$

where $\delta a_{lm} \equiv e\delta A_{lm}/m_e c^2$ is the normalized amplitude, ω_b is the ambient beam plasma frequency, and the sources are

$$S_{lm}^{(1)} \equiv H_{lm} \left\langle \frac{v_r}{|v_z|} \frac{l}{\kappa_{lm}r} Z_l(\kappa_{lm}r) \sin\alpha_{lm} + \frac{v_\theta}{|v_z|} Z_l'(\kappa_{lm}r) \cos\alpha_{lm} \right\rangle ,$$

and

$$S_{lm}^{(2)} \equiv H_{lm} \left\langle \frac{v_r}{|v_z|} \frac{l}{\kappa_{lm}r} Z_l(\kappa_{lm}r) \cos\alpha_{lm} - \frac{v_\theta}{|v_z|} Z_l'(\kappa_{lm}r) \sin\alpha_{lm} \right\rangle .$$

Here $H_{lm} \equiv 2\kappa_{lm}^2 R_g^2/(\kappa_{lm}^2 R_g^2 - l^2)J_l^2(\kappa_{lm}R_g)$ for a cylindrical waveguide, and

$$H_{lm} \equiv \frac{2\kappa_{lm}^2(b^2 - a^2)}{(\kappa_{lm}^2 b^2 - l^2)Z_l^2(\kappa_{lm}b) - (\kappa_{lm}^2 a^2 - l^2)Z_l^2(\kappa_{lm}a)} ,$$

for a coaxial waveguide. Finally, the averaging operator is defined as the average over the initial conditions of an ensemble of electrons. An initial momentum distribution is defined as

$$F(\mathbf{p}_0) = Ae^{-(p_{z0}-p_0)^2/\Delta p_z^2}\delta(p_0^2 - p_{\perp 0}^2 - p_{z0}^2)H(p_{z0}) ,$$

where the normalization constant is

$$A \equiv \left[\pi \int_0^{p_0} dp_{z0}\,e^{-(p_{z0}-p_0)^2/\Delta p_z^2} \right]^{-1} .$$

This distribution describes a monoenergetic beam with a pitch angle spread, and the axial energy spread corresponding to this pitch angle spread can be expressed as

$$\frac{\Delta\gamma_z}{\gamma_0} = 1 - \left[1 + 2(\gamma_0^2 - 1)\frac{\Delta p_z}{p_0}\right]^{-1} ,$$

where $\gamma_0 \equiv (1 + p_0^2/m_e^2 c^2)^{1/2}$. As a result, the averaging operator takes the form

$$\langle\langle\cdots\rangle\rangle \equiv \frac{A}{4\pi A_g}\int_0^{2\pi}d\phi_0\int_0^{P_0}dp_{z0}\beta_{z0}e^{-(p_{z0}-p_0)^2/\Delta p_z^2}$$

$$\times \iint_{A_g}dx_0dy_0\sigma_\perp(x_0,y_0)\int_0^{2\pi}d\psi_0\sigma_\parallel(\psi_0)(\cdots) ,$$

where A_g is the cross-sectional area of the waveguide, ψ_0 ($\equiv -\omega t_0$) is the initial phase corresponding to an entry time t_0, $\phi_0 = \tan^{-1}(p_{y0}/p_{x0})$, and $\sigma_\perp$ and $\sigma_\parallel$ represent the initial distributions in cross-section and phase. These equations exhibit no direct mode-mode coupling. All coupling is through the electron beam. Hence, to complete the formulation the electron trajectories must also be specified. For this purpose, we use the full Lorentz force equations in the fields composed of the wiggler, the electromagnetic wave(s), and the self-fields (to be discussed below). Thus, we integrate

$$v_z\frac{d}{dz}\mathbf{p} = -e\left[\delta\mathbf{E} + \mathbf{E}^{(s)} + \frac{1}{c}\mathbf{v}\times(B_0\hat{\mathbf{e}}_z + \mathbf{B}_w + \delta\mathbf{B} + \mathbf{B}^{(s)})\right] ,$$

for an ensemble of electrons, where $\mathbf{B}_w$ denotes the wiggler, $\mathbf{E}^{(s)}$ and $\mathbf{B}^{(s)}$ denote the self-fields,

$$\delta\mathbf{E} = -\frac{1}{c}\frac{\partial}{\partial t}\delta\mathbf{E}, \quad \text{and} \quad \delta\mathbf{B} = \nabla\times\delta\mathbf{A} ,$$

describes the electromagnetic field, and an axial guide field is included as well. Observe that the Lorentz force equations need not be averaged since they are implicitly slowly-varying for waves near resonance. This constitutes the principal difference between the formulation pioneered by SAIC and nonlinear approaches developed elsewhere. This non-averaged approach to orbit dynamics permits the self-consistent inclusion of beam injection into the wiggler as well as the treatment of wiggler tapering for efficiency enhancement and all harmonic interactions.

Finally, before proceeding to the detailed discussion of the work performed on the contract, it is important to remark that this nonlinear formulation can also be applied to the TM modes as well as other waveguide geometries by the simple expedient of using the vacuum modes of other configurations. Of particular relevance to the work performed on the contract is the rectangular waveguide, and dielectric-lined waveguides.

A. Thermal Effects on the Linear Gain

The interaction in a ubitron is crucially sensitive to the beam quality, and even small thermal spreads can result in substantial degradations in the gain and efficiency of the interaction. As a result, SAIC conducted a study of the effect of the beam thermal spread on the linear gain in both helical and planar wiggler ubitrons. This analysis has been published in the IEEE Journal of Quantum Electronics [vol. 27, p. 2550 (1991)], and was conducted by Dr. Freund in collaboration with Dr. D. Kirkpatrick of SAIC and Dr. R.C.

5

Davidson at the Princeton Plasma Physics Laboratory. A copy of the paper is given in Appendix I.

As expected, the analysis showed a steep decline in the gain with increasing thermal spreads. However, there were differences in the analysis in comparison with the previously commonplace approach to thermal effects in ubitrons. The typical analysis of thermal effects in ubitrons made use of a Maxwellian velocity distribution, and resulted in an expression for the dispersion equation which contained the Plasma Dispersion function. This is the most common approach used to describe thermal effects in drifting plasmas. However, it is incorrect to apply this formalism to ubitrons. The reason for this twofold. The first is that it is implicitly assumed in this analysis that the axial velocity is a constant of the motion. This is true for uniformly magnetized beams, but not for electron propagation through a wiggler. Here, the constants of the motion are the total energy and the canonical momenta. Orbits with constant axial velocity can be found for a helical wiggler, but they represent a special class of trajectory which breaks down if there is any thermal spread. The situation is even worse for planar wigglers, since there are no orbits with constant axial velocity in this geometry. The second reason is that the Maxwellian distribution does not apply either since this distribution does not describe the beams in a ubitron. In the ubitron the electron beam will be characterized by a maximum energy corresponding to the potential applied across the diode. Hence, there will be no long exponentially decaying tail at very high energies. As a consequence, the Maxwellian distribution is an approximation at best. Since the Plasma Dispersion function appears only in the context of the Maxwellian distribution in which the axial velocity is a constant of the motion, this also represents a questionable approximation.

In order to overcome these problems, a completely new analysis was developed. The first consideration was to construct an appropriate distribution function. Since the beams in most ubitrons of interest to Code 6840 are produced in a diode with a fixed potential, a monoenergetic beam was assumed. The source of the thermal spread, therefore, is the pitch angle spread induced by electron transport across the cathode/anode gap. Hence, a distribution of the form

$$F(P_x, P_y, p) = \frac{n_b}{\pi \Delta P^2} \frac{p_z}{p} e^{-(P_x^2 + P_y^2)/\Delta P^2} \delta(p - p_0) ,$$

was chosen, where P_x and P_y are the canonical momenta, p is the total momentum, nb is the ambient density, and p_0 and ΔP denote the total beam momentum and momentum spread. Using this distribution, we obtained dispersion equations for both helical and planar wiggler configurations which included a thermal function of the form

$$T(\zeta) \equiv \zeta [1 - \zeta e^\zeta E_1(\zeta)] ,$$

where E_1 is the exponential integral function and

$$\zeta \equiv \frac{\gamma_0^2 m_e^2}{\Delta P^2} \left(\frac{\omega^2}{k^2} - v_z^2 \right) ,$$

where v_z denotes the bulk axial beam velocity.

The result found using this approach differed from that found using the Maxwellian and the Plasma Dispersion function. The difference consisted in the fact that we found that the gain remains relatively constant for small increases in the thermal spread, and only begins to decrease after a threshold is reached in the thermal spread. No such plateau is found using the Maxwellian/Plasma Dispersion function analysis. Since the Maxwellian

approach represents an approximation at best, this newer analysis constitutes an advance in our understanding of the physics of ubitrons.

B. Optical Guiding and the Relative Phase

The issue of optical guiding in ubitrons and free-electron lasers has received a great deal of attention with respect to short wavelength FELs in which the radiation is quasi-optical. In this regime, it was feared that diffraction could cause to radiation beam to expand outside the bounds of the electron beam, and that this could result in a reduction in the gain and efficiency of the interaction. The work on optical guiding was predicated on the hypothesis that the dielectric effect of the beam acts as an optical fiber which will confine the radiation to within the electron beam envelope. On the basis of previous theoretical formulations, this appeared to be quite feasible.

The effect of optical guiding at short wavelengths is related to the phase shift induced by the beam at microwave frequencies. Hence, we felt that a study of the relative phase could have relevance to the question of whether optical guiding works at short wavelengths. The relative phase can be defined in the following manner

$$\Delta\phi_{lm}(z) \equiv \int_0^z dz' \left[k_{lm}(z') - \sqrt{\frac{\omega^2}{c^2} - \kappa_{lm}^2} \right] ,$$

which measures the change in the evolution of the phase in the beam-loaded system with respect to the vacuum waveguide. Using the nonlinear codes described above, it was found that the relative phase could be either positive or negative over the band of unstable frequencies. Typically, at the low (high) frequency portion of the gain band the relative phase is negative (positive), and there is one frequency at which the relative phase remains unchanged. Since optical guiding requires a positive relative phase in order for the refractive effect of the beam to result in guiding of the wave, this implies that guiding is found only over a part of the gain band.

In order to test this conclusion Dr. Freund, in collaboration with Dr. T.M. Antonsen at the University of Maryland, performed a theoretical analysis of optical guiding and showed that it did indeed correspond to the variations in the relative phase. This work was published in the IEEE Journal of Quantum Electronics [vol. 27, p. 2539 (1991)], and is included in Appendix II.

C. Wiggler Imperfections

Since the ubitron/FEL is so sensitive to the effects of beam thermal spreads, it is feared that imperfections in the wiggler magnet can also have a deleterious impact on the gain and efficiency. The reason for this is that variation in the wiggler field can induce variations in the particle velocity which can result in resonance broadening. Much of the analysis of the effect of wiggler imperfections has been based upon orbit averaged formulations in which the effect of wiggler imperfections is included via some assumed random walk model of electron motion in a randomly varying wiggler. Dr. Freund had some reservations about this model which stemmed from the fact that the random walk model was originally constructed to deal with Brownian motion in which small particles experience random and discontinuous impulses. In this way, the particle "walk off" from their initial location , and the displacement varies as the square root of the number of impulses they receive. This is not what happens in a wiggler however. In this case, while the wiggler may vary in an random (i.e., unknown or unplanned) manner, the field is continuous. Thus, the electrons don't experience random and sudden impulses. Rather, they follow a meander line associated with the field variations. A better model for this

7

motion might be a bead sliding on a wire which has been bent or twisted in a random manner. By this analogy, the electrons would not be expected to walk off.

In order to test this hypothesis, Dr. Freund modified the nonlinear simulation codes to treat random variations in the wiggler field. This was a relatively straightforward process since the formulation integrates the electron trajectories in a given wiggler field. Thus, all that was required was to modify the wiggler model to include a randomly chosen set of imperfections in the wiggler amplitude. These analyses were conducted in collaboration with Dr. R.H. Jackson and have been published in Phys. Rev. A [vol. 45, p. 7488 (1992)] and Nucl. Instrum. Meth. [vol. A341, p. 225 (1994)]. These papers are include din Appendices III and IV.

The detailed model employed was based upon the fact that a planar wiggler is constructed of a stack of permanent magnets, and that random imperfections can result form variations in the magnetization of each element in the magnet stack. Thus, the field amplitude can vary in a random way from pole face to pole face, which occurs regularly at some fractional length of the wiggler period. As a result, a wiggler model was constructed in which the amplitude varied on some length scale $\Delta z = \lambda_w/N_p$, where λ_w denotes the wiggler period and N_p is the number of pole faces per wiggler period. A random sequence of wiggler variations in then chosen $\{\Delta B_n\}$ where $\Delta B_n \equiv \Delta B_w(n\Delta z)$. The variation in the wiggler amplitude between these points is then constructed from a continuous map as follows

$$\Delta B_w(n\Delta z + \delta z) = \Delta B_n + (\Delta B_{n+1} - \Delta B_n) \sin^2\left(\frac{\pi\delta z}{2\Delta z}\right) ,$$

for $0 \le \delta z \le \Delta z$. Given this variation in the wiggler amplitude, it is possible to integrate the electron trajectories for a large number of different error distributions. In this way, it is possible to construct an ensemble average of the efficiency as a function of the rms magnitude of the wiggler error.

The results of the study indicate that the effect of wiggler imperfections is much less severe than the effect of beam thermal spread, and that for most experiments (at least at long wavelengths) there is no cause for alarm based upon the current manufacturing tolerances for wiggler magnets.

It is also interesting to note that this approach to treating wiggler imperfections also allows us to model the effect of a specific set of imperfections in any given wiggler magnet.

D. Tunability of Tapered Free-Electron Lasers

It is widely known, and practiced, that the efficiency in ubitrons can be substantially enhanced by using a tapered wiggler. The physical basis of this process is that as the electrons decelerate as they lose energy to the wave and drop out of resonance. However, the electrons can be accelerated if the wiggler amplitude decreases and the resonance condition can, therefore, be maintained over an extended interaction length. The efficiency enhancement in such cases is extremely sensitive to both the slope of the taper and the start-taper position. The start of the taper must be chosen in such a way that the electrons have just become trapped in the ponderomotive potential formed by the beating of the wiggler and radiation fields but have not had time to undergo one half of an oscillation in the trough of the wave. The slope of the taper must not be so fast that the electrons "slosh" out of the trough nor so slow that no effective enhancement occurs. Because of this sensitivity, it had been felt if the start-taper point and slope of the taper had been chosen for optimum performance at one given frequency, then the efficiency enhancement at other

8

frequencies would suffer. In other, words, that the tapered wiggler interaction would have a narrow instantaneous bandwidth.

In order to test this hypothesis, Dr. Freund collaborated with Drs. B. Levush and T.M. Antonsen of the University of Maryland. The procedure used in the study was to use one-dimensional (B. Levush and T. Antonsen) and three-dimensional (H. Freund) simulations for tapered wiggler configurations optimized at one frequency to test the output efficiency at other frequencies. In other words, the parameters were optimized at a given frequency, and then held fixed while the frequency was changed.

The results of the study showed that the previously accepted hypothesis of a narrow bandwidth for the tapered wiggler interaction was in error. In fact, it was shown that the bandwidth for the tapered wiggler case was as broad as that for the uniform wiggler.

E. A Slow-Wave Ubitron

One important goal of the ubitron program in Code 6840 at NRL is the development of ubitrons which can operate at high frequencies but low voltages. Three principal strategies are being used for this purpose: (1) harmonic interactions, (2) short period wigglers, and (3) slow-wave circuits. It is the latter approach which will be discussed in this subsection.

In order to study the effect of a slow-wave circuit, Dr. Freund adapted the aforementioned nonlinear formulation to treat the case of a dielectric-lined rectangular waveguide and a planar wiggler. The waveguide chosen had a dielectric liner applied to the long dimension of the waveguide (the x-direction) which coincided with the direction of wiggler motion. The mode structure in such a waveguide is not strictly TE or TM with respect to the longitudinal axis of the waveguide. Instead it is TE and TM with respect to the y-direction. These are referred to as the LSE and LSM modes respectively. The analysis has been published in Nucl. Instrum. Meth. [vol. A304, 555 (1991)], and is included in Appendix VI. This paper includes a detailed discussion of the formulation as well as the results of the simulation.

The results of the analysis indicate that high efficiencies and voltage reductions are possible with such a slow-wave circuit. However, dielectric liners are subject to problems of charging and breakdown, not to mention mechanical failure. Hence, an actual slow-wave ubitron might be better constructed with a more robust slow-wave circuit such as a grating or rippled wall.

F. Cerenkov Masers

The Cerenkov maser is essentially a traveling wave tube in which the slow-wave circuit is composed of a dielectric liner. Cerenkov masers have been built and operated at Dartmouth for many years, and hold promise for low voltage operation at relatively high frequencies. In order to understand the interaction and its limitations Dr. Freund, in collaboration with Dr. A.K. Ganguly at NRL, has formulated a nonlinear slow-time-scale analysis of the Cerenkov maser for a configuration in which a cylindrical waveguide is lined with a dielectric material. This formulation was conducted under a previous contract SAIC with NRL. However, more recently a high power X-Band Cerenkov maser experiment has been performed at General Dynamics which recorded power levels of more than 280 MW at 8.6 GHz. Drs. Freund and Ganguly applied their previously written simulation code in order to study this experiment. This work has been published in Nucl. Instrum. Meth. [vol. A304, p. 612 (1991) and is included in Appendix VII.

Details of the formulation and the comparison are given in Appendix VII and will not be repeated here. Briefly, the experiment employed a 788 kV/3.1 A annular electron beam with a mean radius of ≈ 1.15 cm and a thickness of 2 mm. The waveguide was lined with stycast ($\varepsilon = 10$) and has a radius of 1.74 cm at the wall and 1.47 cm at the inner surface of the dielectric, and an overall length of 23.9 cm. It was operated as an amplifier with a 100 kW driver at 8.6 GHz. The measured output power was 280 MW for a gain of 34.5 dB (1.44 dB/cm). The results of the simulation were in substantial agreement with the experiment as regards the gain over the 23.9 cm of the experiment. However, the simulation indicates that the interaction had not saturated over that length. Saturation in the simulation occurs at a power of 620 MW over a length of 28 cm for an efficiency of 32% and an average gain of between 14.4-1.6 dB/cm. More importantly, the simulation indicates that the device is relatively insensitive to thermal spread. In particular, the efficiency is seen to drop to 18% for an energy spread of $\Delta\gamma_z/\gamma_0 \approx 30\%$. These are remarkable figures, and indicate that there is promise in this technology for high power applications.

G. Self-Field Effects in Ubitrons

It has long been known that the interaction in intense beam ubitrons is based upon stimulated Raman scattering in which the negative energy beam space-charge wave scatters off the wiggler field to result in the output signal. A great deal of effort has been expended in the study of these Raman interactions. However, the effect of the DC self-electric and self-magnetic fields has received relatively little attention. Recently, it became apparent that the self-field effects were important to the operation of the ubitron in Code 6840 at NRL, and Dr. Freund, in collaboration with Dr. R.H. Jackson at NRL and Dr. D.E. Pershing at MRC, undertook the task of including these effects in the nonlinear slow-time-scale analyses.

This work was published in Phys. Fluids B [vol. 5, p. 2318 (1993)], and is included in Appendix VIII. The formulation makes use of an approximate form for the self-fields. Under the assumption of a flat-top density profile with a uniform axial velocity, the self-electric and self-magnetic fields can be written in the form

$$\mathbf{E}^{(s)} = -\frac{m_e}{2e}\,\omega_b^2\left[(x - \langle x\rangle)\,\hat{\mathbf{e}}_x + (y - \langle y\rangle)\,\hat{\mathbf{e}}_y\right]\ ,$$

and

$$\mathbf{B}^{(s)} = -\frac{m_e}{2e}\,\omega_b^2\,\langle\beta_z\rangle\left[(y - \langle y\rangle)\,\hat{\mathbf{e}}_x - (x - \langle x\rangle)\,\hat{\mathbf{e}}_y\right]\ .$$

These representations for the self-fields are then used in the nonlinear formulations to study both helical and planar geometries using circular beams.

The results of this study indicated that the self-fields are relatively unimportant for ubitrons/FELs which have been constructed at MIT and at LLNL. However, this was not the case for the ubitron under construction at NRL. For this experiment, the self-fields were predicted to have a major impact on beam transmission and interaction efficiency. At the time this paper was written, no experimental results from the NRL ubitron were available. However, the experiment became operational before the end of the contract, and confirmed this prediction. These comparisons will be discussed in more detail in the next section dealing with the theoretical support for the experiment.

H. Simulation of a High Power FEL

Dr. Freund, in collaboration with Dr. A.K. Ganguly, has applied the nonlinear simulation codes to the analysis of a recent experiment conducted at MIT. This experiment employed a helical wiggler field in conjunction with an axial guide field to produce an FEL amplifier at 35 GHz. The novel feature of this experiment was that the axial guide field was oriented anti-parallel with the bulk streaming velocity of the electron beam. This work has been published in the IEEE Trans. Plasma Sci. [vol. 20, p. 245 (1992)] and in Phys. Fluids B [vol. 5, p. 1869 (1993)], and these papers are included in Appendices IX and X. We will merely summarize the essential points of the study here.

The experiment used a 750 kV/300A electron beam with a radius of 0.25 cm. The wiggler had a period of 3.18 cm and a maximum amplitude of about 1.8 kG, and the guide field could reach an amplitude of approximately 12 kG. The experiment was operated as an amplifier at 35 GHz and could be driven with powers of about 8.5 kW. Output power was peaked at 61 MW for a wiggler amplitude of 1.47 kG and a reversed guide field of 10.92 kG. Significantly, there was a sharp dip in the output power for the reversed field cases at an axial field of about 7.5 kG. This corresponded to the magnetic antiresonance in which the Larmor period associated with the cyclotron motion corresponded to the wiggler period. This was a previously unexpected phenomenon.

The simulation has proven to be in remarkably good agreement with the reversed field measurements. Choosing an initial axial energy spread of 1.5% in accord with the experimentally quoted figure for beam quality, the simulation predicts an output power of 60 MW for the 10.92 kG reversed field case. This is exceptionally close agreement. In addition, the simulation also shows the dip in the output power near the magnetic antiresonance. The source of this effect has proven to be an antiresonant perturbation in the orbits of the off-axis electrons. In effect, an electron which is undergoing wiggler-driven helical oscillations far from the axis of symmetry experiences a periodic driving force due to the wiggler inhomogeniety which becomes very large near the antiresonance. The fact that this unexpected effect was correctly described by the simulation represents a success for the non-averaged orbit analysis.

I. Space-Charge Effects in Ubitrons

The nature of the Raman regime in ubitrons/FELs is often poorly understood. This is because there are several effects which contribute to the relative importance of the beam space charge waves. For example, an experiment conducted at MIT by J. Fajans and G. Bekefi was unambiguously in the Raman regime despite a current of only 4 A, while another experiment (also at MIT) conducted by D. Kirkpatrick and Bekefi was not in the Raman regime despite a current of 900 A. In order to explain this, Dr. Freund studied a group of four experiments with the view of evaluating their Raman status based upon three different criteria. This work was published in Nucl. Instrum. Meth. [vol. A331, p. 496 (1993)], and is include in Appendix XI.

The three essential criteria for Raman effects to be important are as follows. Firstly, the beam current must be high enough that the space-charge potential of the beam-plasma waves exceeds the ponderomotive potential formed by the beating of the wiggler and radiation fields. Secondly, the frequency shift associated with the beam-plasma waves [i.e., the beam plasma frequency] must exceed the gain bandwidth of the interaction. Thirdly, the beam plasma waves must not be subject to Landau damping. This last condition is equivalent to the requirement that the Debye length be greater than the wavelength of the beam-plasma waves.

Four experiments were considered in this study. These included the three experiments at MIT and one experiment at LLNL. Of these four experiments, the two with the highest currents were found to be not in the Raman regime, while the two lower current ones were found to be in the Raman regime.

The highest current was found in the Kirkpatrick and Bekefi experiment at MIT. As mentioned, this experiment used a 900 A electron beam and operated at $\approx$ 500 GHz. In this case, the space-charge potential was comparable to the ponderomotive potential, but the beam plasma frequency ($\approx$ 5.5 GHz) was much less than the bandwidth of the interaction ($\approx$ 50 GHz). In addition, the Debye length was $\approx$ 0.09 cm is comparable to the space-charge wavelength ($\approx$ 0.06 cm); hence, the space-charge waves should be damped. This experiment, therefore, is not expected to be in the Raman regime.

The next highest current is found in the LLNL experiment which was a 35 GHz amplifier using a 3.5 MV/850 A electron beam. In this case, the ponderomotive and space-charge potentials also were comparable, but the plasma frequency ($\approx$ 2.2 GHz) was much less than the bandwidth ($\approx$ 15 GHz). In addition, the Debye length was $\approx$ 0.8 cm while the space-charge wavelength was also $\approx$ 0.8 cm. Hence, the space-charge waves experienced sever Landau damping. Hence, this experiment was not in the Raman regime either.

The third highest current was found in the reversed field experiment at MIT described in a previous subsection. This experiment employed a 750 kV/300 A electron beam. In this case the space-charge potential exceeded the ponderomotive potential, and the Debye length ($\approx$ 0.14 cm) was much less than the space-charge wavelength ($\approx$ 0.8 cm). Hence, Landau damping was unimportant. Finally, the plasma frequency ($\approx$ 5.2 GHz) was comparable to the bandwidth. This experiment, therefore, was in the Raman regime.

The lowest current was found in the Fajans and Bekefi experiment which was a 9.3 GHz amplifier that used a 155 kV/4 A electron beam. The space-charge potential in this experiment also exceeded the ponderomotive potential, and the plasma frequency ($\approx$ 0.72 GHz) was comparable to the bandwidth. In addition, the low energy spread ($\approx$ 0.3%) minimized the Debye length and kept Landau damping small. hence, this experiment was also unambiguously in the Raman regime.

It should also be mentioned that the nonlinear simulation codes are in agreement with these general conclusions on the applicability of the Raman interaction in these four experiments.

J. The CHI Wiggler

It was previously mentioned that the goal of the ubitron research program is to operate at high frequencies with relatively low voltage beams, and that one means of accomplishing this is to develop short period wigglers. One impediment to the development of short period wigglers is that the construction of a wiggler necessitates the juxtaposition of oppositely directed magnets. This means that the shorter the period, the more field cancellation there will be which, in turn, means that the lower the maximum achievable field amplitude. In order to ease this limitation, a novel wiggler design has been invented by a team composed of Dr. R.H. Jackson at NRL, H.P. Freund at SAIC, D.E. Pershing at MRC, and J.M. Taccetti from the University of Maryland. This wiggler is called the Coaxial Hybrid Iron wiggler, or CHI wiggler for short.

The CHI wiggler is formed by the coaxial insertion of a central rod and an outer ring into a solenoid. Both the central rod an the outer ring are composed of alternating spacers made of ferromagnetic and non-ferromagnetic material in such a manner that the

ferromagnetic (non-ferromagnetic) spacer on the central rod corresponds to the non-ferromagnetic (ferromagnetic) spacer on the outer ring. Such a design is relatively inexpensive and easy to manufacture, and permits the creation of a high amplitude/short period wiggler by the relatively simple expedient of using high field solenoids. The wiggler component of the resulting field is limited primarily by the saturation of the ferromagnetic material used.

The initial work on this design has been published in Nucl. Instrum. Meth. [vol. A341, p. 454 (1994)] and Phys. Plasmas [vol. 1, p. 1046 (1994)], and are included in Appendices XII and XIII. A good description of the CHI wiggler is contained in these papers along with schematic illustrations of the wiggler and perspective and contour plot of the field itself. In addition, the latter paper describes a nonlinear simulation of the interaction based upon the aforementioned slow-time-scale analysis for a coaxial waveguide. The essential conclusion of this work is that the CHI wiggler does indeed hold promise as a design which can achieve the necessary short periods and high amplitudes to operate at high frequency with relatively low beam voltage. In view of this, NRL has submitted a patent application for the CHI wiggler in the names of the co-inventors.

More recently, the CHI wiggler has been applied to the design of a G-band FEL for application to the cyclotron resonant heating of magnetic fusion reactors. A paper describing this work has been submitted to Phys. Rev. Lett. and represents a collaboration between Dr. Freund at SAIC, Dr. M.E. Read at PSI, Dr. R.H Jackson at NRL, Dr. D.E. Pershing at MRC, and J.M. Taccetti from the University of Maryland. This paper is included in Appendix XIV. The results indicate that it should be possible to build a G-band amplifier using the CHI wiggler capable of producing 3.5 MW with no beam loss over the course of the interaction. Hence, we have concluded that this design holds promise for meeting the requirements for such a source of RF power.

Finally, Dr. Freund is providing theory support for the design of a Ka-band CHI wiggler ubitron amplifier in Code 6840 at NRL. This experiment represents the Ph.D. thesis work of J.M. Taccetti. An initial paper describing the design phase of this project has been submitted for publication in Nucl. Instrum. Meth., and is included in Appendix XV. SAIC expects to continue providing theoretical support for this experiment under a new contract.

III. THEORETICAL SUPPORT

Theoretical support has been provided for three experimental projects. One has already been described in the preceding section and deals with the start of the CHI wiggler experiment. This was presented in the last section in the interests of a more coherent presentation. The two other projects involve a fundamental mode ubitron and a harmonic ubitron. Each one will now be discussed in turn.

A. The Fundamental Mode Ubitron

The fundamental mode ubitron experiment in Code 6840 at NRL employs a well-known helical wiggler/axial guide field configuration and an electron beam (230 kV/100 A) propagating through a cylindrical waveguide. The experiment has a been conducted largely by D. Pershing of MRC and R. Jackson of NRL with H. Freund providing the theory support. The experiment is designed for long pulse operation ($\approx$ 1 μsec) with a rep rate of several Hz. The ubitron was operated as a Ku-band amplifier. This experiment has been under study for several years, and the start predates this contract. SAIC has been providing theoretical support for this experiment over its complete lifetime under the aegis of several

13

consecutive contracts. Recently, the experiment has come to fruition and recorded an output of approximately 4.2 MW at 16.6 GHz. Given the pulse time and rep rate, this represents an average power of 36 W, which is the record high average power for a ubitron/FEL to date.

Two papers describing the experiment have been published/submitted in refereed journals during the contract: Nucl. Instrum. Meth. [vol. A304, p. 127 (1991)], and Nucl. Instrum. Meth. [submitted in 1994]. These papers are included in Appendices XVI and XVII.

The earlier paper recorded gains of the order of 16-20 dB and the theory was in some agreement with the results. However, there were some unsatisfying discrepancies. At that time, the self-fields had not been included in the simulation. Inclusion of these effects resulted in much better agreement, as described in the second paper in Appendix XVII. There are still some uncertainties; however, we feel that they can be largely accounted for by two effects. The first is the uncertainty in the calibrations for the beam voltage and the wiggler and guide field amplitudes. It has been found in both theory and the experiment that the output power is extremely sensitive to variations in these parameters, and a few percent change in any of them can result in substantial variations in the power. Hence, this uncertainty can explain a large part of the discrepancies that still remain. The second is that the effect of reflections in a long pulse system like this can also affect the output power by causing an effective increase in the drive power. This is important in the current experiment since there is not enough drive power to run the ubitron to saturation. The specific level of these reflections is not known with certainty, but only a percent or less of total reflection would be required to account for a substantial variation in the output. Together, these two uncertainties can account for a large measure of any discrepancies between the theory and the experiment.

One notable success in the theory is the prediction of beam loss. There was substantial beam loss observed in the ubitron which increased monotonically with output power. After inclusion of the self-fields in the simulation, the theory has been shown to closely predict this scaling of beam loss with output power [see Fig. 7 in Appendix XVII].

B. The Harmonic Ubitron

The harmonic ubitron experiment in Code 6840 at NRL was conducted largely by H. Bluem of the University of Maryland as a thesis project. Also represented on the experiment were R. Jackson, V. Granatstein, and D. Pershing, and H. Freund provided theory support. The results of this experiment were published in Phys. Rev. Lett. [vol. 67, p. 824 (1991)] and is included in Appendix XVIII. This experiment differed from the fundamental mode ubitron in that it employed a planar wiggler and a rectangular waveguide. Also, since it operated on a harmonic interaction in the Ku-band, the beam voltage was much less than the nominal 200 kV used in the fundamental mode ubitron.

The experiment used a 100 kV/7 A beam and found gains of the order of 7 dB at frequencies in the range of 14-15 GHz. This was a second harmonic interaction making use of the periodic position interaction. This experiment marked the first experimental demonstration of this interaction in a ubitron, and we note that the nonlinear theory was in substantial agreement with the experimental observations. Once again, we attribute the fact that the simulation was able to treat this new interaction mechanism without modification to the non-averaged nature of the electron dynamics.

IV. SUMMARY AND DISCUSSION

The preceding contents of the final report represent the technical work performed under this contract, and the 18 Appendices include the refereed papers either published or submitted for publication during the contract term. However, this does not include a list of invited and contributed papers presented at conferences (which may be published in such non-archival formats as conference proceedings). In this regard, three invited papers were presented during the contract period, and more than 35 contributed papers were presented at a variety of professional conferences. In addition, Dr. Freund, in collaboration with Dr. R. Parker of NRL, has written a chapter on Free-Electron Lasers for inclusion in the Encyclopedia of Science and Technology [Academic Press, San Diego (1992), vol. 98, p. 523].

APPENDIX I

Thermal Effects on the Linear Gain in Free-Electron Lasers

H.P. Freund, R.C. Davidson, and D.A. Kirkpatrick

Thermal Effects on the Linear Gain in Free-Electron Lasers

H. P. Freund, R. C. Davidson, and D. A. Kirkpatrick

Abstract—The effect of an axial energy spread on the linearized gain in free-electron lasers is considered for configurations which employ both helical and planar wiggler fields. The analysis includes collective effects and is valid for either the Raman or high-gain Compton regimes. A thermal function is obtained which applies to both the helical and planar wiggler configurations at the fundamental, and which is generalized to treat the thermal effect on the harmonics for a planar wiggler. It is assumed that the displacement of the electron beam from the axis of symmetry for a helical wiggler, or the plane of symmetry for a planar wiggler, is much less than the wiggler period, and an idealized one-dimensional model is considered. The electron-beam model used to describe the axial energy spread is based upon the assumption of a monoenergetic beam which exhibits a pitch angle spread. This is described in the analysis by the inclusion of nonvanishing components of the canonical momenta in the single-particle trajectories of the electrons, and the specific distribution used is that of a Gaussian spread in the canonical momenta. The linearized Vlasov–Maxwell equations are then used to derive the dispersion equations, including collective Raman effects, for both the helical and planar wigglers. The analysis treats the interaction at the fundamental resonance frequency in the case of the helical wiggler, and a general thermal function is derived which describes the effect of the axial energy spread. The planar wiggler configuration admits interactions at odd harmonics as well as the fundamental, and a general dispersion equation is derived which includes the thermal effect at each harmonic as well as the fundamental. In addition, the nonvanishing canonical momenta results in an oscillation in the axial velocity at the wiggler period which gives rise to emission at all harmonics. This effect is included in the analysis for the planar wiggler configuration.

I. INTRODUCTION

AN IMPORTANT issue in the generation of coherent radiation at short wavelengths from the free-electron laser (FEL) is the effect of a beam thermal spread on the interaction. Indeed, in many cases, the thermal spread available from various electron-beam sources constitutes the essential limiting factor for many FEL applications. In this paper, we address the question of the effect of an axial energy spread upon the linear gain of the FEL at *both* the fundamental resonance frequency and at harmon-

ics of the fundamental. Coherent harmonic radiation is an important approach to the reduction in the beam energy required to achieve short-wavelength operation, and has been observed in the laboratory over a wide spectral range [1]–[5]. The question of the effect of beam thermal spread upon the gain at the harmonics, therefore, is of particular importance.

Theoretical analyses of harmonic radiation in FELs have dealt with both the linear [6]–[9] and nonlinear [10]–[16] interactions. Results of these analyses indicate that substantial gains and efficiencies are possible for the harmonic interactions, but that the sensitivity of the interaction to the beam thermal spread increases with harmonic number. Hence, the beam quality required for coherent emission rises dramatically at the higher harmonic numbers. Analytical formulations of the interaction which include thermal effects have considered both a distribution in the pitch angle spread [8] and the axial velocity, typically specified by a Gaussian [9], [17]. In the former case dealing with the pitch-angle spread, the effect of three-dimensional wiggler geometry has been included via betatron oscillations arising from the wiggler inhomogeneity; however, the analysis is restricted to the low-gain Compton regime. The formulations in the latter case describe a beam with an energy spread but a vanishing emittance (or pitch-angle spread), and treat either harmonic emission from a planar wiggler configuration in the high-gain Compton regime [9] or the fundamental interaction in a variety of operating regimes [17]. In addition, non-linear analyses and simulation of both the fundamental and harmonic interactions for a planar wiggler configuration in the high-gain Compton regime in three dimensions have been presented [10], [12], [14] which include both the effects of a pitch-angle spread (for a monoenergetic beam) and the wiggler inhomogeneity.

In contrast with the preceding work, our purpose in this paper is to develop a unified formulation of thermal effects on the linear gain in both the high-gain Compton and collective Raman regimes. We assume that the beam is monoenergetic but characterized by a pitch-angle spread, and treat both the fundamental (for both helical and planar wigglers) and harmonic (for a planar wiggler) interactions. In order to treat this problem analytically, we shall impose an idealized one-dimensional approximation in which we neglect the wiggler inhomogeneity, and treat the pitch-angle spread by the inclusion of nonvanishing

canonical momenta in the single-particle trajectories. As such, we assume that the electron displacements from either the axis (helical wiggler) or plane (planar wiggler) of symmetry are much smaller than a wiggler period. In practical terms, this implies that the bulk transverse velocity associated with the pitch-angle spread be much less than the wiggler-induced transverse oscillation.

The effect of the pitch-angle spread is twofold. In the first place, the resultant axial energy spread acts to degrade the interaction, and a general thermal function which describes this effect for both the helical and planar wigglers is derived for the interaction at the fundamental resonance. The effect of the axial energy spread on the odd harmonics excited in planar wiggler configurations is also described, and a generalized thermal function is derived for the linear gain at the harmonics. In the second place, the pitch angle spread induces an oscillation in the axial velocity which can also act to excite harmonic radiation, and this is treated for the case of a planar wiggler.

Indeed, for many classes of electron beam, the source of the axial energy spread is predominantly the pitch-angle spread rather than a spread in the total energy. For example, electron beams produced by MIG and Pierce guns are accelerated by voltages of up to several mega-electronvolts and focused, prior to injection into the interaction region, either by shaped electric or magnetic fields. The coils and/or electrodes which produce the external fields in these guns must be carefully designed in order to offset the effects of the self-electric and magnetic fields of the beam. While the accelerating voltage may vary over the duration of the beam pulse, the electrons are instantaneously characterized by a largely monoenergetic distribution. However, the focussing process itself gives rise to a pitch-angle spread due to a variety of causes (such as field imperfections, shot noise, and self-field effects of the beam). Similar effects are found in a variety of accelerating mechanisms, and the description of the axial energy spread as arising from a pitch-angle distribution, rather than a spread in the total energy, is appropriate to a wide range of FEL designs.

The organization of the paper is as follows. A summary of the single-particle orbits in both helical and planar wigglers is given in Section II. The general formalism used to derive the linear growth rates for helical and planar wigglers is described in Section III. Sections IV and V include the linear stability analyses for the helical and planar wigglers, respectively. In the case of helical wigglers, the effect of an axial energy spread is included only upon the growth rate at the fundamental. In this case a general thermal function is derived which describes the axial thermal effect upon the instability. In the case of planar wigglers, the analysis includes the effect of the axial energy spread upon the fundamental and the harmonics. Here we observe that one effect of the axial energy spread derived by means of a nonvanishing canonical momentum is to give rise to growth at both even and odd harmonics. A summary and discussion is given in Section VI.

II. SINGLE-PARTICLE ORBITS

The physical configurations we consider in this paper are those of a relativistic electron beam propagating through either a helical or a planar wiggler within the context of the idealized, one-dimensional limit. As such, we implicitly assume that the displacements of the electron beam from the axis or plane of symmetry are much smaller than the wiggler period (i.e., $k_w r \ll 1$). The helical wiggler field is assumed to be generated by a bifilar helical current winding which produces a field of the form

$$\mathbf{B}_w = B_w(\hat{e}_x \cos k_w z + \hat{e}_y \sin k_w z) \qquad (1)$$

in the idealized limit, where B_w denotes the wiggler amplitude, and k_w is the wiggler wavenumber ($\equiv 2\pi/\lambda_w$, where λ_w is the wiggler period). The representation for a planar wiggler in the idealized limit is given by

$$\mathbf{B}_w = B_w \hat{e}_y \sin k_w z. \qquad (2)$$

Since x and y are ignorable coordinates in the idealized representation for the wiggler fields, these components of the canonical momenta (denoted by P_x and P_y) are constants of the motion. In addition, the total energy is also a conserved quantity. As a result, the single-particle orbits in a helical wiggler are given by

$$p_x = P_x + p_w \cos k_w z \qquad (3)$$

$$p_y = P_y + p_w \sin k_w z \qquad (4)$$

and

$$p_z = \sqrt{P_\parallel^2 - 2p_w(P_x \cos k_w z + P_y \sin k_w z)} \qquad (5)$$

where $\gamma \equiv (1 + p^2/m_e^2 c^2)^{1/2}$ is the relativistic factor corresponding to the total electron energy and momentum p, $p_w \equiv \gamma m_e v_w$, $v_w \equiv -\Omega_w/k_w$ is the wiggler-induced velocity, $\Omega_w \equiv |eB_w/\gamma m_e c|$, m_e is the electron mass, c is the speed of light *in vacuo*, and $P_\parallel^2 \equiv p^2 - p_w^2 - P_x^2 - P_y^2$ defines the bulk axial momentum. Observe that the magnitude of both the transverse and axial components of the velocity are constant in the limit in which both P_x and P_y vanish, and the orbit describes a helix which is in phase with the wiggler field and characterized by an axial momentum $p_\parallel \equiv (p^2 - p_w^2)^{1/2}$.

The single-particle orbits in the idealized planar wiggler are given by (3) for the x component of the momentum

$$p_y = P_y \qquad (6)$$

and

$$p_z = \sqrt{P_\parallel^2 - \tfrac{1}{2}p_w^2 \cos 2k_w z - 2p_w P_x \cos k_w z} \qquad (7)$$

where

$$P_\parallel^2 \equiv p^2 - \tfrac{1}{2}p_w^2 - P_x^2 - P_y^2 \qquad (8)$$

for a planar wiggler. Since the y component of the momentum is constant, the magnitude of the transverse wiggler-induced velocity in a planar wiggler oscillates at the wiggler period. This results in an oscillation in the axial

momentum and velocity as well. which broadens the wave-particle resonance. and gives rise to harmonic interactions. In addition. the principal resonance and coupling coefficient are determined by the bulk transverse velocity $\langle v_\perp \rangle = v_w/\sqrt{2}$. This reduces the effective wiggler field with respect to the helical wiggler.

The assumption of small displacements from either the symmetry axis (for a helical wiggler) or plane (for a planar wiggler) is equivalent to the condition that $|v_w/v_\parallel| \ll 1$. It is also evident from (5) and (8) that the existence of a nonvanishing canonical momentum introduces an oscillation into the axial velocity in the case of both helical and planar wigglers, which can also give rise to harmonic emission when $V_\perp \approx v_w$, where $V_\perp \equiv (P_x^2 + P_y^2)^{1/2}/\gamma m_e$ is the velocity which corresponds to the transverse canonical momenta. In most FEL experiments, however, $V_\perp \ll v_w$. and the effect of a nonvanishing canonical momentum is largely on the broadening of the wave-particle resonance and the consequent degradation of the interaction strength. It should be remarked that this inequality is identical to that required in order to neglect the effect of betatron oscillations and wiggler inhomogeneities. Hence, in the remainder of this paper we will discuss the effect of the axial momentum spread due to a nonvanishing canonical momentum on the gain at the fundamental in both helical and planar wiggler FEL's, and on the gain in planar wiggler FEL's at harmonics of the fundamental.

III. GENERAL FORMULATION

In this section, we derive the general formalism for obtaining the linearized dispersion equation for the FEL in the idealized one-dimensional representation within the context of a linearized Vlasov–Maxwell formalism. The Vlasov equation in the combined wiggler and electromagnetic fields is

$$\left[\frac{\partial}{\partial t} + v \cdot \nabla - e \left(\delta E(z, t) + \frac{1}{c} v \right. \right.$$
$$\left. \left. \times \left[B_w(z) + \delta B(z, t) \right] \right) \cdot \nabla_p \right] f_b(z, p, t) = 0 \quad (9)$$

where $f_b(z, p, t)$ is the distribution function of the electron beam, $\delta E(z, t)$ and $\delta B(z, t)$ denote the fluctuating electric and magnetic fields of the wave, and

$$\nabla_p \equiv \hat{e}_x \frac{\partial}{\partial p_x} + \hat{e}_y \frac{\partial}{\partial p_y} + \hat{e}_z \frac{\partial}{\partial p_z}. \quad (10)$$

The Vlasov equation is linearized by expanding the distribution in powers of the fluctuating fields. To this end we write $f_b(z, p, t) = F_b(z, p) + \delta f_b(z, p, t)$ where F_b and δf_b are the equilibrium and perturbed components of the distribution, and it is assumed that the perturbed distribution is of the order of the fluctuating fields and $|\delta f_b| \ll |F_b|$. The equilibrium distribution must satisfy the lowest order Vlasov equation

$$\left[\frac{\partial}{\partial t} + v \cdot \nabla - \frac{e}{c} v \times B_w(z) \cdot \nabla_p \right] F_b(z, p) = 0. \quad (11)$$

This is satisfied for any equilibrium distribution which is a function of the constants of the motion. As discussed in Section II, these constants are the total energy (or momentum) as well as the canonical momenta for both helical and planar wigglers in the one-dimensional representation; hence, we may express the equilibrium distribution in the form $F_b(z, p) = F_b(P_x, P_y, p)$. Correct to first order in the fluctuation fields, the perturbed distribution satisfies

$$\left[\frac{\partial}{\partial t} + v \cdot \nabla - \frac{e}{c} v \times B_w(z) \cdot \nabla_p \right] \delta f_b(z, p, t)$$
$$= e \left(\delta E(z, t) + \frac{1}{c} v \times \delta B(z, t) \right) \cdot \nabla_p F_b. \quad (12)$$

The perturbed Vlasov equation may be solved by the method of characteristics in which we integrate

$$\delta f_b(z, p, \tau(z)) = e \int_0^z \frac{dz'}{v_z(z')} \left[\delta E(z, \tau(z')) \right.$$
$$\left. + \frac{1}{c} v(z') \times \delta B(z, \tau(z')) \right] \cdot \nabla_p F_b \quad (13)$$

over the unperturbed trajectories under the assumption that the perturbations are negligibly small at time $t = 0$. Observe that we treat the case of spatial growth and have adopted Lagrangian coordinates in which $v(z)$ denotes the unperturbed velocity of an electron as a function of the axial position, and

$$\tau(z) \equiv t_0 + \int_0^z \frac{dz'}{v_z(z')} \quad (14)$$

represents the time it takes an electron to reach a particular axial position after crossing the $z = 0$ plane at time t_0.

The solution to the perturbed Vlasov equation is solved in conjunction with Maxwell's equations. We choose to deal with the scalar $\delta\varphi(z, t)$ and vector potentials $\delta A_\perp(z, t)$ in the Coulomb gauge. Note that since we treat a one-dimensional model, the scalar and vector potentials describe plane waves. Hence, the vector potential represents a purely transverse electromagnetic wave. In terms of this representation, Maxwell's equations are

$$\left(\nabla^2 - \frac{1}{c^2} \frac{\partial^2}{\partial t^2} \right) \delta A_\perp = -\frac{4\pi}{c} \delta J_\perp \quad (15)$$

and

$$\frac{\partial^2}{\partial t \partial z} \delta\varphi = 4\pi \delta J_z. \quad (16)$$

Observe that the scalar potential is described in terms of the z component of Ampere's Law rather than with Poisson's equation. The perturbed source current is given in terms of the perturbed distribution function as follows:

$$\delta J(z, t) = -\frac{e}{m_e} \int d^3p \frac{1}{\gamma} p \delta f_b(z, p, t). \quad (17)$$

The dispersion equation governing the growth and/or damping of the electromagnetic field is obtained by the simultaneous solution of (13), (15), and (16).

Since the FEL operates by means of an axial bunching mechanism, it is the axial velocity spread which is most important. As a consequence, in the treatment of thermal effects on the linear stability properties we shall impose the simplification that the electron beam is monoenergetic but exhibits a pitch-angle spread. The effect of the pitch-angle spread is to include velocity spreads in both the axial and transverse directions, and may be described by a distribution function of the form [18]

$$F_b(P_x, P_y, p) = n_b G_\perp(P_x, P_y) \frac{p_z}{p} \delta(p - p_0) \quad (18)$$

where n_b denotes the bulk ambient density, and $G_\perp(P_x, P_y)$ represents the transverse distribution. For convenience we shall assume that this transverse distribution takes the form of a Gaussian

$$G_\perp(P_x, P_y) = \frac{1}{\pi \Delta P^2} \exp(-P_\perp^2/\Delta P^2) \quad (19)$$

where $P_\perp^2 \equiv P_x^2 + P_y^2$, and ΔP represents the thermal spread. An alternate distribution which includes the effects of both emittance and Betatron oscillations has also been developed [19].

IV. HELICAL WIGGLER CONFIGURATIONS

In treating the case of a helical wiggler under the assumption of plane-wave solutions, the vector and scalar potentials for a wave with angular frequency ω are of the form

$$\delta A_\perp(z, t) = \tfrac{1}{2} \delta \hat{A}_\perp(z) \exp(-i\omega t) + \text{c.c.} \quad (20)$$

and

$$\delta \varphi(z, t) = \tfrac{1}{2} \delta \hat{\varphi}(z) \exp(-i\omega t) + \text{c.c.} \quad (21)$$

After transformation to the basis

$$\ell_\pm = \tfrac{1}{2}(\ell_x \pm i\ell_y) \quad (22)$$

which is convenient for the description of left- and right-hand circularly polarized electromagnetic waves, the perturbed distribution function can be written as

$$\delta f_b(z, p, \tau(z)) = \delta \hat{f}_b(z, p) \exp(-i\omega\tau(z)) + \text{c.c.} \quad (23)$$

where

$$\delta \hat{f}_b(z, p) = \frac{e}{2c} \left[D_+ \left(\frac{\partial}{\partial P_x} + i \frac{\partial}{\partial P_y} \right) \right.$$
$$+ D_- \left(\frac{\partial}{\partial P_x} - i \frac{\partial}{\partial P_y} \right) + D_z \frac{\partial}{\partial p} \right]$$
$$\cdot F_b(P_x, P_y, p). \quad (24)$$

The orbit integrals in (24) are defined as

$$D_\pm = \int_0^z dz' \frac{\exp(i\omega\tau(z, z'))}{v_z(z')} \left(i\omega - v_z(z') \frac{\partial}{\partial z'} \right) \delta \hat{A}_\pm(z')$$

$$(25)$$

and

$$D_z = \frac{1}{p} \int_0^z dz' \frac{\exp(i\omega\tau(z, z'))}{v_z(z')}$$
$$\times \left(-cp_z(z') \frac{\partial}{\partial z'} \delta \hat{\varphi}(z') \right.$$
$$+ i\omega[p_-(z') \delta \hat{A}_+(z') + p_+(z') \delta \hat{A}_-(z')] \right) \quad (26)$$

where $p_\pm \equiv p_x \mp p_y$, $\tau(z, z') \equiv \tau(z) - \tau(z')$, and

$$\delta \hat{A}_\pm = \tfrac{1}{2}(\delta \hat{A}_x \mp i\delta \hat{A}_y) \quad (27)$$

denotes the amplitudes of the circularly polarized electromagnetic waves.

The source current

$$\delta J(z, t) = [\delta \hat{J}_+(z) \ell_+ + \delta \hat{J}_-(z) \ell_- + \delta \hat{J}_z(z) \ell_z]$$
$$\cdot \exp(-i\omega t) + \text{c.c.} \quad (28)$$

is determined by means of the perturbed distribution as follows:

$$\begin{pmatrix} \delta \hat{J}_\pm(z) \\ \delta \hat{J}_z(z) \end{pmatrix} = -\frac{e}{m_e} \int dP_x \, dP_y \, dp \, \frac{p}{\gamma p_z} \delta \hat{f}_b(z, p) \begin{pmatrix} p_\pm \\ p_z \end{pmatrix}.$$

$$(29)$$

The interaction principally couples the space-charge and right-hand circularly polarized modes; hence, we neglect the left-hand circular polarization state. Therefore, the orbit integrals can be written as

$$D_\pm = \delta \hat{A}_\pm(0) \exp(i\omega\tau(z, 0)) - \delta \hat{A}_\pm(z) \quad (30)$$

and

$$D_z = \frac{\gamma m_e c}{p} \int_0^z dz' \exp[i\omega\tau(z, z')]$$
$$\cdot \left[-\frac{\partial}{\partial z'} \delta \hat{\varphi}(z') + \frac{i\omega}{c} \frac{p_-}{p_z} \delta \hat{A}_+(z') \right]. \quad (31)$$

The Lagrangian time coordinate which appears in the orbit integrals can be evaluated using the single-particle trajectories in (3)–(5), and we obtain

$$\tau(z, z') \cong \frac{\gamma m_e}{P_\parallel} \left[(z - z') - \frac{p_w P_x}{k_w P_\parallel^2} \right.$$
$$\cdot (\sin k_w z - \sin k_w z')$$
$$+ \frac{p_w P_y}{k_w P_\parallel^2} (\cos k_w z - \cos k_w z') \right] \quad (32)$$

correct to terms of order in $p_w^2 P_{x,y}^2/P_\parallel^4$. In the evaluation of the source currents, we substitute for the perturbed distribution function and integrate by parts in P_x and P_y.

Hence

$$\delta \hat{J}_+(z) = \frac{e^2}{2m_e c} \int dP_x\, dP_y\, dp\, \frac{p}{\gamma p_z} \left[\left(2 + \frac{p_+ p_-}{p_z^2} \right) D_+ \right.$$

$$+ p_+ \left(\frac{\partial}{\partial P_x} + i \frac{\partial}{\partial P_y} \right) D_+ - p_+ D_z \frac{\partial}{\partial p} \Bigg]$$

$$\cdot F_b(P_x, P_y, p) \tag{33}$$

and

$$\delta \hat{J}_z(z) = \frac{e^2}{2m_e c} \int dP_x\, dP_y\, dp\, \frac{p}{\gamma}$$

$$\cdot \left[\left(\frac{\partial}{\partial P_x} + i \frac{\partial}{\partial P_y} \right) D_+ - D_z \frac{\partial}{\partial p} \right] F_b(P_x, P_y, p)$$

$$\tag{34}$$

where we observe that from the single-particle trajectories

$$\left(\frac{\partial}{\partial P_x} + i \frac{\partial}{\partial P_y} \right) p_+ = 2 \tag{35}$$

and

$$\left(\frac{\partial}{\partial P_x} + i \frac{\partial}{\partial P_y} \right) p_z = -\frac{p_-}{p_z}. \tag{36}$$

The orbit integrals may be evaluated using the single-particle trajectories. We retain only the lowest order contributions due to P_x and P_y in the steady-state trajectories; hence, these contributions appear principally in the resonance condition. We consider the high-gain regime in which

$$\delta \hat{A}_+(z) = \delta \hat{A}_+(0) \exp(-ik_+ z)$$

and

$$\delta \hat{\varphi}(z) = \delta \hat{\varphi}(0) \exp(-ikz). \tag{37}$$

Under these conditions, the axial orbit integral can be approximated as

$$D_z \cong \frac{\gamma m_e}{p} \left[\delta \hat{\varphi}(z') \frac{kv_\parallel}{\omega - kV_\parallel} - \frac{v_w}{c} \delta \hat{A}_+(z') \right.$$

$$\left. \cdot \exp(ik_w z') \frac{\omega}{\omega - (k + k_w) V_\parallel} \right] \tag{38}$$

where $V_\parallel \equiv P_\parallel / \gamma_0 m_e$ is the axial velocity corresponding to the generalized steady-state trajectory. In addition, we retain only the term which varies as $\exp(ik_+ z)$ in D_+. Hence, the source currents can be written as

$$\delta \hat{J}_+(z) \cong -\frac{e^2}{m_e c} \delta \hat{A}_+(z) \int dP_x\, dP_y\, dp \left[\frac{p}{\gamma P_\parallel} \left(1 + \frac{\beta_w^2}{2} \right) \right.$$

$$- \frac{\beta_w^2}{2} \frac{\omega m_e v_\parallel}{\omega - kV_\parallel} \frac{\partial}{\partial p} \Bigg] F_b(P_x, P_y, p)$$

$$- \frac{e^2}{2m_e} p_w \delta \hat{\varphi}(z) \exp(-ik_w z) \int dP_x\, dP_y\, dp$$

$$\cdot \frac{k}{\gamma(\omega - kV_\parallel)} \frac{\partial}{\partial p} F_b(P_x, P_y, p), \tag{39}$$

and

$$\delta \hat{J}_z(z) \cong \frac{e^2}{2m_e c} p_w \delta \hat{A}_+(z) \exp(ik_w z) \int dP_x\, dP_y\, dp$$

$$\cdot \frac{\omega}{\gamma(\omega - kV_\parallel)} \frac{\partial}{\partial p} F_b(P_x, P_y, p)$$

$$- \frac{e^2}{2m_e} \delta \hat{\varphi}(z) \int dP_x\, dP_y\, dp\, \frac{m_e kv_\parallel}{\omega - kV_\parallel} \frac{\partial}{\partial p}$$

$$\cdot F_b(P_x, P_y, p) \tag{40}$$

$\gamma_0 \equiv (1 + p_0^2/m_e^2 c^2)^{1/2}$, $v_\parallel \equiv (p_0^2 - p_w^2)^{1/2}/\gamma_0 m_e$, and $\beta_w^2 \equiv v_w^2/v_\parallel^2$. Note that $v_\parallel$ and v_w now denote the axial and transverse velocities for the steady-state trajectory corresponding to γ_0.

The derivatives of the distribution with respect to p which appear in the above expressions for the source currents may be integrated by parts and the results substituted into Maxwell's equations to give

$$\left[\omega^2 - k_+^2 c^2 - \frac{\omega_b^2}{\gamma_0} \left(1 - \frac{v_w^2}{c^2} \frac{\omega^2 - k^2 c^2}{(\omega - kv_\parallel)^2} T(\zeta) \right) \right] \delta \hat{A}_+(0)$$

$$= -\frac{\omega_b^2}{2\gamma_0} \frac{v_w}{c} \frac{ck(ck - \omega \beta_\parallel)}{(\omega - kv_\parallel)^2} T(\zeta)\, \delta \hat{\varphi}(0) \tag{41}$$

and

$$\left[(\omega - kv_\parallel)^2 - \frac{\omega_b^2}{\gamma_0 \gamma_\parallel^2} T(\zeta) \right] \delta \hat{\varphi}(0)$$

$$= -\frac{\omega_b^2}{\gamma_0} \frac{v_w}{c} \left(1 - \frac{\omega}{ck} \beta_\parallel \right) T(\zeta)\, \delta \hat{A}_+(0) \tag{42}$$

where we identify $k = k_+ + k_w$ from the wavenumber matching condition, $\beta_\parallel \equiv v_\parallel/c$, $\gamma_\parallel^2 \equiv (1 - v_\parallel^2/c^2)^{-1}$, and $T(\zeta)$ defines the thermal function which arises from the Gaussian distribution in the canonical momenta. This thermal function is defined as

$$T(\zeta) \equiv \zeta[1 - \zeta \exp(\zeta) E_1(\zeta)] \tag{43}$$

for the argument

$$\zeta \equiv \frac{\gamma_0^2 m_e^2}{\Delta P^2} \left(\frac{\omega^2}{k^2} - v_\parallel^2 \right) \tag{44}$$

where

$$E_1(\zeta) \equiv \int_\zeta^\infty dt\, \frac{\exp(-t)}{t} \tag{45}$$

denotes the exponential integral function defined over the domain $|\arg \zeta| < \pi$.

The dispersion equation which results from this formulation is

$$\left[(\omega - kv_\parallel)^2 - \frac{\omega_b^2}{\gamma_0 \gamma_\parallel^2} T(\zeta) \right] \left[\omega^2 - k_+^2 c^2 - \frac{\omega_b^2}{\gamma_0} \right]$$

$$= -\frac{\omega_b^2}{2\gamma_0} \frac{v_w^2}{c^2} T(\zeta) \left[\omega^2 - k^2 c^2 - \frac{\omega_b^2}{\gamma_0} T(\zeta) \right] \tag{46}$$
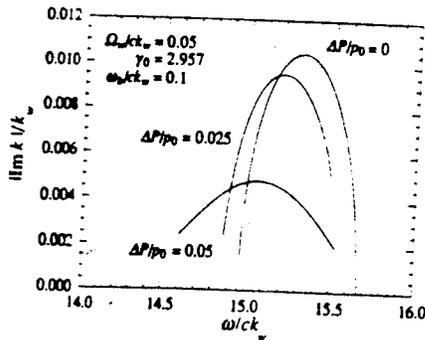
Fig. 1. Graph of the magnitude of the growth rate versus frequency for $\Delta P/p_0 = 0$, 0.025, and 0.05, and $\Omega_w/ck_w = 0.05$, $\gamma_0 = 2.957$, and $\omega_b/ck_w = 0.1$.
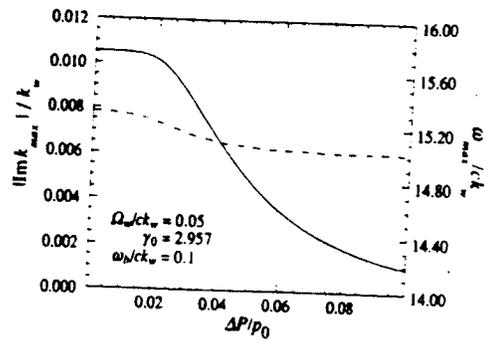

Fig. 2. Graph of the magnitude of the maximum growth rate (solid line) and the corresponding frequency (dashed line) as a function of $\Delta P/p_0$ for $\Omega_w/ck_w = 0.05$, $\gamma_0 = 2.957$, and $\omega_b/ck_w = 0.1$.

correct to lowest nontrivial order in v_w/c. In order to verify that this dispersion equation reproduces that found in the idealized beam limit, we observe that $\lim_{\Delta P \to 0} |\zeta| = \infty$. Expanding the exponential integral function in the asymptotic limit, therefore, we find that $\lim_{\Delta P \to 0} T(\zeta) = 1$ and that the ideal beam dispersion equation is recovered. Thermal effects become dominant whenever $\mathrm{Im}\, k/(\mathrm{Re}\, k + k_w) \approx \Delta v_\parallel/v_\parallel$, where the wavenumber is to be evaluated at the peak growth rate in the ideal beam limit. On the basis of the perturbed trajectories, it is clear that $\Delta v_\parallel/v_\parallel \approx \Delta P^2/2p_0^2$; hence, thermal effects are important when

$$\frac{\delta P^2}{p_\parallel^2} \approx \frac{\sqrt{3}}{2\gamma_\parallel^2}\left(\frac{\beta_w^2}{2\beta_\parallel^2} - \frac{\omega_b^2}{\gamma_0 k_w^2 v_\parallel^2}\right)^{1/3} \quad (47)$$

in the high-gain Compton regime, and

$$\frac{\Delta P^2}{p_\parallel^2} \approx \frac{\beta_w}{2\gamma_\parallel^2\beta_\parallel}\sqrt{\frac{\omega_b}{\gamma_0^{1/2}ck_w}} \quad (48)$$

in the collective Raman regime.

The effect of the thermal spread on the linear growth rate is threefold. In the first place, the wider range of axial velocities introduced thereby results in a broader resonance condition in which the unstable frequency band increases. In the second place, the fact that the bulk axial velocity decreases means that the center frequency of the gain band also decreases. In the third place, the peak growth rate decreases with increasing ΔP. Each of these properties is illustrated in Fig. 1 in which we solve (46) numerically for the growth rate, and plot the magnitude of the growth rate as a function of the frequency for $\Omega_w/ck_w = 0.05$, $\gamma_0 = 2.957$, and $\omega_b/ck_w = 0.1$. Observe that the growth rate peaks for $|\mathrm{Im}\, k|/k_w \approx 0.011$ in the absence of the thermal spread, and decreases by over 100% as the thermal spread increases to $\Delta P/p_0 = 5\%$.

The detailed variation in the peak growth rate and the frequency corresponding to peak growth as a function of ΔP is illustrated in Fig. 2. As shown in the figure, the peak growth rate remains relatively constant for $\Delta P/p_0 < 2\%$ and decreases rapidly thereafter. As a consequence, thermal effects become dominant for $\Delta P/p_0 \geq 3\%$. We expect that for thermal effects to be important

$\Delta v_\parallel/v_\parallel \approx \mathrm{Im}\, k/(k_w + \mathrm{Re}\, k) \approx 0.067\%$ (where $\mathrm{Im}\, k/k_w \approx 0.011$ and $\mathrm{Re}\, k/k_w \approx 15.4$ at peak growth) for this example. This yields an estimate of $\Delta P/p_0 \approx 3.7\%$, which is in reasonable agreement with the numerical solution for the growth rate shown in the figure. The frequency at which peak growth is found drops approximately 2% over this range.

V. PLANAR WIGGLER CONFIGURATIONS

In this case, the interaction occurs principally for plane waves polarized in the direction of the wiggler-induced oscillation, and the vector and scalar potentials for a wave with angular frequency ω are of the form

$$\delta A(z, t) = \tfrac{1}{2}\delta\hat{A}(z)\hat{e}_x \exp(-i\omega t) + \text{c.c.} \quad (49)$$

and

$$\delta\varphi(z, t) = \tfrac{1}{2}\delta\hat{\varphi}(z) \exp(-i\omega t) + \text{c.c.} \quad (50)$$

The analysis is similar to that described for the helical wiggler configuration. As in the case of the helical wiggler analysis, the perturbed distribution function takes the form

$$\delta\hat{f}_b(z, p) = \frac{e}{2c}\left[D_x\frac{\partial}{\partial P_x} + D_z\frac{\partial}{\partial p}\right]F_b(P_x, P_y, p) \quad (51)$$

where the orbit integrals are defined as

$$D_x = \int_0^z dz'\,\frac{\exp(-i\omega\tau(z, z'))}{v_z(z')}\left(i\omega - v_z(z')\frac{\partial}{\partial z'}\right)\delta\hat{A}(z')$$
$$\quad (52)$$

and

$$D_z = \frac{1}{p}\int_0^z dz'\,\frac{\exp(i\omega\tau(z, z'))}{v_z(z')}$$
$$\cdot\left[-cp_z(z')\frac{\partial}{\partial z'}\delta\hat{\varphi}(z') + i\omega p_x(z')\delta\hat{A}(z')\right] \quad (53)$$

$\tau(z, z') \equiv \tau(z) - \tau(z')$. Observe that D_x may be integrated directly to give

$$D_x = -\delta\hat{A}(z) + \delta\hat{A}(0)\exp(i\omega\tau(z, 0)). \quad (54)$$

The source current

$$\delta J(z, t) = [\delta \hat{J}_x(z)\hat{e}_x + \delta \hat{J}_z(z)\hat{e}_z] \exp(-i\omega t) + \text{c.c.} \quad (55)$$

is determined by integration over the perturbed distribution

$$\delta \hat{J}(z) = -\frac{e}{m_e} \int dP_x\, dP_y\, dp\, \frac{p}{\gamma} \delta \hat{f}_b \left[\frac{p}{p_z}\hat{e}_x + \hat{e}_z\right]. \quad (56)$$

Substitution of the perturbed distribution yields, after integration by parts over P_x,

$$\delta \hat{J}_x(z) = \frac{e}{m_e} \int dP_x\, dP_y\, dp\, \frac{p}{\gamma} \left[\frac{\partial}{\partial P_x}\left(\frac{p_x}{p_z}D_x\right) - \frac{p_x}{p_z}D_z\frac{\partial}{\partial p}\right]$$
$$\cdot F_b(P_x, P_y, p) \quad (57)$$

and

$$\delta \hat{J}_z(z) = \frac{e}{m_e} \int dP_x\, dP_y\, dp\, \frac{p}{\gamma} \left[\frac{\partial}{\partial P_x}D_x - D_z\frac{\partial}{\partial p}\right]$$
$$\cdot F_b(P_x, P_y, p). \quad (58)$$

The orbit integrals D_x and D_z which appear in the source currents represent an integration over the unperturbed electron trajectories in the planar wiggler. The characteristic trajectories in a planar wiggler differ from those in a helical wiggler in that the magnitudes of the axial and transverse velocity components are not constant but, rather, oscillate at harmonics of the wiggler period. This, in turn, introduces harmonic components into the dynamics of the interaction. In particular, we observe that in a planar wiggler the Lagrangian time variable characteristic of the electron trajectories is of the approximate form

$$\tau(z) \cong t_0 + \frac{z}{V_\parallel} + \frac{P_x}{P_\parallel}\frac{v_w}{V_\parallel}\frac{1}{k_w V_\parallel}\sin k_w z$$
$$+ \frac{v_w^2}{8V_\parallel^2}\frac{1}{k_w V_\parallel}\sin 2k_w z \quad (59)$$

where it is assumed that both $v_w < V_\parallel$ and $P_x < P_\parallel$. Observe that existence of a nonvanishing canonical momentum introduces an oscillation at the wiggler period into the trajectory.

We express the vector and scalar potentials by application of Floquet's theorem for periodic systems in the form

$$\delta \hat{A}(z) = \sum_{n=-\infty}^{\infty} \delta \hat{A}_n \exp(ik_n z) \quad (60)$$

and

$$\delta \hat{\varphi}(z) = \sum_{n=-\infty}^{\infty} \delta \hat{\varphi}_n \exp(ik_n z) \quad (61)$$

where $k_n = k + nk_w$. Since the gain is exponential in this regime, we may neglect the initial value contributions to the orbit integrals. In the analysis of the thermal regime the dominant contribution of the axial thermal spread occurs within the resonance condition. Hence, if we restrict

the analysis to the resonance associated with the Doppler upshift in frequency then the source currents can be expressed in the form

$$\delta \hat{J}_x(z) \cong -\frac{\omega_b^2}{8\pi\gamma_0 c}\sum_{n=-\infty}^{\infty}\delta \hat{A}_n \exp(ik_n z)$$

$$\times \left(1 - \frac{v_w^2}{4c^2}\sum_{l,m=-\infty}^{\infty}K_m^{(+)}(b_2)\right)$$

$$\cdot \iint dP_x\, dP_y\, G_\perp(P_x, P_y)J_l^2(b_1)$$

$$\cdot \frac{\omega^2 - c^2 k_{n+l+2m+1}^2}{(\omega - k_{n+l+2m+1}V_\parallel)^2}\Bigg)$$

$$+ \frac{\omega_b^2}{16\pi\gamma_0}\sum_{n,l,m=-\infty}^{\infty}k_n\delta\hat{\varphi}_n \exp(ik_{n-1}z)J_m(b_2)$$

$$\cdot [J_m(b_2) - J_{m+1}(b_2)]$$

$$\times \iint dP_x\, dP_y\, G_\perp(P_x, P_y)J_l^2(b_1)$$

$$\cdot \frac{v_w\left(k_{n+l+2m} - \omega\frac{v_\parallel}{c^2}\right)}{(\omega - k_{n+l+2m}V_\parallel)^2} \quad (62)$$

and

$$\delta \hat{J}_z \cong \frac{\omega_b^2}{8\pi\gamma_0\gamma_\parallel^2}\sum_{n,m=-\infty}^{\infty}k_n\,\delta\hat{\varphi}_n \exp(ik_n z)J_m^2(b_2)$$

$$\times \iint dP_x\, dP_y\, G_\perp(P_x, P_y)J_l^2(b_1)$$

$$\cdot \frac{\omega}{(\omega - k_{n+l+2m}V_\parallel)^2}$$

$$- \frac{\omega_b^2}{16\pi\gamma_0}\frac{\omega}{c}\sum_{n,l,m=-\infty}^{\infty}\delta\hat{A}_{n-1}\exp(ik_n z)J_m(b_2)$$

$$\cdot [J_m(b_2) - J_{m+1}(b_2)]$$

$$\times \iint dP_x\, dP_y\, G_\perp(P_x, P_y)J_l^2(b_1)$$

$$\cdot \frac{v_w\left(k_{n+l+2m} - \omega\frac{v_\parallel}{c^2}\right)}{(\omega - k_{n+l+2m}V_\parallel)^2} \quad (63)$$

where $V_\parallel$ and $v_\parallel$ are the bulk axial velocities with and without the pitch angle spread, respectively, and J_l denotes the regular Bessel function of the first kind. In addition

$$b_1 \equiv \frac{\omega}{k_w V_\parallel}\frac{v_w}{V_\parallel}\frac{P_x}{P_\parallel} \quad (64)$$

$$b_2 \equiv \frac{\omega}{k_w V_\parallel}\frac{v_w^2}{8V_\parallel^2} \quad (65)$$

$$K_m^{(+)}(b_2) \equiv [J_m(b_2) - J_{m\pm 1}(b_2)]^2 \quad (66)$$

and we have made use of the Bessel function relations

$$\frac{2n}{x} J_n(x) = J_{n-1}(x) + J_{n-1}(x) \qquad (67)$$

$$\exp(ib \sin\theta) = \sum_{n=-\infty}^{\infty} J_n(b) \exp(in\theta). \qquad (68)$$

The integrals over the canonical momenta in (62) and (63) may be evaluated using the transverse distribution function, and we find that in the limit in which $P_\perp \ll p_\parallel$

$$\iint dP_x \, dP_y \, G_\perp(P_x, P_y) \frac{J_l^2(b_1)}{(\omega - kV_\parallel)^2} \cong \frac{T_l(\zeta)}{(\omega - kv_\parallel)^2} \qquad (69)$$

where

$$T_l(\zeta) = \frac{\zeta^2}{2\pi} \int_0^{2\pi} d\phi \int_0^{\infty} dz \, \exp(-z) \frac{J_l^2(b_1)}{(z + \zeta)^2} \qquad (70)$$

$$\zeta = \frac{\gamma_0^2 m_e^2}{\Delta P^2} \left(\frac{\omega^2}{k^2} - v_\parallel^2 \right) \qquad (71)$$

and we write that

$$b_1 = \frac{\omega}{k_w v_\parallel} \frac{v_w}{v_\parallel} \frac{\Delta P}{p_\parallel} z^{1/2} \cos\phi. \qquad (72)$$

If we now select a specific harmonic (i.e., for fixed l and m), then the coupled mode equations may be written as

$$\left[(\omega - k_{n+l+2m} v_\parallel)^2 - \frac{\omega_b^2}{\gamma_0 \gamma_\parallel^2} T_l(\zeta_{n+l+2m}) \right] \delta\hat{\varphi}_n J_m(b_2)$$

$$\cong -\frac{\omega_b^2}{\gamma_0 k_n} \frac{v_w}{2c} \delta\hat{A}_{n-1} T_l(\zeta_{n+l+2m}) \left(k_{n+l+2m} - \omega \frac{v_\parallel}{c^2} \right)$$

$$\cdot [J_m(b_2) - J_{m+1}(b_2)] \qquad (73)$$

and

$$\left[\omega^2 - c^2 k_{n-1}^2 - \frac{\omega_b^2}{\gamma_0} \left(1 - \frac{v_w^2}{4c^2} K_m^{(+)}(b_2) \right. \right.$$

$$\left. \left. \cdot \frac{\omega^2 - k_{n+l+2m}^2 c^2}{(\omega - k_{n+l+2m} v_\parallel)^2} T_l(\zeta_{n+l+2m}) \right) \right] \delta\hat{A}_{n-1}$$

$$\cong -\frac{\omega_b^2}{2\gamma_0} \frac{k_n v_w}{(\omega - k_{n+l+2m} v_\parallel)^2} \delta\hat{\varphi}_n T_l(\zeta_{n+l+2m})$$

$$\times \left(k_{n+l+2m} - \omega \frac{v_\parallel}{c^2} \right) J_m(b_2) [J_m(b_2) - J_{m+1}(b_2)] \qquad (74)$$

where

$$\zeta_{n+l+2m} = \frac{\gamma_0^2 m_e^2}{\Delta P^2} \left(\frac{\omega^2}{k_{n+l+2m}^2} - v_\parallel^2 \right). \qquad (75)$$

The dispersion equation is found by requiring that the determinant of the coefficients vanishes. Therefore, for a specific choice of harmonic interaction, the dispersion equation which results is expressed as a straightforward generalization of that found in the cold beam limit; specifically

$$\left[(\omega - k_{n+l+2m} v_\parallel)^2 - \frac{\omega_b^2}{\gamma_0 \gamma_\parallel^2} T_l(\zeta_{n+l+2m}) \right]$$

$$\cdot \left(\omega^2 - c^2 k_{n-1}^2 - \frac{\omega_b^2}{\gamma_0} \right)$$

$$\cong -\frac{v_w^2}{4c^2} \frac{\omega_b^2}{\gamma_0} K_m^{(+)}(b_2) T_l(\zeta_{n+l+2m})$$

$$\cdot \left(\omega^2 - c^2 k_{n+l+2m}^2 - \frac{\omega_b^2}{\gamma_0} T_l(\zeta_{n+l+2m}) \right). \qquad (76)$$

This dispersion equation which includes the effect of an axial energy spread for a planar configuration is similar to that found for the corresponding case for a helical wiggler geometry. The differences are as stated previously in that 1) the wiggler amplitude is replaced by the root-mean-square (rms) value, 2) the oscillation in the axial velocity introduces modifications in $K_m^{(\pm)}(b_2)$ and $J_l^2(b_1)$, and 3) harmonic amplification is found in the one-dimensional formulation. The effect of the pitch-angle spread on the axial velocity is the source of the lth harmonic contribution, which has the effect of modifying the thermal function T_l. In order to describe this effect in more detail, we assume that $b_1 \ll 1$ which is valid as long as $P_\perp \ll p_\parallel$. As a result, we expand

$$J_l(b_1) \cong \frac{1}{(l!)^2} \left(\frac{v_w}{2v_\parallel} \right)^{2l} \left(\frac{\omega}{k_w v_\parallel} \right)^{2l} \left(\frac{\Delta P}{p_\parallel} \right)^{2l} z^l \cos^{2l}\phi.$$

$$\qquad (77)$$

As a consequence

$$T_l(\zeta) \cong \frac{(2l)!}{(l!)^4} \left(\frac{v_w}{2v_\parallel} \right)^{2l} \left(\frac{\omega}{k_w v_\parallel} \right)^{2l} \left(\frac{\Delta P}{p_\parallel} \right)^{2l} \zeta^2$$

$$\cdot \exp(\zeta) \int_\zeta^\infty dt \frac{\exp(-t)}{t^2} (t - \zeta)^l. \qquad (78)$$

As in the case of the helical wiggler, the thermal function may be expressed in terms of the exponential integral function. To this end we observe that

$$\zeta^2 \exp(\zeta) \int_\zeta^\infty dt \frac{\exp(-t)}{t^2} (t - \zeta)^l$$

$$= (-1)^l \zeta^{l+1} [1 - (\zeta + l)$$

$$\cdot \exp(\zeta) E_1(\zeta)] + U_l(\zeta) \qquad (79)$$

where

$$U_l(\zeta) = 0, \qquad\qquad\qquad\qquad l < 2$$

$$\sum_{k=2}^{l} \sum_{n=0}^{k-2} \frac{(-1)^{k-n} l! n! \zeta^{l-n}}{k!(l-k)!(k-2-n)!}, \qquad l \geq 2.$$

$$\qquad (80)$$

As a consequence

$$T_l(\zeta) \cong \frac{(2l)!}{(l!)^4} \left(\frac{v_w}{2 v_\parallel}\right)^{2l} \left(\frac{\omega}{k_w v_\parallel}\right)^{2l} \left(\frac{\Delta P}{p_\parallel}\right)^{2l}$$

$$\cdot \{(-1)^l \zeta^{l+1}[1 - (\zeta + l)$$

$$\cdot \exp (\zeta) E_1(\zeta)] + U_l(\zeta)\}. \tag{81}$$

We observe that for $l = 0$ the planar wiggler thermal function reduces to that found for the helical wiggler (43), i.e.,

$$T_0(\zeta) \cong \zeta[1 - \zeta \exp (\zeta) E_1(\zeta)]. \tag{82}$$

This will reproduce a thermal response for the interaction at the fundamental which is similar to that found for the helical geometry

The general dispersion equation (76) has been solved numerically for a case which illustrates the relative growth of the fundamental and the third harmonic. In general, strong harmonic amplification requires a relatively large oscillation in the axial velocity; hence, the growth rate at the harmonics increases rapidly with Ω_w/ck_w. Indeed, the growth rate at the harmonics as predicted by (76) can be larger than that at the fundamental when Ω_w/ck_w exceeds unity. However, this is an unjustifiable conclusion based upon the present type of formulation. It is important to bear in mind that the analysis cannot be applied for arbitrarily large values of this parameter because 1) the idealized one-dimensional model breaks down when the displacement of the electrons from the plane of symmetry becomes large, and 2) the Lagrangian time coordinate (14) has been integrated in (59) under the assumption that $v_w \ll v_\parallel$. Therefore, the analysis of cases in which Ω_w/ck_w is greater than unity requires a fully three-dimensional analysis. We restrict the numerical analysis herein to the case for which $\Omega_w/ck_w = 1$. This is a physically interesting case which is at the fringe of the range of validity of the formulation, and will serve to clearly illustrate the relationship of the harmonics to the fundamental. In addition, we shall assume that $\gamma_0 = 2.957$ and $\omega_b/ck_w = 0.1$ as well. It should also be remarked that in order for the thermal effects to result in substantial growth at the even harmonics, $\Delta P/p_0$ must be of the order of unity as well. Since this is unreasonably high for any well-designed experiment, we shall ignore this effect henceforth, and concentrate on the emission at the odd harmonics.

The magnitude of the growth rate is plotted as a function of frequency in Fig. 3 for the fundamental and the third harmonic. The fundamental exhibits a peak growth rate of $|\text{Im } k|/k_w \approx 0.065$ at a normalized frequency of $\omega/ck_w \approx 1.55$. In contrast, the magnitude of the growth rate at the third harmonic is $|\text{Im } k|/k_w \approx 0.012$ at a frequency of $\omega/ck_w \approx 4.80$. Observe that both the magnitude and bandwidth of the harmonic is reduced relative to the fundamental.

The effect of the thermal spread on the fundamental and the third harmonic is shown in Fig. 4. Here we plot the normalized growth rate (defined as the ratio of the maxi-
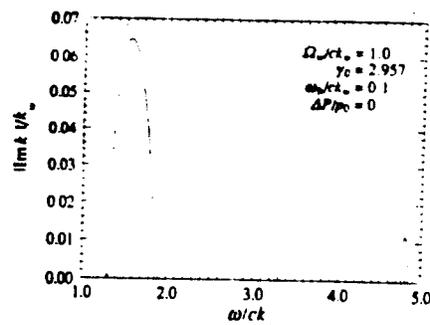

Fig. 3. Graph of the growth rate versus frequency for the fundamental and third harmonic interactions.
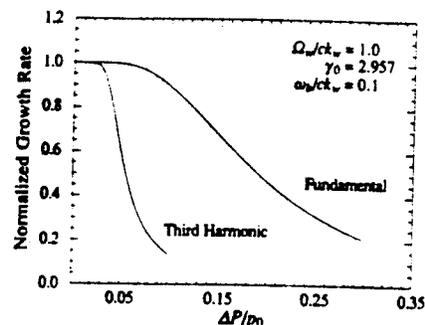

Fig. 4. Variation of the normalized growth rates at the fundamental and third harmonic with the axial momentum spread.

mum growth rate for a specific value of $\Delta P/p_0$ to the maximum growth rate for $\Delta P/p_0 = 0$) as a function of $\Delta P/p_0$ for the fundamental and third harmonic. Observe that thermal effects are expected to become important on the fundamental when $\Delta v_\parallel/v_\parallel \approx |\text{Im } k|/(k_w + \text{Re } k) \approx 0.025$, which corresponds to $\Delta P/p_0 \approx 22\%$ (recall that $\Delta v_\parallel/v_\parallel \approx \Delta P^2/2p_0^2$). This is in substantial agreement with the results shown in the figure. For the case of the harmonics, thermal effects are expected to become important at a much reduced thermal spread [7], [10]; specifically, when $\Delta v_\parallel/v_\parallel \approx |\text{Im } k|/[(1 + 2m)k_w + \text{Re } k]$. For the third harmonic in the present example $\Delta v_\parallel/v_\parallel \approx |\text{Im } k|/(3k_w + \text{Re } k) \approx 0.0015$. This corresponds to $\Delta P/p_0 \approx 5.5\%$, which is also in good agreement with the calculation.

VI. SUMMARY AND DISCUSSION

In this paper, we have developed a self-consistent formulation of the linear gain in both helical and planar wiggler configurations in the presence of an axial energy spread derived from a beam pitch-angle spread. Such a beam may be thought of as monoenergetic but with a non-vanishing emittance. The analysis included collective Raman effects for both the helical and planar wiggler systems, and described the gain at harmonics in the case of a planar wiggler. General dispersion equations were derived, and solved numerically, for each wiggler configuration which included a general thermal function which described the effect of the pitch-angle spread.

The conclusions from the analysis are consistent with those found previously on the basis of an analytic model of thermal effects due to an energy spread [7] and a nonlinear simulation using the pitch-angle spread model [13], [14]. Specifically, that the gain at the harmonics is more sensitive to the effects of a thermal spread than is the fundamental. In particular, the thermal effect becomes important when $\Delta v_\parallel / v_\parallel \approx |\text{Im } k| / [(1 + 2m)k_w + \text{Re } k]$. In addition, it is clear that the thermal effect itself can give rise to amplification at the even as well as odd harmonics. However, this process requires a large energy spread which will result in relatively low growth rates, and is not likely to be of practical use.

References

[1] B. Girard, Y. Lapierre, J. M. Ortega, C. Bazin, M. Billardon, P. Ellaume, M. Bergher, M. Velghe, and Y. Petroff, "Optical frequency multiplication by an optical klystron," *Phys. Rev. Lett.*, vol. 53, pp. 2405–2408, 1984.

[2] S. V. Benson and J. M. J. Madey, "Demonstration of harmonic lasing in a free electron laser," in *Proc., Int. Conf. Lasers '88*, R. C. Sze and F. J. Duarte, Eds. McLean, VA: STS Press, 1989, pp. 189–195.

[3] D. J. Bamford and D. A. G. Deacon, "Measurement of the coherent harmonic emission from a free electron laser oscillator," *Phys. Rev. Lett.*, vol. 62, pp. 1106–1109, 1989.

[4] S. V. Benson and J. M. J. Madey, "Demonstration of harmonic lasing in a free electron laser," *Phys. Rev. A*, vol. 39, pp. 1579–1581, 1989.

[5] R. W. Warren, L. C. Haynes, D. W. Feldman, W. E. Stein, and S. J. Gitomer, "Lasing on the third harmonic," *Nucl. Instrum. Methods*, vol. A296, pp. 84–88, 1990.

[6] W. B. Colson, "The nonlinear wave equation for higher harmonics in free-electron lasers," *IEEE J. Quantum Electron.*, vol. QE-17, pp. 1417–1426, 1981.

[7] R. C. Davidson and W. A. McMullin, "Intense free electron laser harmonic generation in a longitudinal magnetic wiggler," *Phys. Fluids*, vol. 26, pp. 840–847, 1983.

[8] W. B. Colson, G. Dattoli, and F. Ciocci, "Angular-gain spectrum of free-electron lasers," *Phys. Rev. A*, vol. 31, pp. 828–842, 1985.

[9] R. C. Davidson, "Kinetic description of harmonic instabilities in a planar wiggler free electron laser," *Phys. Fluids*, vol. 29, pp. 267–274, 1986.

[10] A. K. Ganguly and H. P. Freund, "Nonlinear analysis of free-electron laser amplifiers in three-dimensions," *Phys. Rev. A*, vol. 32, pp. 2275–2286, 1985.

[11] M. J. Schmitt and C. J. Elliot, "Even-harmonic generation in free electron lasers," *Phys. Rev. A*, vol. 34, pp. 4843–4850, 1986.

[12] H. P. Freund, C. L. Chang, and H. Bluem, "Harmonic generation in free electron lasers," *Phys. Rev. A*, vol. 36, pp. 3218–3221, 1987.

[13] M. J. Schmitt and C. J. Elliot, "The effects of harmonic wiggler field components on free electron laser operation," *IEEE J. Quantum Electron.*, vol. QE-23, pp. 1552–1557, 1987.

[14] H. Bluem, H. P. Freund, and C. L. Chang, "Harmonic content in a planar wiggler based free electron laser amplifier," *Nucl. Instrum. Methods*, vol. A272, pp. 579–585, 1988.

[15] M. J. Schmitt, C. J. Elliot, and B. E. Newman, "Harmonic power implications on free electron laser mirror design," *Nucl. Instrum. Methods*, vol. A272, pp. 586–589, 1988.

[16] H. P. Freund, H. Bluem, and C. L. Chang, "Nonlinear theory and design of a harmonic ubitron/free electron laser," *Nucl. Instrum. Methods*, vol. A285, pp. 169–175, 1989.

[17] E. Jerby and A. Gover, "Investigation of the gain regimes and gain parameters of the free electron laser dispersion equation," *IEEE J. Quantum Electron.*, vol. QE-21, pp. 1041–1058, 1985.

[18] C. W. Roberson, Y. Y. Lau, and H. P. Freund, "Emittance, brightness, free electron laser beam quality, and the scaled thermal velocity," in *High-Brightness Accelerators*, A. K. Hyder, M. F. Rose, and A. H. Guenter, Eds. New York: Plenum, 1986, pp. 627–646.

[19] E. Jerby, "The axial-velocity distribution function and the longitudinal susceptibility of an e-beam in a planar wiggler free-electron laser," *Nucl. Instrum. Methods*, vol. A272, pp. 457–466, 1988.

H. P. Freund, photograph and biography not available at the time of publication.

R. C. Davidson, photograph and biography not available at the time of publication.

D. A. Kirkpatrick, photograph and biography not available at the time of publication.

APPENDIX II

The Relationship Between Optical Guiding and the Relative Phase in Free-Electron Lasers

H.P. Freund and T.M. Antonsen, Jr.

The Relationship Between Optical Guiding and the Relative Phase in Free-Electron Lasers

H. P. Freund and Thomas M. Antonsen, Jr., *Member, IEEE*

Abstract—The relationship between the relative phase and optical guiding in the free-electron laser is studied. The relative phase in this case is defined as the shift in the wavenumber from the vacuum value integrated over the interaction length. In terms of the optical guiding of the signal in free-electron lasers, the relative phase must be positive in order for refractive guiding of the signal to occur. The relative phase is studied from the standpoint of the linear stability analysis in both the high- and low-gain regimes, and the qualitative implications in each of these regimes of the relative phase on the refractive guiding of the signal are identical. Specifically, the relative phase is found to be negative at the low-frequency end of the gain band. The relative phase increases with increasing frequency over this bands until it turns positive at a frequency approximately 10% below the frequency of peak gain. Thus optical guiding is indicated over a large portion, but not all, of the gain band. A quantitative measure of the optical guiding of the signal is obtained by an analytic formulation of the guiding of the signal. This formulation is based upon a separable beam approximation in which the evolution of the signal is determined by a Green's function analysis. The specific example of interest involves the low-gain regime prior to saturation. In this case, it is shown that the analytic result is in substantial agreement with the calculation of the relative phase.

I. Introduction

OPTICAL guiding during the course of the interaction in free-electron lasers refers to the self-focusing of the electromagnetic wave by the electron beam [1]–[12]. Optical guiding of the signal occurs by two related mechanisms referred to as gain and refractive guiding. Gain guiding describes the preferential amplification of radiation in the region occupied by the electron beam. Therefore, an optical ray will undergo amplification as long as it is coincident with the beam. If it propagates out of the beam, then the interaction will cease. Refractive guiding describes the focusing (or defocusing) of the radiation by means of the shift in the refractive index due to the dielectric response of the electron beam. In particular, if the wavenumber is shifted upward due to the interaction with respect to the vacuum state, then the phase velocity of the

wave decreases and the beam acts as an optical guide. It should be remarked, however, that gain and refractive guiding are intimately linked and are not independent processes.

The process of refractive guiding is related to variation in the relative phase, since this quantity measures the shift in the wavenumber due to the dielectric effect of the beam. As shown in the nonlinear simulations of both the helical and planar wiggler configurations the relative phase decreases with axial position at the low-frequency portion of the gain spectrum [13]–[15]. This decrease occurs because the dielectric shift induced by the beam reduces the wavenumber below that of the vacuum state, and corresponds to a defocusing of the signal. As the frequency increases, however, the downshift in the wavenumber decreases until a critical frequency is reached at which the relative phase remains approximately constant. This corresponds to a wavenumber which is comparable to the vacuum state, and for which there is no refraction of the signal. The frequency at which this is found is, typically, below the frequency of peak growth rate. For frequencies higher than the critical point, the relative phase increases with axial position, corresponding to the guiding of the signal.

The organization of the paper is as follows. The behavior of the relative phase as determined from a linear theory of the interaction mechanism is described in Section II. The configuration we employ is that of a planar wiggler model in the idealized one-dimensional limit. In this regard the shift in the wavenumber in the high-gain regime is calculated by the numerical solution of the dispersion equation. This formulation is capable of treating both the collective Raman and the high-gain Compton regimes. In the low-gain regime, the relative phase is calculated on the basis of the evolution of the untrapped electron trajectories in the ponderomotive potential. It should be noted that the results of each of these treatments are in qualitative agreement with the description of either guiding or defocusing described above. The evolution of the wavefront is determined analytically in Section III on the basis of a separable beam model [8]–[11]. In this case, we assume that the electron trajectories are given in the idealized one-dimensional limit. This is valid as long as the electron displacement from the symmetry plane is less than the wiggler period. In addition, it is assumed that the cross-sectional profile of the beam is cylindrically symmetric and determined by a Gaussian decrease in the den-

sity. The radiation field is modeled by the injection of an optical Gaussian mode whose subsequent evolution can be calculated by means of a Green's function. The integration of the kernel is accomplished for parameters consistent with the low-gain regime, and the results are shown to be in substantial agreement with the behavior of the relative phase. A summary and discussion is given in Section IV.

II. OPTICAL GUIDING AND THE RELATIVE PHASE

The physical basis of the optical guiding mechanism can be best understood in terms of the behavior of the relative phase, which is defined as the integrated difference between the wavenumber in the interaction region and the free-space wavenumber. This can be understood most clearly on the basis of the idealized one-dimensional analysis. We first consider the high-gain regime. Under the assumption that $|v_w/v_{\parallel}| \ll 1$, the dispersion equations for both the helical and planar wiggler geometries can be expressed as

$$\left([\omega - (k + k_w)v_{\parallel}]^2 - \frac{\omega_b^2}{\gamma_0\gamma_{\parallel}^3}\right)$$

$$\cdot \left(\omega^2 - c^2k^2 - \frac{\omega_b^2}{\gamma_0}\right) \cong \frac{v_w^2}{c^2}\frac{\omega_b^2}{\gamma_0}\omega c k_w. \quad (1)$$

where ω and k are the angular frequency and wavenumber of the electromagnetic wave, γ_0 denotes the relativistic factor corresponding to the bulk energy of the beam, $v_{\parallel}$ is the bulk axial velocity of the beam $\gamma_{\parallel} = (1 - v_{\parallel}^2/c^2)^{-1/2}$, ω_b is the beam plasma frequency, and

$$\left|\frac{v_w}{c}\right| = \begin{cases} \dfrac{\Omega_w}{ck_w}, & \text{helical wiggler} \\[2mm] \dfrac{\Omega_w}{\sqrt{2}ck_w}, & \text{planar wiggler} \end{cases} \quad (2)$$

denotes the bulk wiggler-induced transverse velocity corresponding to $\Omega_w = eB_w/\gamma_0 m_e c$ for a wiggler amplitude B_w and wavenumber k_w. In order to illustrate the refractive shift in the wavenumber, we transform the wavenumber in (1) to $\delta k = k - \omega/c$, which measures the shift from the vacuum wavenumber. Note that the bulk axial velocity is given by $v_{\parallel}/c = 1 - \gamma_0^{-2} - v_w^2/c^2$. Under the assumptions that $|\delta k| \ll k_0 = (\omega^2 - \omega_b^2/\gamma_0)^{1/2}/c$, and $\omega_b/\gamma_0^{1/2} \ll \omega$, the dispersion equation can be written in the form of a cubic equation

$$(\delta k - k_0)\left[\delta k^2 v_{\parallel}^2 - 2\Delta\omega\,\delta k v_{\parallel} - \left(\Delta\omega^2 - \frac{\omega_b^2}{\gamma_0\gamma_{\parallel}^3}\right)\right] \cong -\frac{v_w^2}{2c^2}\frac{\omega_b^2}{\gamma_0}k_w \quad (3)$$

where $\Delta\omega = (1 - v_{\parallel}/c)\omega - k_w v_{\parallel}$.

The solution to (3) for the real (solid line) and imaginary (dashed line) parts of δk as functions of frequency is shown in Fig. 1 for $\gamma_0 = 3.5$, $v_w/c = 0.05$, and $\omega_b/\gamma_0^{1/2}ck_w = 0.1$. The frequency corresponding to the
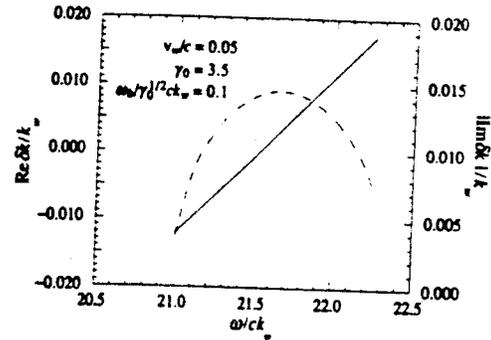

Fig. 1. Graph showing the growth rate (dashed line) and the shift in the wavenumber (solid line) as functions of frequency.

peak growth rate for this choice of parameters is $\omega/ck_w \approx 21.6$. It is clear that the wavenumber is shifted downward from ω/c in the absence of the wiggler (i.e., $\delta k < 0$) for frequencies below $\omega/ck_w \lesssim 21.5$, which is below the frequency of peak growth. In contrast, for frequencies above this critical value, including at peak growth, the wavenumber is shifted upward from the vacuum wavenumber. Hence, the qualitative behavior for the wavenumber in the idealized one-dimensional analysis is the same as that from the three-dimensional nonlinear formulation. The conclusion to be drawn from these results is that the refractive effect of the wave-particle interaction in the wiggler can either guide or defocus the electromagnetic wave depending upon the interaction frequency.

In order to understand the process of optical guiding in the low-gain regime, we consider an analysis of the evolution of the relative phase in an idealized one-dimensional model in which the vector potential of the optical signal is represented in the form

$$\delta A(z, t) = \delta A(z)\hat{e}_x \cos(\omega(z/c - t) + \Delta\phi(z)) \quad (4)$$

where $\Delta\phi$ denotes the relative phase, and both $\Delta\phi$ and the amplitude δA are assumed to be real. The wiggler field is assumed to be given by the idealized one-dimensional representation in which $B_w = B_w\hat{e}_y \sin k_w z$. Substitution of this form for the vector potential into Maxwell's equations yields an equation of the form

$$\delta k(z)\,\delta A(z) \cos[\omega(z/c - t)] + \frac{d}{dz}\delta A(z)$$

$$\cdot \sin[\omega(z/c - t)] \cong \frac{2\pi}{\omega}\delta J_x \quad (5)$$

where δJ_x denotes the source current, $\delta k = d[\delta\phi]/dz$ denotes the perturbed wavenumber, and it is assumed that $|\delta k| \ll \omega/c$. Note that second-order derivatives of the amplitude and phase have been neglected in (5). Multiplication by $\cos[\omega(z/c - t)]$ and subsequent averaging of the resulting equation over a wave period yields

$$\delta k \cong \frac{2}{\delta A}\int_0^{2\pi/\omega} dt\,\delta J_x \cos[\omega(z/c - t)]. \quad (6)$$

Under the assumption that $v_x \approx v_w \cos k_w z$, therefore, the perturbed wavenumber becomes

$$\delta k \cong \frac{\omega_b^2}{2\omega c}\frac{v_w}{c}\frac{1}{\delta a}\langle\cos\psi\rangle \quad (7)$$

where ψ denotes the ponderomotive phase, ω_b is the beam plasma frequency, $\delta a = e\delta A/m_e c^2$ is the normalized amplitude, and the average is taken over the initial phase. Observe that the corresponding equation for the small-signal gain is obtained by multiplication by $\sin[\omega(z/c - t)]$.

The phase average may be determined by solution of the pendulum equation in the untrapped limit. The evolution of the ponderomotive phase in the combined electromagnetic and magnetostatic fields is governed by the nonlinear pendulum equation

$$\frac{d^2}{dz^2}\psi = K^2 \sin\psi \qquad (8)$$

where

$$K^2 = \delta a \frac{v_w}{v_\parallel} \frac{\omega^2/c^2}{2\gamma_0\gamma_\parallel^3\beta_\parallel^3}. \qquad (9)$$

In the linear regime, the solutions describe untrapped trajectories which may be determined by a perturbative solution to (8). In this case we expand $\psi = \psi_0 + \Delta kz + \delta\psi$, where ψ_0 is the initial phase

$$\Delta k = -\frac{\omega}{v_\parallel}\left(1 - \frac{v_\parallel}{c}\right) + k_w \qquad (10)$$

describes the mismatch parameter, and it is assumed that $|\delta\psi/\psi| \ll 1$. To lowest order in the perturbation, therefore, the pendulum equation can be expressed in the form

$$\frac{d^2}{dz^2}\delta\psi \cong K^2 \sin(\psi_0 + \Delta kz). \qquad (11)$$

Subject to the initial conditions that $\delta\psi(z = 0) = 0$ and $d\delta\psi(z = 0)/dz = 0$, this equation has the solution

$$\delta\psi \cong -\frac{K^2}{\Delta k^2}[\sin(\psi_0 + \Delta kz) - \sin\psi_0 + \Delta kz \cos\psi_0]. \qquad (12)$$

As a consequence

$$\langle\cos\psi\rangle \cong \frac{K^2}{2\Delta k^2}[1 - \cos\Delta kz - \Delta kz \sin\Delta kz] \qquad (13)$$

and

$$\langle\sin\psi\rangle \cong -\frac{K^2}{2\Delta k^2}[\sin\Delta kz - \Delta kz \cos\Delta kz]. \qquad (14)$$

Hence, the perturbed wavenumber is given by

$$\delta k(z) \cong \frac{\omega_b^2}{8\gamma_0\gamma_\parallel^2 v_\parallel^2} \frac{v_w^2}{v_\parallel^2} \frac{\omega}{c\Delta k^2}$$

$$\cdot [1 - \cos\Delta kz - \Delta kz \sin\Delta kz]. \qquad (15)$$

The relative phase is found by integration of (15) over axial position; hence, the relative phase at the end of the wiggler (i.e., $z = L$) is given by
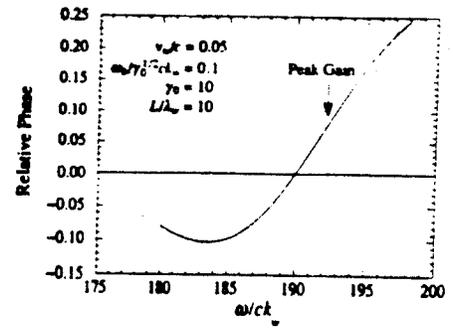

Fig. 2. The relative phase as a function of frequency within the gain band as calculated from the idealized one-dimensional model of the low-gain regime.

$$\delta\phi(L) \cong \frac{\omega_b^2 kL^3}{16\gamma_0\gamma_\parallel^2 v_\parallel^2} \frac{v_w^2}{2v_\parallel^2} \frac{4}{\Delta k^2 L^2}$$

$$\cdot \left[1 + \cos\Delta kL - \frac{2}{\Delta kL}\sin\Delta kL\right]. \qquad (16)$$

The relative phase has been evaluated for a choice of parameters in which $\gamma_0 = 10$, $v_w/c = 0.05$, $\omega_b/\gamma_0^{1/2}ck_w = 0.1$, and a wiggler with $L = 10\lambda_w$ in length, and the results are illustrated in Fig. 2. The gain band for this choice of parameters ranges over $\omega/ck_w \approx 180$–200, and a peak gain of approximately 20% is found at $\omega/ck_w \approx 192$. As shown in the figure, the relative phase is positive at the high-frequency portion of the gain band which includes the frequency of peak gain.

III. THE SEPARABLE BEAM LIMIT

The fundamentals of the optical guiding process can best be understood in terms of a separable beam approximation [8]–[11] in which the wiggler-driven source current is decomposed into a product of functions depending upon radius and axial position. Hence, the electron beam is assumed to be cylindrically symmetric. The electron trajectories are treated in the context of an idealized one-dimensional approximation of the planar wiggler geometry. This model has the considerable advantage of allowing an analytic solution for the radiation spot size, and is generally valid as long as the beam radius is much less than either the spot size of the radiation and the wiggler period.

The idealized planar wiggler geometry implies that the interaction will be with a cylindrically symmetric plane polarized wave in which the vector potential of the electromagnetic field is expressed in the form

$$\delta A(r, z, t) = \frac{1}{2}\delta A(r, z)\ell_x \exp[i\omega(z/c - t)] + c.c. \qquad (17)$$

for an angular frequency ω and wavenumber ω/c. Substitution of this form of the vector potential into Maxwell's equations yields a dynamical equation of the form

$$\left(\frac{1}{r}\frac{\partial}{\partial r}r\frac{\partial}{\partial r} + 2i\frac{\omega}{c}\frac{\partial}{\partial z}\right)\delta A(r, z)$$

$$= -\frac{8\pi}{c}\delta J_x(r, z)\exp[-i\omega(z/c - t)] \qquad (18)$$

where the source current is defined as

$$\delta J_x(r, z) = -en_b(r)v_{z0} \int_{-\infty}^{\infty} dt_0\, \sigma(t_0)\, \frac{v_x}{|v_z|}\, \delta[t - \tau(z, t_0)]$$

(19)

where $n_b(r)$ notes the radial variation of the ambient beam density, $\tau(z, t_0)$ is the Lagrangian time coordinate which describes the time at which an electron which enters the interaction region at time t_0 reaches the axial position z, v_{z0} denotes the initial axial velocity, and $\sigma(t_0)$ denotes the distribution in entry times. As a consequence, averaging (18) over a wave period gives a dynamical equation of the form

$$\left(\frac{1}{r}\frac{\partial}{\partial r}r\frac{\partial}{\partial r} + 2i\frac{\omega}{c}\frac{\partial}{\partial z}\right)\delta a(r, z)$$

$$= \frac{\omega_b^2(r)}{c^2}\beta_{z0}\frac{v_w}{v_\parallel}\langle\exp(-i\psi)\rangle$$

(20)

where $\beta_{z0} \equiv v_{z0}/c$, $\omega_b^2(r) \equiv 4\pi e^2 n_b(r)/m_e$, $\psi \equiv (\omega/c + k_w)z - \omega t$ denotes the ponderomotive phase, $\delta a \equiv e\delta A/m_e c^2$, the orbits are given in the idealized approximation subject to the requirement that $|v_w/v_\parallel| \ll 1$, and the average is over the initial phase. The dynamical equation is solved for an electron beam with a Gaussian density profile

$$n_b(r) = n_{b0}\exp(-r^2/r_b^2)$$

(21)

where n_{b0} denotes the maximum density on-axis and r_b is the Gaussian beam radius.

The solution of the dynamical equation is may be written in terms of a Green's function which satisfies the equation

$$\left(\frac{1}{r}\frac{\partial}{\partial r}r\frac{\partial}{\partial r} + 2i\frac{\omega}{c}\frac{\partial}{\partial z}\right)G(r, z - z')$$

$$= \frac{\omega}{c}\exp(-r^2/r_b^2)\delta(z - z').$$

(22)

Equations (20) and (22) can be combined to yield

$$\int_0^{\infty} dr \int_0^{z'+0^+} dz \left[\delta a(r, z)\,\delta(z - z')\right.$$

$$\left. - \frac{\omega_{b0}^2}{\omega c}\beta_{z0}\frac{v_w}{v_\parallel}G(r, z' - z)\langle\exp(-i\psi(z))\rangle\right]$$

$$= \frac{c}{\omega}\int_0^{\infty} dr \int_0^{z'+0^+} dz \left[\frac{\partial}{\partial r}\left(r\delta a(r, z)\frac{\partial}{\partial r}G(r, z' - z)\right)\right.$$

$$\left. - \frac{\partial}{\partial r}\left(rG(r, z' - z)\frac{\partial}{\partial r}\delta a(r, z)\right)\right]$$

$$- 2i\int_0^{\infty} dr\,r \int_0^{z'+0^+} dz \left[\delta a(r, z)\frac{\partial}{\partial z}G(r, z' - z)\right.$$

$$\left. + G(r, z' - z)\frac{\partial}{\partial z}\delta a(r, z)\right].$$

(23)

The first integral on the right-hand side of (23) vanishes subject to the requirements that

$$\delta a(r = \infty, z) = G(r = \infty, z - z') = 0$$

(24)

and

$$\left.\frac{\partial}{\partial r}\delta a(r, z)\right|_{r=\infty} = \left.\frac{\partial}{\partial r}G(r, z - z')\right|_{r=\infty} = 0.$$

(25)

The second integral on the right-hand side yields the homogeneous solution in the absence of the interaction. Hence, the solution in terms of the this Green's function is

$$\delta a(r, z) = \delta a_h(r, z) + \frac{\omega_{b0}^2}{c^2}\beta_{z0}\frac{v_w}{v_\parallel}\frac{c}{\omega}$$

$$\cdot \int_0^z dz'\,G(r, z' - z)\langle\exp(-i\psi(z'))\rangle$$

(26)

where $\omega_{b0}^2 \equiv 4\pi e^2 n_{b0}/m_e$, and $\delta a_h(r, z)$ denotes the homogeneous solution which describes the evolution of the vector potential in the absence of the beam.

We now consider the low-gain regime. In order to describe the focusing or defocusing of the radiation due to the interaction, we define an *average* field in the form

$$\langle\delta a(r, z)\rangle_r \equiv \frac{2}{r_b^2}\int_0^{\infty} dr\,r\exp(-r^2/r_b^2)\delta a(r, z).$$

(27)

This is a weighted average over the cross section of the electron beam which is a measure of the effective field experienced by the electrons. In the low-gain regime, the ponderomotive phase is determined by the solution of the pendulum equation (8) in the untrapped regime. Utilization of this average vector potential in the definition of K^2 in (9), therefore, gives a phase average which varies as

$$\langle\exp(\pm i\psi(z))\rangle \cong \frac{K^2}{2\Delta k^2}[1 - \exp(\pm i\Delta kz)$$

$$\pm i\Delta kz\exp(\pm i\Delta kz)]$$

(28)

where

$$K^2 \equiv \langle\delta a(r, z)\rangle_r \frac{v_w}{v_\parallel}\frac{\omega^2/c^2}{2\gamma_0\gamma_\parallel^2\beta_\parallel^2}.$$

(29)

It may be verified by substitution that the Green's function is

$$G(r, z - z') = \frac{1}{2i}\frac{\exp[r^2/r_b^2(1 + 2i(z - z')/z_b)]}{1 + 2i(z - z')/z_b}$$

$$\cdot H(z - z')$$

(30)

where $H(z)$ denotes the Heaviside function, and $z_b \equiv \omega r_b^2/c$. As a consequence, the average field can be expressed as

$$\langle\delta a(r, z)\rangle_r = \frac{\langle\delta a_h(r, z)\rangle_r}{S(z)}$$

(31)

where

$$S(z) = 1 + \left(\frac{v_w'}{v_1}\right)^2 \frac{\omega_{b0}^2 r_b^2}{16\gamma_0\gamma_\parallel^2 v_\parallel^2} \frac{\omega^2}{c^2\Delta k^2}$$

$$\cdot \left\{ 1 + \ln\left(1 + i\frac{z}{z_b}\right) - \exp(-i\Delta kz) \right.$$

$$- i[1 + \Delta k(z_b + iz)] \exp(-i\Delta kz)$$

$$\left. \cdot \int_0^{z/z_b} dx \frac{\exp(i\Delta ikz_b x)}{1 + ix} \right\}. \tag{32}$$

If the homogeneous solution is given in terms of a Gaussian beam which is focused down to the minimum spot size at $z = 0$, then [16]

$$\delta a_h(r, z) = \delta a_0 \frac{\exp[r^2/r_0^2(1 + 2iz/z_0)]}{1 + 2iz/z_0} \tag{33}$$

where δa_0 is real and denotes the initial amplitude of the field, r_0 denotes the Gaussian radius of the beam, and $z_0 = \omega r_0^2/c$ denotes the Rayleigh length. As a consequence

$$\langle\delta a_h(r, z)\rangle_r = \frac{\delta a_0}{1 + \frac{r_b^2}{r_0^2} + 2i\frac{z}{z_0}}. \tag{34}$$

An effective *focusing factor* may be defined in terms of this average field in the form

$$\mathcal{F}(z) = \frac{|\langle\delta a(r, z)\rangle_r|^2}{\frac{2}{r_b^2}\int_0^\infty drr |\delta a(r, z)|^2}. \tag{35}$$

Since the homogeneous solution for the vector potential describes the propagation of the signal in the absence of the beam, the focusing factor measures the evolution of the radiation spot size relative to the diffraction of the Gaussian beam in free space.

The denominator can be determined by energy conservation arguments. Returning to the dynamical equation for the field (20), we observe that

$$\delta a^* \left(\nabla_\perp^2 + 2i\frac{\omega}{c}\frac{\partial}{\partial z}\right)\delta a$$

$$= \frac{\omega_{b0}^2}{c^2}\beta_{z0}\frac{v_w}{v_1}\exp(-r^2/r_b^2)\delta a^*\langle\exp(-i\psi)\rangle \tag{36}$$

and

$$\delta a \left(\nabla_\perp^2 - 2i\frac{\omega}{c}\frac{\partial}{\partial z}\right)\delta a^*$$

$$= \frac{\omega_{b0}^2}{c^2}\beta_{z0}\frac{v_w}{v_1}\exp(-r^2/r_b^2)\delta a\langle\exp(i\psi)\rangle. \tag{37}$$

Subtracting the second equation from the first, we find that

$$2i\frac{\omega}{c}\frac{\partial}{\partial z}|\delta a|^2 = \frac{\omega_{b0}^2}{c^2}\beta_{z0}\frac{v_w}{v_\parallel}\exp(-r^2/r_b^2)$$

$$\cdot [\delta a^*\langle\exp(-i\psi)\rangle - \delta a\langle\exp(i\psi)\rangle]. \tag{38}$$

Observe that we have omitted the terms in $\delta a^*\nabla_\perp^2\delta a - \delta a\nabla_\perp^2\delta a^*$ since they will vanish upon integration over radius. Integration of (38) over both axial position and radius, therefore yields

$$\frac{2}{r_b^2}\int_0^\infty drr |\delta a(r, z)|^2$$

$$\cong \frac{\delta a_0^2}{\left(1 + \frac{r_b^2}{r_0^2} + 4\frac{z^2}{z_0^2}\right)}\left[1 + \frac{r_b^2}{r_0^2} + 4\frac{z^2}{z_0^2} + G(z)\right] \tag{39}$$

where

$$G(z) \cong -\frac{\omega_{b0}^2 kz^3}{16\gamma_0\gamma_\parallel^2 v_\parallel^2}\frac{v_w^2}{v_\parallel^2}\frac{d}{d\theta}\left(\frac{\sin\theta}{\theta}\right)^2 \tag{40}$$

is the expression for the power gain in the idealized one-dimensional formulation of the fundamental interaction in the low-gain regime, $k = \omega/c$, and $\theta = \Delta kz/2$. Combining (33)–(35) and (39), we find that the focusing-factor over the total length of the system L may be approximated in the form

$$\mathcal{F}(L) \cong \frac{1}{\left[1 + \frac{r_b^2}{r_0^2} + 4\frac{L^2}{z_0^2} + G(L)\right]|S(L)|^2}. \tag{41}$$

Observe that in the limit in which the interaction vanishes (i.e., in the absence of either the beam or the wiggler field) the gain also vanishes and the focusing factor describes the free-space diffraction of the optical beam

$$\mathcal{F}_{fs}(L) \cong \frac{1}{1 + \frac{r_b^2}{r_0^2} + 4\frac{L^2}{z_0^2}}. \tag{42}$$

Hence, the effect of the interaction upon the diffraction of the optical beam can be effectively measured by a normalized focusing factor defined as

$$\mathcal{F}_n(L) = \frac{\mathcal{F}(L)}{\mathcal{F}_{fs}(L)}. \tag{43}$$

Hence, when $\mathcal{F}_n(L) > 1$ the diffraction of the signal is slower than in the free-space limit, and the signal is effective guided. Conversely, when $\mathcal{F}_n(L) < 1$, the diffraction is more rapid than in free space. It is important to remark at this point that the focussing factor as determined by the separable beam analysis implicitly includes the effects of both gain and refractive guiding.

The specific example under consideration is that of a system for which $v_w/c = 0.05$, $\omega_{b0}/\gamma_0^{1/2}ck_w = 0.1$, and
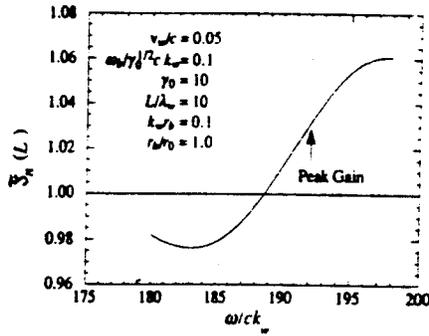
Fig. 3. Illustration of the normalized focussing factor for representative parameters in the low-gain regime.

$\gamma_0 = 10$. Further, it is assumed that there are 10 wiggler periods within the interaction length (i.e., $L/\lambda_w = 10$), $k_w r_b = 0.1$, and that the optical beam radius is focused down to the beam radius upon the entry to the wiggler (i.e., $r_b = r_0$). Observe that this choice of parameters corresponds to that used in the calculation of the relative phase in the idealized one-dimensional regime shown in Fig. 2. The peak gain in the idealized one-dimensional limit for this choice of parameters over length L is of the order of 20% and occurs for $\omega/ck_w \approx 191.7$. The focusing-factor at $z = L$ associated with this choice of parameters is shown in Fig. 3 for frequencies within the gain band. It is evident that the indicated diffraction of the radiation found on the basis of the calculation of the relative phase and the separable beam limits is qualitatively similar. That is, that the diffraction is slower than the free-space value for the low-frequency portion of the gain

The separable beam model can also be used to analyze optical guiding in the high-gain regime [9], [11]. The dispersion relation is obtained from (26) and the one-dimensional equation of motion by looking for solutions which grow exponentially in axial position. Rather than repeat the derivation here, we merely quote the result. First, we note that in the Compton regime (1) can be rewritten as

$$[\omega - (k + k_w)v_1]^2 = -\frac{v_w^2}{c^2}\frac{\omega_b^2}{\gamma_0}\frac{\omega k_w/c}{k^2 - \omega^2/c^2}. \quad (44)$$

Inclusion of the effects of diffraction modifies this result, and we find that

$$[\omega - (k + k_w)v_1]^2$$
$$= 2\pi \frac{v_w^2}{c^2}\frac{\omega_{b0}^2 r_b^2}{\gamma_0}\frac{\omega k_w}{c} E\left[\frac{r_b^2}{2}(k^2 - \omega^2/c^2)\right] \quad (45)$$

where $E(\nu)$ is defined as

$$E(\nu) \equiv \frac{1}{4\pi i}\int_0^\infty dx \frac{\exp(-i\nu x)}{1 + ix}. \quad (46)$$

Observe that (45) reduces to (44) in the limit in which $|r_b^2[k^2 - \omega^2/c^2]| \ll 1$ where diffraction is unimportant. Solutions for growth rates and filling factors in the high-gain limit obtained from (45) can be found in [11].

IV. SUMMARY AND DISCUSSION

A great deal of work has been devoted to the question of optical guiding in free-electron lasers [1]–[12]. The principal thrust of the present work has been to clarify the connection between the relative phase, which measures the shift in the wavenumber induced by the free-electron laser interaction, and the optical guiding of the signal. In this regard, we have evaluated the relative phase within the context of a linear theory of the interaction in both the high- and low-gain regimes. The qualitative conclusions drawn from this analysis indicate that optical, or at least the refractive, guiding of the signal does not occur over the entire gain band. In particular, we find that the relative phase is negative indicating that a defocusing of the signal should occur at the low-frequency portion of the gain band. As the frequency increases, the relative phase also increases, however, until a critical frequency is reached at which the relative phase vanishes. This point typically is found to occur at a frequency approximately 10% below the frequency of maximum growth rate. For still higher frequencies, the relative phase is positive and some guiding of the signal should occur.

The qualitative estimates of refractive guiding based upon the relative phase are compared with a more quantitative analysis of the diffraction of an optical Gaussian mode by means of a Green's function solution of Maxwell's equations in the low-gain regime under the assumption of a separable beam approximation. In this case, a *focusing factor* was derived which measures the diffraction of the signal due to the interaction relative to the diffraction in free space. It is important to note here that this Green's function approach implicitly includes both gain and refractive guiding. The results of this analysis are in substantial agreement with the qualitative conclusions based upon the behavior of the relative phase, and indicate that a small degree of guiding is possible even in the low-gain regime.

REFERENCES

[1] N. M. Kroll, P. L. Morton, and M. N. Rosenbluth, "Free-electron lasers with variable parameter wigglers," *IEEE J. Quantum Electron.*, vol. QE-17, pp. 1436–1468, 1981.

[2] P. Sprangle and C. M. Tang, "Three-dimensional nonlinear theory of the free-electron laser," *Appl. Phys. Lett.*, vol. 39, pp. 677–679, 1981.

[3] G. T. Moore, "High-gain small-signal modes of the free-electron laser," *Opt. Commun.*, vol. 52, pp. 46–51, 1984.

——, "High-gain small-signal modes of the free-electron laser: II. The effect of electron energy spread," *Opt. Commun.*, vol. 54, pp. 121–125, 1985.

[4] ——, "The high gain regime of the free-electron laser," *Nucl. Instrum. Methods*, vol. A239, pp. 19–28, 1985.

[5] E. T. Scharlemann, A. M. Sessler, and J. S. Wurtele, "Optical guiding in a free-electron laser," *Phys. Rev. Lett.*, vol. 54, pp. 1925–1928, 1985.

[6] M. Xie and D. A. G. Deacon, "Theoretical study of FEL active guiding in the small signal regime," *Nucl. Instrum. Methods*, vol. A250, pp. 426–431, 1986.

[7] P. Sprangle, A. Ting, and C. M. Tang, "Radiation focusing and guiding with application to the free-electron laser," *Phys. Rev. Lett.*, vol. 59, pp. 202–205, 1987.

[8] R. H. Pantell and J. Feinstein, "FEL mode propagation at satura-

tion," *IEEE J. Quantum Electron.*, vol. QE-23, pp. 1534-1538, 1987.

[9] T. M. Antonsen and B. Levush. "Optical guiding in the separable beam limit," *Nucl. Instrum. Methods*, vol. A272, pp. 472-476, 1988.

[10] T. M. Antonsen and G. Laval. "Suppression of sidebands by diffraction in a free-electron laser," *Phys. Fluids B*, vol. 1, pp. 1721-1727, 1989.

[11] N. Metzler, T. M. Antonsen, and B. Levush, "Nonlinear optical guiding in the separable beam limit," *Phys. Fluids*, vol. B2, pp. 1038-1045, 1990.

[12] H. P. Freund and C. L. Chang. "Effect of the lower beat wave on optical guiding in planar wiggler free-electron lasers," *Phys. Rev. A*, vol. 42, pp. 6737-6751, 1990.

[13] H. P. Freund and A. K. Ganguly. "Phase variation in free-electron lasers," *IEEE J. Quantum Electron.*, vol. QE-23, pp. 1657-1665, 1987.

[14] H. P. Freund, H. Bluem, and C. L. Chang. "Three-dimensional nonlinear analysis of free-electron laser amplifiers with planar wigglers," *Phys. Rev. A*, vol. 36, pp. 2182-2198, 1987.

[15] H. P. Freund, "Multimode nonlinear analysis of free-electron laser amplifiers in three dimensions." *Phys. Rev. A*, vol. 37, pp. 3371-3380, 1988.

[16] A. Yariv. *Quantum Electronics*, 2nd ed. New York: Wiley, 1967, p. 110.

H. P. Freund, photograph and biography not available at the time of publication.

Thomas M. Antonsen, Jr. (M'87), photograph and biography not available at the time of publication.

APPENDIX III

Self-Consistent Analysis of Wiggler-Field Errors in Free-Electron Lasers

H.P. Freund and R.H. Jackson

Self-consistent analysis of wiggler-field errors in free-electron lasers

H. P. Freund* and R. H. Jackson
Naval Research Laboratory, Washington, D.C. 20375
(Received 9 December 1991)

A self-consistent analysis of wiggler-field errors in free-electron lasers is described using the three-dimensional simulation code WIGGLIN. A random variation is chosen for the pole-to-pole wiggler amplitude, and a continuous map is used between the pole faces. On average, increases in the root-mean-square value of the field causes a decrease in the interaction efficiency; however, this is relatively benign for the specific case studied, and particular error distributions can result in efficiency enhancements.

Free-electron lasers (FEL's) have operated over wavelengths from microwaves [1,2] to the infrared [3,4] and visible spectra [5]. The FEL operates by the coherent axial bunching of electrons in the ponderomotive wave formed by the beating of the wiggler and radiation fields. The interaction is extremely sensitive to the axial energy spread of the electron beam, and an energy spread of 1% or less [6] is sufficient to cause substantial reductions in the efficiency due to the detuning of the wave-particle resonance.

A related effect is caused by random wiggler-field errors. Wigglers can easily exhibit a random rms fluctuation of 0.5% from pole to pole [7]. This yields a velocity fluctuation which causes a phase jitter that also detunes the wave-particle resonance. The purpose of this paper is to explore the effects of wiggler errors on FEL performance, and to compare the effects of wiggler errors with those of an axial energy spread. To this end, a self-consistent treatment of random wiggler errors has been incorporated into the three-dimensional nonlinear simulation code WIGGLIN [8].

The effects of random wiggler errors have been studied using a random-walk model for the electron trajectories, and their effects upon both spontaneous emission [9] and the linear gain [10,11]. Nonlinear modeling of wiggler field errors has been based [11–14] upon the inclusion of an analytic model of the random walk in a wiggler-period averaged formalism of the electron trajectories. In contrast, no average over a wiggler period is performed in WIGGLIN, and no explicit assumption of the random walk is included.

Consideration of the effects of wiggler errors shows that any perturbation induced in one of the pole pieces will induce a series of correlated changes in the field over several adjacent wiggler periods. This effect has been measured in the laboratory on a prototype planar wiggler design [15]. Here, an error was introduced by reducing the gap spacing between one set of pole pieces. An axial scan of the on-axis field showed that the error propagated through ±1 wiggler period (±2 pole pieces for this design) with an increase in amplitude at the adjacent poles of ≈55% and at the next poles of ≈10%. The amplitude and extent of these correlations are dependent upon the detailed design of any given wiggler, and can be substantial. Thus the question of the nature of "random" errors in wiggler magnets requires further study. As a first step, a continuous mapping of random field errors from pole to pole has been included. The effects of correlated errors will be dealt with in later studies for specific wiggler designs.

The WIGGLIN formulation [8] includes the simultaneous integration of a slow-time-scale formulation of Maxwell's equations for an ensemble of TE and TM modes of a rectangular waveguide ($-a/2 \leq x \leq a/2$, $-b/2 \leq y \leq b/2$), as well as the complete Lorentz force equations for an ensemble of electrons. We emphasize that no average of the orbits equations is imposed. The wiggler model includes an adiabatic entry taper which describes the injection of the beam into the wiggler, as well as a model for the description of the wiggler-field errors. As a result, the initial conditions on the electron beam are specified at the entrance to the wiggler, and the subsequent evolution of the electromagnetic field and the electron beam are integrated in a self-consistent manner. Thermal effects are included under the assumption that the electron beam is initially monoenergetic but with a pitch angle spread to describe the axial energy spread.

The configuration employed is that of a planar wiggler with parabolic pole faces for enhanced focusing [1], and can be represented as

$$\mathbf{B}_w(\mathbf{x}) = [B_w(z) + \Delta B_w(z)] \left\{ \cos k_w z \left[\hat{\mathbf{e}}_x \sinh\left[\frac{k_w x}{\sqrt{2}}\right] \sinh\left[\frac{k_w y}{\sqrt{2}}\right] + \hat{\mathbf{e}}_y \cosh\left[\frac{k_w x}{\sqrt{2}}\right] \cosh\left[\frac{k_w y}{\sqrt{2}}\right] \right] \right.$$
$$\left. - \sqrt{2}\,\hat{\mathbf{e}}_z \cosh\left[\frac{k_w x}{\sqrt{2}}\right] \sinh\left[\frac{k_w y}{\sqrt{2}}\right] \sin k_w z \right\}, \tag{1}$$

where k_w denotes the wiggler wave number for a wiggler period λ_w, $B_w(z)$ and $\Delta B_w(z)$ denote the systematic (i.e., nonrandom) and random variations in the amplitude, respectively. The systematic variation in the wiggler amplitude is assumed to be

$$B_w(z) = \begin{cases} B_w \sin^2\left[\dfrac{k_w z}{4N_w}\right], & 0 \le z \le N_w \lambda_w \\ B_w, & N_w \lambda_w < z, \end{cases} \qquad (2)$$

which describes the adiabatic entry taper over N_w wiggler periods.

The random component of the amplitude is chosen at regular intervals using a random number generator, and a continuous map is used between these points. Since a particular wiggler may have several sets of pole faces per wiggler period, the interval is chosen to be $\Delta z = \lambda_w / N_p$, where N_p is the number of pole faces per wiggler period. Hence a random sequence of amplitudes $\{\Delta B_n\}$ is generated, where $\Delta B_n \equiv \Delta B_w(n\Delta z)$. The only restriction is that $\Delta B_w = 0$ over the entry taper region [i.e., $\Delta B_n = 0$ for $0 \le n \le 1 + N_p N_w$] to ensure a positive amplitude. The variation in $\Delta B_w(z)$ between these points is given by

$$\Delta B_w(n\Delta z + \delta z) = \Delta B_n + (\Delta B_{n+1} - \Delta B_n)\sin^2\left[\frac{\pi}{2}\frac{\delta z}{\Delta z}\right],$$

$$(3)$$

where $0 \le \delta z \le \Delta z$. In the rest of this paper it shall be assumed, for simplicity, that $N_p = 1$. Note that it is possible to model the effects of pole-to-pole variations in specific wiggler magnets with this formulation.

The configuration under study is one in which a 3.5-MeV, 850-A electron beam with an initial radius of 1.0 cm propagates through a rectangular waveguide [$a = 9.8$ cm, $b = 2.9$ cm] in the presence of a wiggler with $B_w = 3.72$ kG, $\lambda_w = 9.8$ cm, and $N_w = 5$. Hence the wiggler parameter a_w [$\equiv eB_w/m_e c^2 k_w$] = 3.404. This corresponds to an experiment at Lawrence Livermore National Laboratory [16], and comparisons between WIGGLIN and the experiment show good agreement [8]. WIGGLIN has also been validated by comparison with a fundamental and second-harmonic free-electron laser (FEL) experiment [17,18]. Resonant interaction occurs with the TE_{01}, TE_{21}, and TM_{21} modes at frequencies of 30–40 GHz, and the efficiency decreases with increasing frequency across this band. For an ideal beam and wiggler [i.e., $\Delta\gamma_z = 0$ and $\Delta B_w = 0$] the efficiency falls off from a maximum $\eta = 12.38\%$ at 30 GHz to a minimum of $\eta = 3.58\%$ at 40 GHz. A frequency of 34.6 GHz ($\eta = 8.57\%$) is selected for the comparison.

The effect of the axial energy spread is illustrated in Fig. 1 in which the extraction efficiency is plotted as a function of $\Delta\gamma_z/\gamma_0$ (for $\Delta B_w = 0$). Note that the initial drive powers in the modes were chosen to be 50 kW in the TE_{01} mode, 500 W in the TE_{21} mode, and 100 W in the TM_{21} mode, and that the saturation length varies with $\Delta\gamma_z$. As shown, the efficiency decreases gradually with the axial energy spread (due to the relatively high
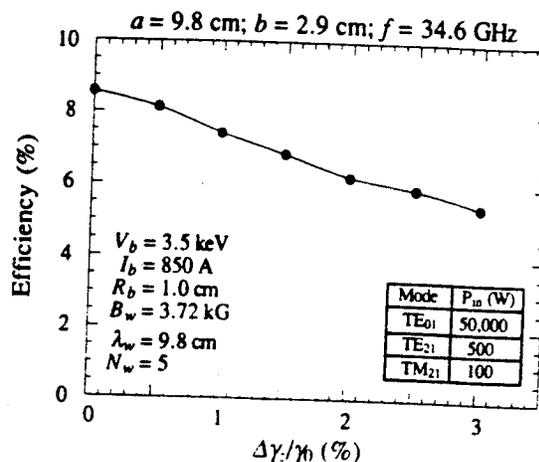

FIG. 1. Variation in the saturation efficiency as a function of the initial axial energy spread.

a_w) for $\Delta\gamma_z/\gamma_0 \le 3\%$, at which point the efficiency has fallen to 5.45%.

Random wiggler fluctuations can take many different forms for a fixed rms value. It is most natural to consider a random fluctuation which is relatively uniform over the interaction region (i.e., $\langle \Delta B_w \rangle = 0$); however, other configurations are possible. For example, fluctuations where the wiggler field is always greater (or less) than the systematic value for B_w are possible, as is one in which ΔB_w is very large over a small range and zero elsewhere. These are only limited examples, and a thorough analysis necessitates a large number of simulation runs with different random wiggler fluctuations to obtain adequate statistics. Typical runs for WIGGLIN on a CRAY-2 supercomputer are ≈ 14 s for $\Delta\gamma_z = 0$. Hence it is possible to make a sufficient number of runs (i.e., if the mean efficiency has converged to within 1%) to obtain good statistics.

The effect of random wiggler errors is shown in Fig. 2 where the efficiency is plotted versus the rms wiggler error (for $\Delta\gamma_z = 0$). The dots represent the average efficiency over the *ensemble* of random fluctuations, and
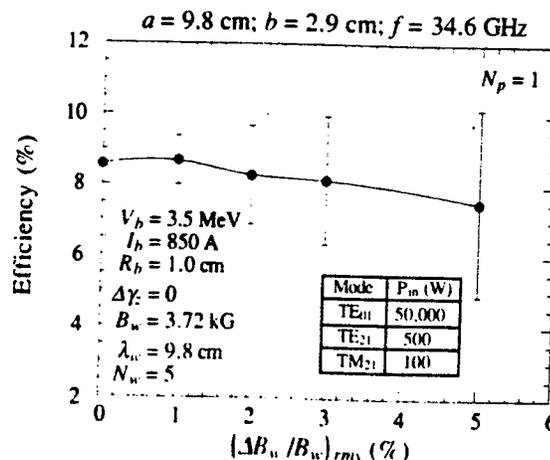

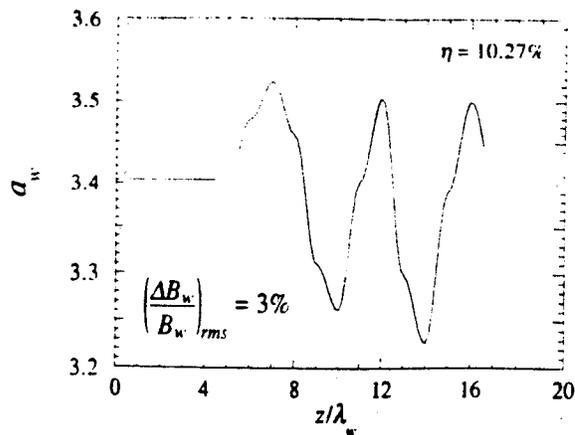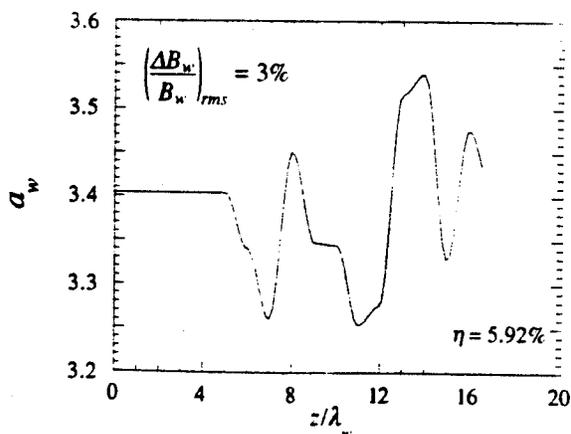FIG. 2. Variation of the saturation efficiency as a function of the rms magnitude of the wiggler-field error.

FIG. 3. The wiggler field as represented by a_w as a function of axial position for $(\Delta B_w/B_w)_{rms} = 3\%$ and a saturation efficiency of $\eta = 10.27\%$.

the error bars denote the standard deviation. As shown, the average efficiency is relatively insensitive to wiggler errors for $(\Delta B_w/B_w)_{rms} \leq 5\%$, although the standard deviation increases with the rms error. For this example, the effect of a given $(\Delta B_w/B_w)_{rms}$ is much more benign than for a comparable $\Delta\gamma_z/\gamma_0$.

Particle loss was not found to be a problem for the range of $(\Delta B_w/B_w)_{rms}$ shown in Fig. 2. As a result, we conclude that the random-walk model is not appropriate for the treatment of wiggler errors. An explanation for this is that, although the wiggler amplitude may vary in a random manner from pole to pole, the field varies in a continuous fashion. As a result, regardless of the detailed model of the wiggler, electrons *do not* experience sudden random impulses but, rather, follow meandering field lines through the wiggler.

Observe that the efficiency increases relative to the ideal wiggler case for some particular wiggler error distributions. In order to understand this, recall that the efficiency varies across the frequency band. This tuning can also be accomplished by variations in the wiggler

magnitude, and an increase (decrease) in the mean B_w can be expected to result in an increase (decrease) in the efficiency as long as the chosen frequency remains in the resonant bandwidth of the interaction. Another way in which the form of the error distribution can affect the efficiency is if the field exhibits a bulk taper either upward or downward over the interaction region. A downward (upward) taper can be expected to increase (decrease) the efficiency. In order to illustrate this, consider the case for which $(\Delta B_w/B_w)_{rms} = 3\%$. Wiggler error distributions which give rise to $\eta = 10.27\%$ and 5.92% (compared to $\eta = 8.57\%$ for an ideal wiggler), respectively, are shown in Figs. 3 and 4. The average a_w for each of these cases is close to the systematic value of 3.404; however, the field exhibits a downward taper in Fig. 3 and an upward taper in Fig. 4.

In general, the statistical distribution of the efficiency differs from the normal distribution, and the standard deviation must be used with some caution. For example, 35 runs were generally required to obtain adequate statistics, and the probability histogram is shown in Fig. 5 for $(\Delta B_w/B_w)_{rms} = 3\%$. Here, the skewness ≈ -0.41 and the kurtosis ≈ 0.92, indicating a distribution skewed below the mean and more peaked than the normal distribution.

In summary, a self-consistent analysis of the effect of random wiggler errors on the saturation efficiency of the FEL has been presented in which no *a priori* assumption of a random walk of the electron orbits has been imposed. For the specific parameters under study, the results indicate that the effects of random wiggler errors are relatively benign, and particle loss was not found to be a problem. Indeed, some error configurations chosen at random were found to result in efficiency enhancements due to effective increases. It is important to note here that experimental quantification of these issues is difficult to obtain. While measurements for $(\Delta B_w/B_w)_{rms}$ are possible to achieve with some accuracy, there is always a greater uncertainty as to beam quality. Hence it is difficult to
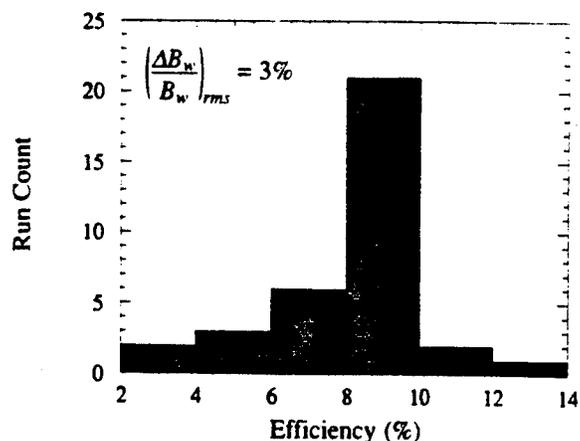

FIG. 4. The wiggler field as represented by a_w as a function of the axial position for $(\Delta B_w/B_w)_{rms} = 3\%$ and a saturation efficiency of $\eta = 5.92\%$.

FIG. 5. Probability histogram of the number of simulation runs vs the saturation efficiency for $(\Delta B_w/B_w)_{rms} = 3\%$. The total number of simulation runs in this sample is 35.

determine the relative importance of wiggler errors in the laboratory. The results of the present work, however, suggest that wiggler errors may not constitute a serious issue for FEL design.

---

*Permanent address: Science Applications International Corporation, McLean, VA 22102.

[1] R. M. Phillips, IRE Trans. Electron Dev. ED-7, 231 (1960).

[2] R. K. Parker, R. H. Jackson, S. H. Gold, H. P. Freund, V. L. Granatstein, P. C. Efthimion, M. Herndon, and A. K. Kinkead, Phys. Rev. Lett. 48, 238 (1982).

[3] L. R. Elias, W. M. Fairbank, J. M. J. Madey, H. A. Schwettman, and T. I. Smith, Phys. Rev. Lett. 36, 717 (1976).

[4] R. W. Warren, B. E. Newnam, J. G. Winston, W. E. Stein, L. M. Young, and C. A. Brau, IEEE J. Quantum Electron. QE-19, 391 (1983).

[5] M. Billardon, P. Ellaume, J. M. Ortega, C. Bazin, M. Bergher, M. Velghe, and Y. Petroff, Phys. Rev. Lett. 51, 1652 (1983).

[6] H. P. Freund and A. K. Ganguly, Phys. Rev. A 34, 1242 (1986).

[7] E. Hoyer, T. Chan, J. Y. G. Chin, K. Halbach, K. J. Kim, H. Winick, and J. Yang, IEEE Trans. Nucl. Sci. NS-30, 3118 (1983).

[8] H. P. Freund, Phys. Rev. A 37, 3371 (1988).

[9] B. M. Kincaid, J. Opt. Soc. Am. B 2, 1294 (1985).

[10] W. P. Marable, E. Esarey, and C. M. Tang, Phys. Rev. A 42, 3006 (1990).

[11] L. H. Yu, S. Krinsky, R. L. Gluckstern, and J. B. J. van Zeijts, Phys. Rev. A 45, 1163 (1992).

[12] C. J. Elliot and B. McVey, in *Undulator Magnets for Synchrotron Radiation and Free Electron Lasers*, edited by R. Bonifacio, L. Fonda, and C. Pellegrini (World Scientific, Singapore, 1987), p. 142.

[13] H. D. Shay and E. T. Scharlemann, Nucl. Instrum. Methods A 272, 601 (1988).

[14] W. P. Marable, C. M. Tang, and E. Esarey, IEEE J. Quantum Electron. QE-27, 2693 (1991).

[15] H. Bluem, Ph.D. thesis, University of Maryland, 1990.

[16] T. J. Orzechowski, B. R. Anderson, J. C. Clark, W. M. Fawley, A. C. Paul, D. Prosnitz, E. T. Scharlemann, S. M. Yarema, D. B. Hopkins, A. M. Sessler, and J. S. Wurtele, Phys. Rev. Lett. 57, 2172 (1986).

[17] H. Bluem, R. H. Jackson, H. P. Freund, D. E. Pershing, and V. L. Granatstein, Phys. Rev. Lett. 67, 824 (1991).

[18] D. E. Pershing, R. H. Jackson, H. Bluem, and H. P. Freund, Nucl. Instrum. Methods A 296, 199 (1990).

APPENDIX IV

Wiggler Imperfections in Free-Electron Lasers

H.P. Freund and R.H. Jackson

Wiggler imperfections in free-electron lasers

H.P. Freund [*,1], R.H. Jackson

Naval Research Laboratory, Washington, DC 20375, USA

A self-consistent 3-D analysis of wiggler imperfections in FELs is described using the WIGGLIN simulation code. WIGGLIN treats the electron dynamics using the 3-D Lorentz force equations, and does not rely on a wiggler-averaged formalism. In the planar wiggler model used, both the divergence and the axial component of the curl vanish identically while the transverse components of the curl are small. In describing wiggler imperfections, a random variation is chosen for the pole-to-pole variations in the amplitude and a continuous map is used between the pole faces. The average efficiency, as well as the standard deviation about the average efficiency, is determined by using an ensemble of different randomly chosen wiggler variations with a fixed rms value. The specific parameters chosen correspond to the 35-GHz ELF experiment conducted at Lawrence Livermore National Laboratory; however, the fundamental physics is relevant to a wide range of FEL experiments. On average, increases in the field imperfections cause a decrease in the efficiency; however, this is relatively benign and is certainly a much less severe constraint than that imposed by electron beam quality considerations. In addition, particular error distributions can result in efficiency enhancements.

1. Introduction

The free-electron laser (FEL) operates by the coherent axial bunching of electrons in the ponderomotive wave formed by the beating of the wiggler and radiation fields. The interaction is extremely sensitive to the axial energy spread of the electron beam, and an energy spread of a percent or less is often sufficient to cause substantial reductions in the efficiency due to the detuning of the wave–particle resonance. A related effect is caused by random wiggler field imperfections. Wigglers can easily exhibit a random rms fluctuation of 0.5% from pole to pole [1]. This yields a velocity fluctuation which causes a phase jitter that also detunes the wave–particle resonance. The purpose of this paper is to explore the effects of wiggler errors on FEL performance, and to compare the effects of wiggler errors with those of an axial energy spread. To this end, a self-consistent treatment of random wiggler errors has been incorporated into the 3-D nonlinear simulation code WIGGLIN [2,3].

The effects of random wiggler imperfections have been studied using a random walk model for the electron trajectories, and their effects upon both spontaneous emission [9] and the linear gain [4,5]. Nonlinear modeling of wiggler field imperfections has been based [5–9] upon the inclusion of an analytic model of the random walk in a wiggler-period averaged formalism of

the electron trajectories. In contrast, no average over a wiggler period is performed in WIGGLIN, and no explicit assumption of the random walk is included.

Consideration of the effects of wiggler errors shows that any perturbation induced in one of the pole pieces will induce a series of correlated changes in the field over several adjacent wiggler periods. This effect has been measured in the laboratory on a prototype REEL planar wiggler design [10]. Here, an error was introduced by reducing the gap spacing between one set of pole pieces. An axial scan of the on-axis field showed that the error propagated through ± 1 wiggler period (± 2 pole pieces for this design) with an increase in amplitude at the adjacent poles of $\approx 55\%$ and at the next poles of $\approx 10\%$. The amplitude and extent of these correlations are dependent upon the detailed design of any given wiggler, and can be substantial. Thus, the question of the nature of "random" imperfections in wiggler magnets requires further study. The effects of correlated imperfections will be dealt with in later studies for specific wiggler designs.

2. The mathematical formulation

The WIGGLIN formulation [2,3] includes the simultaneous integration of a slow-time-scale formulation of Maxwell's equations for an ensemble of TE and TM modes of a rectangular waveguide $[-a/2 \leq x \leq a/2, -b/2 \leq y \leq b/2]$, as well as the complete Lorentz force equations for an ensemble of electrons. The wiggler model includes an adiabatic entry taper which

* Corresponding author.
1 Permanent address: Science Applications International Corp., McLean, VA 22102, USA.

IV. THEORY

describes the injection of the beam into the wiggler, as well as a model for the description of the wiggler field imperfections. As a result, the initial conditions on the electron beam are specified at the entrance to the wiggler, and the subsequent evolution of the electromagnetic field and the electron beam are integrated in a self-consistent manner. Thermal effects are included under the assumption that the electron beam is initially monoenergetic but with a pitch angle spread to describe the axial energy spread.

The effect of wiggler imperfections using the WIGGLIN formulation has been studied in an earlier work using a wiggler model for a planar wiggler based upon parabolic pole faces which is both divergence- and curl-free for the case of a uniform wiggler. However, the divergence and curl for this model were nonvanishing for the case of a nonuniform wiggler. Thus, random imperfections on a short length scale can result in significant deviations from the self-consistent wiggler model even for relatively small wiggler fluctuations. In order to remedy this deficiency, we reconsider the effects of random wiggler imperfections in this paper using an improved planar wiggler model in which [12]

$$
\begin{aligned}
B_{w,x}(x) &= B_w(z)\left[\sin k_w z - \frac{\cos k_w z}{k_w B_w(z)}\frac{\mathrm{d}}{\mathrm{d}z}B_w(z)\right] \\
&\quad \times \left[\sinh k_w y - \frac{Y(k_w y)}{2k_w^2}\frac{\mathrm{d}^2}{\mathrm{d}x^2}\right]\frac{1}{k_w}\frac{\mathrm{d}}{\mathrm{d}x}X(x),
\end{aligned}
\tag{1}
$$

$$
\begin{aligned}
B_{w,y}(x) &= B_w(z)\left[\sin k_w z - \frac{\cos k_w z}{k_w B_w(z)}\frac{\mathrm{d}}{\mathrm{d}z}B_w(z)\right] \\
&\quad \times \left[\cosh k_w y - \frac{k_w y \sinh k_w y}{2k_w^2}\frac{\mathrm{d}^2}{\mathrm{d}x^2}\right]X(x),
\end{aligned}
\tag{2}
$$

$$
\begin{aligned}
B_{w,z}(x) &= B_w(z)\cos k_w z\left[\sinh k_w y\right. \\
&\quad \left. - \frac{Y(k_w y)}{2k_w^2}\left(1 + \frac{1}{k_w^2}\frac{\mathrm{d}^2}{\mathrm{d}x^2}\right)\frac{\mathrm{d}^2}{\mathrm{d}x^2}\right]X(x),
\end{aligned}
\tag{3}
$$

where $B_w(z)$ denotes the axial variation in the wiggler amplitude, $Y(k_w y) \equiv k_w y \cosh k_w y - \sinh k_w y$, and $X(x) \equiv 1 + (x/\alpha_x)^{2m}/2$. Here α_x and m are arbitrary and are used to denote the wiggler gradient in the x-direction.

The wiggler amplitude is decomposed into systematic and random components as follows

$$
B_w(z) = B_w^{(s)}(z) + \Delta B_w(z).
\tag{4}
$$

where

$$
B_w^{(s)}(z) = \begin{cases} B_w \sin^2\left(\dfrac{k_w z}{4N_w}\right); & 0 \le z \le N_w \lambda_w, \\ B_w; & N_w \lambda_w < z, \end{cases}
\tag{5}
$$

describes the systematic component. The random component of the amplitude, $\Delta B_w(z)$, is chosen at regular intervals using a random number generator, and a continuous map is used between these points. The systematic variation in the wiggler amplitude given in Eq. (5) describes an adiabatic entry taper over N_w wiggler periods, and allows us to self-consistently describe the injection of the beam into the wiggler. In the description of the random variation, we note that a particular wiggler may have several sets of pole faces per wiggler period, each of which may vary in a random fashion. Hence, the interval between the random fluctuations in the amplitude is chosen to be $\Delta z = \lambda_w/N_p$, where N_p is the number of pole faces per wiggler period. A random sequence of amplitudes $\{\Delta B_n\}$ is then generated, where $\Delta B_n = \Delta B_w(n\Delta_z)$. The only restriction is that we require $\Delta B_w = 0$ over the entry taper region [i.e., $\Delta B_n = 0$ for $0 \le n \le 1 + N_p N_w$] to ensure a positive amplitude. The variation in $\Delta B_w(z)$ between these points is given by

$$
\Delta B_w(n\Delta z + \delta z) = \Delta B_n + [\Delta B_{n+1} - \Delta B_n] \times \sin^2\left(\frac{\pi}{2}\frac{\delta z}{\Delta z}\right).
\tag{6}
$$

where $0 \le \delta z \le \Delta z$. Note that it is also possible to model the effects of the measured pole-to-pole variations in specific wiggler magnets with this formulation.

Both the divergence and the z-component of the curl vanish identically for arbitrary choices of $B_w(z)$ for this model of the field. In addition, the transverse components of the curl are given by

$$
|\nabla \times B_w|_\perp = \frac{N_p(2 + N_p)}{8}k_w \Delta B_w,
\tag{7}
$$

subject to the assumptions that $k_w \alpha_x < 1$, $a_w/\gamma_0 < 1$, and $k_w R_b < 1$ where $a_w [= eB_w/k_w m_e c^2]$ denotes the wiggler parameter, and R_b is the beam radius. Hence, these contributions remain small as long as the rms level of the wiggler imperfections are small.

3. Numerical analysis

The configuration under study is one in which a 3.5 MeV/850 A electron beam with an initial radius of 1.0 cm propagates through a rectangular waveguide ($a = 9.8$ cm, $b = 2.9$ cm) in the presence of a wiggler with $B_w = 3.72$ kG, $\lambda_w = 9.8$ cm, and $N_w = 5$. This corresponds to an experiment at LLNL [13], which mea-

sured an output power of approximately 180 MW over a saturation length of 1.3 m.

Comparisons between WIGGLIN in the absence of wiggler imperfections and the experiment show good agreement. Resonant interaction occurs with the TE_{01}, TE_{21} and TM_{21} modes at frequencies of 30–40 GHz, and the efficiency decreases with increasing frequency across this band. For an ideal beam and wiggler [i.e., $\Delta\gamma_z = 0$ and $\Delta B_w = 0$] the efficiency falls off from a maximum $\eta \approx 12.4\%$ at 30 GHz to a minimum of $\eta \approx 3.6\%$ at 40 GHz. A frequency of 34.6 GHz ($\eta \approx 6.9\%$) is selected for the comparison.

In Fig. 1 we plot the evolution of the total power in all the modes and the power in the TE_{01} mode at 34.6 GHz for the choice of $\Delta\gamma_z/\gamma_0 = 1.5\%$. Note that the axial energy spread is known to be less than 2% through electron spectrometer measurements of the beam. The initial drive powers in the modes were chosen to be 50 kW in the TE_{01} mode, 500 W in the TE_{21} mode, and 100 W in the TM_{21} mode. Observe that although the TE_{01} mode is overwhelmingly dominant at the start of the interaction, it accounts for only about 60% of the signal at saturation. This is due to the fact that the TE_{21} mode had the higher growth rate. The oscillation in the power occurs at a period of $\lambda_w/2$ and is due to the effect of the lower beat wave between the wiggler and the radiation field [2,3]. Agreement between the simulation and the experimental measurement is good. The peak saturated power found in simulation is approximately 190 MW, which falls to approximately 180 MW when averaged over the lower beat wave, which is in good agreement with the measurements. In addition, the saturation length is found to be approximately 1.45 m which is also close to the experimental value. Finally, we note that WIGGLIN has also been validated by comparison with a
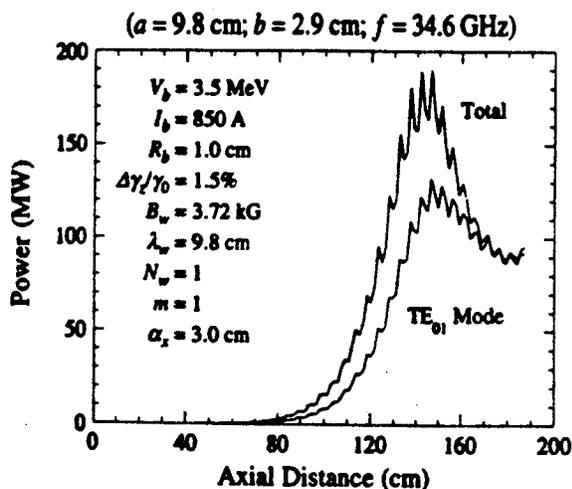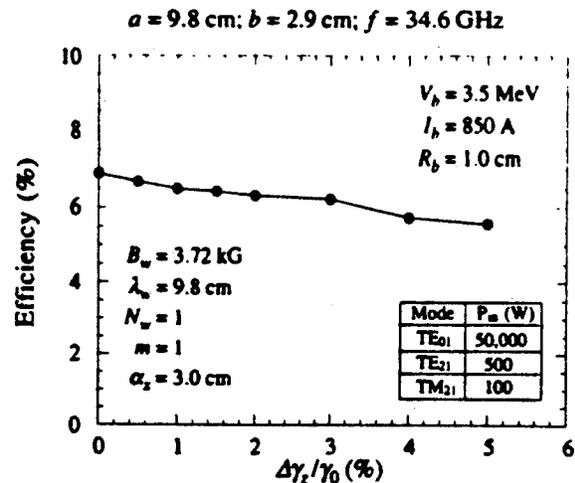
Fig. 2. Variation in the saturation efficiency as a function of the initial axial energy spread.

fundamental and second harmonic FEL experiment [14].

The effect of the axial energy spread is illustrated in Fig. 2 in which the extraction efficiency is plotted as a function of $\Delta\gamma_z/\gamma_0$ (for $\Delta B_w = 0$). Observe that the saturation length varies with $\Delta\gamma_z$ and that this figure represents the efficiencies at saturation. As shown, the efficiency decreases gradually with the axial energy spread due to the extremely high value of the wiggler parameter ($a_w \approx 3.4$) for this experiment. Note that the decline in the efficiency with the axial energy spread was found to be more rapid with the parabolic pole face wiggler model [2,3] than with the present model, although good agreement with the experiment is also found for the parabolic pole face model with $\Delta\gamma_z/\gamma_0 = 1.5\%$. This is due to the fact that the gradient in the wiggler in the direction of the bulk wiggler-induced transverse motion is higher for the parabolic pole face model.

Random wiggler fluctuations can take many different forms for a fixed rms value. It is most natural to consider a random fluctuation which is relatively uniform over the interaction region [i.e. $\langle \Delta B_w \rangle = 0$]; however, other configurations are possible. For example, fluctuations where the wiggler field is always greater (or less) than the systematic value for B_w are possible, as is one in which ΔB_w is very large over a small range and zero elsewhere. These are only limited examples, and a thorough analysis necessitates a large number of simulation runs with different random wiggler fluctuations to obtain adequate statistics. The effect of random wiggler errors is shown in Fig. 3 where the efficiency is plotted versus the rms wiggler error (for $\Delta\gamma_z = 0$) for $N_p = 2$. The dots represent the average efficiency over the ensemble of random fluctuations, and the error bars denote the standard deviation. A
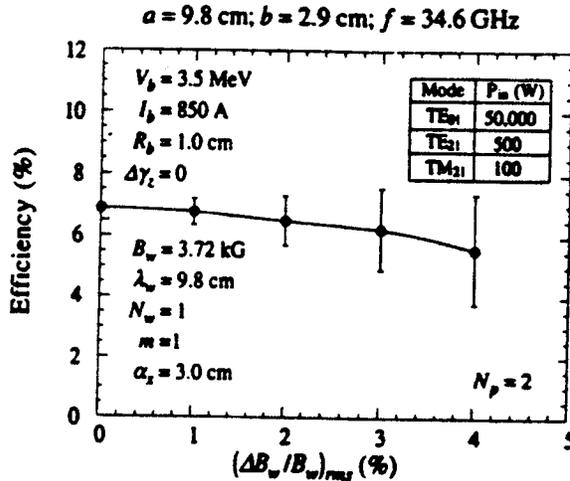

Fig. 1. Evolution of the power versus axial distance in the absence of wiggler imperfections.

IV. THEORY

$a = 9.8$ cm; $b = 2.9$ cm; $f = 34.6$ GHz

Fig. 3. Variation of the saturation efficiency as a function of the rms magnitude of the wiggler field imperfection.
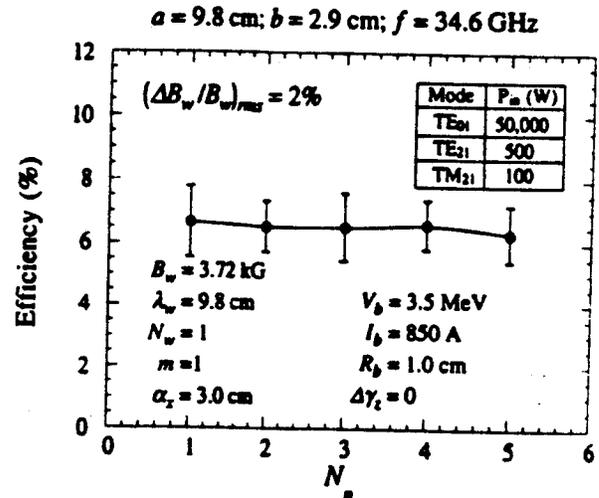
$a = 9.8$ cm; $b = 2.9$ cm; $f = 34.6$ GHz

Fig. 4. Variation of the saturation efficiency as a function of the number of pole faces per wiggler period.

total of 35 runs (for 35 different random distributions in the wiggler fluctuation distributions) was found to give convergence to within $\approx 1\%$. As shown, the average efficiency is relatively insensitive to wiggler errors for $(\Delta B_w/B_w)_{rms} \leq 4\%$, although the standard deviation increases with the rms error. For this example, the effect of a given $(\Delta B_w/B_w)_{rms}$ is much more benign than for a comparable $\Delta\gamma_z/\gamma_0$. Particle loss was not found to be a problem for the range of $(\Delta B_w/B_w)_{rms}$ shown in Fig. 3.

The effect of variations in the number of pole faces per wiggler period is shown in Fig. 4 for $(\Delta B_w/B_w)_{rms} = 2\%$. Note that the choice of $N_p = 1$ is primarily of mathematical interest only as most actual wiggler designs have more than one pole face per wiggler period. As is evident in the figure, the efficiency is relatively insensitive to the number of pole faces per wiggler period, although a very weak relative minimum is found for $N_p = 2$. It should be noted that this relative minimum was found to be more pronounced in Ref. [11] in which a parabolic pole face model was used for the wiggler field. Although the general conclusion that the effect of the wiggler field imperfections is much weaker than a corresponding axial energy spread is found for both wiggler models, we attribute the greater variation in the efficiency with N_p for the parabolic pole face wiggler model to be due to the fact that this model was neither curl- nor divergence-free under variations in the amplitude.

Note that the efficiency increases relative to the ideal wiggler case for some particular wiggler fluctuation distributions. Variations in the efficiency can occur due to a retuning in the average wiggler magnitude, and an increase (decrease) in $\langle \Delta B_w \rangle$ can be expected to result in an increase (decrease) in the efficiency. Another way in which the form of the error distribu-

tion can affect the efficiency is if the field exhibits a bulk taper either upwards or downwards over the interaction region. A downward (upward) taper can be expected to increase (decrease) the efficiency. In order to illustrate this, consider the case for which $(\Delta B_w/B_w)_{rms} = 4\%$ and $N_p = 1$. The wiggler fluctuation distribution which gives rise to $\eta = 9.13\%$ (compared to a mean $\eta \approx 6.2\%$) is shown in Fig. 5. The average a_w for this case is close to the systematic value of 3.4; however, the field exhibits a bulk downward taper which acts to enhance the efficiency. In addition, the minimum efficiency case was found to exhibit a bulk upward taper in the wiggler field.

In general, the statistical distribution of the efficiency differs from the normal distribution, and the standard deviation must be used with some caution. The probability histogram showing the breakdown in
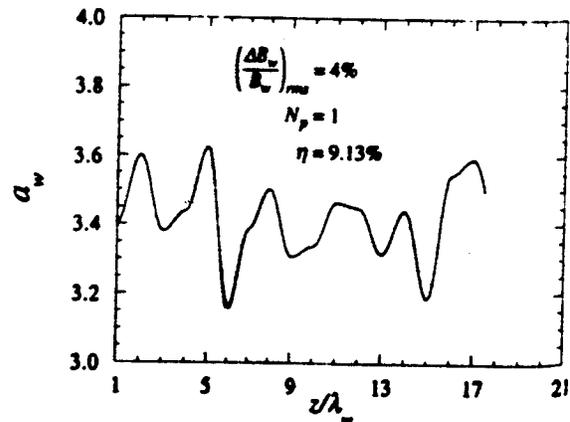

Fig. 5. Plot of the fluctuations in the wiggler parameter which give rise to an increased efficiency.
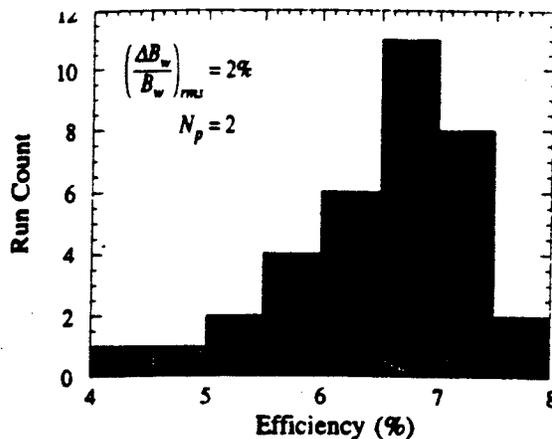
Fig. 6. Probability histogram of the number of simulation runs versus the saturation efficiency for $(\Delta B_w / B_w)_{rms} = 2\%$ and $N_p = 2$. The total number of simulation runs in this sample is 35.

the 35 runs used to obtain the bulk efficiency to within approximately 1% is shown in Fig. 6 for $(\Delta B_w / B_w)_{rms} = 2\%$ and $N_p = 2$. Here, the skewness ≈ -0.87 and the kurtosis ≈ 0.74 indicating a distribution skewed below the mean and more peaked than the normal distribution. In general, we find that the probability histograms are skewed below the mean. However, the distribution is not always more peaked than the normal distribution, and the kurtosis can be either positive or negative depending upon both $(\Delta B_w / B_w)_{rms}$ and N_p. Hence, the actual statistics of the wiggler imperfections must be studied on a case-by-case basis.

4. Summary and discussion

In summary, a self-consistent analysis of the effect of random wiggler imperfections on the saturation efficiency of the FEL has been presented in which no a priori assumption of a random walk of the electron orbits has been imposed. For the specific parameters under study, the results indicate that the effects of random wiggler errors are relatively benign, and particle loss was not found to be a problem. Indeed, some imperfection configurations chosen at random were found to result in efficiency enhancements due to effective increases. Hence, we conclude that wiggler imperfections are not a major factor below a certain level (depending upon the specific parameters). It is

important to note here that experimental quantification of these issues is difficult to obtain. While measurements for $(\Delta B_w / B_w)_{rms}$ are possible to achieve with some accuracy, there is always a greater uncertainty as to beam quality. Hence, it is difficult to determine the relative importance of wiggler errors in the laboratory. The results of the present work, however, suggest that while wiggler imperfections may provide a more severe constraint for short wavelength FELs than the present case studied, wiggler imperfections constitute a less serious issue for FEL design than does the problem of beam quality.

References

[1] E. Hoyer, T. Chan, J.Y.G. Chin, K. Halbach, K.J. Kim, H. Winick and J. Yang, IEEE Trans. Nucl. Sci. NS-30 (1983) 3118.
[2] H.P. Freund, Phys. Rev. A 37 (1988) 3371.
[3] H.P. Freund and T.M. Antonsen, Jr., Principles of Free-Electron Lasers (Chapman & Hall, London, 1992) chap. 5.
[4] B.M. Kincaid, J. Opt. Soc. Am. B 2 (1985) 1294.
[5] W.P. Marable, E. Esarey and C.M. Tang, Phys. Rev. A 42 (1990) 3006.
[6] L.H. Yu, S. Krinsky, R.L. Gluckstern and J.B.J. van Zeijts, Phys. Rev. A 45 (1992) 1163.
[7] C.J. Elliot and B. McVey, in: Undulator Magnets for Synchrotron Radiation and Free Electron Lasers, eds. R. Bonifacio, L. Fonda and C. Pellegrini (World Scientific, Singapore, 1987) p. 142.
[8] H.D. Shay and E.T. Scharlemann, Nucl. Instr. and Meth. A 272 (1988) 601.
[9] W.P. Marable, C.M. Tang and E. Esarey, IEEE J. Quantum Electron. QE-27 (1991) 2693.
[10] H. Bluem, Ph.D. Thesis, University of Maryland (1990).
[11] H.P. Freund and R.H. Jackson, Phys. Rev. A 45 (1992) 7488.
[12] T.M. Antonsen, Jr., private communication (1992).
[13] T.J. Orzechowski, B.R. Anderson, J.C. Clark, W.M. Fawley, A.C. Paul, D. Prosnitz, E.T. Scharlemann, S.M. Yarema, D.B. Hopkins, A.M. Sessler and J.S. Wurtele, Phys. Rev. Lett. 57 (1986) 2172.
[14] H. Bluem, R.H. Jackson, H.P. Freund, D.E. Pershing and V.L. Granatstein, Phys. Rev. Lett. 67 (1991) 824.

APPENDIX V

Tunability of Tapered Free-Electron Lasers

B. Levush, H.P. Freund and T.M. Antonsen, Jr.

Tunability of tapered free electron lasers *

B. Levush **, H.P. Freund [1], T.M. Antonsen, Jr.

Laboratory for Plasma Research, University of Maryland, College Park, MD 20742, USA

Free electron laser amplifiers are tunable sources under development as high power, high frequency radiation sources for magnetic fusion applications. High efficiencies can be achieved by varying the wiggler field strength and/or the wiggler period. In addition to the requirement of high efficiency, the free electron laser must be tunable for electron cyclotron heating and current drive applications in magnetic fusion devices. Although the tunability of free electron lasers is well established, the tunability of a tapered free electron laser amplifier has not been studied. In this paper we present an investigation of the tunability of a tapered wiggler free electron laser amplifier operating in the neighborhood of 94 GHz. The configuration of the free electron laser is one in which a sheet electron beam propagates through a rectangular waveguide in the presence of a planar wiggler field with tapered period. We found that the tapered free electron laser amplifier is tunable over a reasonably wide range of frequencies by small adjustments in the energy and current of the electron beam.

1. Introduction

A prime characteristic of free electron lasers (FELs) is their ability to be tuned over a broad frequency range by simply changing the beam voltage. A number of schemes have been suggested to achieve high electronic efficiencies. One of the most promising schemes involves tapering of the wiggler amplitude and/or the wiggler period [1]. Designs of tapered wiggler FELs have been optimized for maximum efficiency at a particular frequency of operation. Therefore, wide tunability of a tapered wiggler FEL is not obvious.

The purpose of this paper is to address the question of the tunability of a tapered wiggler amplifier. In particular, we are interested in how the efficiency varies with the frequency of the drive signal in a tapered wiggler FEL amplifier optimized to operate at a specific frequency. In addition, we address the related question of the required tuning of the beam voltage and/or current to maintain a relatively constant efficiency over a broad range of frequencies. These issues have not been adequately addressed in the literature, and are of interest in applications of high power FELs to electron cyclotron resonance heat-ing and current drive for thermonuclear fusion applications.

2. Design of a tapered FEL amplifier

The specific parameters used herein correspond to the University of Maryland short period, sheet beam FEL experiment [2–9]. In this experiment, an electron beam 0.1 cm thick and 2.0 cm wide, having a current of about 10 Å and a voltage of about 500 kV, is injected into a rectangular waveguide (4.0 cm–0.32 cm) placed inside a magnetic wiggler. The amplitude of the magnetic wiggler field is $B_w \approx 5.1$ kG and the period $\lambda_w \approx 0.96$ cm. The corresponding normalized wiggler parameter $a_w = qB_w/mc^2k_w$ (where q and m are the electron charge and mass, respectively, c is the speed of light, and $k_w = 2\pi/\lambda_w$ is the wiggler wavenumber) is less than unity.

The enhancement of the efficiency in a tapered wiggler FEL is accomplished by reducing the resonant energy for the interaction as the electron beam loses energy to the wave. The resonance for a wave with frequency ω and wavenumber k_z in a planar wiggler in which $a_w \ll 1$ is given approximately by

$$\gamma_r^2 \approx \frac{1 + a_w^2/2}{1 - k_s^2/(k_z + k_w)^2},\qquad (1)$$

where γ_r denotes the relativistic dilation factor, and the wavenumbers in the waveguide are related via

---

$\omega^2/c^2 = k_s^2 = k_z^2 + \kappa_\infty^2$ for a cutoff wavenumber κ_∞. In order to maintain the resonance as the beam loses energy, at fixed wavelength $\lambda = 2\pi/k_s$, the wiggler taper must vary with the energy loss as

$$\frac{\Delta\gamma_r}{\gamma_r} \approx \frac{\lambda_w}{4\gamma_r^2\lambda}\left[a_w^2\frac{\Delta B_w}{B_w} + \left(1 + \tfrac{3}{2}a_w^2\right)\frac{\Delta\lambda_w}{\lambda_w}\right], \qquad (2)$$

where we have assumed that $k_z \gg k_w$, κ_∞ for simplicity. It is evident, therefore, that high efficiencies can only be achieved in systems in which $a_w \ll 1$ by tapering of the period. It is this scheme which we shall investigate in this paper.

Specifically, we assume that starting at some distance z_0 the rate of change of the wiggler wave number is constant, namely

$$k_w(z) = \begin{cases} k_w(0) & \text{if } z < z_0, \\ k_w(0) + b(z - z_0) & \text{if } z > z_0, \end{cases} \qquad (3)$$

where $k_w(0)$ is the wiggler wave number in the untapered region, and z_0 is the axial distance at which the tapering starts. As described in ref. [7], with a short-period wiggler the wiggler strength depends on the wiggler period via the following relation:

$$B_w(z) = B_w(0)\frac{\cosh[k_w(0)\delta/2]}{\cosh[k_w(z)\delta/2]}, \qquad (4)$$

where δ is the gap spacing (we assume that the gap spacing is equal to the waveguide thickness). We solve the FEL equations for different values of the parameters z_0 and b. The optimum tapering parameters yield maximum efficiency. The FEL amplifier equations consist of the wave equation and the particle motion equations. In this paper, we limited ourselves mainly to the one-dimensional model. In the Appendix, we present the final form of the equations we used in our analysis.

We introduced into the 1D particle motion model a spread in the particle injection angle. This mimics the effects of the radial variation of the wiggler field for the beam with finite size. In this case, the particles are injected with non-zero perpendicular momentum, $p_\perp^2 \approx p^2\theta^2$, where θ is the injection angle and p is the total initial particle momentum. This will introduce spread in the axial velocity according to

$$\beta_z = \sqrt{1 - \frac{1 + \left(p_\perp^2/m^2c^2\right) + 0.5a_w^2}{\gamma^2}}. \qquad (5)$$

We assume that the distribution for θ has the Gaussian form, $f(\theta) = \bar\theta^{-2}\exp(-\theta/\bar\theta)^2$, where $\bar\theta$ is the characteristic spread in the injection angle. We estimated that for the parameters of the Maryland FEL experiment the 1D model with $\bar\theta \approx 2°-4°$ would mimic well the interaction process. The angular spread has been estimated on the basis of the betatron motion due to

the transverse wiggler inhomogeneity and the finite size of the beam. To confirm this result, we also employed the 3D FEL simulation code WIGGLIN [8,9] under the assumption of the injection of a finite size beam with a zero initial axial energy spread. WIGGLIN includes three-dimensional wiggler effects in a self-consistent manner, and the finite size beam assumption introduces the transverse particle motion due only to wiggler inhomogeneities. The results of the WIGGLIN simulation indicate a saturated power RF of approximately 245 kW for a uniform wiggler. The 1D simulation indicates a saturated power which decreases from 290 kW to 163 kW as θ increases from 2° to 4°. Hence, the 1D simulation is in substantial agreement with the 3D simulation code WIGGLIN for the presumed angular beam spread corresponding to the betatron motion of the beam.

In the 1D simulations we assumed that 1 kW of power in the TE_{01} mode is injected into the rectangular waveguide. The tapering parameters were optimized to yield maximum FEL efficiency for an injected signal at 94 GHz. We found that for a 200 cm long wiggler the maximum efficiency is achieved at beam voltage $V = 476.8$ kV and tapering parameters $z_0 = 74.5$ cm and $b = 0.021$ cm^{-2}. The beam current was fixed at 10 A. The results of the simulation indicate an optimum output power of about 540 kW for an interaction efficiency of 11.3%. We now turn to the question of the tunability of this design.
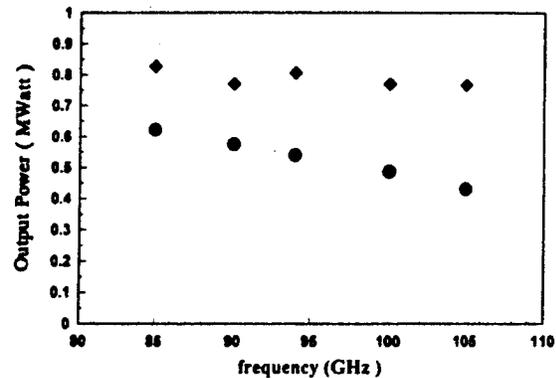

Fig. 1. Output power versus frequency for a tapered short period wiggler sheet beam in the University of Maryland FEL amplifier. The tapering parameters are optimum for operation at 94 GHz. The total length of the wiggler is 200 cm. The wiggler strength in the untapered section is 5.1 kG and the wiggler period is 0.96 cm. The length of the untapered section is 74.5 cm. The injected power is 1 kW. The circle symbols correspond to simulations with a beam current of 10 A. The diamond symbols correspond to simulations in which the efficiency was optimized with respect to beam current in addition to the beam voltage. The first two diamonds correspond to a beam current of 12 A and the remaining diamonds correspond to a beam current of 13 A.
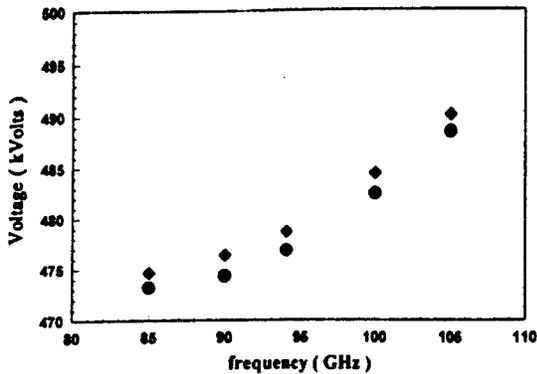
IV. THEORY

Fig. 2. The optimum beam voltage corresponding to the data shown in Fig. 1.

3. Tunability of a tapered FEL amplifier

For the tunability studies we fixed the aforementioned tapering parameters in the case of 94 GHz injection frequency. We also fixed the beam current, the length of the wiggler, and the injected power. The simulations were then performed for a given wiggler design with an injected signal at different frequencies and optimized for beam energy. Fig. 1 shows the output power versus frequency and Fig. 2 gives the corresponding beam voltage versus frequency tuning curve.

Fig. 1 shows the variation in the output power versus frequency for two cases. The circles correspond to the output power at fixed current and optimum beam voltage, while the diamonds show the output power subject to both voltage and current optimization. It is evident from the figure that the variation in power over the frequency band is relatively mild at fixed current. The variation in beam voltage with frequency used to generate Fig. 1 is shown in the circles in Fig. 2. However, when the current optimization is performed as well, then the output power variation across this frequency band is negligible. The specific currents used in this case are: at 85 and 90 GHz the current was 12 A, and at 94–105 GHz the current was 13 A. Observe that the corresponding voltage tuning for the currents is shown by the diamonds in Fig. 2.

4. Summary

The results of our study clearly illustrate that tapered FEL amplifiers are tunable sources for all practical purposes. We performed simulations to determine the tunability characteristics of a tapered FEL amplifier. In the computation, we used the parameters of the University of Maryland short period wiggler FEL experiment. We found that in this FEL a tunability of about 25% can be achieved without significant reduc-

tion in the output power. This is particularly important for applications in which the radiation source is required to operate at high efficiency. For example, the tunability requirement for some fusion applications is on the order of 5% for a source with multi-megawatt output power at frequencies around 150 GHz. This can be met by using a tapered FEL amplifier.

It should be noted that there are discrepancies between the 1D analysis and the 3D WIGGLIN simulation of the tapered wiggler configuration. In this regard, we observe that there is an optimum slope for the taper in any nonuniform wiggler configuration, since at extremely high degrees of taper the beam cannot remain in the bucket. The discrepancy at this time seems to lie in the fact that the 3D model predicts an optimum taper which is much less than that seen in the 1D model although both models are consistent with the simplified bucket efficiency predicted from Eq. (2). This issue is currently under study and will be discussed at length in a future publication. The preliminary results seem to indicate that the 3D model predicts a transverse spreading of the beam at high power level which results in enhanced detrapping of the beam. This enhanced detrapping then acts to limit the extracted power and forces a reduction in the optimum slope of the taper.

Appendix

In this appendix, we present the FEL amplifier equations in 1D approximation which we used to perform our analysis. The equations for particle phase $\psi = (k_s + k_w)z - \omega t$ and energy γmc^2 are

$$\frac{d\psi}{dz} = \frac{k_s}{\beta_{zr}(z)}\left(1 - \frac{\beta_{zr}(z)}{\beta_z}\right), \qquad (A.1a)$$

and

$$\frac{d\gamma}{dz} = k_s \frac{a_w(z)C(z)}{\gamma_r(z)\beta_{zr}(z)} 2\,\mathrm{Im}\big(a_s\,e^{i\psi}\big), \qquad (A.1b)$$

where $a_s = qA_s/mc^2$ is the normalized signal field amplitude (A_s signal field vector potential). The coupling coefficient has the form

$$C(z) = \tfrac{1}{2}\big[J_0(u(z)) - J_1(u(z))\big], \qquad (A.2)$$

where

$$u(z) = \frac{a_w^2(z)}{4(1 + 0.5a_w^2(z))}$$

and J_0, J_1 are ordinary Bessel functions. The wave equation is

$$\frac{da_s}{dz} = -i2\pi \frac{I}{I_A} \frac{g a_w(z)C(z)}{k_s(\omega)S\gamma_r(z)\beta_{zr}(z)}\langle e^{-i\psi}\rangle, \qquad (A.3)$$

where $I_A = mc^3/q = 1.7 \times 10^4$ (A), I is the beam current, S is the waveguide area, the brackets $\langle \cdots \rangle$ represent an average over initial particle phases, and g is a normalized factor for transverse average of the radiation profile

$$g^{-1} = \frac{1}{S} \int \frac{|a_s(x_\perp)|^2}{a_s^2} \, dx_\perp ,$$

where a_s is the peak signal amplitude at $x_\perp = 0$. Note that the ratio gS_b/S serves as the beam filling factor, where S_b is the beam area. For TE_{01} mode in the rectangular waveguide $g \simeq 2$.

Eqs. (A.1)–(A.3) are the model equations which have been used in our analysis.

References

[1] T.J. Orzechowski, B.R. Anderson, J.C. Clark, W.M. Fawley, A.C. Paul, D. Prosnitz, E.T. Scharlemann, S.M. Yarema, D.B. Hopkins, A.M. Sessler and J. Wurtele, Phys. Rev. Lett. 57 (1986) 2172.

[2] J.H. Booske, A. Serbeto, T.M. Antonsen, Jr. and B. Levush, J. Appl. Phys. 65 (1989) 1453.

[3] J.H. Booske, S. Bidwell, B. Levush, T.M. Antonsen, Jr. and V. Granatstein, J. Appl. Phys. 69 (1991) 7503.

[4] J.H. Booske, D.J. Radack, T.M. Antonsen, Jr., S.W. Bidwell, Y. Carmel, W.W. Destler, H.P. Freund, V.L. Granatstein, P.E. Latham, B. Levush, I.D. Mayergoyz and A. Serbeto, IEEE Trans. Plasma Sci. PS-18 (1990) 399.

[5] S.W. Bidwell, D.J. Radack, T.M. Antonsen, Jr., J.H. Booske, Y. Carmel, W.W. Destler, V.L. Granatstein, B. Levush, P.E. Latham, I.D. Mayergoyz and Z.X. Zhang, Nucl. Instr. and Meth. A 304 (1991) 187.

[6] W.W. Destler, S. Cheng, Z.X. Zhang, T.M. Antonsen, Jr., V.L. Granatstein, B. Levush and J. Rodgers, Phys. Fluids B (1994) in press.

[7] W.W. Destler, V.L. Granatstein, I.D. Mayergoyz and Z. Segalov, J. Appl. Phys. 60 (1986) 521.

[8] H.P. Freund, Phys. Rev. A 37 (1988) 3371.

[9] H.P. Freund and T.M. Antonsen, Jr., Principles of Free-electron Lasers (Chapman & Hall, London, 1992) chap. 5.

APPENDIX VI

Nonlinear Theory of Slow-Wave Ubitrons/Free-Electron Lasers

H.P. Freund

Nonlinear theory of slow-wave ubitrons/free electron lasers

H.P. Freund [1]

Naval Research Laboratory, Washington, DC 20375, USA

A three-dimensional nonlinear formulation of a slow-wave ubitron/free electron laser is presented. The configuration is that of an electron beam propagating through a dielectric-lined rectangular waveguide in the presence of a planar wiggler field. The wiggler field model describes parabolic pole faces for enhanced beam focussing. The electromagnetic field is described in terms of a multimode ensemble of the normal modes of the vacuum waveguide. In this case, the dielectric liner is imposed along the y-axis of the guide (which is also the principal orientation of the wiggler) and there are no orthogonal TE or TM modes. Instead, we deal with modes which are transverse electric (LSE) or magnetic (LSM) to the y-axis. Equations are derived which describe the evolution of the amplitude and phase of these modes in terms of the microscopic particle currents. These equations are solved in conjunction with the complete Lorentz force equations for the electron trajectories. The essential purpose of employing a slow-wave structure is to reach shorter wavelengths at relatively low beam energies, and numerical results will be presented to demonstrate the potentialities of this concept.

Ubitrons and free electron lasers have been constructed with a wide range of waveguide and optical geometries [1–8]. In the bulk of these cases, the electron beam interacts with a supraluminous wave in which the resonant wavelength scales inversely as the square of the beam energy. In many cases, however, this imposes too high a requirement on the electron beam energy, and methods for reducing the beam energy requirement have been eagerly sought. One technique is to pursue the interaction at harmonics of the resonant frequency. Unfortunately, the harmonic interaction poses difficulties in that (1) some method of suppressing the fundamental interaction must be found, (2) there is some penalty to be paid in terms of reductions in both the gain and efficiency at the harmonics, and (3) the requirements of high beam quality become progressively more severe as the harmonic number increases. In this article, therefore, an alternative method of reducing the beam energy requirement is studied; specifically, the use of a dielectric liner to slow the phase velocity of the wave. The interaction that results can be either with a supraluminous or a subluminous wave, but in either case the beam energy required for interaction at a given frequency is reduced.

The configuration employed is that of a single-frequency amplifier in which a relativistic electron beam propagates through a dielectric-lined rectangular waveguide in the presence of a planar wiggler field. The waveguide is characterized as shown in fig. 1 in which the dimensions of the outer walls are at $x = 0$, a and $y = \pm \frac{1}{2}b$. The dielectric is aligned parallel to the long (i.e., x) axis of the waveguide with a thickness Δ and an inner surface at $y = \pm d$, where $d = \frac{1}{2}b - \Delta$. The wiggler field model is chosen to describe the effect of parabolic pole faces for enhanced focussing [1,9], i.e.,

$$
\begin{aligned}
\boldsymbol{B}_w = B_w(z)\Big\{ &\cos(k_w z)\big[\, \hat{e}_x \sinh(k_w x/\sqrt{2})\, \sinh(k_w y/\sqrt{2}) \\
&+ \hat{e}_y \cosh(k_w x/\sqrt{2})\cosh(k_w y/\sqrt{2})\big] \\
&- \sqrt{2}\,\hat{e}_z \sin(k_w z)\cosh(k_w x/\sqrt{2}) \\
&\times \sinh(k_w y/\sqrt{2})\Big\},
\end{aligned} \tag{1}
$$

where k_w ($\equiv 2\pi/\lambda_w$, where λ_w denotes the wiggler period) is the wiggler wavenumber, and $B_w(z)$ describes the amplitude. The wiggler amplitude is allowed to vary slowly in z as follows:

$$
B_w(z) = \begin{cases}
B_w \sin^2(k_w z/4N_w), & 0 < z < N_w\lambda_w, \\
B_w, & N_w\lambda_w < z < z_0, \\
B_w[1 + \epsilon_w k_w(z - z_0)], & z > z_0.
\end{cases} \tag{2}
$$

in order to describe (1) the injection of the beam through an adiabatic entry taper over N_w wiggler periods, and (2) the efficiency enhancement by means of a tapered wiggler amplitude (in which ϵ_w describes the slope of the taper). This wiggler model is both curl- and divergence-free for a uniform wiggler amplitude, and we

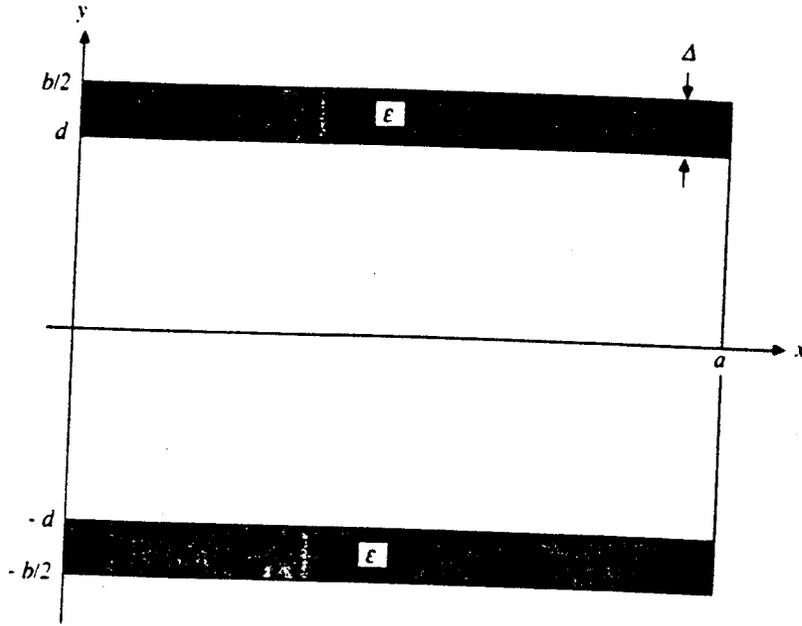[1] Permanent address: Science Applications International Corp., McLean, Virginia 22102, USA.

Fig. 1. Schematic illustration of the configuration of the dielectric-lined waveguide.

implicitly assume that the gradients imposed by the amplitude tapering are small (i.e., $N_w \gg 1$ and $\epsilon_w \ll 1$). Observe that the orientation of this wiggler model implies that the direction of the transverse wiggler-induced oscillations are aligned parallel to the dielectric liner. This was chosen, along with the enhanced focussing provided by the parabolic pole faces, in order to minimize loss of the beam to the dielectric.

The electromagnetic field is represented by means of an expansion in terms of the vacuum modes (i.e., in the absence of the electron beam) of the waveguide. The standard TE and TM modes of a rectangular waveguide do not exist in the presence of the dielectric liner. Instead, there are normal modes which are either transverse electric (LSE) or transverse magnetic (LSM) with respect to the y-axis in the present configuration [10]. We focus on the LSE modes since only this polarization presents an electric field component which is aligned with the bulk wiggler-induced transverse velocity. The electric and magnetic fields of these modes can be represented in the form

$$\delta E(x, t) = -\frac{\omega}{c} \sum_{l,n} \delta A_{ln} Z_{ln}(y)\left[\hat{e}_x \cos(l\pi x/a) \sin \alpha \right.$$

$$\left. -\frac{l\pi}{k_{ln}a}\hat{e}_z \sin(l\pi x/a) \cos \alpha \right]. \tag{3}$$

and

$$\delta B(x, t) = \sum_{l,n} k_{ln}\delta A_{ln}\left[\frac{l\pi}{ak_{ln}^2} Z'_{ln}(y)\hat{e}_x \sin(l\pi x/a)\right.$$

$$\times \sin \alpha - \left(1 + \frac{l^2\pi^2}{a^2 k_{ln}^2}\right) Z_{ln}(y)\hat{e}_y$$

$$\times \cos(l\pi x/a) \sin \alpha - \frac{1}{k_{ln}} Z'_{ln}(y)\hat{e}_z$$

$$\left. \times \cos(l\pi x/a) \cos \alpha \right], \tag{4}$$

where we assume that the amplitude δA_{ln} and the wavenumber k_{ln} are slowly-varying functions of z, and the phase is given by

$$\alpha \equiv \int_0^z dz' k_{ln}(z') - \omega t. \tag{5}$$

There are even and odd modes which are differentiated by the dispersion equations and the transverse mode patterns $Z_n(y)$. For the even modes, the dispersion equation is

$$\kappa_{ln} \tan \kappa_{ln}d = \kappa'_{ln} \cot \kappa'_{ln}\Delta, \tag{6}$$

where

$$\frac{\epsilon \omega^2}{c^2} = k_{ln}^2 + \frac{l^2\pi^2}{a^2} + \kappa'^2_{ln}, \tag{7}$$

in the dielectric, and

$$\frac{\omega^2}{c^2} = k_{ln}^2 + \frac{l^2\pi^2}{a^2} + \kappa^2_{ln}, \tag{8}$$

in the vacuum. The transverse variation for these modes is given by

$$
Z_{ln}(y) \equiv \begin{cases} \sin \kappa'_{ln}(\tfrac{1}{2}b - y), & d < y < \tfrac{1}{2}b, \\ \dfrac{\kappa'_{ln}}{\kappa_{ln}} \dfrac{\cos \kappa'_{ln}\Delta}{\sin \kappa_{ln}d} \cos \kappa_{ln}y, & -d < y < d, \\ \sin \kappa'_{ln}(\tfrac{1}{2}b + y), & -\tfrac{1}{2}b < y < -d. \end{cases}
$$

(9)

For the odd modes, we have the dispersion equation

$$
\kappa_{ln} \cot \kappa_{ln}d = -\kappa'_{ln} \cot \kappa'_{ln}\Delta, \tag{10}
$$

and the transverse mode structure

$$
Z_{ln}(y) \equiv \begin{cases} \sin \kappa'_{ln}(\tfrac{1}{2}b - y), & d < y < \tfrac{1}{2}b, \\ -\dfrac{\kappa'_{ln}}{\kappa_{ln}} \dfrac{\cos \kappa'_{ln}\Delta}{\cos \kappa_{ln}d} \kappa_{ln}y, & -d < y < d, \\ -\sin \kappa'_{ln}(\tfrac{1}{2}b + y), & -\tfrac{1}{2}b < y < -d. \end{cases}
$$

(11)

The dynamical equations which govern the evolution of the slowly varying amplitude and wavenumber are obtained by substitution of the representation of the electric field, eq. (3), into Maxwell's equations

$$
\left(\nabla^2 - \frac{1}{c^2} \frac{\partial^2}{\partial t^2} \right) \delta E(x, t) - \nabla(\nabla \cdot \delta E(x, t))
$$

$$
= \frac{4\pi}{c^2} \frac{\partial}{\partial t} \delta J(x, t), \tag{12}
$$

where the source current is given by

$$
\delta J(x, t)
$$

$$
= -en_b \iiint dp_0\, v_{z0} F_b(p_0) \int_{A_g} \int dx_0\, dy_0\, \sigma_\perp
$$

$$
(x_0, y_0) \int_{-T/2}^{T/2} dt_0\, \sigma_\parallel(t_0) v(z; x_0, y_0, t_0, p_0)
$$

$$
\times \delta[x_\perp - x_\perp(z; x_0, y_0, t_0, p_0)]
$$

$$
\times \frac{\delta[t - \tau(z; x_0, y_0, t_0, p_0)]}{|v_z(z; x_0, y_0, t_0, p_0)|}, \tag{13}
$$

where v_{z0} is the initial axial velocity, p_0 is the initial momentum, A_g is the cross-sectional area of the waveguide, $T = L/v_{z0}$ (where L is the length of the system), and $\sigma_\parallel$, $\sigma_\perp$, and F_b describe the distribution of the initial conditions of the beam.

Substitution of the field representation into Maxwell's equation yields

$$
\left(1 + \frac{l^2\pi^2}{a^2 k_{ln}^2} \right) \left(\frac{\omega^2}{c^2} - k_{ln}^2 - \kappa_{ln}^2 \right) \delta a_{ln}
$$

$$
= 8 \frac{\omega_b^2}{c^2} \frac{G_l}{F_{ln}} \left\langle Z_{ln}(y) \right.
$$

$$
\left. \times \left[\frac{v_x}{v_z} \cos\left(\frac{l\pi x}{a} \right) \cos \alpha + \frac{l\pi}{ak_{ln}} \sin\left(\frac{l\pi x}{a} \right) \sin \alpha \right] \right\rangle, \tag{14}
$$

and

$$
2\left(k_{ln} + \frac{l^2\pi^2}{a^2 k_{ln}} \right) \frac{d}{dz} \delta a_{ln}
$$

$$
= -8 \frac{\omega_b^2}{c^2} \frac{G_l}{F_{ln}} \left\langle Z_{ln}(y) \right.
$$

$$
\left. \times \left[\frac{v_x}{v_z} \cos\left(\frac{l\pi x}{a} \right) \sin \alpha - \frac{l\pi}{ak_{ln}} \sin\left(\frac{l\pi x}{a} \right) \cos \alpha \right] \right\rangle, \tag{15}
$$

after averaging over a wave period and neglecting second-order derivatives of the amplitude and phase, where $\delta a_{ln} \equiv e\delta A_{ln}/m_e c^2$, $\omega_b^2 \equiv 4\pi e^2 n_b/m_e$, n_b denotes the ambient beam density, $G_l = \tfrac{1}{2}$ when $l = 0$ and unity otherwise,

$$
F_{ln} \equiv \frac{\sin^2 \kappa'_{ln}\Delta}{\cos^2 \kappa_{ln}d} \left(1 + \frac{\sin 2\kappa_{ln}d}{2\kappa_{ln}d} \right) + \frac{\Delta}{d} \left(1 - \frac{\sin 2\kappa'_{ln}\Delta}{2\kappa'_{ln}\Delta} \right), \tag{16}
$$

for the even modes, and

$$
F_{ln} \equiv \frac{\sin^2 \kappa'_{ln}\Delta}{\sin^2 \kappa_{ln}d} \left(1 - \frac{\sin 2\kappa_{ln}d}{2\kappa_{ln}d} \right) + \frac{\Delta}{d} \left(1 - \frac{\sin 2\kappa'_{ln}\Delta}{2\kappa'_{ln}\Delta} \right), \tag{17}
$$

for the odd modes. The averaging operator in eqs. (14) and (15) is defined over the initial conditions of the beam, and includes the effect of an *initial* momentum spread by means of the distribution function

$$
F_b(p_0) = A \exp\left[-(p_{z0} - p_0)^2/\Delta p_z^2 \right]
$$

$$
\times \delta(p_0^2 - p_{\perp 0}^2 - p_{z0}^2) H(p_{z0}). \tag{18}
$$

where p_0 and Δp_z describe the initial bulk momentum and momentum spread, $H(x)$ is the Heaviside function, and the normalization constant is

$$
A \equiv \left\{ \pi \int_0^{p_0} dp_{z0} \exp\left[-(p_{z0} - p_0)^2/\Delta p_z^2 \right] \right\}^{-1}. \tag{19}
$$

Observe that this distribution describes a beam which is monoenergetic but with a pitch-angle spread which is equivalent to an *axial* energy spread of

$$
\frac{\Delta \gamma_z}{\gamma_0} = 1 - \frac{1}{\sqrt{1 + 2(\gamma_0^2 - 1)\Delta p_z/p_0}}. \tag{20}
$$

where $\gamma_0 \equiv (1 + p_0^2/m_e^2 c^2)^{1/2}$. As a result, the averaging operator takes the form

$$
\langle\langle \cdots \rangle\rangle \equiv \frac{A}{4\pi A_g} \int_0^{2\pi} d\phi_0 \int_0^{p_0} dp_{z0}\, \beta_{z0}
$$

$$
\times \exp\left[-(p_{z0} - p_0)^2/\Delta p_z^2 \right] \int_0^{2\pi} d\psi_0\, \sigma_\parallel(\psi_0)
$$

$$
\times \iint_{A_g} dx_0\, dy_0\, \sigma_\perp(x_0, y_0)(\cdots). \tag{21}
$$

VII. 3D FEL THEORY

LSE$_{01}$ (a = 9.8 cm; b = 2.9 cm; Δ = 0.5 cm; ϵ = 4.2)

V_b = 1.35 MeV
I_b = 1.0 kA
R_b = 0.25 cm
$\Delta\gamma/\gamma_0$ = 0
B_w = 1.0 kG
λ_w = 9.8 cm
N_w = 5
f = 5.1 GHz
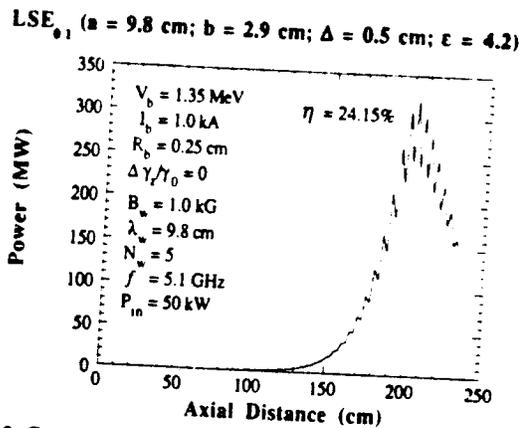P_{in} = 50 kW
η = 24.15%

Fig. 2. Graph of the evolution of the power in the LSE$_{01}$ mode as a function of axial distance.

In order to complete the formulation, we must specify the orbit equations for the electron ensemble. Since we deal with an amplifier model, we integrate the complete three-dimensional Lorentz force equations in z. No average of these equations over a wiggler period is performed.

The numerical example we consider deals with a waveguide with dimensions a = 9.8 cm, b = 2.9 cm and Δ = 0.5 cm, and the dielectric constant is ϵ = 4.2 which corresponds to boron nitride. The wiggler field has a period λ_w = 9.8 cm and increases to a constant value B_w = 1 kG over an entry taper region which is five wiggler periods in length. We assume an ideal (i.e., $\Delta\gamma_z$ = 0) solid pencil electron beam with an energy of 1.35 MeV, a current of 1.0 kA, and with a radius of 0.25 cm. This example corresponds to a resonance at a frequency of 5.1 GHz in the LSE$_{01}$ mode which is still in the supraluminous range, but has a phase velocity well below that of the TE$_{01}$ mode in the absence of the dielectric. As shown in fig. 2, we inject a 50 kW signal in the LSE$_{01}$ mode, which subsequently grows to a peak power level of approximately 324 MW for a saturation efficiency of 24.15%. The oscillation seen in the power occurs with a period of $\frac{1}{2}\lambda_w$, and corresponds to the effect of the lower beat wave upon the interaction in planar wiggler configurations [11]. No attempt has yet been made to optimize these parameters.

In summary, a nonlinear formulation and simulation code has been developed which is capable of treating the interaction between a relativistic electron beam and a planar wiggler field in the presence of a dielectric-lined rectangular waveguide. Note that a dielectric liner is

only one way of slowing the wave, and that alternative techniques include a variety of slow-wave structures including gratings and rippled wall geometries. An example showing high gain and efficiency is given for the case of the resonant interaction of the LSE$_{01}$ mode in the supraluminous regime. Although this does not represent a slow wave (which usually denotes a subluminous wave), there is still a substantial advantage to be gained in achieving high frequency operation at relatively lower voltages than would be possible in the absence of a dielectric. However, future studies will extend this analysis to the subluminous regime. Finally, it should also be remarked that this formulation is capable of treating the Cherenkov maser interaction for subluminous waves as well by the simple expedient of letting the wiggler field amplitude vanish.

References

[1] R.M. Phillips, IRE Trans. Electron. Devices ED-7 (1960) 231.

[2] L.R. Elias, W.M. Fairbanks, J.M.J. Madey, H.A. Schwettman and T.I. Smith, Phys. Rev. Lett. 36 (1976) 717.

[3] R.K. Parker, R.H. Jackson, S.H. Gold, H.P. Freund, V.L. Granatstein, P.C. Efthimion, M. Herndon and A.K. Kinkead, Phys. Rev. Lett. 48 (1982) 238.

[4] M. Billandon, P. Ellaume, J.M. Ortega, C. Bazin, M. Bergher, M. Velghe, Y. Petroff, D.A.G. Deacon, K.E. Robinson and J.M.J. Madey, Phys. Rev. Lett. 51 (1983) 1652.

[5] J. Fajans, G. Bekefi, Y.Z. Yin and B. Lax, Phys. Rev. Lett. 53 (1984) 246.

[6] B.E. Newman et al., IEEE J. Quantum Electron. QE-21 (1985) 867.

[7] T.J. Orzechowski, B. Anderson, W.M. Fawley, D. Prosnitz, E.T. Scharlemann, S. Yarema, D. Hopkins, A.C. Paul, A.M. Sessler and J. Wurtele, Phys. Rev. Lett. 54 (1985) 889.

[8] J. Masud, T.C. Marshall, S.P. Schlesinger and F.G. Yee, Phys. Rev. Lett. 56 (1986) 1567.

[9] E.T. Scharlemann, J. Appl. Phys. 58 (1985) 2154.

[10] R.F. Harrington, Time-Harmonic Electromagnetic Fields (McGraw-Hill, New York, 1961) chap. 4.

[11] H.P. Freund, Phys. Rev. A37 (1988) 3371.

APPENDIX VII

High Efficiency Operation of Cerenkov Masers

H.P. Freund and A.K. Ganguly

High efficiency operation of Cherenkov masers

H.P. Freund [1] and A.K. Ganguly

Naval Research Laboratory, Washington, DC 20375, USA

A nonlinear simulation of the Cherenkov maser amplifier is presented for a configuration in which an electron beam propagates through a dielectric-lined cylindrical waveguide. The parameters used correspond to an experiment at General Dynamics which measured a total efficiency of 11.5% at 8.6 GHz. The simulation is in agreement with this but indicates that the system was too short to reach saturation and that an efficiency of 30% would have been possible for a longer system, and the performance is not significantly degraded by thermal spreads up to 20%.

The Cherenkov maser has been demonstrated over a broad spectral range and operates by means of an interaction between an energetic electron beam and a subluminous electromagnetic wave. Cherenkov masers have been operated at 100 kW power levels at 1 mm wavelengths [1–3], at 200 MW power levels at 8 cm wavelengths [4] as well as wavelengths as short as in the far-infrared at 100 μm [5]. In the present work, we describe a comparison between a nonlinear formulation of the Cherenkov maser amplifier [6] and an experiment conducted at General Dynamics [7]. This experiment achieved a total output power of 280 MW at a frequency of 8.6 GHz. The nonlinear theory is in substantial agreement with the experimental measurements for the quoted beam and waveguide parameters, but indicates that the experiment was too short to reach saturation and that a total output power in the neighborhood of 800 MW could have been achieved with a longer system. The response of the system to the beam thermal spread is also remarkable in that the gain and saturation efficiency are not substantially degraded by energy spreads as high as 20%.

The configuration employed in the analysis is that of an electron beam propagating through a cylindrical, dielectric-lined waveguide. We use R_g and R_d to denote the inner radii of the waveguide and dielectric liner (with a dielectric constant of ϵ) respectively. The boundary conditions imposed on the electromagnetic field are satisfied by expanding the field in terms of the normal modes of the cold waveguide. The beam interacts with the parallel component of the electric field and couples primarily with the TM modes. We make the further assumption of azimuthal symmetry, and represent the field as an expansion of the TM_{0n} modes of the vacuum waveguide [8] for which

$$\delta E(x, t) = -\sum_{n=1}^{\infty} \frac{\omega}{c} \delta A_{0n} \left[Z_{1n}(r) \hat{e}_r \sin \alpha_n + \frac{\kappa_n}{k_n} Z_{0n}(r) \hat{e}_z \cos \alpha_n \right], \tag{1}$$

$$\delta B(x, t) = -\sum_{n=1}^{\infty} k_n \left(1 - \frac{\kappa_n^2}{k_n^2} \right) \delta A_{0n} Z_{1n}(r) \hat{e}_\theta \sin \alpha_n, \tag{2}$$

where δA_{0n} measures the amplitude and has the dimensions of a vector potential, ω and k_n denote the frequency and wavenumber, and

$$\alpha_n \equiv \int_0^z dz' k_n(z') - \omega t, \tag{3}$$

is the phase of the TM_{0n} mode. Both the amplitude and the wavenumber are assumed to be slowly varying functions of z in the sense that both vary slowly with respect to the wavelengths of interest. The radial

---

[1] Permanent address: Science Applications International Corp., McLean, VA 22102, USA.

dependence of these eigenmodes is given by ($l = 0, 1$)

$$Z_{ln}(r) = \begin{cases} I_l(\kappa_n r), & 0 \leq r \leq R_d, \\ a_n J_l(\kappa_n' r) + b_n Y_l(\kappa_n' r), & R_d < r \leq R_g. \end{cases} \tag{4}$$

where J_n and Y_n represent the regular Bessel and Neumann functions, I_n denotes the modified Bessel function of the first kind, and

$$a_n \equiv \tfrac{1}{2}\pi\kappa_n' R_d \left[\frac{\kappa_n'}{\epsilon\kappa_n} I_1(\kappa_n R_d) Y_0(\kappa_n' R_d) - I_0(\kappa_n R_d) Y_1(\kappa_n' R_d) \right],$$

$$b_n \equiv -\tfrac{1}{2}\pi\kappa_n' R_d \left[\frac{\kappa_n'}{\epsilon\kappa_n} I_1(\kappa_n R_d) J_0(\kappa_n' R_d) - I_0(\kappa_n R_d) J_1(\kappa_n' R_d) \right]. \tag{5}$$

Both κ_n and κ_n' are analogues of the cutoff wavenumbers and are defined by

$$\frac{\omega^2}{c^2} = k_n^2 - \kappa_n^2, \tag{6}$$

in the vacuum, and

$$\epsilon\frac{\omega^2}{c^2} = k_n^2 + \kappa_n'^2, \tag{7}$$

in the dielectric. It should be remarked that the choice of k_n in eqs. (6) and (7) denotes the vacuum value which, under the present assumptions, is the initial condition for the wavenumber. The vacuum dispersion equation [1–5] for this configuration is

$$\frac{I_1(\kappa_n R_d)}{I_0(\kappa_n R_d)} - \frac{\epsilon\kappa_n}{\kappa_n'} \frac{Y_0(\kappa_n' R_g) J_1(\kappa_n' R_d) - J_0(\kappa_n' R_g) Y_1(\kappa_n' R_d)}{Y_0(\kappa_n' R_g) J_0(\kappa_n' R_d) - J_0(\kappa_n' R_g) Y_0(\kappa_n' R_d)} = 0, \tag{8}$$

which, in combination with eqs. (5) and (6), relates ω and k_n.

The dynamical equations which govern the evolution of the slowly varying amplitude and phase have been derived by Freund and Ganguly [6]. The dispersion of each mode in the presence of the electron beam is described by

$$\left(1 - \frac{\kappa_n^2}{k_n^2}\right)\left(\frac{\omega^2}{c^2} - k_n^2 + \kappa_n^2\right)\delta a_{0n} = \frac{2\omega_b^2}{A_n c^2}\left\langle I_1(\kappa_n r) \frac{v_r}{|v_z|} \cos\alpha_n - \frac{\kappa_n}{k_n} I_0(\kappa_n r) \sin\alpha_n \right\rangle, \tag{9}$$

and

$$2k_n\left(1 - \frac{\kappa_n^2}{k_n^2}\right)\frac{d}{dz}\delta a_{0n} = -\frac{2\omega_b^2}{A_n c^2}\left\langle I_1(\kappa_n r) \frac{v_r}{|v_z|} \sin\alpha_n + \frac{\kappa_n}{k_n} I_0(\kappa_n r) \cos\alpha_n \right\rangle, \tag{10}$$

where $\omega_b^2 \equiv 4\pi n_b e^2/m_e$ is the square of the beam plasma frequency, $\delta a_{0n} \equiv e\delta A_{0n}/m_e c$, and

$$A_n \equiv \frac{\epsilon - 1}{\epsilon}\left[I_1^2(\kappa_n R_d) - \frac{\epsilon\kappa_n^2}{\kappa_n'^2} I_0^2(\kappa_n R_d) \right.$$

$$+ \frac{2}{\kappa_n R_d} \frac{\epsilon\omega^2}{c^2\kappa_n'^2} I_0(\kappa_n R_d) I_1(\kappa_n R_d) \Bigg]$$

$$+ \epsilon\frac{R_g^2}{R_d^2} \frac{\kappa_n^2}{\kappa_n'^2}\left[a_n J_1(\kappa_n' R_g) + b_n Y_1(\kappa_n' R_g) \right]^2. \tag{11}$$

VIII. NUMERICAL SIMULATIONS

The neglect of beam space-charge modes from the formulation is valid as long as (1) $\omega_b \ll \omega$, and (2) the exponentiation time is much less than the period of the beam-plasma wave.

The averaging operator is defined over the initial conditions of the beam, and includes the effect of an *initial* momentum spread by means of the distribution function

$$F_0(p_0) = A \exp\left[-(p_{z0}-p_0)^2/\Delta p_z^2\right] \delta\left(p_0^2 - p_{\perp 0}^2 - p_{z0}^2\right) H(p_{z0}), \tag{12}$$

where p_0 and Δp_z describe the initial bulk momentum and momentum spread, $H(x)$ is the Heaviside function, and the normalization constant is

$$A \equiv \left\{\pi \int_0^{p_0} \mathrm{d}p_{z0}\, \exp\left[-(p_{z0}-p_0)^2/\Delta p_z^2\right]\right\}^{-1}. \tag{13}$$

Observe that this distribution describes a beam which is monoenergetic but with a pitch-angle spread which is equivalent to an *axial* energy spread of

$$\frac{\Delta\gamma_z}{\gamma_0} = 1 - \frac{1}{\sqrt{1 + 2(\gamma_0^2 - 1)\dfrac{\Delta p_z}{p_0}}}, \tag{14}$$

where $\gamma_0 \equiv (1 + p_0^2/m_e^2 c^2)^{1/2}$. As a result, the averaging operator takes the form

$$\langle(\cdots)\rangle \equiv \frac{A}{2\pi R_d^2} \int_0^{2\pi} \mathrm{d}\phi_0 \int_0^{p_0} \mathrm{d}p_{z0}\, \beta_{z0} \exp\left[-(p_{z0}-p_0)^2/\Delta p_z^2\right]$$

$$\times \int_0^{2\pi} \mathrm{d}\psi_0\, \sigma_\parallel(\psi_0) \int_0^{R_d} \mathrm{d}r_0\, r_0 \sigma_\perp(r_0)(\cdots), \tag{15}$$

where ψ_0 ($\equiv -\omega t_0$) is the initial phase, $\phi_0 \equiv \tan^{-1}(p_{y0}/p_{x0})$, $\beta_{z0} \equiv v_{z0}/c$, and $\sigma_\parallel(\psi_0)$ and $\sigma_\perp(r_0)$ describe the initial beam distribution in phase and cross section.

In order to complete the formulation, the electron orbit equations must also be specified. Since we are interested in amplifier configurations, we integrate the complete Lorentz force equations in z using an axial guide magnetic field to provide for the confinement of the beam, and the electromagnetic field given in eqs. (1) and (2).

This formulation is compared with an amplifier experiment at General Dynamics [7] which employed an intense relativistic electron beam (788 keV and 3.1 kA) produced by a cold "knife-edge" cathode which resulted in an annular beam with a mean radius of approximately 1.15 cm and a thickness of 2 mm. After correction for the space-charge depression, the beam energy is of the order of 736 keV. No diagnostic measurement of the beam quality (ie., thermal energy spread) was made. The dielectric-liner was Stycast ($\epsilon = 10$) with a radius $R_s = 1.74$ cm and $R_d = 1.47$ cm. The dielectric had a 3.3 cm taper at both ends to suppress oscillation, and a uniform central region which was 23.9 cm in length. Beam transport was accomplished with a 15 kG solenoid. The amplifier was driven by a 100 kW input signal which was tunable over the band from 8.4–9.6 GHz. At these frequencies only the TM_{01} mode can interact with the beam. A total gain of 34.5 dB (1.44 dB/cm over the uniform dielectric) was observed at a power level of approximately 280 MW (for an efficiency of 11.5%), with an uncertainty of approximately 3 dB.

The simulation is in reasonable agreement with the observations, and shows that the power has not saturated over the 23.9 cm length of the uniform dielectric. As a result, the power predicted in simulation shows a substantial sensitivity to the specific choice of any parameter which modifies the linear gain. In particular, the simulation exhibits a large sensitivity to the thickness of the dielectric. For example, a power level of approximately 60 MW over the 23.9 cm length is predicted in simulation for $R_d = 1.47$ cm. However, there is an uncertainty in the dielectric thickness of the order of ± 0.005 cm due to the fabrication process [9]. If we choose $R_d = 1.475$ cm corresponding to a thinner dielectric, then the power found in simulation over this length rises to approximately 131 MW, which is within the experimental

TM$_{01}$ Mode (R$_g$ = 1.74 cm; R$_d$ = 1.475 cm; ε = 10)
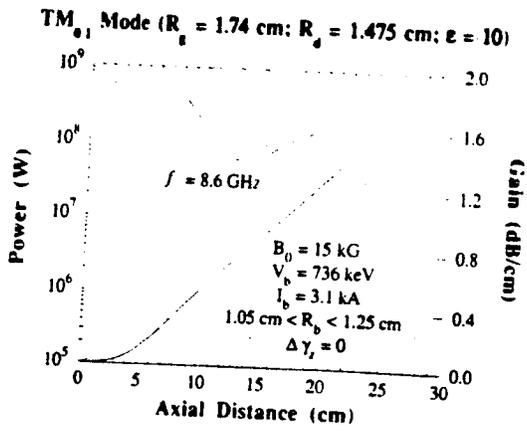

Fig. 1. Graph of the evolution of the power (solid line) and gain (dashed line) with axial distance.

uncertainty. This parametric sensitivity is largely confined to the linear gain. The saturated power is not substantially altered by variations in R_d over this range, and we find that the saturated power rises from approximately 600 to 620 MW as the inner radius of the dielectric changes from 1.47 to 1.475 cm. Since the larger figure for R_d is in better agreement with the observations and is within the range of experimental uncertainty, we shall use this value henceforth in the numerical analysis.

The gain band found in simulation covers the range of 7.8–8.8 GHz, and the efficiency at saturation for an ideal beam (i.e., $\Delta\gamma_z = 0$) increases from 16.4% at 7.8 GHz to approximately 30.3% at 8.8 GHz. A graph of the evolution of the power and gain versus axial distance is shown in fig. 1 at a frequency of 8.6 GHz. The power saturates at 620 MW after a length of approximately 28 cm for an efficiency of 31.6%, and the average gain over is in the neighborhood of 1.4–1.6 dB/cm. These figures are in reasonable agreement with the observations.

The effect of a thermal spread is shown in fig. 2 where the efficiency is plotted versus the energy spread at 8.6 GHz. The saturation efficiency is not significantly degraded by energy spreads as high as 20–25%. This high tolerance for the energy spread is due to the high growth rate found for this intense beam experiment. Since this mechanism relies on the Cherenkov resonance in which $\omega - kv_b \approx 0$, thermal effects become important when $\Delta v_b/v_b \approx \mathrm{Im}\,k/\mathrm{Re}\,k$. In this case, the growth rate is extremely high with $\mathrm{Im}\,k \approx 0.18$ cm^{-1}. Since $\mathrm{Re}\,k \approx 2.35$ cm^{-1}, this gives $\Delta v_b/v_b \approx 7.5\%$ which (using eq. (14)) corresponds to an axial energy spread of $\Delta\gamma_z/\gamma_0 \approx 24\%$.

In view of the power levels found both in the laboratory and in simulation, the simplicity of the configuration, and the relative insensitivity to beam thermal effects in the case of intense relativistic

TM$_{01}$ Mode (R$_g$ = 1.74 cm; R$_d$ = 1.475 cm; ε = 10)
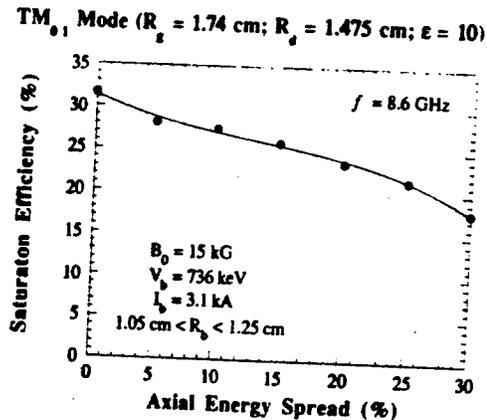
Fig. 2. Graph of the variation of the saturation efficiency vs axial energy spread.

VIII. NUMERICAL SIMULATIONS

electron beams, the Cherenkov maser is an attractive competitor for gyrotrons, free electron lasers, and relativistic klystrons for a wide variety of applications. In particular, the potentiality of producing single-mode powers in excess of 700 MW at frequencies in the neighborhood of 9 GHz compares favorably with recent results obtained with relativistic klystrons [10,11]; however, unlike the relativistic klystron, the Cherenkov maser is easily scalable to higher frequencies. We anticipate that the level of performance demonstrated herein at 8.6 GHz can be achieved at frequencies as high as 35 GHz as well. It should be remarked that Cherenkov masers based upon dielectric liners can exhibit both dielectric and mechanical breakdown at high power levels, and that these effects may have operated to limit the power and/or pulse length in the experiment at General Dynamics [9]. However, this configuration represents only one approach to the interaction, and other slow wave structures may be used to overcome these difficulties. In general, this device falls into the category of relativistic intense-beam traveling wave tubes (TWTs), and similar levels of performance have been obtained using a rippled wall slow-wave structure in both backward wave oscillators [12] and TWT amplifiers [13].

Acknowledgements

References

[1] K.L. Felch, K.O. Busby, R. Layman and J.E. Walsh, Appl. Phys. Lett. 38 (1981) 601.
[2] S. Von Laven, J. Branscum, J. Golub, R. Layman and J.E. Walsh, Appl. Phys. Lett. 41 (1982) 408.
[3] E.P. Garate, R. Cook, P. Heim, R. Layman and J.E. Walsh, J. Appl. Phys. 58 (1985) 627.
[4] W. Main, R. Cherry and E.P. Garate, Appl. Phys. Lett. 55 (1989) 1498.
[5] J.E. Walsh, C.H. Shaughnessy, R. Layman, G. Dattoli, G.P. Gallerano and A. Renieri, Nucl. Instr. and Meth. A272 (1988) 132.
[6] H.P. Freund and A.K. Ganguly, Phys. Fluids B2 (1990) 2506.
[7] W. Main, E.P. Garate, R. Cherry and J. Weatherall, submitted to Phys. Fluids.
[8] R.F. Harrington, Time-Harmonic Electromagnetic Fields (McGraw–Hill, New York, 1961) chap. 5.
[9] W. Main, personal communication.
[10] M.A. Allen et al., SLAC Pub. nos. 4801 and 5070 (1989).
[11] M. Friedman, J.A. Krall, Y.Y. Lau and V. Serlin, Rev. Sci. Instr. 61 (1990) 171.
[12] D. Shiffler, J.A. Nation and G. Kerslick, IEEE Trans. Plasma Sci. PS-18 (1990) 546.
[13] Y. Carmel, K. Minami, R.A. Kehs, W.W. Destler, V.L. Granatstein, D. Abe and W.L. Lou, Phys. Rev. Lett. 62 (1989) 2389.

APPENDIX VIII

The Nonlinear Analysis of Self-Field Effects in Free-Electron Lasers

H.P. Freund, R.H. Jackson, and D.E. Pershing

The nonlinear analysis of self-field effects in free-electron lasers

H. P. Freund,[a] R. H. Jackson, and D. E. Pershing[b]
Naval Research Laboratory, Washington, D.C. 20375

A model of the self-fields associated with the charge density and current of the electron beam is incorporated into three-dimensional nonlinear formulations of the interaction in free-electron lasers for both planar and helical wiggler configurations. The model assumes the existence of a cylindrically symmetric electron beam with a flat-top density profile and a uniform axial velocity, and the self-electric and self-magnetic fields are determined from Poisson's equation and Ampère's law. Diamagnetic and paramagnetic effects due the electron beam interaction with the wiggler field are neglected; hence, the model breaks down when the wiggler-induced transverse displacement is comparable to the beam radius. The nonlinear formulations are based upon the ARACHNE and WIGGLIN codes, which represent slow-time-scale formulations for the evolution of the amplitudes and phases of a multimode superposition of vacuum waveguide modes. The electron dynamics in these codes are treated by means of the complete three-dimensional Lorentz force equations, and the representations for the self-fields are incorporated directly into this formulation. The results of the simulations are compared directly with an experiment at Lawrence Livermore National Laboratory based upon a planar wiggler and experiments at the Massachusetts Institute of Technology and the Naval Research Laboratory, which employed helical wigglers. These experiments employed intense electron beams with current densities of 200–1200 A/cm^2 and comparable space-charge depressions of $\Delta \gamma_{\text{self}}/\gamma_0 \approx 0.53\%$–$0.78\%$ across the beam. The simulations are in reasonable agreement with the experiments, and indicate that the self-fields tend to (1) reduce saturation efficiencies and (2) enhance beam spreading depending upon the magnitude of external beam focusing.

I. INTRODUCTION

Free-electron laser (FEL) experiments that operate in the millimeter and submillimeter wave bands generally use intense-beam accelerators such as modulators,[1] pulse-line accelerators,[2-6] and induction linacs.[7,8] These intense-beam experiments have often operated in the collective Raman regime in which the space-charge potential from the electrostatic beam–plasma waves is dominant over the ponderomotive potential due to the beating of the wiggler and radiation fields. However, the direct current (dc) self-electric and self-magnetic fields due to the charge and current densities of the beam are typically assumed to be negligible in most theoretical treatments of these experiments. In this paper, we describe a nonlinear treatment of the FEL interaction, which includes a model of the dc self-fields of the beam in the formulation.

The dc self-fields have been treated in one-dimensional analyses of FEL's in both linear theory[9,10] and by means of a nonlinear particle-in-cell simulation.[10] Our goal in the present work is to develop a nonlinear model of dc self-fields in FEL's in three dimensions. Of course, the most general treatment of dc self-fields arises in the context of a fully three-dimensional particle-in-cell simulation of the FEL. In many cases, however, this poses an insurmountable computational obstacle. Instead, we have constructed a model of the dc self-fields, which is incorporated into

slow-time-scale simulation codes for both helical and planar wiggler geometries.[11-13] These slow-time-scale formulations require considerably less computer time than a corresponding particle-in-cell simulation, yet are capable of accurate point-by-point descriptions of FEL experiments. These nonlinear formulations, including the dc self-fields, are compared with intense-beam experiments using a planar wiggler at the Lawrence Livermore National Laboratory,[8] and helical wigglers at the Massachusetts Institute of Technology[6] and the Naval Research Laboratory.[1]

The organization of the paper is as follows. A description of the self-field model and the slow-time-scale formulation is given in Sec. II. Section III is devoted to the numerical analysis of the experiments at LLNL, MIT, and NRL. Results indicate that the dc self-field effects in these experiments provide for a reduction in the interaction efficiency relative to that computed without the self-fields as well as enhanced beam spreading. However, the overall results are within the experimental uncertainties in the measurements of the output power. A summary and discussion is given in Sec. IV.

II. THE MATHEMATICAL FORMULATION

An electron beam in a physically realizable FEL is born and accelerated and/or transported for some distance before it enters the wiggler. Various focusing schemes are often employed to transport the beam to the wiggler, which can rely upon external magnetic (typically either solenoids or magnetic quadrupoles) or electric fields. In addition,

---

[a] Permanent address: Science Applications International Corp., McLean, Virginia 22102.
[b] Permanent address: Mission Research Corp., Newington, Virginia 22122.

many experiments employ some form of beam scraping (sometimes referred to as emittance selection) to ensure a beam with a small axial velocity spread.[2,8] Hence, the electron beam, and the self-fields, can exhibit a complex structure at the entrance to the wiggler, and a complete treatment of the initial conditions and self-fields in the electron beam in a FEL would require a full-scale particle-in-cell simulation for each specific configuration, including the accelerator and beam transport system as well as the FEL. Such an end-to-end simulation is beyond the scope of this paper. Instead, we develop a model of the self-fields in an FEL based upon the simplest treatment of the self-fields in an electron beam derived from an idealized model of a beam with uniform, azimuthally symmetric profiles in both the density and velocity. This describes the case of the injection of a uniform parallel-propagating beam.

In such a case, the beam density is given by $n_b(r) = n_b$ for $r < R_b$ and zero otherwise, where R_b denotes the beam radius; then the self-electric field, $\mathbf{E}^{(s)}$, is determined by

$$\frac{1}{r}\frac{\partial}{\partial r}(rE_r^{(s)}) = -4\pi en_b(r), \tag{1}$$

which has the solution

$$\mathbf{E}^{(s)} = -\frac{m_e}{2e}\omega_b^2 r\hat{\mathbf{e}}_r, \tag{2}$$

where e and m_e are the electronic charge and mass, and $\omega_b^2 \equiv 4\pi e^2 n_b/m_e$ is the square of the beam–plasma frequency. Energy conservation for this configuration is given by the sum of the kinetic and potential (due to the self-electric field) energies. Within the beam, the Lorentz force equations yield

$$\frac{d}{dt}\left(\gamma - \frac{\omega_b^2}{4c^2}r^2\right) = 0, \tag{3}$$

where γ is the relativistic factor. This results in a space-charge depression in the kinetic energy across the beam, which may be expressed as

$$\gamma(r) = \gamma_0 + \frac{\omega_b^2}{4c^2}(r^2 - R_b^2). \tag{4}$$

In Eq. (4), γ_0 denotes the kinetic energy at the edge of the beam or, alternatively, the total energy.

The lowest-order representation for the self-magnetic field is obtained under the assumption that the beam propagates paraxially with $\mathbf{v} = v_z\hat{\mathbf{e}}_z$ for $r < R_b$, and zero otherwise. This assumption requires that the space-charge depression across the beam be small. Observe from (4) that the space-charge depression in the kinetic energy at the center of the beam depends upon $\omega_b^2 R_b^2/4c^2$ and is proportional to the total beam current through

$$\frac{\Delta\gamma_{\text{self}}}{\gamma_0} \approx 5.88 \times 10^{-5}\frac{I_b}{\sqrt{\gamma_0^2 - 1}}, \tag{5}$$

where the beam current I_b is in amperes. For the specific cases under consideration here $\Delta\gamma_{\text{self}}/\gamma_0 < 1\%$, and the assumption of a uniform axial velocity provides a good approximation for the self-magnetic field. In this case, the self-magnetic field is determined by Ampère's law,

$$\frac{1}{r}\frac{\partial}{\partial r}(rB_\theta^{(s)}) = -\frac{4\pi e}{c}n_b(r)v_z; \tag{6}$$

hence,

$$\mathbf{B}^{(s)} = -\frac{m_e}{2e}\omega_b^2\beta_z r\hat{\mathbf{e}}_\theta, \tag{7}$$

where c is the speed of light in vacuo and $\beta_z \equiv v_z/c$.

The nonlinear formulation for the analysis of self-field effects in FEL's described in this paper is based upon a generalization of the three-dimensional nonlinear simulation codes ARACHNE[11,13] and WIGGLIN[12,13] for FEL amplifiers. These codes represent slow-time-scale formulations, where the electromagnetic field is expanded in a superposition of the transverse electric (TE) and transverse magnetic (TM) modes of either a cylindrical or rectangular waveguide, and the space-charge field describing the beam–plasma modes is expanded in a superposition of the Gould–Trivelpiece modes of the beam. Note that the space-charge field associated with the Gould–Trivelpiece mode is distinct from the self-electric field. Slow-time-scale equations govern the evolution of the amplitude and phase of each TE, TM, and Gould–Trivelpiece mode due to the interaction with the beam and wiggler/axial guide field. These equations are integrated simultaneously with the three-dimensional Lorentz force equations in the complete ensemble of electromagnetic, electrostatic, and magnetostatic fields. We emphasize that no averaging procedure is imposed on the orbit equations.

There are two major distinctions between ARACHNE and WIGGLIN. The first is that ARACHNE deals with a helical wiggler/axial guide field and a cylindrical waveguide, while WIGGLIN deals with a planar wiggler and a rectangular waveguide. Hence, the external fields used in ARACHNE are given by

$$\mathbf{B}_{\text{ext}}(\mathbf{x}) = B_0\hat{\mathbf{e}}_z + \mathbf{B}_w(\mathbf{x}), \tag{8}$$

where the wiggler field is

$$\mathbf{B}_w(\mathbf{x}) = 2B_w(z)[I_1'(\lambda)\hat{\mathbf{e}}_r\cos\chi - (1/\lambda)I_1(\lambda)\hat{\mathbf{e}}_\theta\sin\chi + I_1(\lambda)\hat{\mathbf{e}}_z\sin\chi], \tag{9}$$

and I_1 and I_1' denote the modified Bessel function of the first kind and its derivative, $\lambda \equiv k_w r$, $\chi \equiv \theta - k_w z$, k_w is the wiggler wave number ($\equiv 2\pi/\lambda_w$), and the wiggler amplitude is assumed to vary adiabatically as

$$B_w(z) = \begin{cases} B_w\sin^2\left(\dfrac{k_w z}{4N_w}\right); & 0 < z < N_w\lambda_w, \\ B_w; & z > N_w\lambda_w. \end{cases} \tag{10}$$

The planar wiggler used in WIGGLIN (no axial guide field is included) is of the form[14,15]

$$B_{w,x}(\mathbf{x}) = B_w(z)\left(\sin k_w z - \frac{\cos k_w z}{k_w B_w(z)}\frac{d}{dz}B_w(z)\right)$$

$$\times\left(\sinh k_w y - \frac{Y(k_w y)}{2k_w^2}\frac{d^2}{dx^2}\right)\frac{1}{k_w}\frac{d}{dx}X(x),$$

$$\tag{11}$$

$$B_{w,y}(\mathbf{x}) = B_w(z)\left(\sin k_w z - \frac{\cos k_w z}{k_w B_w(z)}\frac{d}{dz}B_w(z)\right)$$

$$\times\left(\cosh k_w y - \frac{k_w y \sinh k_w y}{2k_w^2}\frac{d^2}{dx^2}\right)X(x), \tag{12}$$

$$B_{w,z}(\mathbf{x}) = B_w(z)\cos k_w z\left[\sinh k_w y - \frac{Y(k_w y)}{2k_w^2}\right.$$

$$\left.\times\left(1+\frac{1}{k_w^2}\frac{d^2}{dx^2}\right)\frac{d^2}{dx^2}\right]X(x), \tag{13}$$

where the amplitude $B_w(z)$ is given by Eq. (10), $Y(k_w y)\equiv k_w y\cosh k_w y - \sinh k_w y$, and $X(x)\equiv 1+(x/a_x)^{2m}/2$. Observe that the bulk direction of wiggler motion for this model is in the x direction. The use of a wiggler model with an adiabatic entry taper for both the helical and planar wigglers allows us to self-consistently describe the injection of the beam into the wiggler. In addition, the wiggler amplitude in this model increases with increases in displacement from the axis of symmetry and provides for an additional focusing force on the beam.

The second major distinction between ARACHNE and WIGGLIN is that the Gould–Trivelpiece space-charge modes are not included in WIGGLIN. As will be discussed in detail later, this does not constitute an important restriction for the case presently under consideration.

The equations governing the evolution of the TE modes in a rectangular waveguide, as used in WIGGLIN,[12,13] are given here for the sake of clarity. A detailed derivation of the corresponding equations for the TM modes may also be found in Refs. 12 and 13, and the TE and TM modes and Gould–Trivelpiece modes in a cylindrical waveguide are treated in Refs. 11 and 13. The electromagnetic field in a rectangular waveguide of dimensions $-a/2<x<a/2$ and $-b/2<y<b/2$ is represented as a superposition of the TE and TM modes of the vacuum waveguide. Hence, the vector potential of the TE modes is given by

$$\delta\mathbf{A}(\mathbf{x},t) = \sum_{l,n=0}^{\infty} {}'\delta A_{l,n}(z)\mathbf{e}_{l,n}(x,y)\cos\alpha_{l,n}(z,t), \tag{14}$$

where the phase for frequency ω and wave number $k_{l,n}$ is given by

$$\alpha_{l,n}(z,t) = \int_0^z dz'\, k_{l,n}(z) - \omega t, \tag{15}$$

the summation Σ' indicates that both l and n are not both zero,

$$\kappa_{l,n} = \pi\sqrt{\frac{l^2}{a^2}+\frac{n^2}{b^2}}, \tag{16}$$

is the cutoff wave number, $X=x+a/2$, $Y=y+b/2$, and the polarization vector is

$$\mathbf{e}_{l,n} \equiv \frac{n\pi}{\kappa_{l,n}b}\hat{\mathbf{e}}_x\cos\left(\frac{l\pi X}{a}\right)\sin\left(\frac{n\pi Y}{b}\right)$$

$$-\frac{l\pi}{\kappa_{l,n}a}\hat{\mathbf{e}}_y\sin\left(\frac{l\pi X}{a}\right)\cos\left(\frac{n\pi Y}{b}\right). \tag{17}$$

It is implicitly assumed that the amplitudes and wave numbers vary slowly in z over a wave period.

The slow-time-scale equations governing the evolution of the amplitudes and wave numbers of each of these modes are obtained by substitution of the field representation into Maxwell's equations and averaging those equations over a wave period. This effectively removes the fast-time-scale oscillation from consideration, and results in two second-order equations for the amplitudes and phases,

$$\frac{d^2}{dz^2}\delta a_{l,n}+\left(\frac{\omega^2}{c^2}-k_{l,n}^2-\kappa_{l,n}^2\right)\delta a_{l,n}$$

$$= 8F_{l,n}\frac{\omega_b^2}{c^2}\left\langle\frac{\cos\alpha_{l,n}}{|v_z|}\mathbf{e}_{l,n}\cdot\mathbf{v}\right\rangle \tag{18}$$

and

$$2k_{l,n}^{1/2}\frac{d}{dz}(k_{l,n}^{1/2}\delta a_{l,n}) = -8F_{l,n}\frac{\omega_b^2}{c^2}\left\langle\frac{\sin\alpha_{l,n}}{|v_z|}\mathbf{e}_{l,n}\cdot\mathbf{v}\right\rangle, \tag{19}$$

where $\delta a_{l,n}\equiv e\,\delta A_{l,n}/m_e c^2$ and $F_{l,n}\equiv\frac{1}{2}$ when either $l=0$ or $n=0$, and unity otherwise. As mentioned previously, similar equations apply for the TM modes in a rectangular waveguide, as well as for the TE and TM modes and Gould–Trivelpiece modes in a cylindrical waveguide.

These equations are equivalent to a calculation of the average $\mathbf{J}\cdot\delta\mathbf{E}_{l,n}$ for each mode. The averaging operator that appears in (18) and (19) is defined over the initial conditions of the beam upon entry to the wiggler (at $z=0$), and includes the effect of a momentum spread by means of the distribution

$$F_b(\mathbf{p}_0) = A\exp[-(p_{z0}-p_0)^2/\Delta p_z^2]$$

$$\times\delta(p_0^2-p_{\perp 0}^2-p_{z0}^2)H(p_{z0}), \tag{20}$$

where p_0 and Δp_z denote the bulk momentum and the axial momentum spread, respectively, H denotes the Heaviside function, and the normalization constant is

$$A \equiv \left[\pi\int_0^{p_0}dp_{z0}\exp\left(-\frac{(p_{z0}-p_0)^2}{\Delta p_z^2}\right)\right]^{-1}. \tag{21}$$

Observe that this distribution describes a monoenergetic beam with a pitch-angle spread. The axial energy spread associated with the distribution is related to the momentum spread via

$$\frac{\Delta\gamma_z}{\gamma_0} = 1-\frac{1}{\sqrt{1+2(\gamma_0^2-1)(\Delta p_z/p_0)}}, \tag{22}$$

where $\gamma_0=1+p_0^2/m_e^2c^2$. As a result, the averaging operator takes the form

2320   Phys. Fluids B, Vol. 5, No. 7, July 1993

Freund, Jackson, and Pershing   2320

$$\langle(\cdots)\rangle \equiv \frac{A}{4\pi A_b} \int_0^{2\pi} d\phi_0 \int_0^{p_0} dp_{x0}\,\beta_{x0}\exp\left(\frac{-(p_{x0}-p_0)^2}{\Delta p_z^2}\right)$$

$$\times \int_{-\pi}^{\pi} d\psi_0\, \sigma_{\parallel}(\psi_0) \int\int_{A_b} dx_0\,dy_0\,\sigma_\perp(x_0,y_0)$$

$$\times(\cdots), \tag{23}$$

where A_b is the initial cross-sectional area of the beam, $\psi_0(\equiv -\omega t_0)$ is the initial value of the ponderomotive phase, $\beta_{x0}\equiv v_{x0}/c$, $\phi_0\equiv\tan^{-1}(p_{y0}/p_{x0})$, and $\sigma_{\parallel}$ and $\sigma_\perp$ describe the initial beam distribution in phase and cross section.

Each mode interacts resonantly with the electrons and is coupled via the Lorentz force equations in the combined static and fluctuating fields, which, in the present analysis, includes the self-electric and self-magnetic fields of the beam. As mentioned previously, a complete self-consistent analysis of self-fields in FEL's requires a full-scale, three-dimensional particle-in-cell simulation. This necessitates a significantly greater computational investment than the slow-time-scale formulation, and is beyond the scope of this paper. Instead, we shall adapt the simplified description of the self-fields given in Eqs. (2) and (7) by allowing for the motion of the beam centroid in the wiggler and using an average axial velocity in the self-magnetic field. As a result, the self-electric and magnetic fields are represented as

$$\mathbf{E}^{(s)} = -\frac{m_e}{2e}\omega_b^2[(x-\langle x\rangle)\hat{\mathbf{e}}_x + (y-\langle y\rangle)\hat{\mathbf{e}}_y] \tag{24}$$

and

$$\mathbf{B}^{(s)} = -\frac{m_e}{2e}\omega_b^2\langle\beta_z\rangle[(y-\langle y\rangle)\hat{\mathbf{e}}_x - (x-\langle x\rangle)\hat{\mathbf{e}}_y]. \tag{25}$$

Given these self-fields, as well as the external fields specified earlier for the axial guide and wiggler fields, the Lorentz force equations take the form

$$v_z\frac{d}{dz}\mathbf{p} = -e(\mathbf{E}^{(s)}+\delta\mathbf{E}) - \frac{e}{c}\mathbf{v}\times(B_0\hat{\mathbf{e}}_z + \mathbf{B}_w + \mathbf{B}^{(s)} + \delta\mathbf{B}), \tag{26}$$

where $\delta\mathbf{E}$ and $\delta\mathbf{B}$ represent the aggregate electric and magnetic fields from each TE, TM, and Gould–Trivelpiece mode.

It is important to observe that several implicit assumptions underlie this approximation for the self-fields in the wiggler. The first is that even while the beam density is assumed to be a uniform flat-top profile with a circular cross section upon entry to the wiggler, it does not necessarily remain either uniform or circular during the course of the interaction. This distortion of the beam in the wiggler has been well documented for both helical[11,13] and planar wigglers[12,13] under the neglect of the self-fields. The second is that the self-magnetic field has been derived under the additional assumptions of uniform paraxial motion of the beam. However, the effect of the wiggler is to induce a bulk transverse wiggle motion and a velocity shear due to the wiggler inhomogeneities, and these distortions to the

beam current can affect the self-magnetic field in the wiggler. In order to estimate the magnitude of this effect, consider the inclusion of the lowest-order wiggler-induced motion in an idealized one-dimensional helical wiggler in the source current for the self-magnetic field. This results in a correction to the self-magnetic field of the form (see the Appendix)

$$\mathbf{B}^{(s)} = -\frac{m_e}{2e}\omega_b^2\beta_{\parallel}\,r\hat{\mathbf{e}}_\theta + \frac{\omega_b^2}{\gamma_0 k_w^2 c^2}\frac{k_w v_{\parallel}}{\Omega_0 - k_w v_{\parallel}}\mathbf{B}_w, \tag{27}$$

where $\Omega_0 \equiv eB_0/\gamma_0 m_e c$. The second term can describe either diamagnetic [$\Omega_0 < k_w v_{\parallel}$] or paramagnetic [$\Omega_0 > k_w v_{\parallel}$] corrections to the wiggler field,[9] but is negligible as long as $k_w R_b > 2|v_w/v_{\parallel}|$, where v_w is the wiggler-induced transverse velocity. Hence, Eqs. (24) and (25) represent a reasonable approximation for the self-fields in the wiggler as long as the transverse electron displacement due to the wiggler is less than the beam radius.

III. NUMERICAL ANALYSIS

The set of coupled nonlinear differential equations for the fields and the electrons is solved numerically for an amplifier configuration in which a single wave of frequency ω is injected into the system at $z=0$ in concert with the electron beam. The solution to this initial value problem can be accomplished by a variety of different algorithms, including Adams–Moulton predictor/corrector and Runge–Kutta techniques. The advantage of the Adams–Moulton technique is that it is more stable than the Runge–Kutta algorithm; however, this occurs at the practical cost of a greatly increased memory requirement. In practice, it is found that the fourth-order Runge–Kutta–Gill technique leads to no serious numerical instabilities and is employed here.

The initial conditions on the waveguide modes are chosen to model the injection of each mode at the same frequency with some arbitrary power level and with a wave number equal to that of the vacuum value [i.e., $k_{l,n}(z=0) = (\omega^2/c^2 - \kappa_{l,n}^2)^{1/2}$]. Since the wiggler field is zero at the start of the wiggler, the growth rate of each mode is also assumed to be zero initially. The initialization of the Gould–Trivelpiece modes for the helical wiggler/cylindrical waveguide configuration is accomplished using the numerical noise associated with the initial particle positions.[11,13]

The initial state of the electron beam is chosen to model the injection of a monoenergetic, uniform, axisymmetric electron beam with a flat-top density profile for $r_0 < R_b$; hence, $\sigma_{\parallel}=1$ for $-\pi < \psi_0 < \pi$, and $\sigma_\perp=1$ for $r_0 < R_b$. The effect of the self-electric field on the initial kinetic energy mirrors the space-charge reduction described in Eq. (6), where γ_0 describes the total energy that is the initial kinetic energy at the edge of the beam. As a result, we scale the initial momentum,

$$p_0(r_0) \simeq p_0\sqrt{1 + \frac{\Delta\gamma(r_0)[2\gamma_0+\Delta\gamma(r_0)]}{\gamma_0^2-1}}, \tag{28}$$

where

2321   Phys. Fluids B, Vol. 5, No. 7, July 1993

Freund, Jackson, and Pershing   2321

$$\Delta\gamma(r_0) \equiv \frac{\omega_b^2}{4c^2}(r_0^2 - R_b^2), \qquad (29)$$

and $|p_0|^2/m_e^2c^2 = \gamma_0^2 - 1$. Thus, the initial kinetic energy of the particles increases with radius from the beam center. The particle averages, as well as the initial particle loading, are performed by an nth-order Gaussian quadrature in each of the initial degrees of freedom (i.e., r_0, θ_0, ψ_0, p_0, ϕ_0). A more detailed description of the numerical procedures is given in Refs. 11–13.

It is important to observe here that no attempt is made to match the beam into the wiggler in order to achieve a beam envelope with a relatively constant radius throughout the wiggler. We treat a simpler model in which a paraxially propagating beam is injected into the wiggler, and the subsequent motion is calculated for the assumed electrostatic, magnetostatic (including the self-magnetic), and electromagnetic fields.

The effect of the self-electric and self-magnetic fields are studied for parameters consistent with two 35 GHz amplifier experiments corresponding to planar and helical wiggler configurations and with a 16 GHz amplifier experiment using a helical wiggler. The planar-wiggler experiment was conducted at Lawrence Livermore National Laboratory and employed a 3.5 MeV/850 A electron beam with an initial radius of 1 cm propagating through a rectangular waveguide ($a = 9.8$ cm and $b = 2.9$ cm) in the presence of a planar wiggler with a period of 9.8 cm and an entry taper of one wiggler period in length. The wiggler was generated by a stack of electromagnets, which could be adjusted to produce fields of more than 4 kG in magnitude. Additional beam focusing in the experiment was accomplished with an external quadrupole field; hence, the self-fields may have been less important in the experiment than indicated in the simulation. However, it is found that the results of the simulation with or without the self-fields are in agreement with the measurements to within the experimental uncertainties. The first helical wiggler experiment we describe is located at the Massachusetts Institute of Technology[6] and employed a 750 keV electron beam, with an initial beam radius of 0.25 cm. The beam current that could propagate through the system varied with the axial magnetic field up to a maximum of approximately 300 A. The beam propagated through a cylindrical waveguide with a radius of 0.51 cm in the presence of a helical wiggler field ($B_w < 1.8$ kG, $\lambda_w = 3.14$ cm), with a six period entry taper and an axial guide field of up to 12 kG. Experiments were conducted with the axial guide field oriented both parallel and antiparallel to the bulk streaming of the electron beam. The second helical wiggler experiment is located at the Naval Research Laboratory[1] and employs a 250 keV/100 A electron beam with an initial beam radius of 0.4 cm. The wiggler field has a period of 2.54 cm, and an entry taper region of five wiggler periods in length, an exit taper of three wiggler periods in length, and an amplitude variable up to 500 G. The axial guide field can be varied up to a field of 3.2 kG. This is an amplifier experiment at frequencies in the range of 12–20 GHz, which employs a waveguide with a radius of 0.815 cm; hence, the primary interaction is with the TE_{11} mode. It should be noted that although the beam parameters were very different in these experiments, the magnitudes of the space-charge depression across the beam in each case are similar, and we find that $\Delta\gamma_{self}/\gamma_0 \approx 0.64\%$ in the LLNL experiment, $\Delta\gamma_{self}/\gamma_0 \approx 0.78\%$ in the MIT experiment (at a current of 300 A), and $\Delta\gamma_{self}/\gamma_0 \approx 0.53\%$ in the NRL experiment.

In order to evaluate the effect of the self-fields in the context of this formulation, we shall compare the experimental measurements with the results of WIGGLIN and ARACHNE, both with and without the inclusion of the self-field models.

A. The planar wiggler configuration

The amplifier experiment at LLNL was driven by a magnetron that produced approximately 50 kW at a frequency of 34.6 GHz. At this frequency, the waveguide is overmoded and the power was predominantly injected into the TE_{01}, TE_{21}, and TM_{21} modes, although the TE_{01} mode was dominant. The experimental results indicated that saturation occurred at a power level of approximately 180 MW over a length of 1.3 m (including the entry taper). The bulk of the output signal was found to be in the TE_{01} mode, but there was also substantial power in the TE_{21} and TM_{21} modes as well. As mentioned earlier, the space-charge (i.e., Gould–Trivelpiece) waves were not important for this experiment. The primary reason for this is that, for these beam parameters, Landau damping of the space-charge waves ensures that the space-charge waves do not reach sufficiently high amplitudes to affect the interaction.[16,17]

In comparing the results from WIGGLIN with the experiment, we must make assumptions as to (1) the initial power levels in each of the three relevant waveguide modes, and (2) the initial axial energy spread of the beam. Experimental measurements[8] indicate that the bulk of the injected power was in the TE_{01} mode and that the initial power in the TE_{21} mode was approximately 1% that of the TE_{01} mode. The power in the TM_{21} mode was found to be still lower than that of the TE_{21} mode. Hence, these modes are initialized at power levels of 50 kW in the TE_{01} mode, 500 W in the TE_{21} mode, and 100 W in the TM_{21} mode. Direct measurements of the initial axial energy spread of the beam[18] with an electron spectrometer were able only to place an upper bound on the initial axial energy spread of approximately 2%.

In the absence of the self-fields, WIGGLIN provided close agreement with the experimental observations for the choice of $\Delta\gamma_z/\gamma_0 = 1.5\%$, which is within the bound set by the experimental measurements. A plot of the growth of the signal versus axial distance for these parameters is shown in Fig. 1, showing both the total power and the power in the TE_{01} mode. Observe that although the TE_{01} mode is overwhelmingly dominant at the start of the interaction, it accounts for only about 60% of the signal at saturation. This is due to the fact that the TE_{21} mode had the higher growth rate. The oscillation in the power occurs at a period of $\lambda_w/2$ and is due to the effect of the lower beat wave between the wiggler and the radiation field.[12,13]
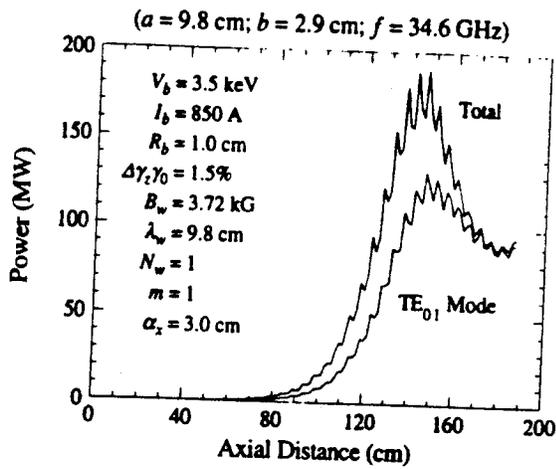
$(a = 9.8$ cm; $b = 2.9$ cm; $f = 34.6$ GHz)

$V_b = 3.5$ keV
$I_b = 850$ A
$R_b = 1.0$ cm
$\Delta\gamma_z/\gamma_0 = 1.5\%$
$B_w = 3.72$ kG
$\lambda_w = 9.8$ cm
$N_w = 1$
$m = 1$
$\alpha_x = 3.0$ cm

Total

TE_{01} Mode

FIG. 1. Evolution of the power versus axial distance in the absence of self-fields.

$(a = 9.8$ cm; $b = 2.9$ cm; $f = 34.6$ GHz)

$V_b = 3.5$ MeV
$I_b = 850$ A
$R_b = 1.0$ cm
$\Delta\gamma_z/\gamma_0 = 0.5\%$
$B_w = 3.72$ kG
$\lambda_w = 9.8$ cm
$N_w = 1$
$m = 1$
$\alpha_x = 3.0$ cm

Total

TE_{01} Mode
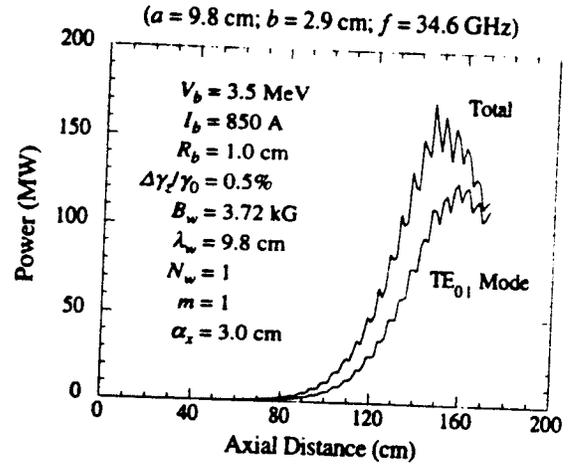
FIG. 3. Evolution of the power versus axial distance in the presence of self-fields.

Agreement between the simulation and the experimental measurement is good. The peak saturated power found in simulation is approximately 190 MW, which falls to approximately 180 MW when averaged over the lower beat wave. The saturation length is found to be approximately 1.45 m.

The interaction efficiency is relatively insensitive to the initial axial energy spread for $\Delta\gamma_z/\gamma_0 < 2\%$ in the absence of the self-fields; however, this is not the case when the self-fields are included in the simulation. The reason for this is that effect of the self-fields and that of an initial axial energy spread both act to increase the spreading of the beam. Recall that the axial energy spread is due to a pitch-angle spread; hence, increases in the axial energy spread imply increases in the transverse momenta of the beam. As a result, the combined effects of the self-fields and an increasing axial energy spread can act to enhance beam loss to the waveguide walls as well as to decrease the coupling between the beam and the waveguide modes. This is illustrated clearly in Fig. 2, in which we plot the variation in the efficiency as a function of the initial axial energy

spread, both with and without the inclusion of the self-fields. As shown in the figure, the efficiency decreases from about 7.12% to 6.35% as the axial energy spread varies up to 2%. In contrast, when self-fields are included, the efficiency falls off rapidly for $\Delta\gamma_z/\gamma_0 > 0.5\%$. Note that the initial increase in the efficiency with the axial energy spread for $\Delta\gamma_z/\gamma_0 < 0.25\%$ is due to the shift in the tuning of the interaction with changes in the energy spread. This effect has been discussed in the literature,[19] and is due to the fact that the increase in the axial energy spread effectively reduces the average streaming velocity of the beam. This shifts the gain band, and can increase the efficiency at fixed frequencies, although the maximum efficiency across the gain band decreases.

It is clear from Fig. 2 is that the power measured in the experiment can be recovered from the simulation for $\Delta\gamma_z/\gamma_0 < 0.5\%$, which is within the experimental uncertainty. The general conclusion to be drawn from this is that the effect of the dc self-fields on the interaction can be significant, but that in this case they are smaller than the effect of the uncertainties in the initial axial energy spread, despite the use of a high current beam.

$(a = 9.8$ cm; $b = 2.9$ cm; $f = 34.6$ GHz)

$V_b = 3.5$ MeV
$I_b = 850$ A
$R_b = 1.0$ cm

$B_w = 3.72$ kG
$\lambda_w = 9.8$ cm
$N_w = 1$
$m = 1$
$\alpha_x = 3.0$ cm

self-fields included

FIG. 2. Plot of the efficiency versus the initial axial energy spread both with and without the self-fields.

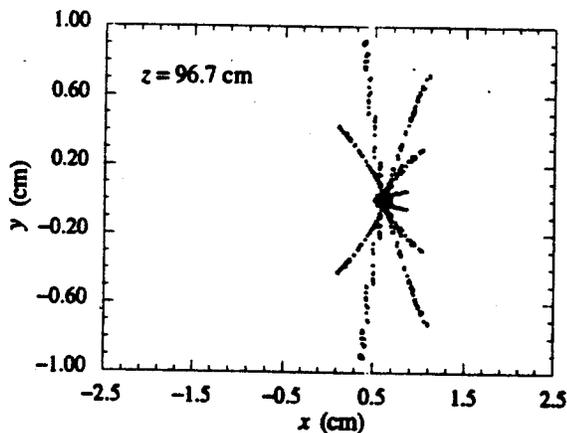
$z = 0$
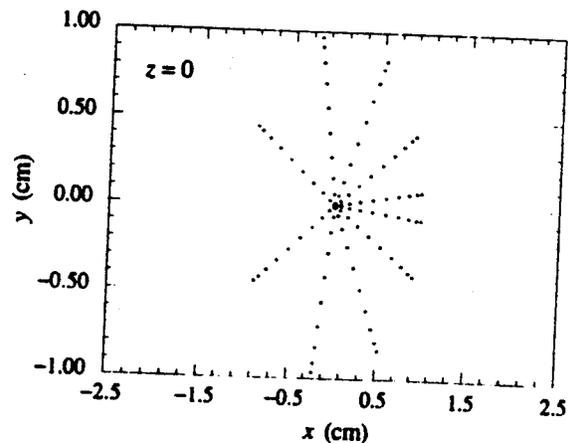
FIG. 4. Beam cross section at the entrance to the wiggler.
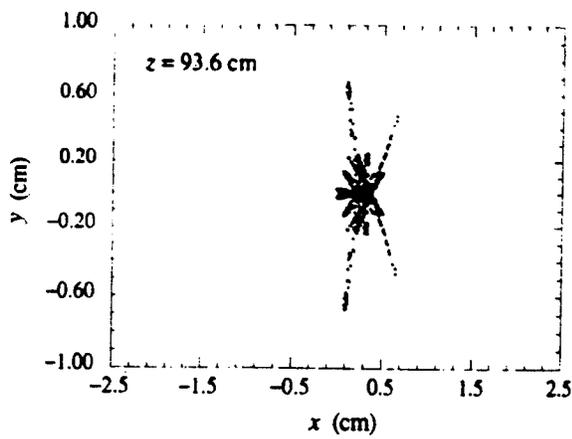
FIG. 5. Beam cross section at $z = 93.6$ cm without self-fields.
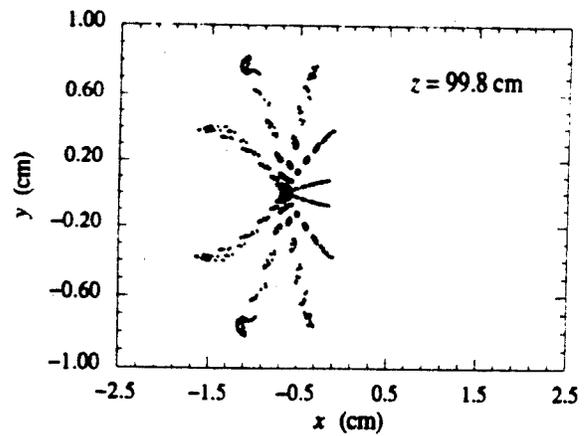
FIG. 7. Beam cross section at $z = 99.8$ cm without self-fields.

The evolution of the power as a function of axial distance subject to the inclusion of the self-fields is shown in Fig. 3 for the choice of an initial axial energy spread of 0.5%. This is chosen for illustrative purposes since the saturated power in the TE_{01} mode is relatively unchanged, in comparison with the results shown in Fig. 1. In this case, a peak saturated power level of approximately 175 MW (falling to ≈ 165 MW when averaged over the lower beat wave) was found over a saturation length of about 1.45 m. Hence, the result of the inclusion of the self-fields is a reduction of approximately 8% in the total saturated power, and somewhat less of a reduction in the growth rate. Recall that no additional focusing due to a magnetic quadrupole field is included in WIGGLIN; hence, the effects of the self-fields seen in simulation may be greater than in the experiment. However, given the experimental uncertainties in the power measurements and the fact that only an upper bound of 2% is known regarding the initial axial energy spread of the beam, the results from WIGGLIN either with or without the self-fields are consistent with the experimental measurements.

It is important to observe, as mentioned previously, that the saturated power in the TE_{01} mode both with and without the self-fields is of the order of 125 MW; hence, the

reduction in the total saturated power is due largely to a decline in the power in the TE_{21} (and to a lesser extent the TM_{21}) mode. A detailed analysis of the electron dynamics is required in order to explain why the TE_{21} and TM_{21} modes are more sensitive to the self-fields for these parameters. In either case, the initial cross section of the electron beam is chosen to model the injection of a cylindrical pencil beam. The initial loading of the electrons by means of a ten-point Gaussian algorithm in r_0 and θ_0 is shown in Fig. 4. Note that (1) the nonuniform spacing between the electrons is characteristic of the Gaussian algorithm that compensates by the assignment of different weights to each electron, and (2) that the noncircular envelope is an artifact due to the scale on the plot.

In the absence of the self-fields, the beam undergoes complex motion, which includes the bulk wiggler-induced transverse oscillation, betatron oscillations due to wiggler inhomogeneities, and responses to the electromagnetic fields. Figures 5–8 show the evolution of the beam cross section over approximately one wiggler period in the linear stage of the interaction well before saturation, without the inclusion of the self-fields. The inclusion of the self-fields can be expected to alter the beam trajectories to some degree depending upon the magnitude of the fields. One im-

FIG. 6. Beam cross section at $z = 96.7$ cm without self-fields.
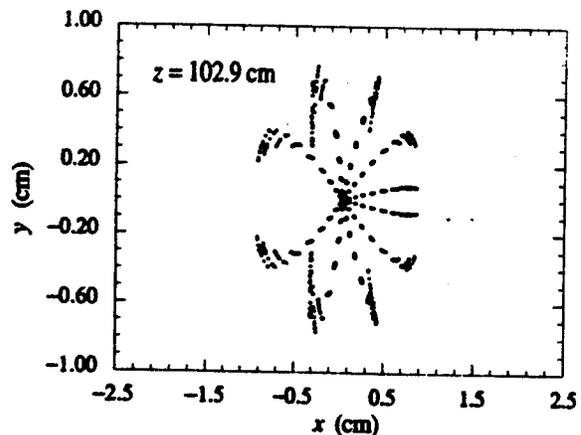
FIG. 8. Beam cross section at $z = 102.9$ cm without self-fields.
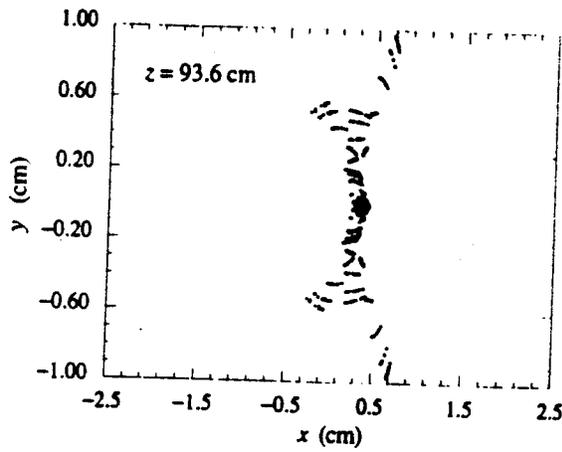
FIG. 9. Beam cross section at $z=93.6$ cm with self-fields.

FIG. 11. Beam cross section at $z=99.8$ cm with self-fields.

portant effect is the spreading of the beam induced by the self-electric field. Figures 9–12 show the beam cross section over the same range, with the self-fields included. It is clear that the beam distortion due to the action of the wiggler, radiation, and self-fields is complex. However, the principal effect that can alter the interaction with the TE_{21} and TM_{21} modes is the spreading induced in beam cross section in the x direction under the action of the self-electric field. The TE_{01} mode will be relatively insensitive to this variation since this field is uniform in the x direction; hence, relatively little variation in the saturated power in this mode is expected. In contrast, since the TE_{21} and TM_{21} modes vary in x, any beam spreading in this direction due to the action of the self-fields can be expected to impact the saturated power—in this case to reduce it.

Energy conservation is preserved to good accuracy whether or not self-fields are included in the simulation, although the potential energy due to the self-electric field must be included in the calculation. In the absence of the self-fields, the relative difference between the energy lost by the electrons and that gained by the radiation is within 0.1%. When self-fields are included, however, the discrepancy increases, and energy conservation is good to within 1%. The reason for this increased discrepancy is that the

self-field model implicitly assumes a cylindrical beam, while the beam distortions due to the action of the wiggler and self-fields results in a more complex shape. However, the inaccuracies introduced by the distortion of the beam cross section are relatively small for the present case since energy conservation is still preserved to within 1%.

B. The helical wiggler configuration

The MIT amplifier experiment was driven by a magnetron that produced from 8–10 kW at a frequency of 33.39 GHz. The TE_{11} mode was the only wave mode, given the waveguide radius, which could resonantly interact with the beam; however, this experiment operated in the Raman regime and the Gould–Trivelpiece modes must be included. In practice, it was found[20] that only the lowest-order Gould–Trivelpiece mode (for azimuthal mode number $l=0$, and radial mode number $n=1$) was required to obtain reasonable agreement between ARACHNE and the experiment in the absence of self-field effects. The experiment operated in three regimes corresponding to an axial magnetic field which was aligned either parallel or antiparallel (or reversed field) to the wiggler and the streaming of

FIG. 10. Beam cross section at $z=93.7$ cm with self-fields.
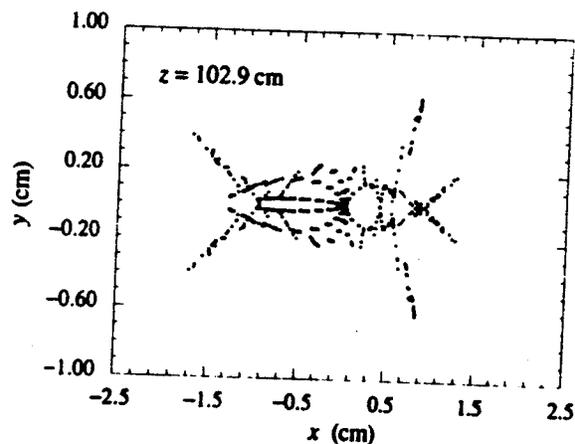
FIG. 12. Beam cross section at $z=102.9$ cm with self-fields.
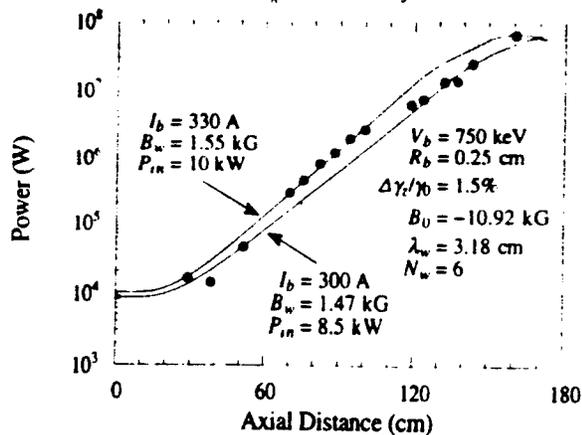
2325   Phys. Fluids B, Vol. 5, No. 7, July 1993

Freund, Jackson, and Pershing   2325

FIG. 13. The evolution of the power versus axial position as determined with ARACHNE and from the experiment (dots) for the reversed-field configuration.
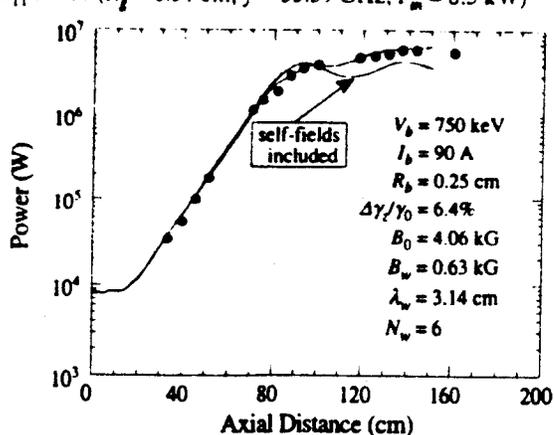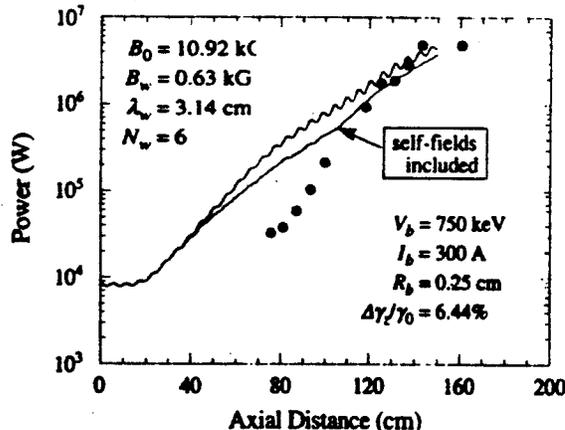
FIG. 15. The evolution of the power as determined with ARACHNE and from the experiment (dots) for the group I case with and without the self-fields.

the electron beam. In the parallel orientation of the magnetic field, two regimes are found, which are referred to in the literature as either group I for which $\Omega_0 < k_w v_\parallel$ or group II for which $\Omega_0 > k_w v_\parallel$, and the experiment was operated for axial fields in both regimes. The third operating regime is the reversed-field case. The maximum operational output power was found to occur in the reversed-field case in which 61 MW. Output powers of the order of 5 MW was obtained in either the group I or group II cases. Detailed descriptions of the comparison of ARACHNE with this experiment in the absence of self-fields can be found in Refs. 20 and 21.

The first case we consider here is that of a field-reversed configuration, in which the nominal experimental magnetic field parameters were an axial field magnitude of 10.92 kG and a wiggler field of 1.47 kG. The transmitted current for these field parameters was 300 A ($\pm 10\%$), and the axial energy spread of the beam is assumed to be

1.5%, as indicated in the experiment. These parameters represent the case of the peak power observed in the experiment of 61 MW.

The comparison of the experiment and ARACHNE in the absence of self-fields is shown in Fig. 13, in which the power is plotted as a function of axial position, and in which the dots represent the power as measured in the experiment. As shown in the figure, ARACHNE was used for two sets of parameters. The first corresponds to the nominal experimental values given above, and the second corresponds to the upper limits on the (1) current, (2) wiggler field, and (3) input power (due to the experimental uncertainties) of 330 A, 1.55 kG, and 10 kW, respectively. As is evident in the figure, the agreement between the experimental measurements and ARACHNE is good, and virtually all the data points fall between these two curves. The saturated power for these two choices of the current, wiggler field, and input power differ only marginally and are

TE$_{11}$ Mode (R_g = 0.51 cm; f = 33.39 GHz; P_{in} = 8.5 kW)

TE$_{11}$ Mode (R_g = 0.51 cm; f = 33.39 GHz; P_{in} = 8.5 kW)
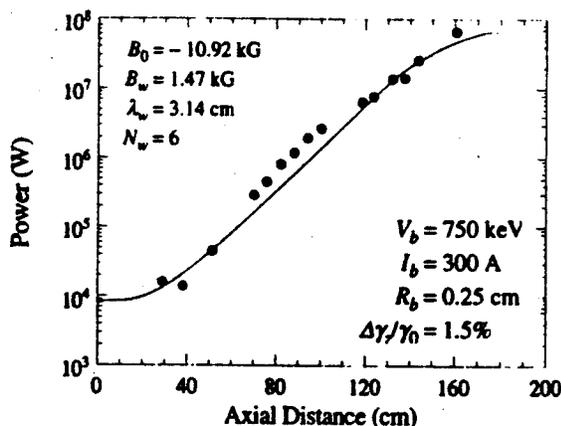
FIG. 14. The evolution of the power as determined with ARACHNE and from the experiment (dots) for the reversed-field configuration subject to the inclusion of the self-fields.

FIG. 16. The evolution of the power as determined with ARACHNE and from the experiment (dots) for the group II case with and without the self-fields.

close to the 61 MW measured in the experiment. The principal difference is in the saturation length, which is due to a small discrepancy in the growth rates for these two cases.

The effect of self-fields on this experiment in the reversed-field regime is relatively small, and the power is plotted as a function of axial position in Fig. 14, as computed with ARACHNE, subject to the inclusion of the self-fields and for the nominal experimental parameters shown in Fig. 13. The experimental data is also represented in the figure by the dots. Observe that the self-field effect is marginal, and a negligible difference is found between the runs with and without the self-fields for the 300 A parameters.

The negligible effect of the self-fields is significant since the magnitudes of the space-charge depression here and for the planar wiggler case described above are comparable. The reason why the self-field effect on the interaction efficiency is negligible here but not in the planar wiggler example lies in the orbit dynamics of the beam. In the case of the planar wiggler, the wiggler itself provided relatively weak focusing of the beam in the wiggle direction; hence, the beam spreading due to the self-fields was relatively large. That is not the case for the helical wiggler/axial guide field configuration. Here, the helical wiggler itself provides substantial focusing of the beam, which is supplemented by the axial guide field. As a result, the effect of the self-fields on the beam dynamics is relatively unimportant—at least for these parameters. It should also be noted that the beam retains its circular cross section in these fields; hence, the energy conservation is unaffected by the inclusion of the self-fields and remains good to within approximately 0.1%.

It is also found that self-field effects introduce small modifications to the output power in the group I and group II regimes as well. It should be noted here that there is a discrepancy between ARACHNE and the experiment, in that using the axial energy spread of 1.5% nominally quoted for the experiment results in predicted efficiencies comparable to that found for the reversed-field case. The assumption of much higher axial energy spreads are required to obtain reasonable agreement with the measured power. The reason for this discrepancy remains uncertain at this time, but it is speculated that some misalignment exists in the transport system from the cathode to the wiggler that results in the increased axial energy spread for these cases. Be that as it may, we shall employ axial energy spreads of approximately 6.4% in these cases, which provide good agreement between the simulation and the measured powers.

The results for the power as calculated with ARACHNE with and without the self-fields is plotted versus the axial position in Fig. 15 along with the experimental data (represented by the dots) for an assumed axial energy spread of $\Delta\gamma_z/\gamma_0 = 6.4\%$. It is evident from the figure that the results from ARACHNE with and without the self-fields are close to the experimental measurements and lie within the experimental uncertainties in the power measurements.

Similar conclusions are found for the group II case shown in Fig. 16, although it is noted that while the simulation is in agreement with the output power measured in

TE$_{11}$ Mode ($R_g = 0.815$ cm; $f = 16$ GHz; $P_{in} = 5$ kW)

$V_b = 250$ keV
$I_b = 100$ A
$R_b = 0.4$ cm
$\Delta\gamma_z/\gamma_0 = 0.3\%$
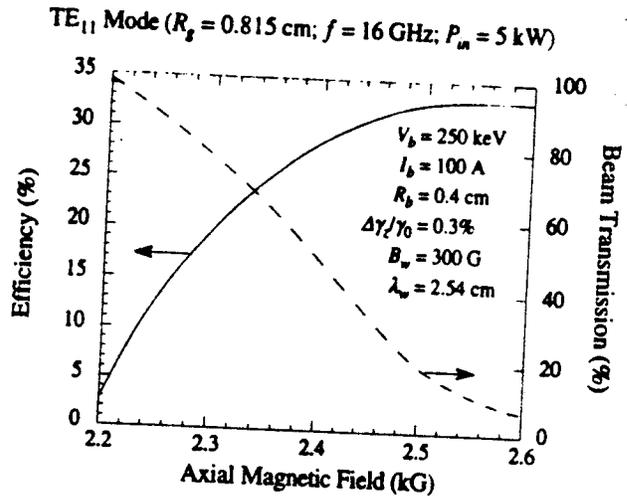$B_w = 300$ G
$\lambda_w = 2.54$ cm

FIG. 17. Plots of the variation in the efficiency and beam transmission versus the axial magnetic field in the absence of the self-fields.

the experiment it is not in agreement with the detailed evolution of the signal.

The NRL experiment has recently been redesigned and is presently in the construction/shakedown phase. It makes use of a 250 keV modulator capable of producing currents in excess of 100 A, and the electron gun is designed to produce a beam with a radius of 0.4 cm and an axial energy spread of 0.3%. The wiggler field is generated by a bifilar helical coil with a period of 2.54 cm and a total length of 33 wiggler periods, including both entrance and exit tapers of five and three wiggler periods, respectively, in length. The wiggler amplitude can be varied up to approximately 500 G. In addition, the axial guide field can be varied up to 3.2 kG. This ensures operation in the group I regime. The experiment is configured as an amplifier driven by a magnetron, which produces up to 5 kW of power over the K$_u$ band from 12–20 GHz. Hence, since the circular waveguide has a radius of 0.815 cm, the interaction is solely with the TE$_{11}$ mode. Observe that the space-charge depression for this experiment $\Delta\gamma_{self}/\gamma_0 \approx 0.53\%$ is comparable to the other two experiments, despite the much lower beam current.

In order to simulate this experiment, we consider operation at 16 GHz and use the following model for the wiggler field amplitude in Eq. (9) for the helical wiggler,

$$B_w(z) = \begin{cases} B_w \sin^2\left(\dfrac{k_w z}{20}\right); & 0 < z < 5\lambda_w, \\ B_w; & 5\lambda_w < z < 30\lambda_w, \\ B_w \cos^2\left(\dfrac{k_w(z - 30\lambda_w)}{12}\right); & 30\lambda_w < z < 33\lambda_w. \end{cases}$$

(30)

Simulations without the inclusion of the self-fields indicate that extremely high efficiencies are possible. Both the efficiency and beam transmission are plotted as functions of the axial guide field in Fig. 17 for the case of a wiggler field amplitude of 300 G. It is clear that the efficiency varies over a wide range from 3%–33% as the axial guide field

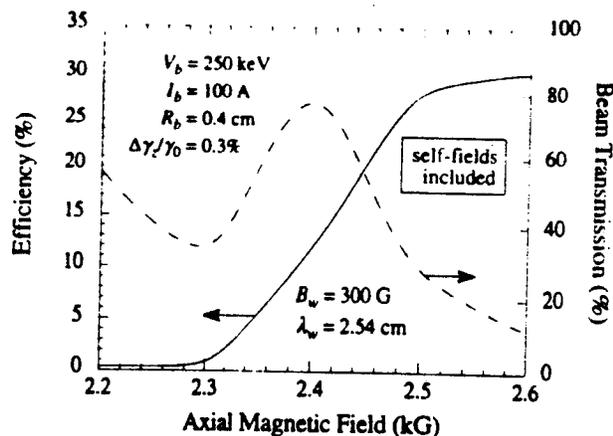TE$_{11}$ Mode (R_g = 0.815 cm; f = 16 GHz; P_{in} = 5 kW)

FIG. 18. Plots of the variation in the efficiency and beam transmission versus the axial magnetic field in the presence of the self-fields.

increases from 2.2 to 2.6 kG. However, the beam transmission falls precipitously with the increase in the efficiency from a value of about 99% at an axial field of 2.2 kG to approximately 5% at an axial field of 2.6 kG. This decline in the beam transmission is due to two factors. The first factor is that the loss of up to 30% of the beam energy to the TE$_{11}$ mode implies that the beam undergoes massive deceleration, which is accompanied by an increase in the radius of the wiggler-induced trajectory. The second factor is that the high-power electromagnetic wave acts to kick the beam away from the axis. It should be noted that, as in the case of the group I and II regimes in the MIT experiment,[20,21] saturation in the NRL experiment occurs due to beam loss rather than the more familiar phase trapping of the beam in the ponderomotive potential formed by the beating of the wiggler and radiation fields. Operation with acceptable levels of beam loss, therefore, should restrict the experiment to efficiencies below approximately 20%.

As might be expected, the effect of the self-fields can act to enhance the beam losses. The effects of the self-fields are more pronounced in this experiment than in the previously analyzed MIT experiment since the space-charge depressions are comparable for the two experiments, but the beam voltage and axial guide field is lower in the NRL experiment. The efficiency and beam transmission are plotted in Fig. 18 as functions of the axial guide field for a wiggler amplitude of 300 G, subject to the inclusion of the space-charge fields. It is evident from the figure that for strong axial guide fields in excess of approximately 2.5 kG the efficiency and beam transmission do not differ greatly from those found in the absence of the self-fields. This is because the axial field acts to confine the beam against the spreading induced by the self-fields. In contrast, both the efficiency and beam transmission are substantially less than that found in the absence of the self-fields for weak axial guide fields below about 2.3 kG. In the intermediate regime for axial guide fields in the range of 2.3–2.5 kG, however, the beam transmission is enhanced relative to both the

weak and strong guide field cases. This occurs for two reasons. The first is that the axial guide field is strong enough to provide appreciable confinement of the electron beam. The second is that the self-fields are strong enough to cause a reduction in the interaction efficiency; hence, the beam has not lost enough energy and the radiation has not gained enough energy to kick the beam appreciably toward the wall. As a result, we expect that operation with axial guide fields in the neighborhood of 2.4 kG for a wiggler field of 300 G is preferred, and will result in efficiencies of approximately 10%–15%.

IV. SUMMARY AND DISCUSSION

The nonlinear formulation of the interaction in FEL's with dc self-fields presented in this paper is based upon an idealized model in which a uniform paraxially propagating beam is injected into either a planar or helical wiggler. The model of the dc self-fields is derived from Poisson's equation and Ampère's law for this idealized beam, and has been employed previously in the study of orbital chaos in FEL's.[22-24] The subsequent beam evolution is followed by the integration of the Lorentz force equations in the combined dc self-fields, the magnetostatic wiggler and axial guide field, and the oscillating electromagnetic fields associated with the waveguide and Gould–Trivelpiece modes. The nonlinear formulation is applied to the study of three experiments using both planar and helical wiggler geometries and currents ranging from 100–850 A, but which all had similar space-charge depressions in the kinetic energy across the beam $0.53\% < \Delta\gamma_{self}/\gamma_0 < 0.78\%$.

The nonlinear formulation and simulation code WIGGLIN for the planar wiggler configuration is applied to the study of the self-fields for parameters that nominally correspond to a 35 GHz FEL amplifier experiment at LLNL. The difference lies in the fact that a magnetic quadrupole field was used in the experiment to provide for additional focusing of the beam, but was not incorporated into the simulation. As a result, the effect of the self-fields is expected to be more pronounced in simulation than in the experiment. Be that as it may, however, the principal result of the simulation is that the experimental uncertainties in the power measurements and in the initial axial energy spread of the beam have a greater impact on the interaction efficiency than the effect of the dc self-fields, despite the relatively high current beam used in the experiment. The most important uncertainty here is in the axial energy spread, which is known only to within an upper bound of approximately $\Delta\gamma_z/\gamma_0 \approx 2\%$. For appropriate choices of the initial axial energy spread, WIGGLIN is found to be in agreement with the power and growth rate measurements in the experiment either with or without the inclusion of the self-fields. Additional conclusions from the simulation are that the additional beam spreading induced by the self-fields (1) renders that interaction more sensitive to the effect of the initial axial energy spread, and (2) is relatively less important for the TE$_{01}$ mode, which is uniform in the direction of the bulk wiggler-induced oscillation than for the TE$_{21}$ and TM$_{21}$ modes, which are not.

The nonlinear formulation and simulation code ARACHNE for helical wiggler configurations is applied to the study of self-field effects in experiments at MIT and NRL. The results of the simulation for the MIT experiment show good agreement with the observations and that the dc self-fields are relatively less important for this experiment than for the planar wiggler experiment at LLNL. This is attributed to the enhanced focusing due to both the helical wiggler and the strong axial guide fields ($B_0 > 4$ kG) used in the experiment. In the case of the NRL experiment, the self-fields are found to have a significant impact on both the beam transmission and the interaction efficiency for axial guide fields below approximately 2.4–2.5 kG. For guide fields above this value, the interaction efficiency is only slightly reduced by the effect of the dc self-fields.

The general conclusion, therefore, from this analysis is that the dc self-fields can have a substantial impact on the operation of FEL's, but that the impact can be difficult to quantify in the laboratory due to various experimental uncertainties.

ACKNOWLEDGMENT

APPENDIX: ANALYTICAL MODEL OF THE SELF-FIELDS

A more detailed analytical model for the self-magnetic field than is given in Eq. (4) is obtained under the assumption that the beam current is determined from the electron trajectories in the wiggler field. A one-dimensional representation for the external fields including both an axial guide magnetic field and a helical wiggler field is given by

$$\mathbf{B}_{ext}(z) = B_0 \hat{e}_z + B_w(\hat{e}_x \cos k_w z + \hat{e}_y \sin k_w z). \quad (A1)$$

This wiggler field admits a class of steady-state helical trajectories, for which

$$\mathbf{v}(z) = v_w(\hat{e}_x \cos k_w z + \hat{e}_y \sin k_w z) + v_\parallel \hat{e}_z, \quad (A2)$$

where the transverse and axial components of the velocity are determined by the simultaneous solution of

$$v_w = \frac{\Omega_w v_\parallel}{\Omega_0 - k v_\parallel} \quad (A3)$$

and

$$v_\parallel^2 + v_w^2 = \left(1 - \frac{1}{\gamma_0^2}\right)c^2, \quad (A4)$$

where $\Omega_{0,w} \equiv |eB_{0,w}/\gamma_0 m_e c|$. Using this representation for the beam velocity, therefore, Ampère's law can be written in the form

$$\frac{1}{r} \frac{\partial}{\partial \theta} B_z^{(s)} - \frac{\partial}{\partial z} B_\theta^{(s)} = -\frac{4\pi e}{c} n_b(r) v_w \cos(k_w z - \theta),$$

$$\frac{\partial}{\partial z} B_r^{(s)} - \frac{\partial}{\partial r} B_z^{(s)} = -\frac{4\pi e}{c} n_b(r) v_w \sin(k_w z - \theta),$$

$$\frac{1}{r} \frac{\partial}{\partial r} (r B_\theta^{(s)}) - \frac{1}{r} \frac{\partial}{\partial \theta} B_r^{(s)} = -\frac{4\pi e}{c} n_b(r) v_\parallel. \quad (A5)$$

We look for solutions of the form

$$B_r^{(s)} = \hat{B}_r(r) \cos(k_w z - \theta),$$

$$B_\theta^{(s)} = \hat{B}_\theta(r) \sin(k_w z - \theta) + \bar{B}_\theta(r), \quad (A6)$$

$$B_z^{(s)} = \hat{B}_z(r) \sin(k_w z - \theta).$$

Substitution of (A6) into (A5) yields

$$k_w r \hat{B}_\theta + \hat{B}_r = \frac{4\pi e n_b}{c} r v_w, \quad (A7)$$

$$k_w \hat{B}_r - \frac{d}{dr} \hat{B}_\theta = \frac{4\pi e n_b}{c} v_w, \quad (A8)$$

$$\frac{d}{dr}(r\bar{B}_\theta) + \left(\frac{d}{dr}(r\hat{B}_\theta) - \hat{B}_r\right)\sin(k_w z - \theta) = -\frac{4\pi e n_b}{c} r v_w. \quad (A9)$$

The last of these equations implies that

$$\frac{d}{dr}(r\bar{B}_\theta) = -\frac{4\pi e n_b}{c} r v_w \quad (A10)$$

and

$$\frac{d}{dr}(r\hat{B}_\theta) = \hat{B}_r, \quad (A11)$$

which can also be obtained by elimination of $\hat{B}_z$ from Eqs. (A7) and (A8). Equation (A10) can be integrated immediately to give

$$\bar{B}_\theta = \frac{m_e}{2e} \omega_b^2 r \frac{v_w}{c}. \quad (A12)$$

The requirement that the divergence of this field vanishes yields

$$\frac{1}{r} \frac{d}{dr}(r\hat{B}_r) - \frac{1}{r} \hat{B}_\theta + k_w \hat{B}_z = 0. \quad (A13)$$

Elimination of $\hat{B}_z$ and $\hat{B}_r$ using Eqs. (A7) and (A11) gives

$$\frac{d^2}{dr^2} \hat{B}_\theta + \frac{3}{r} \frac{d}{dr} \hat{B}_\theta - k_w^2 \hat{B}_\theta = -\frac{m_e}{e} \frac{\omega_b^2}{c} k_w v_w. \quad (A14)$$

The simplest solution to Eq. (A14) is

$$\hat{B}_\theta = \frac{\omega_b^2}{k_w^2 c^2} \frac{k_w v_\parallel}{\Omega_0 - k_w v_\parallel} B_w, \quad (A15)$$

which implies that

$$\hat{B}_r = \frac{\omega_b^2}{k_w^2 c^2} \frac{k_w v_\parallel}{\Omega_0 - k_w v_\parallel} B_w, \quad (A16)$$

and

$$\hat{B}_z = 0. \quad (A17)$$

Together, Eqs. (A12) and (A15)–(A17) give the self-field shown in Eq. (27).

[1] D. E. Pershing, R. H. Jackson, H. Bluem, and H. P. Freund, Nucl. Instrum. Methods A **304**, 127 (1991).

[2] R. K. Parker, R. H. Jackson, S. H. Gold, H. P. Freund, V. L. Granatstein, P. C. Efthimion, M. Herndon, and A. K. Kinkead, Phys. Rev. Lett. **48**, 238 (1982).

[3] J. Fajans, G. Bekefi, Y. Z. Yin, and B. Lax. Phys. Rev. Lett. **53**, 246 (1984).

[4] J. Masud, T. C. Marshall, S. P. Schlesinger, and F. G. Yee, Phys. Rev. Lett. **56**, 1567 (1986).

[5] D. A. Kirkpatrick, G. Bekefi, A. C. DiRienzo, H. P. Freund, and A. K. Ganguly, Phys. Fluids B **1**, 1511 (1989).

[6] M. E. Conde and G. Bekefi, Phys. Rev. Lett. **67**, 3082 (1991).

[7] J. A. Pasour, R. F. Lucey, and C. Kapetanakos, Phys. Rev. Lett. **53**, 1728 (1984).

[8] T. J. Orzechowski, B. Anderson, W. M. Fawley, D. Prosnitz, E. T. Scharlemann, S. M. Yarema, D. Hopkins, A. C. Paul, A. M. Sessler, and J. Wurtele, Phys. Rev. Lett. **54**, 889 (1985).

[9] N. S. Ginzburg, IEEE Trans. Plasma Sci. PS-15, 411 (1987).

[10] T. J. T. Kwan and J. M. Dawson, Phys. Fluids **22**, 1089 (1979).

[11] A. K. Ganguly and H. P. Freund, Phys. Fluids **31**, 387 (1988).

[12] H. P. Freund, Phys. Rev. A **37**, 3371 (1988).

[13] H. P. Freund and T. M. Antonsen, Jr., *Principles of Free-Electron Lasers* (Chapman & Hall, London, 1992), Chap. 5.

[14] T. M. Antonsen, Jr. (private communication, 1991).

[15] H. Bluem, R. H. Jackson, H. P. Freund, D. E. Pershing, and V. L. Granatstein, Phys. Rev. Lett. **67**, 824 (1991).

[16] C. A. Brau, *Free-Electron Lasers* (Academic, Boston, MA, 1990).

[17] H. P. Freund, Nucl. Instrum. Methods (in press).

[18] T. J. Orzechowski (private communication, 1987).

[19] C. W. Roberson, Y. Y. Lau, and H. P. Freund, in *High-Brightness Accelerators*, edited by A. K. Hyder, M. F. Rose, and A. H. Gunther (Plenum, New York, 1986), p. 627.

[20] H. P. Freund and A. K. Ganguly, IEEE Trans. Plasma Sci. PS-20, 245 (1992).

[21] H. P. Freund, Phys. Fluids B **5**, 1869 (1993).

[22] C. Chen and R. C. Davidson, Phys. Rev. A **43**, 5541 (1991).

[23] L. Michel, A. Bourdier, and J. M. Buzzi. Nucl. Instrum. Methods A **304**, 465 (1991).

[24] G. Spindler and G. Renz, Nucl. Instrum. Methods A **304**, 492 (1991).

2330   Phys. Fluids B, Vol. 5, No. 7, July 1993

Freund, Jackson, and Pershing   2330

APPENDIX IX

Nonlinear Simulation of a High-Power Collective Free-Electron Laser

H.P. Freund and A.K. Ganguly

Nonlinear Simulation of a High-Power, Collective Free-Electron Laser

H. P. Freund and A. K. Ganguly

Abstract— A comparison is described between the three-dimensional nonlinear analysis and simulation code, ARACHNE, and a recent 33.4-GHz, collective, free-electron laser amplifier experiment at MIT. The experiment has demonstrated power levels of 61 MW ($\approx$ 27% efficiency) without recourse to tapered magnetic fields, using a 750–keV/300–A electron beam with a nominal axial energy spread of 1.5% propagating through a cylindrical drift tube in the presence of a helical wiggler ($B_w \leq 1.8$ kG, $\lambda_w = 3.18$ cm) and an axial guide magnetic field ($B_0 \leq 12$ kG). Significant differences in the character of the emission were found based upon the direction of the guide magnetic field. When the wiggler and guide fields were parallel, observed power levels reached approximately 4 MW for both the strong and weak guide field regimes, but vanished in the neighborhood of the magnetic *resonance* (when the Larmor and wiggler periods are comparable). In this case, *resonance* refers to the enhancement of the transverse wiggle-induced velocity, and the reduction in the emission is due to the fact that the electron beam cannot propagate in this regime due to orbital instabilities. However, the maximum power was observed in the reversed field case when the wiggler and guide fields were antiparallel. In this case, no resonant enhancement in the transverse velocity is expected to occur; however, a significant reduction in the output power was found to occur in the neighborhood of the *antiresonance*. The ARACHNE simulation is in substantial agreement with the experiment. In the reversed field case, the simulation shows peak power levels of 60 MW at the nominal axial energy spread of the experiment, as well as providing good correspondence with the power reduction at the anti-resonance. The source of this power reduction appears to be a previously unsuspected effect on the electron orbits due to the wiggler inhomogeneity. Agreement with the much lower power levels found when the wiggler and guide fields are parallel, however, requires the assumption of a substantial increase in the energy spread of the beam.

I. INTRODUCTION

THE free-electron laser (FEL) has demonstrated operation over wavelengths extending from microwaves [1]–[18] through the optical spectrum [19]–[29]. Free-Electron Laser experiments have been conducted with electron beams produced by virtually every type of accelerator, including radio-frequency linacs, microtrons, storage rings, electrostatic accelerators, induction linacs, pulse-line accelerators, and modulators. High energy/low current accelerators (i.e., RF linacs, storage rings, microtrons, and electrostatic accelerators) are typically employed at wavelengths in the infrared or shorter wavelengths, and the maximum efficiencies achieved are of the order of 4%, even using tapered wiggler designs [24], [25]. In contrast, low-energy/high-current electron beams (from induction linacs, pulse-line accelerators, and modulators) are employed at longer wavelengths in the microwave or millimeter wave regime. In the past, the optimal performance demonstrated in this regime is represented by efficiencies of the order of approximately 12% for a uniform wiggler configuration [1], [6], and approximately 35% for the case of a tapered wiggler [10].

The present paper is concerned with the theoretical description of a recent experiment conducted by Conde and Bekefi [30], [31] at the Massachusetts Institute of Technology (MIT), which demonstrated a peak efficiency of approximately 27% at a frequency of 33.4 GHz using a uniform wiggler configuration. The above-mentioned tapered wiggler experiment achieved a 35% efficiency at the same frequency using a 3.5-MeV/850-A electron beam produced by the ETA induction linac at the Los Alamos National Laboratory (LLNL) in conjunction with a planar wiggler with a tapered amplitude [10]. In contrast, the MIT experiment employed a 750–keV/300-A electron beam produced by a pulse-line accelerator in conjunction with a uniform helical wiggler/axial guide field configuration. This latter configuration has been used in the past to produce a 35-GHz FEL amplifier; however, the maximum efficiency obtained was of the order of 7% with a tapered axial magnetic field [4]. In addition, the maximum efficiency in the MIT experiment was observed when the wiggler and axial guide magnetic fields were directed antiparallel to each other. This reversed-field geometry is a previously untried configuration. Hence, this experiment has broken new ground in the performance of FEL amplifiers, and illustrates some novel aspects in the interaction physics of the FEL.

For convenience, we refer to the three-dimensional nonlinear simulation code used to analyze this experiment as "ARACHNE." This code was first developed to treat the case of FEL amplifiers in the high-gain Compton regime [32]–[36] in which the coupling with the fluctuating beam space-charge waves can be ignored. However, ARACHNE was subsequently extended to treat the collective Raman regime [37] and has been benchmarked, with good results, against two earlier FEL experiments at MIT [12], [16], as well as against a series of experiments at the Naval Research Laboratory [17]. The ARACHNE code represents a slow-time-scale formulation in which the electromagnetic field is expanded in terms of a superposition of the vacuum TE and TM modes of a cylindrical

waveguide. The space-charge field is expanded in terms of a superposition of the Gould–Trivelpiece modes [38] of a beam propagating through the waveguide in the absence of the wiggler field. A series of slow-time-scale equations are then derived for the evolution of the amplitude and phase of each TE, TM, and Gould–Trivelpiece mode in the presence of the interaction with the electron beam in the wiggler. These equations are then integrated simultaneously with the three-dimensional Lorentz force equations for the electrons in the complete ensemble of electromagnetic, electrostatic, and magnetostatic fields. We emphasize that while Maxwell's equations are averaged over the wave period in order to derive the slow-time-scale equations for the field amplitudes and phases, no averaging procedure is imposed on the orbit equations. It will be demonstrated that this is an essential feature of the formulation required to explain many aspects of the experiment.

The organization of the paper is as follows. A brief description of the experiment is given in Section II. Section III is devoted to a brief description of the single-particle orbit dynamics in a combined helical wiggler/axial guide field system, and the associated implications for the FEL interaction. A more complete description of the ARACHNE formulation is given in Section IV. The detailed comparison with the experiment is presented in Section V, which is divided into two subsections dealing with the parallel and antiparallel alignment of the wiggler and guide magnetic fields. A summary and discussion is given in Section VI.

II. EXPERIMENTAL DESCRIPTION

In this section, we provide a brief description of the experiment for purposes of comparison. The interested reader is referred to the original paper by Conde and Bekefi [30], [31] for a complete description. The basic configuration is that of an amplifier in which a weakly relativistic electron beam is injected into a cylindrical waveguide in the presence of both a helical wiggler field and an axial guide solenoidal field. The wave-particle interaction is with the fundamental TE_{11} mode of the waveguide at a frequency of 33.39 GHz, which corresponds to the frequency of the magnetron used to drive the amplifier.

The electron beam is generated by a Physics International Pulserad 100A by means of field emission from a graphite cathode, and the beam energy used in the experiment is 750 keV ($\pm$50 keV). The quality (i.e., the emittance and energy spread) of the beam delivered to the interaction region is controlled by scraping the beam with a shaped graphite anode. This technique was originally pioneered at the Naval Research Laboratory for use in an FEL experiment driven by the VEBA accelerator [3], [4]. In the MIT experiment, the shaped anode–cathode geometry results in a beam with a radius of 0.25 cm (corresponding to the radius of the anode aperture) and an axial energy spread estimated to be approximately $\Delta\gamma_z/\gamma_0 \approx 1.5\%$. This energy spread corresponds to a normalized RMS beam emittance of $\epsilon_n \leq 4.4 \times 10^{-2}$ cm–rad. The current available using this configuration was of the order of 300 A($\pm$30 A) as delivered to the interaction region
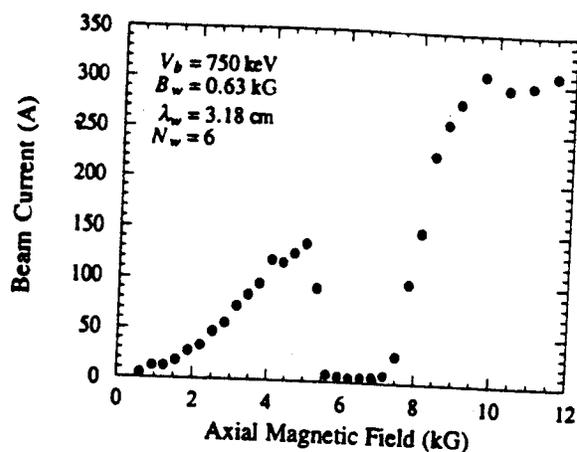

Fig. 1. Current propagation as a function of the axial guide field for the parallel orientation of the field (data courtesy of Conde and Bekefi [30], [31]).
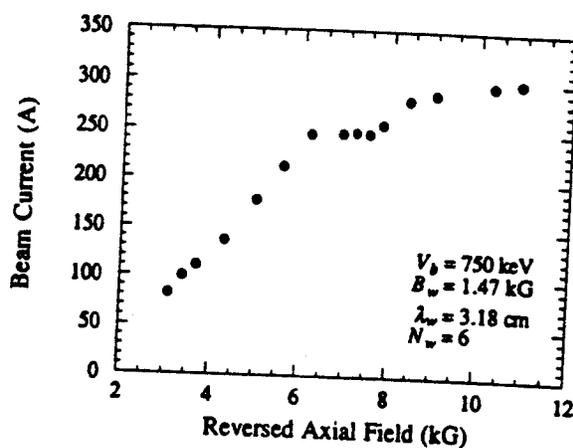

Fig. 2. Current propagation as a function of the axial guide field for the reversed-field configuration (data courtesy of Conde and Beketi [30], [31]).

at the entrance to the wiggler. However, the amount of current which could be propagated through the wiggler/guide field configuration varied based upon the stability of the electron trajectories. Current propagation data indicated quite different results depending upon the orientation of the axial guide field. The results found for the current propagated through the wiggler as a function of the magnitude of the axial guide field for orientations in which the guide field is directed parallel and antiparallel (referred to as the reversed-field configuration) to the wiggler are shown in Figs. 1 and 2, respectively. In each case, the amount of current which could be propagated generally increased with increases in the magnitude of the guide field. An exception to this, however, was found when the guide field was oriented parallel to the wiggler in the vicinity of the magnetic resonance at which the Larmor period associated with the guide field is comparable to the wiggler period. In this case, there is a well-known instability in the electron trajectories which prevents propagation of the beam [38]–[42]. In addition, the increase in the propagated current leveled off in the field-reversed case when the Larmor and wiggler periods were comparable. For convenience, we shall refer to this as the *antiresonance*.

The explanation for this antiresonant effect was discovered independently by Chu and Lin [39], who found that the inhomogeneity in the wiggler field introduces a sinusoidal driving term to the electron orbit equations. This term arises from the fact that an electron on a helical orbit centered off the axis of symmetry experiences a sinusoidally varying wiggler field which acts to drive the electrons at a period close to the wiggler period. Hence, this effect becomes important for electron beams which are big enough that a substantial fraction of the electrons are located relatively far from the symmetry axis. In addition, it is resonant for axial fields close to the antiresonance. We shall discuss this in more detail during the comparison of the simulation with the power measurements, since the orbital irregularities introduced by this effect have a significant impact on the growth of the signal.

The wiggler field is produced by a bifilar helix with a period of $\lambda_w = 3.18$ cm, a length of $50\lambda_w$, and an adiabatic entry taper which is six wiggler periods in length. The wiggler amplitude was continuously adjustable up to an amplitude of approximately 1.8 kG. The axial guide field could be adjusted up to a maximum amplitude of almost 12 kG.

The beam propagated through a cylindrical waveguide of 0.51 cm in radius, which provided for a wave-particle resonance with the fundamental TE_{11} mode in the vicinity of 35 GHz. The FEL was operated as an amplifier, and a magnetron which produced approximately 17 kW ($\pm 10\%$) at a frequency of 33.39 GHz was used as a driver. Since the output from the magnetron was linearly polarized, this corresponded to approximately 8.5 kW in the right-hand, circularly polarized state which was capable of interacting with the helical wiggler geometry.

This constitutes a summary of the experimental configuration which is relevant to the discussion of the theoretical analysis. Further discussion of such aspects of the experiment as the input coupler and the detection system are not directly relevant to the discussion in this paper, and the interested reader is referred to Conde and Bekefi [30], [31] for a complete presentation.

The output from the amplifier showed the greatest efficiency for the field-reversed configuration. In this case, a peak power of 61 MW for a conversion efficiency of 27% was found for a wiggler-field magnitude of approximately 1.47 kG and an axial magnetic field of 10.92 kG. The current which could be propagated in these fields was near the maximum of 300 A. The output power for the field-reversed configuration also showed a severe decrease in the vicinity of the antiresonance, dropping by more than three orders of magnitude. The power observed when the axial magnetic field was oriented parallel to the wiggler was much less than for the field-reversed configuration, and showed a maximum measured power of approximately 4 MW. Details of the output power spectra will be presented in the comparison with the theoretical results.

III. SINGLE-PARTICLE DYNAMICS

Before we describe the nonlinear simulation, it is useful to summarize the essential properties of the single-particle orbits in FEL configurations, which consist in a combination of a helical wiggler and an axial guide magnetic field. The three-dimensional representation of the magnetostatic fields for this geometry in cylindrical coordinates is [40]

$$
\begin{aligned}
B_{\text{ext}}(x) = & B_0 \hat{e}_z \\
& + 2B_w \left[I_1'(\lambda)\hat{e}_r \cos \chi - \frac{1}{\lambda} I_1(\lambda)\hat{e}_\theta \sin \chi + I_1(\lambda)\hat{e}_z \sin \chi \right]
\end{aligned}
\tag{1}
$$

where B_0 and B_w denote the axial and wiggler field amplitudes, $\lambda = k_w r$, $\chi = \theta - k_w z$, $k_w (= 2\pi/\lambda_w)$ denotes the wiggler wavenumber, and I_n and I_n' denote the modified Bessel function of the first kind of order n and its derivative, respectively.

The dynamics of electrons in these combined fields have been discussed in both one [41], [42] and three dimensions [40], [43], [44]. The fundamental equations governing the electron trajectories can be most simply analyzed in the coordinate frame which rotates with the wiggler field and is defined by the basis vectors: $\hat{e}_1 = \hat{e}_x \cos k_w z + \hat{e}_y \sin k_w z$, $\hat{e}_2 = -\hat{e}_x \sin k_w z + \hat{e}_y \cos k_w z$, and $\hat{e}_3 = \hat{e}_z$. We shall henceforth refer to this as the *wiggler frame*. In this coordinate frame, the three-dimensional Lorentz force equations can be expressed as [43]

$$
\begin{aligned}
\dot{v}_1 = & -\left(\Omega_0 - k_w v_\parallel + 2\Omega_w I_1(\lambda) \sin \chi\right)v_2 \\
& + \Omega_w v_3 I_2(\lambda) \sin 2\chi
\end{aligned}
\tag{2}
$$

$$
\begin{aligned}
\dot{v}_2 = & \left(\Omega_0 - k_w v_\parallel + 2\Omega_w I_1(\lambda) \sin \chi\right)v_1 \\
& - \Omega_w v_3 [I_1(\lambda) + I_2(\lambda) \cos 2\chi]
\end{aligned}
\tag{3}
$$

$$
\dot{v}_3 = \Omega_w v_2 [I_1(\lambda) + I_2(\lambda) \cos 2\chi] - \Omega_w v_1 I_2(\lambda) \sin 2\chi.
\tag{4}
$$

$$
\dot{\lambda} = k_w (v_1 \cos \chi + v_2 \sin \chi)
\tag{5}
$$

and

$$
\dot{\chi} = \frac{k_w}{\lambda}(v_2 \cos \chi - v \sin \chi - \lambda v_3)
\tag{6}
$$

where $\Omega_{0,w} \equiv eB_{0,w}/\gamma m_e c, \gamma \equiv \left(1 - v^2/c^2\right)^{-1/2}$

These equations exhibit a class of steady-state helical trajectories which may be found by requiring the derivatives in (2)–(6) to vanish. This implies that $v_1 = v_w$, $v_2 = 0$, $v_3 = v_\parallel$, $\chi = \pm \pi/2$, and $\lambda = \lambda_0$, where $v_\parallel$ is constant, $\lambda_0 = \mp v_w/v_\parallel$, and

$$
v_w = \frac{2\Omega_w v_\parallel I_1(\lambda_0)/\lambda_0}{\Omega_0 - k_w v_\parallel \pm 2\Omega_w I_1(\lambda_0)}.
\tag{7}
$$

In addition, we must require that v_w and $v_\parallel$ satisfy the energy-conservation requirement which implies that

$$
\sqrt{\frac{\gamma^2 - 1}{1 + \lambda_0^2}} = \frac{\Omega_0}{ck_w} \pm 2\frac{\Omega_w}{ck_w}\left(\frac{1 + \lambda_0^2}{\lambda_0^2}\right)I_1(\lambda_0).
\tag{8}
$$

These equations constitute a set of two transcendental equations for v_w and $v_\parallel$ as functions of the parameters which define the fields and the total energy.

We first consider the solution of these equations in the case in which the axial guide fields are directed parallel to the wiggler field. A solution for the axial velocity as a function
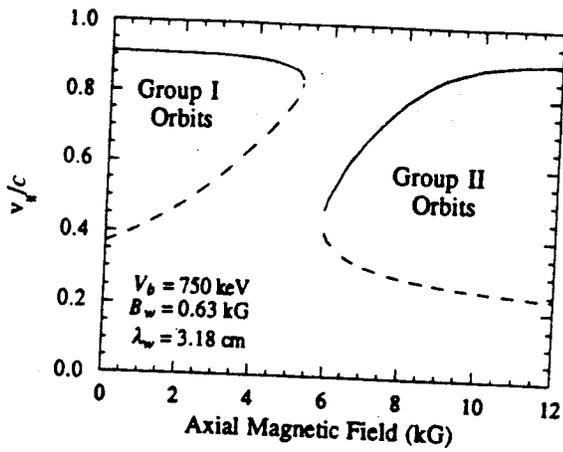
Fig. 3. Plot of the axial velocity versus the magnitude of the axial guide field for the parallel orientation of the wiggler and axial guide fields.
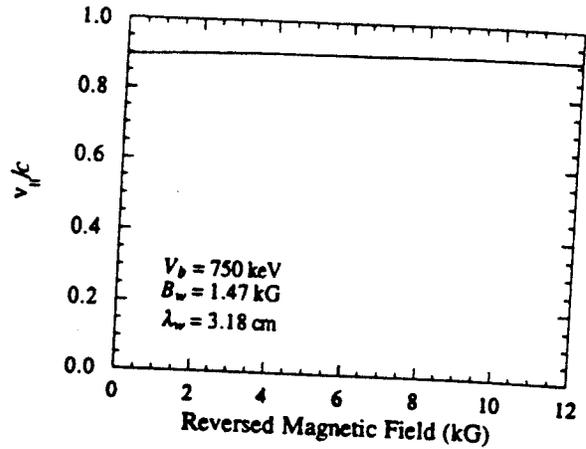

Fig. 4. Plot of the axial velocity versus the magnitude of the axial guide field in the reversed-field orientation.

of the magnitude of the axial guide field is shown in Fig. 3 for parameters consistent with the experiment. This consists of a beam energy of 750 keV, a wiggler field amplitude of 0.63 kG, and a wiggler period of 3.18 cm. As shown in this figure, there are two distinct regimes which are referred to as Group I (when $\Omega_0 < k_w v_\parallel$) in the weak-guide field regime, and Group II (when $\Omega_0 > k_w v_\parallel$) in the strong-guide field regime. The transitional resonant regime for $\Omega_0 \approx k_w v_\parallel$ occurs in this case for axial fields between approximately 5–8 kG. In this regime the transverse velocity becomes large, which requires the axial velocity to decrease. The dashed lines in the figure denote unstable trajectories.

The stability of the Group I and II orbits can be determined by a perturbation analysis [43] in which we write $v_1 = v_w + \delta v_1, v_2 = \delta v_2, v_3 = v_\parallel + \delta v_3, \chi = \pm\pi/2 + \delta\chi$, and $\lambda = \lambda_0 + \delta\lambda$. As a result, we may isolate the perturbed variables by means fourth- and fifth-order differential equations of the form

$$\left(\frac{d^2}{dt^2} + \Omega_+^2\right)\left(\frac{d^2}{dt^2} + \Omega_-^2\right)\begin{bmatrix}\delta v_2 \\ \delta\chi\end{bmatrix} = 0 \qquad (9)$$

and

$$\frac{d}{dt}\left(\frac{d^2}{dt^2} + \Omega_+^2\right)\left(\frac{d^2}{dt^2} + \Omega_-^2\right)\begin{bmatrix}\delta v_1 \\ \delta v_3 \\ \delta\lambda\end{bmatrix} = 0 \qquad (10)$$

where

$$\Omega_\pm^2 \equiv \frac{1}{2}\left(\omega_1^2 + \omega_2^2\right)$$
$$\pm \frac{1}{2}\sqrt{(\omega_1^2 - \omega_2^2)^2 + k_w v_\parallel \Omega_w \omega_3^2} \qquad (11)$$

$$\omega_1^2 \equiv k_w^2 v_\parallel^2 + 2\Omega_w k_w v_w \left(\frac{1 + \lambda_0^2}{\lambda_0^2}\right) I_2(\lambda_0) \qquad (12)$$

$$\omega_2^2 \equiv \frac{(\Omega_0 - k_w v_\parallel)^2}{1 + \lambda_0^2} - 2\Omega_w k_w v_w \left(\frac{1 + \lambda_0^2}{\lambda_0^2}\right) I_2(\lambda_0) \qquad (13)$$

and

$$\omega_3^2 \equiv 8\frac{v_\parallel}{v_w}\left(\Omega_0 - 2k_w v_\parallel\right)$$
$$\cdot \left[\Omega_0 I_2(\lambda_0) + \lambda_0 k_w v_\parallel (I_1(\lambda_0) + 2\lambda_0 I_2(\lambda_0))\right]. \qquad (14)$$

Examination of the definitions of $\Omega_\pm^2$ shows that $\Omega_+^2 \geq 0$. Orbital instability occurs whenever $\Omega_-^2 < 0$, which is the case shown by the dashed lines in Figs. 3 and 4.

A similar plot of the axial velocity as a function of the magnitude of the axial magnetic field in the reversed field case is shown in Fig. 4 for a wiggler amplitude of 1.47 kG, which corresponds to the experimental value of the wiggler field used in this configuration. As shown in this figure, there is no resonant enhancement in this case when the Larmor and wiggler periods are comparable (in the vicinity of the antiresonant at which $\Omega_0 \approx -k_w v_\parallel$), and the axial velocity varies only weakly with the magnitude of the guide field. In addition, there is no orbital instability. It will be shown in Section V, in which we discuss the results of the simulation and electron trajectories in the vicinity of the antiresonance, that the degradation in the output power seen in the experiment results from the effects of the wiggler inhomogeneity on electron trajectories which are displaced far from the axis of symmetry. Hence, the reason that these steady-state orbits do not display this behavior is that they have been obtained subject to the assumption of axi-centered motion.

IV. THE THEORETICAL FORMULATION

For the sake of brevity, we do not provide a discussion of the detailed dynamical equations employed in the ARACHNE formulation here. Rather, we give a summary of the essential properties of the ARACHNE formulation, and refer the interested reader to the original papers [32]–[37] for a complete derivation and description.

The ARACHNE formulation represents, fundamentally, a slow-time-scale description of a steady-state FEL amplifier in three-dimensions. To this end, it is assumed that only a single frequency propagates and, therefore, Maxwell's equations can be averaged over a wave period. This results in two related simplifications of the numerical problem. Specifically, (i) that the fast-time-scale oscillation is removed from the problem and only the slow-time-scale growth (or damping) of the wave need be resolved, and (ii) that only an electron *beamlet* (i.e., a group of electrons which enter the interaction region within one wave period) needs to be included in the simulation.

Together, these two simplifications result in both a substantial increase in the step size and a reduction in the number of electrons in the simulation with respect to the requirements of a full-scale particle-in-cell simulation. Hence, the numerical requirements for the simulation of an FEL amplifier are relatively modest. Typical run times for the cases presented herein are in the range of 5–10 min. on a Cray-2 supercomputer.

The electromagnetic field in this formulation is represented in terms of a superposition of the TE and TM modes of the vacuum waveguide. Note that this does not violate the single-frequency assumption, since the wavenumbers of the modes which are included in the superposition will vary depending upon the specific cut-off frequencies. One restriction, however, which is imposed is that only propagating modes (in which the cutoff frequency is lower than the wave frequency) can be included in the formulation. The space-charge field is represented in terms of a superpostion of the Gould–Trivelpiece modes (at the same frequency as the electromagnetic wave) for a beam which completely fills the waveguide [38]. Observe that the transverse variation of the axial electric field of the Gould–Trivelpiece modes is identical to that of the TM modes of a cylindrical waveguide. The fundamental assumption in the case of both the electromagnetic and electrostatic field is that while the transverse mode structure is determined by the waveguide or the beam conditions, the amplitude and phase vary slowly (with respect to the wave period) in the axial direction due to the interaction with the electron beam. Since both the fluctuating electromagnetic and electrostatic fields are at the same frequency, the dynamical equations for both cases can be averaged over the wave period in order to obtain the equations for the slow variations.

In order to complete the formulation, the orbit equations for an ensemble of electrons must be specified. For this purpose we employ the three-dimensional Lorentz-force equations. This requires the integration of the electron trajectories in the complete set of electrostatic (Gould–Trivelpiece modes), magnetostatic (wiggler and axial guide fields), and electromagnetic fields (TE and TM modes of the waveguide). It is important to bear in mind that it is not necessary to perform an average of these equations, since the Lorentz force equations are inherently slowly varying for waves in near-resonance with the beam. The generality of this formulation of the electron orbits is a crucial feature which permits the simulation to describe not only the primary oscillation induced by the wiggler, but also Larmor effects due to the presence of the axial field and Betatron oscillations and guiding-center drifts due to the wiggler inhomogenieties. This is the critical requirement in the simulation of the field-reversed configuration near the antiresonance.

The initial conditions on the electron beam are chosen to describe the beam as it is prior to the entry into the wiggler. We assume a uniform distribution in both inital phase and cross section. The beam is assumed to have a flat-top density profile for simplicity. The effect of an axial energy spread is included by means of a momentum space-distribution function which is monoenergetic, but displays a pitch-angle spread. The wiggler field model includes the adiabatic entry taper from zero to a fixed value, and ARACHNE then describes the self-consistent

injection of the electron beam into the wiggler. This procedure has a practical advantage, since it is easier to determine the characteristics of the electron beam prior to the injection into the wiggler.

The initial conditions imposed on the TE and TM modes are that the initial amplitude of each mode is chosen to reflect the injected power into the system, and the initial wavenumber corresponds to the vacuum value appropriate to the mode. ARACHNE then determines the self-consistent evolution of both the amplitude and wavenumber due to the dielectric effect of the beam in the wiggler. The initial growth rates are assumed to be zero, since the wiggler field is initially zero as well.

The initialization of the Gould–Trivelpiece modes is accomplished by evaluation of the appropriate initial phase averages of the electron beam. Note that the assumption of a uniform electron beam implies that the phase averages which appear in Poisson's equation will initially vanish. However, the use of a discrete ensemble of electrons introduces a small numerical error into the initial phase averages (i.e., $\langle \sin \varphi \rangle$ and $\langle \cos \varphi \rangle$). We find that in practice, the use of these numerical uncertainties for the phase averages in Poisson's equation to select the initial amplitudes and wavenumbers smooths the initial transients associated with the subsequent phase bunching of the electron beam.

Within the context of this initialization scheme, ARACHNE subsequently self-consistently integrates the dynamical equations for the field amplitudes and phases of each of the electromagnetic and electrostatic waves included in the simulation in conjunction with the Lorentz force equations for the electron ensemble (which typically includes 9600 electrons). Since the complete Lorentz force equations are used, this permits the self-consistent description of the effects of the injection of the beam into the wiggler, the bulk wiggler motion, Larmor motion, the effects of wiggler inhomogenieties (i.e., Betatron motion and the associated guiding-center drifts, velocity shear effects, orbital instabilities in the Group I and II regimes, etc.), and harmonic interactions. Of the greatest significance to the current experiment, however, it is the implicit inclusion of the antiresonance phenomena in the reversed-field configuration.

V. The Experimental Comparison

The experiment has been operated with the axial magnetic field oriented both parallel and antiparallel with the wiggler field, and we shall discuss the comparison with each of these regimes separately. Features common to both regimes, however, involve the choice of various system parameters as well as the initialization of the modes included in the simulation.

Features common to all cases studied derive from the geometry of the system. Specifically, we take the waveguide radius to be $R_g = 0.51$ cm, the wiggler period to be $\lambda_w = 3.18$ cm, and the wiggler entry taper as $N_w = 6$ wiggler periods in length. In addition, while the beam current varies with the magnitude of the axial guide field, the beam energy

is 750 keV and the radius is fixed at the aperture of the anode to $R_b = 0.25$ cm.

Since the frequency of the amplifier experiment is fixed by the 33.39-GHz magnetron, the beam energy of 750 keV and waveguide radius of 0.51 cm insures that a resonant interaction is possible only with the fundamental TE_{11} mode of the guide. Since the magnetron produces approximately 17 kW with a linear polarization, we assume that only half of this power is available with the correct circular polarization to interact with the beam. Hence, the initial power of the TE_{11} mode is chosen to be 8.5 kW. The collective Raman interaction in an FEL couples the TE_{11} mode, in principle, with each of the Gould–Trivelpiece modes having an azimuthal mode number of $l = 0$ [37]. In practice, however, we find that inclusion of only the lowest-order radial mode is required to give reasonable agreement with the experiment. Note that the axial electric field of this mode has the same transverse variation of the TM_{01} waveguide mode. Hence, the following simulations have been performed using only one waveguide mode and one Gould–Trivelpiece mode.

A. The Reversed-Field Configuration

The first case we consider is that of a field-reversed configuration in which the nominal experimental magnetic field parameters were an axial field magnitude of 10.92 kG and a wiggler field of 1.47 kG. The transmitted current for these field parameters was 300 A($\pm 10\%$) and the axial energy spread of the beam is assumed to be 1.5%, as indicated in the experiment. These parameters represent the case of the peak power observed in the experiment of 61 MW.

The comparison of the experiment and ARACHNE is shown in Fig. 5, in which we plot the power as a function of axial position, and in which the dots represent the power as measured in the experiment. As shown in the figure, ARACHNE was used for two sets of parameters. The first corresponds to the nominal experimental values given above, and the second corresponds to the upper limits on the (i) current, (ii) wiggler field, and (iii) input power (due to the experimental uncertainties) of 330 A, 1.55 kG, and 10 kW, respectively. As is evident in this figure, the agreement between the experimental measurements and ARACHNE is good, and virtually all the data points fall between these two curves. The saturated power for these two choices of the current, wiggler field, and input power differ only marginally and are close to the 61 MW measured in the experiment. The principal difference is in the saturation length, which is due to a small discrepancy in the growth rates for these two cases.

The interaction efficiency in this case is approximately 27%, which is far above that found in the laboratory previously for uniform wiggler configurations and is comparable to the maximum efficiency obtained for a tapered wiggler configuration [10]. It should be noted, however, that efficiencies of this magnitude have been predicted in previous simulations using ARACHNE for uniform wiggler configurations [32], [36] and is comparable to that which is expected due to the phase trapping of the electron beam in the ponderomotive wave formed by the beating of the wiggler and radiation fields. The efficiency estimated by this technique represents the energy
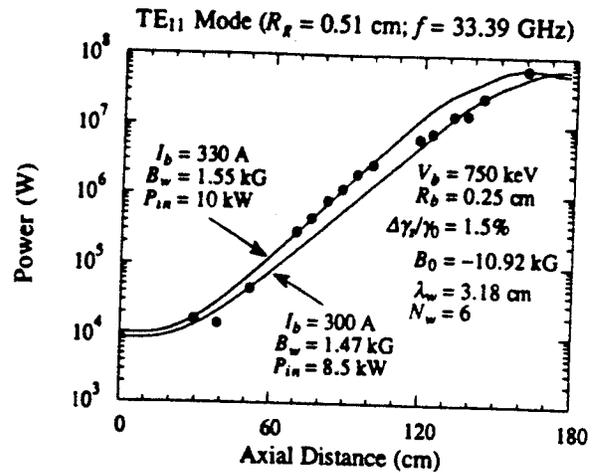
Fig. 5. The evolution of the power with axial position as determined with ARACHNE and from the experiment (dots) for a field-reversed configuration.

lost by the electron as the axial velocity decreases by an amount $\Delta v_z = 2(v_z - v_{ph})$, where $v_{ph} = \omega/(k + k_w)$ is the phase velocity of the ponderomotive wave. Here, (ω, k) are the angular frequency and wavenumber of the electromagnetic wave, and k_w is the wiggler wavenumber. The phase-trapping estimate for the efficiency can be expressed in the form:

$$\eta \approx 2\gamma_{\parallel}^2 \frac{v_{\parallel}}{c}\left(\frac{v_{\parallel}}{c} - \frac{\omega/c}{k + k_w}\right). \tag{15}$$

The inclusion of Raman effects in this estimate is accomplished by the choice of the appropriate frequency and wave number in the phase velocity of the ponderomotive wave. ARACHNE includes collective Raman effects and for the example shown, results in a normalized wavenumber of $k/k_w \approx 2.98$ for the TE_{11} mode at a frequency of 33.39 GHz (ie., $\omega/ck_w \approx 3.5$). As a consequence, the phase velocity of the ponderomotive wave is $v_{ph}/c \approx 0.879$. Note that this wavenumber differs from the normalized wavenumber for a vacuum TE_{11} mode for which $k/k_w \approx 2.985$, and that the dielectric loading of the waveguide due to the interaction in either the Raman or Compton regimes is included in ARACHNE. In addition, the axial electron velocity for the steady-state orbit in this field configuration is $v_z/c \approx 0.911$, which gives $\gamma_{\parallel}^2 \approx 5.89$. As a result, the estimate of the phase-trapping efficiency is approximately 34%. It is important to recognize that estimates such as this must be employed with caution and should be taken in the present case to indicate the possibility of high-efficiency operation. However, it should also be noted that while the estimate is higher than that found in either the simulation or experiment, it does not include the effects of an axial energy spread.

The variation in the output power over an interaction length of 150 cm as a function of the magnitude of the reversed magnetic field is shown in Fig. 6. Again, the dots represent the experimentally measured power, and the curve is the result from ARACHNE. The current used in the simulation for each value of the axial field corresponds to the transmitted current shown in Fig. 2. Agreement between the experiment and theory is good across the entire range studied. Of particular importance is the sharp decrease in the output power in the
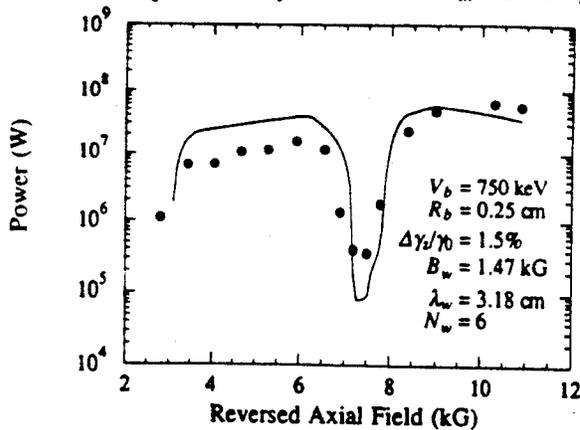
Fig. 6. The variation in the output power versus the magnitude of the reversed axial field as measured in the experiment (dots) over an interaction length of 150 cm and with ARACHNE.
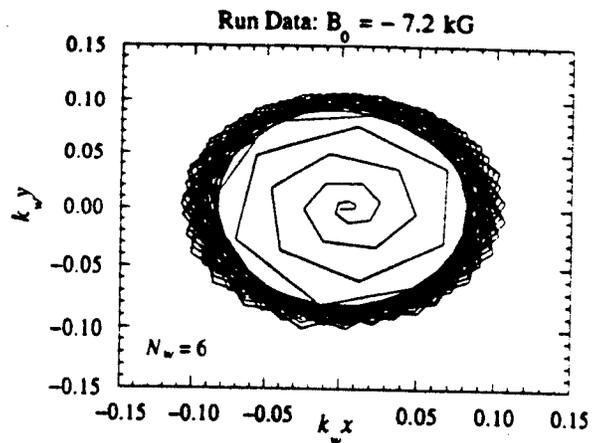

Fig. 7. The cross-sectional evolution of the trajectory of an electron injected near the center of the beam for an axial field in the vicinity of the antiresonance.
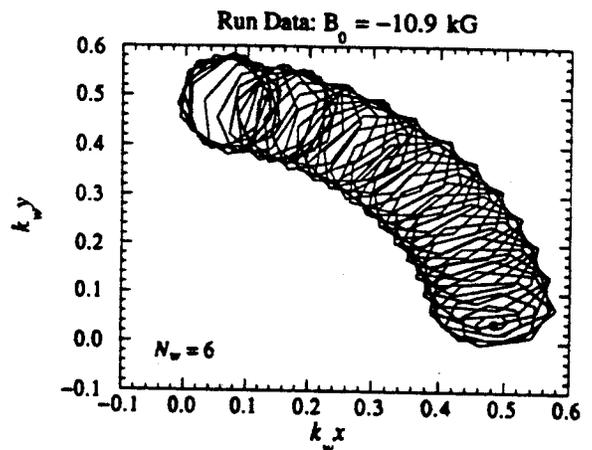

Fig. 8. The cross-sectional evolution of the trajectory of an electron injected at the edge of the beam for an axial field far from the antiresonance.

vicinity of the antiresonance at axial field magnitudes between approximately 7–8.5 kG.

The source of this antiresonant decrease in the interaction efficiency is the irregularities introduced into the electron trajectories by the transverse inhomogeniety in the wiggler. For this particular example, the radius of the wiggler-induced motion (i.e., the radius of the helical steady-state trajectory) is approximately 0.04 cm. However, the beam radius is 0.25 cm in this experiment. As a consequence, the electrons at the outer regions of the beam are quite sensitive to the wiggler inhomogeniety and experience a sinusoidally varying wiggler field during the course of their trajectories. These effects are implicitly included in the ARACHNE formulation, and we can illustrate their effect on the electron beam by examining the orbits of selected electrons in the simulation.

The first case we shall consider is that of a electron which is located near the center of the beam upon entry to the wiggler for a reversed axial field of 7.2 kG, which is in the center of the antiresonance region. The evolution of the trajectory in the transverse plane is shown in Fig. 7, in which the jaggedness is a artifact introduced into the figure by plotting only every tenth point in the integration. The orbit shown in the figure exhibits the expected *spin-up* of the electron trajectory due to the adiabatic injection into the wiggler field, and the electron executes a near-helical steady-state orbit upon transition to the uniform-wiggler region (i.e., after the six wiggler periods of the entry taper region). The principal characteristics of such an orbit are the regular wiggler-induced transverse velocity, which mediates the interaction, and a near-uniform axial velocity, which permits the resonant wave–particle interaction to occur over an extended interaction length. This behavior is also found for electrons at the center of the beam for axial fields away from the antiresonance. The differences occur principally for the edge electrons.

In order to show the nature of these differences, we focus on a characteristic electron which is initially located at the edge of the beam ($x \approx 0.25$ cm and $y \approx 0$) upon entry to the wiggler. The cross-sectional evolution of the trajectory of such an electron for a reversed axial field of 10.92 kG is shown in

Fig. 8. This case is not in the vicinity of the antiresonance, and the orbit illustrates several features. The predominant feature is the aforementioned spin-up of the electron due to the bulk wiggler motion. However, the electron also executes slower motion which corresponds to Betatron and Larmor motion due to the wiggler inhomogeneity which manifests as a guiding-center drift in the counter-clockwise direction. This orbit is fairly regular and does not result in any significant degradation in the interaction efficiency (see Fig. 5).

However, the situation is quite different for an edge electron in the vicinity of the antiresonance. The cross-sectional evolution of such a trajectory is shown in Fig. 9 for an axial field magnitude of 7.2 kG. The orbit in this case exhibits the initial spin-up due to the bulk wiggler action, but subsequently undergoes what appears to quite irregular motion. The effect of this motion on the axial momentum is shown in Fig. 10, in which we plot the axial momentum versus axial position for the central and the edge electrons. It is clear from this figure that the axial momentum exhibits regular oscillations about the bulk value for the central electron, but not for the edge electron. In the latter case the motion exhibits far more structure, reflecting the Betatron and Larmor motions as
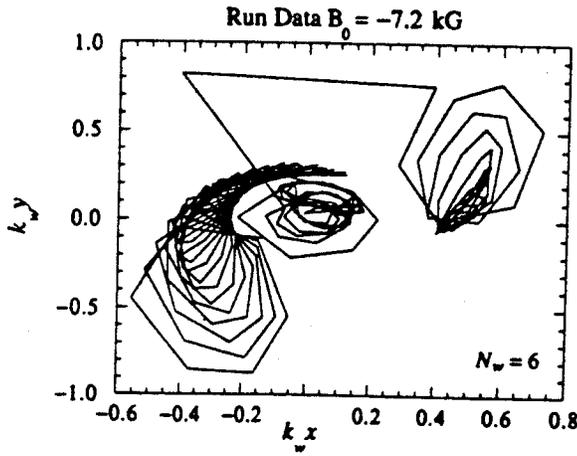
Fig. 9. The cross-sectional evolution of the trajectory of an electron injected at the edge of the beam for an axial field in the vicinity of the antiresonance.
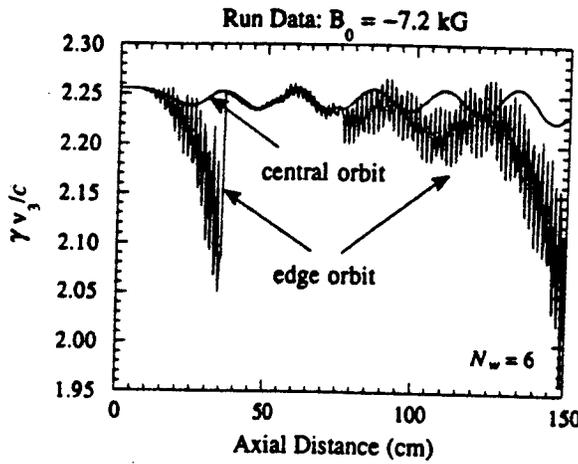

Fig. 10. The evolution of the axial momentum versus axial position for electrons injected at the edge of the beam and the center of the beam in the vicinity of the antiresonance.

well as sudden transitions. Similar behavior is found for the transverse components of the momentum as well. These rapid and large variations in the axial momentum are the major cause of the degradation in the interaction efficiency, since they act to disrupt the resonant wave–particle interaction.

The fundamental physics of this antiresonant process [39] can be understood by means of a relatively simple treatment of the single-particle orbit dynamics. In order to accomplish this, we return to the formulation presented in [43]. In this treatment, the electron position and velocity are written as $x = x_c + x_{osc}$, where the subscript c denotes the guiding-center position, and "osc" denotes the various oscillatory motions. Under the assumption that the guiding-center position is fixed (i.e., $v = v_{osc}$), expansion of the orbit equations (2)–(4) about the guiding-center position results in the following equations for the electron velocity (where we drop the subscript "osc" for convenience):

$$\dot{v}_1 = -(\Omega_0 - k_w v_3)v_2 + \Omega_w v_3 I_2(\lambda_c) \sin 2\chi_c \quad (16)$$

$$\dot{v}_2 = (\Omega_0 - k_w v_3)v_2 - \Omega_w v_3 [I_0(\lambda_c) \cos 2\chi_c] \quad (17)$$

$$\dot{v}_3 = \Omega_w v_2 [I_0(\lambda_c) + I_2(\lambda_c) \cos 2\chi_c] \\ - \Omega_w v_1 I_2(\lambda_c) \sin 2\chi_c \quad (18)$$

where (r_c, θ_c) denote the guiding-center position in cylindrical coordinates, and $\lambda_c \equiv k_w r_c$ and $\chi_c \equiv \theta_c - k_w z$. If we now expand about the steady-state orbits via $v_1 = v_w + \delta v_1$, $v_2 = \delta v_2$, $v_3 = v_\| + \delta v_3$, where

$$v_w \equiv \frac{\Omega_w v_\|}{\Omega_0 - k_w v_\|} I_0(\lambda_c) \quad (19)$$

then the equations for the perturbations are

$$\delta\dot{v}_1 = -(\Omega_0 - k_w v_\|)\delta v_2 + \Omega_w v_\| I_2(\lambda_c) \sin 2\chi_c \quad (20)$$

$$\delta\dot{v}_2 = (\Omega_0 - k_w v_\|)\delta v_1 - \frac{v_w}{v_\|}\Omega_0\delta v_3 \\ - \Omega_w v_\| I_2(\lambda_c) \cos 2\chi_c \quad (21)$$

$$\delta\dot{v}_3 = \Omega_w \delta v_2 I_0(\lambda_c) - \Omega_w v_w I_2(\lambda_c) \sin 2\chi_c. \quad (22)$$

Note that we have also neglected terms which vary as $\delta v I_2(\lambda_c)$ under the assumption that $\lambda_c < 1$ as well. In this representation, the electrons execute a helical trajectory centered about the guiding center. In addition, this representation is quasi-idealized in the sense that the transverse velocity includes three-dimensional effects only in the inclusion of the $I_0(\lambda_c)$ function, which describes the effect of the off-axis increase in the magnitude of the field at the guiding center. These equations may be reduced to a set of second-order differential equations:

$$\left(\frac{d^2}{dt^2} + \Omega_r^2\right)\begin{bmatrix}\delta v_1 \\ \delta v_2 \\ \delta v_3\end{bmatrix}$$
$$= \Omega_w I_2(\lambda_c) \cdot \begin{bmatrix} v_\|(\Omega_0 - 3k_w v_\|)\cos 2\chi_c \\ v_\|\left(\Omega_0 - 3k_w v_\| + \frac{v_w^2}{v_\|^2}\right)\sin 2\chi_c \\ -v_\|(\Omega_0 - 3k_w v_\|)\cos 2\chi_c \end{bmatrix} \quad (23)$$

where

$$\Omega_r^2 \equiv (\Omega_0 - k_w v_\|)\left[\left(1 + \frac{v_w^2}{v_\|^2}\right)\Omega_0 - k_w v_\|\right]. \quad (24)$$

Observe that Ω_-^2 corresponds with Ω_r^2 in the limit in which $v_w^2/v_\|^2 \ll 1$, and this set of equations shows the orbital instability which is expected for the Group I orbits when $\Omega_r^2 < 0$ (note that there is no orbital instability for the Group II orbits in the idealized representation or for the field-reversed configuration), and it will also show the antiresonant effect. To see the latter, we can generate the particular solutions of these equations, which are

$$\begin{bmatrix}\delta v_1 \\ \delta v_2 \\ \delta v_3\end{bmatrix}$$
$$= \frac{\Omega_w v_\| I_2(\lambda_c)}{(\Omega_0 + k_w v_\|)(\Omega_0 - 3k_w v_\|) + \frac{v_w^2}{v_\|^2}\Omega_0(\Omega_0 - k_w v_\|)}$$
$$\times \begin{bmatrix} (\Omega_0 - 3k_w v_\|)\cos 2\chi_c \\ \left(\Omega_0 - 3k_w v_\| + \frac{v_w^2}{v_\|^2}\Omega_0\right)\sin 2\chi_c \\ -\frac{v_w}{v_\|}(\Omega_0 - 3k_w v_\|)\cos 2\chi_c \end{bmatrix} \quad (25)$$

In the limit in which $v_w^2/v_{\parallel}^2 \ll 1$ (which is appropriate for this experiment), these particular solutions reduce to the simpler form:

$$\begin{bmatrix} \delta v_1 \\ \delta v_2 \\ \delta v_3 \end{bmatrix} = \frac{\Omega_w \cdot v_{\parallel} I_2(\lambda_c)}{(\Omega_0 + k_w \cdot v_{\parallel})} \begin{bmatrix} \cos 2\chi_c \\ \sin 2\chi_c \\ -\dfrac{v_w}{v_{\parallel}} \cos 2\chi_c \end{bmatrix} \quad (26)$$

which clearly show the antiresonant enhancement in the perturbation when $\Omega_0 \approx -k_w \cdot v_{\parallel}$. However, since the particular solution also depends upon $I_2(\lambda_c)$, this effect will not become appreciable unless the electron guiding-center is located relatively far from the symmetry axis. This perturbation describes an oscillation at the wiggler period in Cartesian coordinates which can become large near the antiresonance. Indeed, this is the period of the rapid oscillation shown in the axial momentum of the edge electron in Fig. 10. Note, however, that this antiresonant enhancement in the perturbation is not as serious a problem for beam transport than the Group I and II orbital instabilities which occur when the axial guide field is oriented parallel to the wiggler field.

This simplified perturbation analysis suffices to illustrate the basic physics of the antiresonant effect, but does not describe either the nonlinear effects associated with the large-amplitude perturbations at the antiresonance or the effect of the fluctuating fields. These effects, however, are implicitly included in ARACHNE.

B. The Group I and II Regimes

The agreement between ARACHNE and the experimental measurements in the Group I and II regimes is not as good as that found for the reversed-field configuration. In the cases in which the axial guide field in oriented parallel to the wiggler field, we find that a much larger energy spread than that estimated for the experiment is required in order to account for the measured power levels. Indeed, we find that the assumption of an energy spread of 1.5% results in efficiencies comparable to that found for the field-reversed configuration, and we note that the efficiency predicted in simulation does not vary appreciably for either orientation of the magnetostatic fields for comparable beam-energy spreads. In order to account for the Group I data we must assume an energy spread of approximately 6.4% to account for the measured power. The Group II data are more difficult to explain. The assumption of a comparable energy spread of 6.4% results in reasonable agreement for the power at the end of the interaction region, but not for the detailed evolution of the signal (i.e., the launching loss and the instantaneous growth rate) during the course of the interaction.

We have no definitive explanation for this discrepancy, but merely suggest that there might be some misalignment or other beam-transport problem from the gun to the wiggler which is exacerbated by the orientation of the axial guide field. A possible source for such a discrepancy could be the existence of irregularities in the wiggler field upstream from the entrance due to the sudden termination of the coils. Such irregularities might give rise to orbital instabilities for a parallel alignment of the wiggler and axial guide fields which result in enhanced
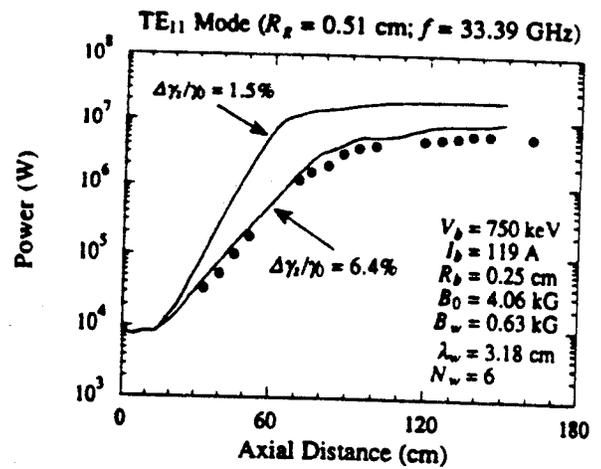

Fig. 11. The evolution of the power with axial position as determined with ARACHNE and in the experiment (dots) for Group I orbit parameters.

emittance growth. A detailed evaluation of these suggestions, however, can only be accomplished by means of a thorough analysis of the experimental configuration.

With all of this in mind, we plot the evolution of the power versus axial position as measured in the experiment and as determined with ARACHNE in Fig. 11 for wiggler and axial guide fields of 0.63 and 4.06 kG, respectively, and for axial energy spreads of 1.5 and 6.4%. These fields correspond to Group I operation, and the transmitted current is 119 A. As shown in this figure, ARACHNE is in substantial agreement with the experiment for the presumed energy spread of 6.4%, both as regards the linear growth rate and the saturation efficiency.

Comparison of ARACHNE with experiment in the case of wiggler and guide fields of 0.63 and 10.92 kG, respectively, and a transmitted current of 300 A is shown in Fig. 12. Again, we plot the results from ARACHNE for energy spreads of both 1.5 and 6.4%. This case corresponds to Group II parameters and shows rough agreement in the case of a 6.4 % energy spread for the power (≈ 4 MW) and saturation efficiency, but not the growth rate. In contrast, the growth rate (but not the saturation efficiency) found in the experiment is in rough agreement with that found in ARACHNE for the case of a 1.5% energy spread. However, the launching loss observed in the experiment is much higher than that seen in simulation, as evidenced by the fact that there is negligible growth in the observed power until after an axial position of 70 cm after the wiggler entrance.

A summary of the comparison between ARACHNE (for axial energy spreads of both 1.5 and 6.4%) and the experiment as a function of the axial fields magnitude is shown in Fig. 13 for the choice of transmitted current as shown in Fig. 1. It is clear from this figure that the agreement between ARACHNE and the experimental measurements is better for the case of Group I parameters than for the case of Group II parameters at high axial fields. In the low axial field Group I regime, the agreement is quite good for the presumed 6.4% energy spread. Quantitative agreement for the Group II regime is not as good; however, ARACHNE does predict the existence of variations
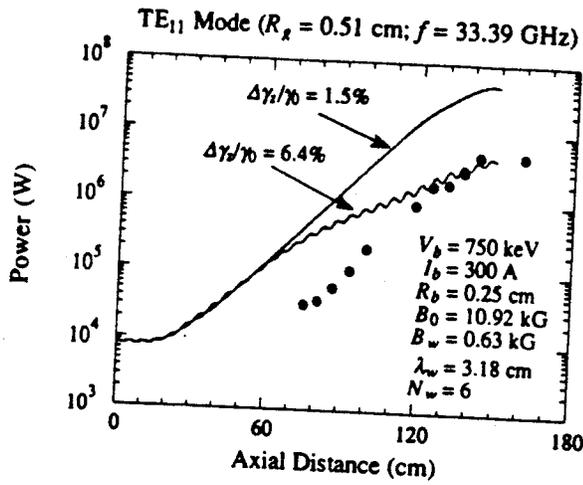
TE$_{11}$ Mode (R_g = 0.51 cm; f = 33.39 GHz)

Fig. 12. The evolution of the power with axial position as determined with ARACHNE and in the experiment (dots) for Group II orbit parameters.

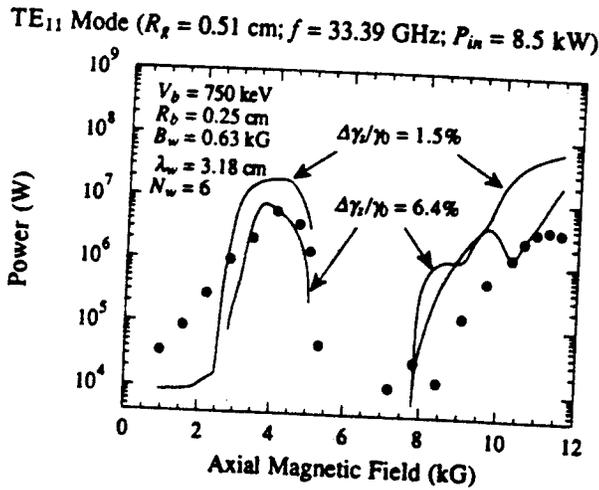**TE$_{11}$ Mode (R_g = 0.51 cm; f = 33.39 GHz; P_{in} = 8.5 kW)**

Fig. 13. The variation in the output power versus the magnitude of the axial field for Group I and II orbit parameters as measured in the experiment (dots) over an interaction length of 150 cm and with ARACHNE.

in the output power as a function of the field magnitude which is similar to that seen in the experiment.

VI. SUMMARY AND DISCUSSION

In this paper, we have presented a detailed comparison between a recent high-power FEL amplifier experiment using a combined helical wiggler/axial guide magnetic-field configuration and a three-dimensional nonlinear formulation of the FEL amplifier in the collective Raman regime (ARACHNE). Two configurations were studied, corresponding to the parallel and antiparallel orientations of the axial guide field and wiggler. Substantial agreement is found between the experiment and ARACHNE for the reversed field configuration. However, agreement between ARACHNE and the experiment for the parallel orientation of the fields in the Group I and II parameter regimes required the assumption of a substantially higher beam-energy spread. In addition, we cannot simultaneously account for the measured growth rate and saturation efficiency in the Group II regime. Fig. 12 shows that the measured growth rate is given approximately by ARACHNE for the

choice of an energy spread of 1.5%, but in order to account for the ultimate efficiency we must assume an energy spread of 6.4%. In addition, the experiment seems to indicate an extremely long region of null growth or launching loss before the signal begins to grow. The only explanation we can suggest for these discrepancies is the existence of problems in the transport of the electron beam from the gun to the wiggler for this configuration. However, it is impossible to confirm these suggestions without a detailed analysis of the design of the experiment.

One further point which merits discussion is the relative efficiencies found for the Group I and II regimes. Previous experiments at the Naval Research Laboratory [3] have found higher efficiencies for Group II than for Group I operation. In addition, extremely high efficiencies of the order of 47% have been predicted for Group II operation at 35 GHz using ARACHNE [36]. However, in both of these cases the high efficiencies resulted from operation in the negative-mass regime, which is close to the resonance at which Larmor and wiggler periods coincide. However, it is difficult to operate in this regime for energies below 1 MeV due to the narrow range of axial magnetic fields for which it occurs, which makes injection of the beam into the wiggler difficult. The Group II measurements reported for the present experiment were not in this negative-mass regime. Hence, it is not surprising that both the experiment and ARACHNE report comparable efficiencies for the Group I and II regimes.

There are two significant new results represented in the experiment. The first is the achievement of a near-30% interaction efficiency with a uniform-wiggler design. While efficiencies of this magnitude are expected on the basis of both simple phase-trapping arguments and detailed numerical simulations, this is the first time such efficiencies have been demonstrated in the laboratory. The second is the existence of the antiresonant degradation in the operating efficiency. This had been previously unsuspected, and the experimental demonstration of the effect has been instrumental in pointing the way toward a theoretical re-examination of the orbital dynamics in this regime.

REFERENCES

[1] R. M. Phillips, in *IRE Trans. Electron Dev.*, vol. ED-7, p. 231, 1960.
[2] D. B. McDermott, T. C. Marshall, S. P. Schlesinger, R. K. Parker, and V. L. Granatstein, in *Phys. Rev. Lett.*, vol. 41, pp. 1368, 1978.
[3] R. K. Parker, *et al.*, in *Phys. Rev. Lett.*, vol. 48, p. 238, 1982.
[4] S. H. Gold, D. L. Hardesty, A. K. Kinkhead, L. R. Barnett, and V. L. Granatstein, in *Phys. Rev. Lett.*, vol. 52, p. 1218, 1984.
[5] J. A. Pasour, R. F. Lucey, and C. A. Kapetanakos, in *Phys. Rev. Lett.*, vol. 53, p. 1728, 1984.
[6] J. Fajans, G. Bekefi, Y. Z. Yin, and B. Lax, in *Phys. Rev. Lett.*, vol. 53, p. 246, 1984.
[7] T. J. Orzechowski, *et al.*, in *Phys. Rev. Lett.*, vol. 54, p. 889, 1985.
[8] J. Mathew and J. A. Pasour, in *Phys. Rev. Lett.*, vol. 56, pp. 1805, 1986.
[9] J. Fajans and G. Bekefi, in *Phys. Fluids*, vol. 29, p. 3461, 1986.
[10] T. J. Orzechowski, *et al.*, in *Phys. Rev. Lett.*, vol. 57, p. 2172, 1986.

[11] Y. Kawamura, B. C. Lee, M. Kawai, and K. Toyoda, in *Phys. Rev. Lett.*, vol. 67, p. 832, 1991.

[12] J. Fajans, J. S. Wurtele, G. Bekefi, D. S. Knowles, and K. Xu, in *Phys. Rev. Lett.*, vol. 57, p. 579, (1986)

[13] J. Masud, T. C. Marshall, S. P. Schlesinger, and F. G. Yee, in *Phys. Rev. Lett.*, vol. 56, p. 1567, 1986.

[14] J. Masud, *et al.*, in *Phys. Rev. Lett.*, vol. 58, p. 763, 1987.

[15] F. Hartemann, K. Xu, G. Bekefi, J. S. Wurtele, and J. Fajans, in *Phys. Rev. Lett.*, vol. 59, p. 1177, 1987.

[16] D. A. Kirkpatrick, G. Bekefi, A. C. DiRienzo, H. P. Freund, and A. K. Ganguly, in *Phys. Fluids*, vol. B1, p. 1511, 1989.

[17] D. E. Pershing, R. H. Jackson, H. Bluem, and H. P. Freund, in *Nucl. Instrum. Meth.*, vol. A304, p. 127, 1991.

[18] H. Bluem, R. H. Jackson, H. P. Freund, D. E. Pershing, and V. L. Granatstein, in *Phys. Rev. Lett.*, vol. 67, p. 824, 1991.

[19] L. R. Elias, W. M. Fairbank, J. M. J. Madey, H. A. Scwettmen, and T. I. Smith, in *Phys. Rev. Lett.*, vol. 36, p. 717, 1976.

[20] D. A. G. Deacon, *et al.*, in *Phys. Rev. Lett.*, vol. 38, p. 892, 1977.

[21] M. Billardon, *et al.*, in *Phys. Rev. Lett.*, vol. 51, p. 1652, 1983.

[22] S. Benson, *et al.*, in *Phys. Rev. Let.*, vol. 48, p. 235, 1982.

[23] H. Boehmer, *et al.*, in *Phys. Rev. Lett.*, vol. 48, p. 141, 1982.

[24] R. W. Warren, *et al.*, in *IEEE J. Quant. Electron.*, vol. QE-19, p. 391, 1983.

[25] J. A. Edighoffer, *et al.*, in *Phys. Rev. Lett.*, vol. 52, p. 344, 1984.

[26] B. E. Newnam, *et al.*, in *IEEE J. Quant. Electron.*, vol. QE-21, p. 882, 1985.

[27] L. R. Elias, G. R. Ramian, J. Hu, and A. Amir, in *Phys. Rev. Lett.*, vol. 57, p. 424, 1986.

[28] S. V. Benson and J. M. J. Madey, in *Phys. Rev. A*, vol. 39, p. 1579, 1989.

[29] A. H. Lumpkin, *et al.*, in *Nucl. Instrum. Meth.*, vol. A296, p. 169, 1990.

[30] M. E. Conde and G. Bekefi, in *Phys. Rev. Lett.*, vol. 67, p. 3082, 1991.

[31] M. E. Conde and G. Bekefi, in *IEEE Trans. Plasma Sci.*, this issue.

[32] A. K. Ganguly and H. P. Freund, in *Phys. Rev. A.*, vol. 32, p. 2275, 1985.

[33] H. P. Freund and A. K. Ganguly, in *Phys. Rev. A.*, vol. 33, p. 1060, 1986

[34] H. P. Freund and A. K. Ganguly, in *Phys. Rev. A.*, vol. 34, p. 1242, 1986.

[35] H. P. Freund and A. K. Ganguly, in *IEEE J. Quant. Electron.*, vol. QE-23, p. 1657, 1987.

[36] A. K. Ganguly and H. P. Freund, in *IEEE Trans. Plasma Sci.*, vol. 16, p. 167, 1988.

[37] A. K. Ganguly and H. P. Freund, in *Phys. Fluids*, vol. 31, p. 387, 1988.

[38] N. A. Krall and A. W. Trivelpiece, *Principles of Plasma Physics*, New York: McGraw-Hill, 1973, p. 202.

[39] K. R. Chu and A. T. Lin, in *Phys. Rev. Lett.*, vol. 67, p. 3235, 1991.

[40] P. Diament, in *Phys. Rev. A*, vol. 23, p. 2537, 1981

[41] L. Friedland, in *Phys. Fluids*, vol. 23, p. 2376, 1980.

[42] H. P. Freund and A. T. Drobot, in *Phys. Fluids*, vol. 25, p. 736, 1982.

[43] H. P. Freund and A. K. Ganguly, in *IEEE J. Quant. Electron.*, vol. QE-21, p. 1073, 1985.

[44] J. Fajans, D. A. Kirkpatrick, and G. Bekefi, in *Phys. Rev. A.*, vol. 32, p. 3448, 1985.

H. P. Freund, photograph and biography not available at the time of publication.

A. K. Ganguly, photograph and biography not available at the time of publication.

APPENDIX X

Beam Transmission in a High-Power Collective Free-Electron Laser

H.P. Freund

Beam transmission in a high-power collective free-electron laser

H. P. Freund[a]

Naval Research Laboratory, Washington, D.C. 20375

A recent free-electron laser amplifier experiment conducted at the Massachusetts Institute of Technology [M. E. Conde and G. Bekefi, Phys. Rev. Lett. 67, 3082 (1991)] has demonstrated high-power operation without recourse to a tapered wiggler field. The experimental configuration consisted in the propagation of an intense electron beam (750 keV/300 A with a nominal axial energy spread of 1.5%) through a cylindrical waveguide in the presence of both a helical wiggler ($B_w < 1.8$ kG and $\lambda_w = 3.18$ cm) and an axial guide magnetic field ($B_0 < 12$ kG). The experiment operated with the axial guide field oriented both parallel and antiparallel to the direction of the wiggler field, and the maximum efficiency was obtained for the antiparallel (i.e., reversed-field) configuration. The reversed-field case demonstrated an output power of 61 MW at 33.39 GHz for an efficiency of approximately 27%. The performance in the more usual parallel alignment of the fields was much less and peak power levels of only about 4 MW were obtained for both the weak (group I) and strong (group II) field regimes of the axial guide field. A detailed analytical characterization of this experiment has been presented in a previous work [H. P. Freund and A. K. Ganguly, IEEE Trans. Plasma Sci. PS-20, 245 (1992)] in which substantial agreement was found between the theory and the experiment for the reversed-field configuration. However, some discrepancies existed for the group I and II cases, and it was conjectured that some problem with beam transport existed for these configurations which led to an increased beam energy spread. In this paper, the question of beam transport in this experiment is analyzed. It is shown that beam transport is not a problem for the reversed-field configuration. However, substantial beam losses are found in the group I and II regimes, both in the entry taper region of the wiggler and due to high-power electromagnetic waves.

I. INTRODUCTION

Recently, a free-electron laser (FEL) experiment at the Massachusetts Institute of Technology (MIT) reported high efficiencies without recourse to the use of a tapered wiggler field.[1,2] The basic configuration is that of an amplifier in which a weakly relativistic electron beam is injected into a cylindrical waveguide in the presence of both a helical wiggler field and an axial guide solenoidal field. The wave–particle interaction is with the fundamental TE_{11} mode of the waveguide at a frequency of 33.39 GHz, corresponding to the frequency of the magnetron used to drive the amplifier. The experiment operated with the axial guide field oriented both parallel and antiparallel to the direction of the wiggler, and the maximum efficiency was obtained for the antiparallel (i.e., reversed-field) configuration. The reversed-field case demonstrated an output power of 61 MW at 33.39 GHz for an efficiency of approximately 27%. The performance in the more usual parallel alignment of the fields was much less and peak power levels of only about 4 MW were obtained for both the weak (group I) and strong (group II) field regimes of the axial guide field. A detailed analytical characterization of this experiment has been presented in a previous work[13] in which substantial agreement was found between the theory and the experiment for the reversed-field configuration. However, some discrepancies existed for the group I and II

cases, and it was conjectured that a problem with beam transport existed for these configurations which led to an increased beam energy spread. In this paper, we further analyze the question of beam transport through the wiggler/axial guide field in this experiment. Before proceeding further, however, a brief description of the experiment is in order.

The electron beam in the experiment was generated by a Physics International Pulserad 110A using field emission from a graphite cathode, and the beam energy used in the experiment is 750 keV (± 50 keV). The quality (i.e., the emittance and energy spread) of the beam delivered to the interaction region is controlled by scraping the beam with a shaped graphite anode. This technique was originally pioneered at the Naval Research Laboratory for use in a FEL experiment.[4] In the MIT experiment, the shaped anode–cathode geometry results in a beam with a radius of 0.25 cm (corresponding to the radius of the anode aperture), and an axial energy spread estimated to be approximately $\Delta \gamma_z / \gamma_0 \approx 1.5\%$. This energy spread corresponds to a normalized rms beam emittance of $\epsilon_n < 4.4 \times 10^{-2}$ cm rad. The current available using this configuration was of the order of 300 A (± 30 A) at the entrance to the wiggler. However, the amount of current which could be propagated through the wiggler/guide-field configuration varied based upon the stability of the electron trajectories. Current propagation data indicated quite different results depending upon the orientation of the axial guide field.

The wiggler field was produced by a bifilar helix with a period of $\gamma_w = 3.18$ cm, a length of $50\lambda_w$, and an adiabatic

---

entry taper which is six wiggler periods in length. The wiggler amplitude was continuously adjustable up to an amplitude of approximately 1.8 kG. The axial guide field could be adjusted up to a maximum amplitude of almost 12 kG in either the parallel or reversed-field orientation.

The beam propagated through a cylindrical waveguide of 0.51 cm in radius, which provided for a wave–particle resonance with the fundamental TE_{11} mode in the vicinity of 35 GHz. The FEL was operated as an amplifier, and a magnetron which produced approximately 17 kW ($\pm 10\%$) at a frequency of 33.39 GHz was used as a driver. Since the output from the magnetron was linearly polarized, this corresponded to approximately 8.5 kW in the right-hand circularly polarized state which was capable of interacting with the helical wiggler geometry.

The output from the amplifier showed the greatest efficiency for the field-reversed configuration. In this case, a peak power of 61 MW for a conversion efficiency of 27% was found for a wiggler-field magnitude of approximately 1.47 kG and an axial magnetic field of 10.92 kG. The current, which could be propagated in these fields, was near the maximum of 300 A. The output power for the field-reversed configuration also showed a severe decrease in the vicinity of the antiresonance, dropping by more than three orders of magnitude. The power observed when the axial magnetic field was oriented parallel to the wiggler was much less than for the field reversed configuration, and showed a maximum measured power of approximately 4 MW.

The organization of the paper is as follows. A brief description of the nonlinear formulation used to describe the experimental configuration is given in Sec. II. Beam transport through the wiggler in the reversed-field configuration is described in Sec. III. The case of beam transport for parallel orientation between the wiggler and axial guide fields is discussed in Secs. III and IV for the weak (group I) and strong (group II) axial guide-field regimes, respectively. A summary and discussion is given in Sec. V.

II. THE THEORETICAL FORMULATION

For the sake of brevity, we do not provide a discussion of the detailed dynamical equations employed in the nonlinear formulation here. Rather, we give a summary of the essential properties of the formulation, and refer the interested reader to Refs. 5–11 for a complete derivation and description. For the sake of convenience, we shall refer to the nonlinear formulation and simulation code as ARACHNE.[5–11]

The ARACHNE formulation represents a slow-time-scale description of a steady-state FEL amplifier in three dimensions. To this end, it is assumed that only a single frequency propagates and, therefore, Maxwell's equations can be averaged over a wave period. This results in two related simplifications of the numerical problem. Specifically, (1) that the fast-time-scale oscillation is removed from the problem and only the slow-time-scale growth (or damping) of the wave need be resolved, and (2) that only an electron *beamlet* (i.e., a group of electrons which enter the interaction region within one wave period) needs to be included in the simulation. Together, these two simplifications result in both a substantial increase in the step size and a reduction in the number of electrons in the simulation with respect to the requirements of a full-scale particle-in-cell simulation. Hence, the numerical requirements for the simulation of a FEL amplifier are relatively modest.

The electromagnetic field in this formulation is represented in terms of a superposition of the TE and TM modes of the vacuum waveguide. Note that this does not violate the single-frequency assumption, since the wave numbers of the modes which are included in the superposition will vary depending upon the specific cutoff frequencies. One restriction, however, which is imposed is that only propagating modes (in which the cutoff frequency is lower than the wave frequency) can be included in the formulation. The space-charge field is represented in terms of a superposition of the Gould–Trivelpiece modes (at the same frequency as the electromagnetic wave) for a beam which completely fills the waveguide.[12] Observe that the transverse variation of the axial electric field of the Gould–Trivelpiece modes is identical to that of the TM modes of a cylindrical waveguide. The fundamental assumption in the case of both the electromagnetic and electrostatic field is that while the transverse mode structure is determined by the waveguide or the beam conditions, the amplitude and phase vary slowly (with respect to the wave period) in the axial direction due to the interaction with the electron beam. Since both the fluctuating electromagnetic and electrostatic fields are at the same frequency, the dynamical equations for both cases can be averaged over the wave period in order to obtain the equations for the slow variations.

In order to complete the formulation, the orbit equations for an ensemble of electrons must be specified. For this purpose, we employ the three-dimensional Lorentz force equations. This requires the integration of the electron trajectories in the complete set of electrostatic (Gould–Trivelpiece modes), magnetostatic (wiggler and axial guide fields), and electromagnetic fields (TE and TM modes of the waveguide). It is important to bear in mind that it is not necessary to perform an average of these equations, since the Lorentz force equations are inherently slowly varying for waves in near resonance with the beam. The generality of this formulation of the electron orbits is a crucial feature which permits the simulation to describe not only the primary oscillation induced by the wiggler, but also Larmor effects due to the presence of the axial field and Betatron oscillations and guiding-center drifts due to the wiggler inhomogeneities. This is the critical requirement in the simulation of the field-reversed configuration near the antiresonance.

The initial conditions on the electron beam are chosen to describe the beam as it is prior to the entry into the wiggler. We assume a uniform distribution in both initial phase and cross section. The beam is assumed to have a flattop density profile for simplicity. The effect of an axial energy spread is included by means of a momentum space distribution function which is monoenergetic but displays a

pitch-angle spread. The wiggler field model includes the adiabatic entry taper from zero to a fixed value, and ARACHNE then describes the self-consistent injection of the electron beam into the wiggler. This procedure has a practical advantage, since it is easier to determine the characteristics of the electron beam prior to the injection into the wiggler.

The initial conditions imposed on the TE and TM modes are that the initial amplitude of each mode is chosen to reflect the injected power into the system, and the initial wave number corresponds to the vacuum value appropriate to the mode. ARACHNE then determines the self-consistent evolution of both the amplitude and wave number due to the dielectric effect of the beam in the wiggler. The initial growth rates are assumed to be zero, since the wiggler field is initially zero as well.

The initialization of the Gould–Trivelpiece modes is accomplished by evaluation of the appropriate initial phase averages of the electron beam. Note that the assumption of a uniform electron beam implies that the phase averages, which appear in Poisson's equation, will initially vanish. However, the use of a discrete ensemble of electrons introduces a small numerical error into the initial phase averages (i.e., $\langle \sin \varphi \rangle$ and $\langle \cos \varphi \rangle$). We find that, in practice, the use of these numerical uncertainties for the phase averages in Poisson's equation to select the initial amplitudes and wave numbers smoothes the initial transients associated with the subsequent phase bunching of the electron beam.

Within the context of this initialization scheme, ARACHNE subsequently self-consistently integrates the dynamical equations for the field amplitudes and phases of each of the electromagnetic and electrostatic waves included in the simulation in conjunction with the Lorentz force equations for the electron ensemble (which typically includes 9600 electrons). Since the complete Lorentz force equations are used, this permits the self-consistent description of the effects of the injection of the beam into the wiggler, the bulk wiggler motion, Larmor motion, the effects of wiggler inhomogeneities (i.e., betatron motion and the associated guiding-center drifts, velocity shear effects, orbital instabilities in the group I and II regimes, etc.), and harmonic interactions.

Features common to all cases studied herein derive from the geometry of the system. Specifically, we take the waveguide radius to be $R_g = 0.51$ cm, the wiggler period to be $\lambda_w = 3.18$ cm, and the wiggler entry taper as $N_w = 6$ wiggler periods in length. In addition, while the beam current varies with the magnitude of the axial guide field, the beam energy is 750 keV and the radius is fixed at the aperture of the anode to $R_b = 0.25$ cm.

Since the frequency of the amplifier experiment is fixed by the 33.39 GHz magnetron, the beam energy of 750 keV and the waveguide radius of 0.51 cm ensures that a resonant interaction is possible only with the fundamental TE_{11} mode of the guide. Further, since the magnetron produces approximately 17 kW with a linear polarization, we assume that only half of this power is available with the correct circular polarization to interact with the beam.

Hence, the initial power of the TE_{11} mode is chosen to be 8.5 kW. The collective Raman interaction in a FEL couples the TE_{11} mode, in principle, with each of the Gould–Trivelpiece modes having an azimuthal mode number of $l = 0$. In practice, however, we find that inclusion of only the lowest-order radial mode is required to give reasonable agreement with the experiment. Note that the axial electric field of this mode has the same transverse variation as the TM_{01} waveguide mode. Hence, the following simulations have been performed using only one waveguide mode and one Gould–Trivelpiece mode.

III. THE REVERSED-FIELD CASE

As discussed Ref. 3, the first case we consider is that of a field-reversed configuration in which the nominal experimental magnetic-field parameters were an axial field magnitude of 10.92 kG and a wiggler field of 1.47 kG. The transmitted current for these field parameters was 300 A ($\pm 10\%$), and the axial energy spread of the beam is assumed to be 1.5% as indicated in the experiment. These parameters represent the case of the peak power observed in the experiment of 61 MW.

A detailed comparison of the experiment and ARACHNE for this case is given in Ref. 3 and shows a saturated power of 16 MW in good agreement with the experiment. Analysis of beam transport through the wiggler in this case indicates that no loss of the beam to the waveguide walls occurs. The reason for this is that the effect of the reversed field is to reduce the magnitude of the wiggler-induced transverse velocity relative to that found for the parallel orientation which results in a corresponding reduction in the displacement of the beam from the axis of symmetry. However, this conclusion is not universally valid for the reversed-field configuration, and we find that reductions in the level of beam transport occur when the Larmor period associated with the reversed axial field is comparable to the wiggler period. This so-called antiresonance also results in substantial reductions in the output power of the FEL.

ARACHNE and the experimental results are in agreement as to the existence of a marked reduction in the saturation efficiency near the antiresonance (see Fig. 6 in Ref. 3) at axial field magnitudes between approximately 7–8.5 kG. The cause of this decrease in the efficiency is the transverse inhomogeneity in the wiggler.[3,13] For this particular example, the radius of the wiggler-induced motion is approximately 0.04 cm while the beam radius is 0.25 cm. As a consequence, electrons at the outer regions of the beam are quite sensitive to the wiggler inhomogeneity, and experience a sinusoidally varying wiggler field during the course of their trajectories. The effect of these orbital irregularities is twofold. In the first place, substantial oscillations are found in the axial velocity[3] which act to degrade the wave–particle resonance driving the interaction. In the second place, these irregularities lead to increased loss of the electron beam to the walls of the waveguide. The effect of the oscillating axial velocity has been extensively discussed in Ref. 3, and we shall focus attention here on the question of particle loss.
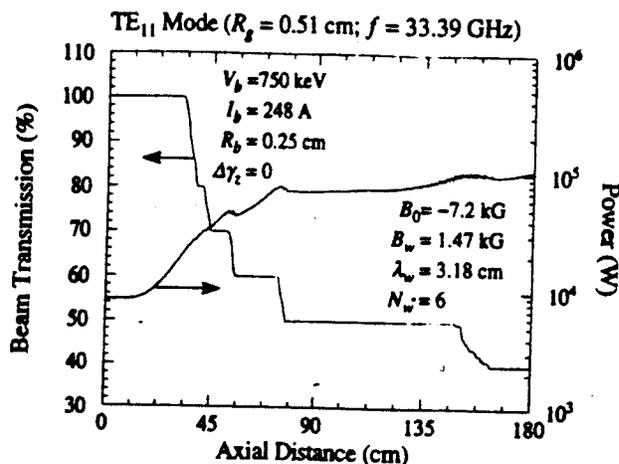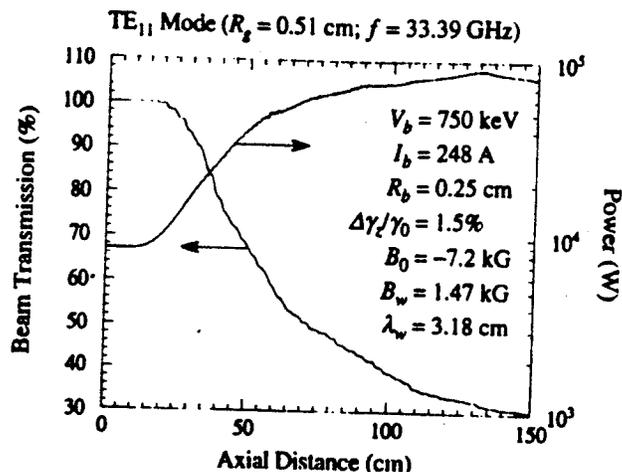
FIG. 1. Plot of the evolution beam transmission as a percentage of the initial beam current and the power versus axial position near the antiresonance for an ideal beam in which the axial energy spread at the entrance to the wiggler is zero.

FIG. 2. Plot of the evolution beam transmission as a percentage of the initial beam current and the power versus axial position near the antiresonance.

We now consider an axial field of $B_0 = -7.2$ kG which is in the center of the antiresonant region. The current at the entrance to the wiggler in this case is approximately 248 A and the wiggler field magnitude is $B_w = 1.47$ kG. We first treat the case of an ideal beam in which the initial (i.e., at the entrance to the wiggler) axial energy spread is zero, and plot the evolution of the power and the transmitted current versus axial position in Fig. 1. It is clear from the figure that substantial particle loss is found over the course of the interaction. Virtually no particle loss occurs in the entry taper region (i.e., the first 19 cm of the wiggler), but is rapid thereafter. Saturation at a power level of approximately 10 kW occurs after a distance of approximately 85 cm at which point 50% of the beam has been lost to the waveguide wall. The total beam loss over the full 150 cm of the interaction region is predicted to be approximately 60%.

If we consider the more realistic case in which the initial axial energy spread of the beam is 1.5%, then we find that these results are not substantially altered. The beam transmission and power versus axial position for this case is shown in Fig. 2. Again, we find no particle loss in the entry taper region, but rapid loss thereafter. Saturation at a power level of slightly less than 10 kW occurs after a distance of approximately 90 cm. Beam loss at this point is approximately 60%, and total beam loss over a 150 cm interaction length is approximately 70%. Thus the effect of the realistic choice in the axial energy spread results in a small decrease in the saturated power and a somewhat more rapid loss of the beam.

III. THE GROUP I CASE

As shown in Ref. 3, the agreement between ARACHNE and the experimental measurements in the group I and II regimes is not as good as that found for the reversed-field configuration. In the cases in which the axial guide field is oriented parallel to the wiggler field, a much larger energy spread than that estimated for the experiment is required

in order to account for the measured power levels. Indeed, we find that the assumption of an energy spread of 1.5% results in efficiencies comparable to that found for the field-reversed configuration, and we note that the efficiency predicted in simulation does not vary appreciably for either orientation of the magnetostatic fields for comparable beam energy spreads. In order to account for the group I data we must assume an energy spread of greater than 6% to account for the measured power. The group II data are more difficult to explain and will be discussed in the following section.

We have no definitive explanation for this discrepancy, but merely suggest that there is some misalignment or other beam transport problem from the gun to the wiggler which is exacerbated by the orientation of the axial guide field. A possible source for such a discrepancy could be the existence of irregularities in the wiggler field upstream from the entrance due to the sudden termination of the coils. Such irregularities might give rise to orbital instabilities for a parallel alignment of the wiggler and axial guide fields which result in enhanced emittance growth. A detailed evaluation of these suggestions, however, can only be accomplished by means of a thorough analysis of the experimental configuration.

With all of this in mind, we plot the evolution of the beam transmission and power versus axial position as measured in the experiment and as determined with ARACHNE in Fig. 3 for wiggler and axial guide fields of 0.63 and 4.06 kG, respectively, and for an axial energy spread of 6.25%. These fields correspond to group I operation, and the initial current at the entrance to the wiggler is assumed to be 90 A. Note that this initial current differs from that used in Ref. 3 (i.e., which was 119 A) due to a further refinement in the current measurements used in the experiment.[14] As shown in the figure, ARACHNE is in substantial agreement with the experiment for the presumed energy spread of 6.25% both as regards the linear growth rate and the saturation efficiency.
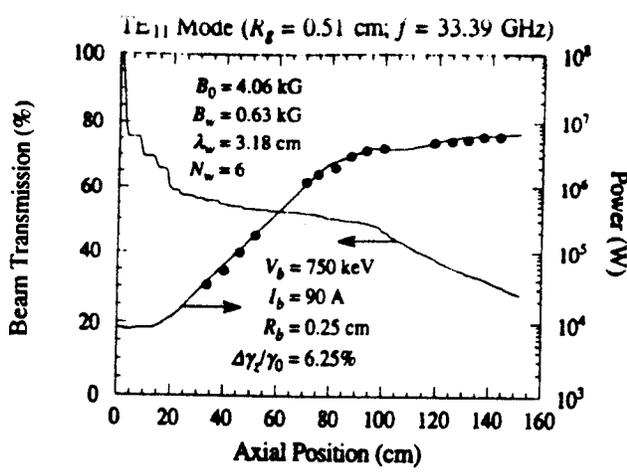
FIG. 3. Plot of the evolution of the transmitted beam and power as seen both in ARACHNE and in the experiment (as indicated by the dots) versus axial position for group I parameters.
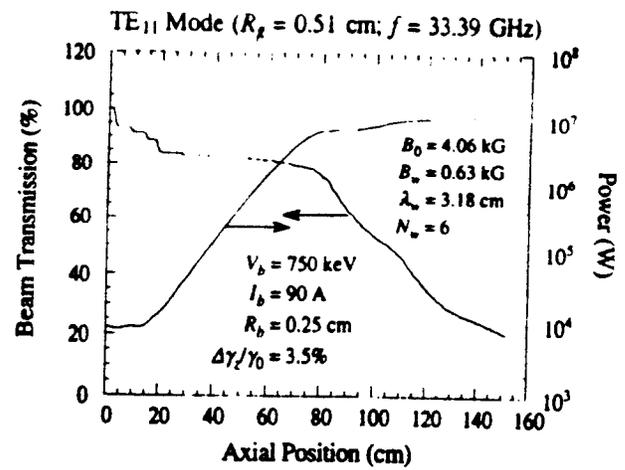
It is evident from Fig. 3 that a substantial fraction of the beam is lost in the entry taper region, but that little beam is lost thereafter until the electromagnetic power reaches a level of approximately 4–5 MW after which beam loss occurs at a faster rate. This implies that the saturation mechanism is not phase trapping in the ponderomotive wave, as in the reversed-field example at $B_0 = -10.92$ kG. Rather, saturation occurs in this case through loss of the beam to the waveguide wall.

This effect of saturation by particle loss is more evident if we consider the case of an ideal beam with an initial energy spread $\Delta\gamma_z/\gamma_0 = 0$. The evolution of the transmitted beam and the power as a function of axial position for this case is shown in Fig. 4. In this case, since the initial axial energy spread is zero, the entire beam is transmitted through the entry taper region. The power is then seen to grow exponentially until it reaches a level of approximately 10 MW, after which beam loss is rapid. Saturation is found

FIG. 5. Plot of the evolution of the transmitted beam and power, as seen in ARACHNE versus axial position for an ideal energy spread of 3.5% for group I parameters.

at a power level of approximately 16 MW, at which point the bulk of the beam has been lost to the waveguide wall.

An intermediate case is shown in Fig. 5 corresponding to an initial axial energy spread of $\Delta\gamma_z/\gamma_0 = 3.5\%$. In this case, a small fraction of the beam is lost in the entry taper region after which the power grows exponentially. During this phase of the interaction the loss rate of the beam is relatively small. However, the loss rate of the beam increases sharply when the power level reaches approximately 8–9 MW. Subsequent beam loss is both rapid and massive culminating in the loss of 78% of the beam over an interaction length of 150 cm. The ultimate saturated power in this case is approximately 11 MW.

A summary of the effect of the initial axial energy spread upon both the saturation efficiency is shown in Fig. 6. It is evident from this figure that the beam transmission increases and the saturation efficiency decreases with increases in the initial axial energy spread. This is a novel
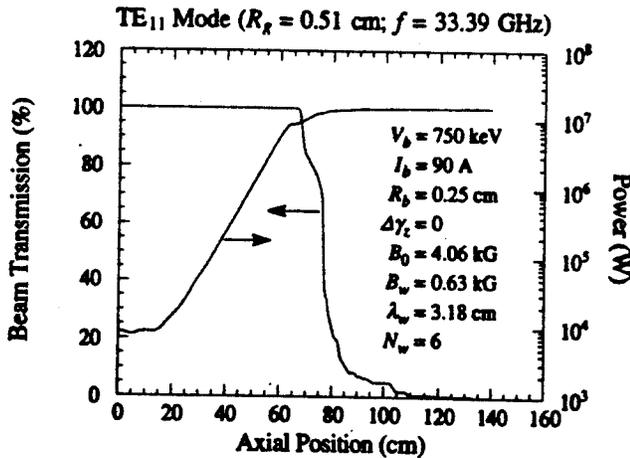
FIG. 4. Plot of the evolution of the transmitted beam and power, as seen in ARACHNE versus axial position for an ideal beam with zero initial energy spread for group I parameters.
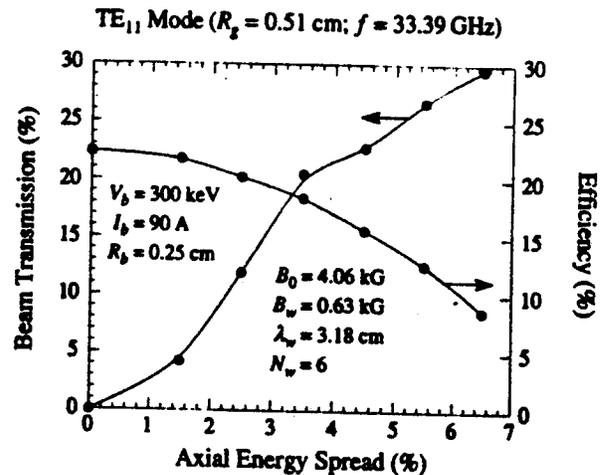

FIG. 6. Variation in the beam transmission and saturation efficiency as functions of the initial axial energy spread.
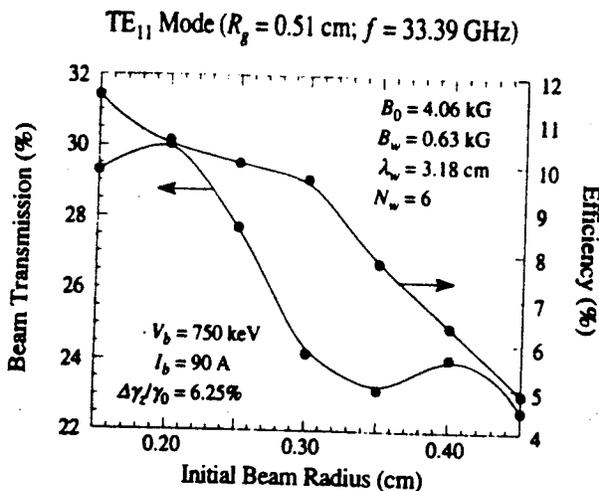
1873   Phys. Fluids B, Vol. 5, No. 6, June 1993

H. P. Freund   1873

TE$_{11}$ Mode (R_g = 0.51 cm; f = 33.39 GHz)

TE$_{11}$ Mode (R_g = 0.51 cm; f = 33.39 GHz)

FIG. 7. Variation in the beam transmission and saturation efficiency as functions of the initial beam radius.
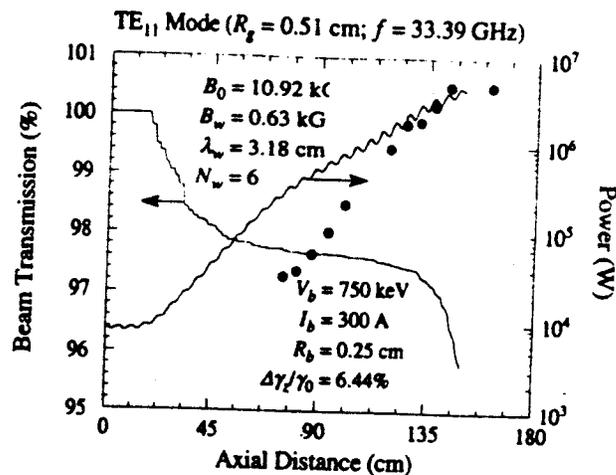
FIG. 8. Plot of the evolution of the transmitted beam and power, as seen both in ARACHNE and in the experiment (as indicated by the dots) versus axial position for group II parameters.

result since the initial axial energy spread (which is assumed to be due to a pitch-angle spread) causes an increase in the transverse electron velocities at the entrance to the wiggler. This, in turn, gives rise to increasing electron displacements from the symmetry axis. In most cases studied, therefore, the effect of increasing the initial axial energy spread is a reduction in the beam transmission. In the present case, however, the wall radius is sufficiently greater than the beam radius that beam loss is not primarily due to this energy spread-induced loss mechanism. Instead, since increases in the beam loss rate are correlated with increases in the saturation efficiency, it may be concluded that beam loss is due to the effect of the high-power TE$_{11}$ mode. Since the magnitude of this mode is greatest along the axis of symmetry and decreases to zero at the waveguide wall, it has the effect of driving the beam away from the axis toward the wall.

The fact that massive beam loss resulting in the saturation of the power occurs in the group I case but not in the reversed-field case can be attributed to the fact that the wiggler-induced transverse velocity is higher for the group I, as opposed to the reversed-field example. Therefore, the wiggler-induced beam displacement from the axis of symmetry is higher for the group I case which, in turn, results in a greater sensitivity by the beam to the effects of a high-power electromagnetic wave. Note also that the wiggler-induced displacement from the symmetry axis is greater near the magnetic resonance for the group I (and, for that matter, the group II) case; hence, the beam loss rates will also be more sensitive to the high-power electromagnetic waves for the group I and II regimes in the vicinity of the resonance.

Of course, the issue of beam loss due to the electron displacement from the symmetry axis is related to the issue of the effect of the initial beam radius on the saturation efficiency and beam transmission. In order to illustrate this effect, the variation in the efficiency and the beam transmission is plotted versus the initial beam radius in Fig. 7. As shown in the figure, the efficiency decreases monoton-

ically with increasing beam radius for 0.15 cm$<R_b<$0.45 cm. This decrease in the efficiency is due primarily to the fact that a smaller beam is less sensitive to wiggler inhomogeneities and so exhibits a smaller variation in velocity (and, hence, the wave–particle resonance) across the beam. However, the effect of the variation in the initial beam radius on the beam transmission is more complex and is controlled by two competing effects. On the one hand, the increasing beam radius means that a relatively greater fraction of the beam is closer to the wall. On the other hand, the decrease in the efficiency means that the high-power electromagnetic wave will be less effective in driving the beam toward the wall. In view of this, the increase in the electron displacements in the initial beam radius over 0.15 cm$<R_b<$0.20 cm shown in Fig. 7 is still too small to cause significant beam loss and the increase in the beam transmission is due to the decrease in the TE$_{11}$ mode power. As the initial beam radius increases further, however, the increasing electron displacements from the symmetry axis become more important, and the beam transmission falls until $R_b\approx$0.35–0.40 cm. As the initial beam radius increases further, the substantial decreases in the TE$_{11}$ mode power cause a small increase in the beam transmission until the initial beam radius begins to approach the wall radius.

IV. THE GROUP II CASE

The group II data are more difficult to explain than the group I case. The assumption of a comparable energy spread of 6.4% results in reasonable agreement for the power at the end of the interaction region, but not for the detailed evolution of the signal (i.e., the launching loss and the instantaneous growth rate) during the course of the interaction.

Comparison of ARACHNE with experiment in the case of wiggler and guide fields of 0.63 and 10.92 kG, respectively, and a transmitted current of 300 A is shown in Fig. 8 in which we plot the evolution of the transmitted current
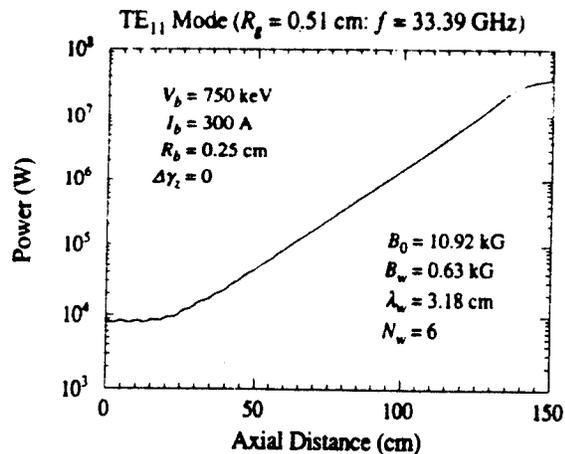
FIG. 9. Plot of the evolution of the transmitted beam and power, as seen in ARACHNE versus axial position for an ideal beam with zero initial energy spread for group II parameters.
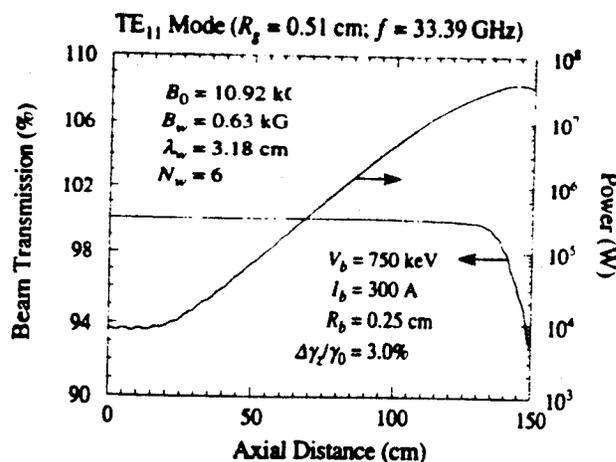

FIG. 10. Plot of the evolution of the transmitted beam and power, as seen in ARACHNE versus axial position for an initial energy spread of 3.0% for group II parameters.

and the power both from ARACHNE and from the experiment (shown by the dots). This case shows rough agreement in the case of a 6.4% energy spread for the power (≈ 4 MW) and saturation efficiency but not the growth rate. In addition, the launching loss observed in the experiment is much higher than that seen in simulation, as evidenced by the fact that there is negligible growth in the observed power until after an axial position of 70 cm after the wiggler entrance. Beam loss is not found in simulation to be a major factor for this case until a power level of approximately 4 MW is reached, after which beam loss occurs at a very rapid rate. Hence, beam loss appears to be the saturation mechanism for this case, as well as for the group I cases.

The case of an ideal beam for these group II parameters reveals very different behavior, as shown in Fig. 9 in which we plot the evolution of the power versus axial position for an ideal beam with an initial energy spread $\Delta\gamma_z/\gamma_0 = 0$. Hence, the power saturates at a power level of approximately 37 MW over a distance of 150 cm. The transmitted beam as a function of axial position is not plotted in the figure because no beam is lost. Hence, saturation in this case is due to phase trapping in the ponderomotive wave.

An intermediate case is shown in Fig. 10 which corresponds to an initial axial energy spread of $\Delta\gamma_z/\gamma_0 = 3.0\%$. In this case, no beam is lost in the entry taper region and exponential growth is found up until the power level reaches approximately 10–20 MW. Subsequent beam loss is rapid, but the saturated power level is comparable to that shown in Fig. 9 for the case of an ideal beam. We conclude that for this case beam loss can contribute only partially to the saturation mechanism unless the initial axial energy spread exceeds 3%.

V. SUMMARY AND DISCUSSION

In this paper, we have presented an analysis of beam transmission in a high-power collective FEL[1,2] which op-

erated with both parallel and reversed guide field configurations. Beam transmission was not found to be a problem in the reversed-field configuration unless the magnitude of the guide field was in the vicinity of the magnetoresonance for which the Larmor period associated with the guide field is comparable to the wiggler period. However, beam transmission was a problem for the parallel orientation of the wiggler and guide magnetic fields.

In the case of group I parameters (i.e., weak axial magnetic fields), ARACHNE was found to be in substantial agreement with the experiment under the assumption of an initial axial energy spread of 6.25%. However, the principal saturation mechanism was found to be beam loss which occurs when the wave power reaches approximately 10 MW. This was found to be the case for all values of the initial axial energy spread. The case of group II parameters (i.e., strong axial magnetic fields) was more difficult to characterize. It was found that a choice of an initial axial energy spread of 6.44% resulted in good agreement with the measured power, but not the measured growth rate. In addition, the initial launching loss found in the experiment was much greater than that predicted in simulation. Hence, there are many unanswered questions regarding group II operation in this experiment. Be that as it may, however, particle loss was not found to be a major problem in the group II regime until the initial axial energy spread exceeded 3%, after which it was a contributing, but not the sole influence on the saturation mechanism.

ACKNOWLEDGMENT

[1]M. E. Conde and G. Bekefi, Phys. Rev. Lett. 67, 3082 (1991).
[2]M. E. Conde and G. Bekefi, IEEE Trans. Plasma Sci. PS-20, 240 (1992).

[3]H. P. Freund and A. K. Ganguly, IEEE Trans. Plasma Sci. PS-20, 245 (1992).

[4]R. K. Parker, R. H. Jackson, S. H. Gold, H. P. Freund, V. L. Granatstein, P. C. Efthimion, M. Herndon, and A. K. Kinkead, Phys. Rev. Lett. 48, 1368 (1982).

[5]A. K. Ganguly and H. P. Freund, Phys. Rev. A 32, 2275 (1985).

[6]H. P. Freund and A. K. Ganguly, Phys. Rev. A 33, 1060 (1986).

[7]H. P. Freund and A. K. Ganguly, Phys. Rev. A 34, 1242 (1986).

[8]H. P. Freund and A. K. Ganguly, J. Quantum Electron. QE-23, 1657 (1987).

[9]A. K. Ganguly and H. P. Freund, IEEE Trans. Plasma Sci. PS-16, 167 (1988).

[10]A. K. Ganguly and H. P. Freund, Phys Fluids 31, 387 (1988).

[11]H. P. Freund and T. M. Antonsen, Jr., *Principles of Free-Electron Lasers* (Chapman and Hall, London, 1992), Chap. 5.

[12]N. A. Krall and A. W. Trivelpiece, *Principles of Plasma Physics* (McGraw-Hill, New York, 1973), p. 202.

[13]K. R. Chu and A. T. Lin, Phys. Rev. Lett 67, 3235 (1991).

[14]M. E. Conde (private communication, 1992).

1876   Phys. Fluids B, Vol. 5, No. 6, June 1993

H. P. Freund   1876

APPENDIX XI

Space-Charge Effects in Free-Electron Lasers

H.P. Freund

NUCLEAR
INSTRUMENTS
& METHODS
IN PHYSICS
RESEARCH
Section A

Space-charge effects in free-electron lasers

H.P. Freund [1]

Naval Research Laboratory, Washington, DC 20375, USA

The questions of the importance and proper description of space-charge effects in free-electron lasers are addressed. The collective Raman regime occurs in free-electron lasers when the electron charge density is sufficiently high that the space-charge potential associated with the beam space-charge waves becomes dominant over the ponderomotive potential. The theoretical nonlinear treatment of collective effects in three-dimensions is discussed, and four intense electron beam experiments are analyzed with the objective of determining the importance of Raman effects on the interactions. Three of these experiments used a helical wiggler and an axial guide field, while the fourth used a planar wiggler. For each of these experiments, the usual well-known Raman/Compton criterion predicts that space-charge effects will be important. However, a three-dimensional analysis of these experiments indicates that only two of these experiments were in the Raman regime. Three essential conclusions are drawn. First, the usual Raman/Compton criterion which was derived via an idealized one-dimensional analysis must be used with caution since three-dimensional effects can alter the relative importance of the ponderomotive and space-charge potentials. In addition, 1) the Raman shift in the resonance condition must be greater than the FEL linewidth, and 2) Landau damping of the space-charge waves must be small in order for space-charge effects to be important.

The free-electron laser (FEL) operates subject to two mechanisms. In the Compton regime, the electron beam interacts with the ponderomotive potential formed by the beating of the wiggler and radiation fields. For high currents, the electrostatic potential due to the beam space-charge waves is dominant over the ponderomotive potential, and the interaction proceeds by stimulated Raman scattering of the negative-energy space-charge wave off the wiggler. Of course, there is also an intermediate regime in which both of these mechanisms are operative. However, some controversy still exists as to the transition between these regimes, and as to the importance of space-charge effects in various FEL experiments. The purpose of this paper is to explore the nature of the Raman interaction by studying the importance of space-charge effects in a selection of FEL experiments [1–4].

The Compton/Raman transition was first studied with an idealized one-dimensional formulation [5], for which the condition required for the dominance of the Raman regime is

$$\frac{\omega_b}{ck_w} \gg \frac{\gamma_z^3}{8} \frac{v_w^2}{c^2}, \tag{1}$$

where $\omega_b^2 = 4\pi e^2 n_b / \gamma_0 m_e$ is the square of the plasma frequency, n_b is the ambient beam density, γ_0 is the relativistic factor corresponding to the bulk beam en-

ergy, and $\gamma_z^2 = (1 - v_z^2/c^2)^{-1}$ for a bulk axial velocity v_z. In addition, $v_w = -\Omega_w/k_w$ is the transverse wiggle-velocity, where $\Omega_w = eB_w/\gamma_0 m_e c$ for a wiggler amplitude B_w, and k_w is the wiggler wavenumber for a period λ_w. For a planar wiggler, the rms wiggler amplitude must be used in v_w. While this criterion (1) is widely used in characterizing FEL experiments, its application to a real system is clouded by several factors. Firstly, the boundary conditions imposed by the drift tube walls reduce the effective plasma frequency. Secondly, the bulk characteristics of the electron orbits are modified by wiggler inhomogeneities, beam thermal effects, and the use of an axial guide magnetic field. Planar wiggler configurations introduce further difficulties since, in contrast to a helical wiggler, the axial and transverse electron velocities are oscillatory. Due to these difficulties, a full 3-dimensional nonlinear analysis is often required to characterize space-charge effects in any given experiment.

A second criterion required for space-charge effects to be important is that the Raman frequency shift be comparable to or greater than the linewidth. The physical interpretation of this criterion is that the wiggler must be long enough for several plasma oscillations during the course of the interaction. Of course, realistic 3-dimensional effects can be expected to modify this condition as well.

Finally, a third criterion required for space-charge effects to play an important role is that Landau damping of the space-charge waves due to the thermal

[1] Permanent address: Science Applications International Corp., McLean, Virginia 22102, USA.

Table 1

A summary of the operational parameters for the experiments under consideration

	Fajans et al. [1]	Orzechowski et al. [2]	Kirkpatrick et al. [3]	Conde and Bekefi [4]
V_b [MeV]	0.155	3.6	2.3	0.75
I_b [A]	4.1	850	930	300
R_b [cm]	0.25	1.0	0.41	0.25
B_w [kG]	0.176 (H)	3.6 (P)	1.275 (H)	1.47 (H)
l_w [cm]	3.3	9.8	3.14	3.18
B_0 [kG]	1.45	N/A	N/A	−10.92
P [MW]	0.08	185	18	61
η [%]	12	6	0.8	27
f [GHz]	9.318	34.6	470	33.4
f_b [GHz]	0.72	2.2	5.5	5.2
f/f_b	0.077	0.063	0.012	0.156
$\omega_b/(ck_w)$	0.069	0.25	0.25	0.35
$(\gamma_z^3/8)(v_w^2/c^2)$	0.0023	0.33	0.079	0.01
Raman	yes	no	no	yes

spread of the beam must be small. In general, Landau damping of space-charge waves is important for wavelengths less than the Debye length.

In order to elaborate on the importance of space-charge effects in FELs, we shall consider four experiments. The operational frequencys of these experiments extended from 9 to 500 GHz, and the beam parameters ranged from currents of 4 to 900 A and energies ranging from 150 keV to 3.5 MeV. Three of the experiments [1,3,4] employed a helical wiggler and two also used an axial guide field [1,4]. Of these two, one used a guide field oriented parallel with the wiggler [1], while the other used a reversed-guide field orientation [4]. The remaining experiment used a planar wiggler configuration [2]. Thus, these experiments cover a wide range of parameter space. It is interesting to observe that only two of these experiments were unequivocally in the Raman regime, and that these were the two with the lowest currents. A summary of these experiments is given in table 1.

The experiments are analyzed using the 3-dimensional nonlinear simulation codes ARACHNE [6] and WIGGLIN [7], which are slow-time-scale formulations where the electromagnetic field is expanded in a superposition of the TE and TM modes of either a cylindrical or rectangular waveguide, and the space-charge field is expanded in a superposition of the Gould–Trivelpiece modes of the beam. Slow-time-scale equations govern the evolution of the amplitude and phase of each TE, TM, and Gould–Trivelpiece mode due to the
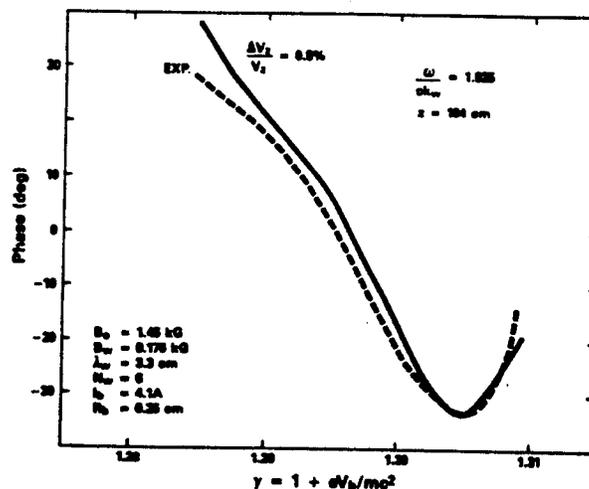
Fig. 1. Variation in the output phase versus beam energy as determined in the experiment [1] and with ARACHNE [6]. TE$_{11}$ mode (R_g = 1.27 cm; P_{in} = 27 kW (lin.)).

IX. RAMAN FEL THEORY

interaction with the beam and wiggler/axial guide field. These equations are integrated simultaneously with the 3-dimensional Lorentz force equations in the complete ensemble of electromagnetic, electrostatic, and magnetostatic fields. We emphasize that no averaging procedure is imposed on the orbit equations. This is an essential feature of the formulation required to explain many aspects of the experiments, including the behavior of the electron trajectories in the reversed-guide field configuration and the accurate description of the bulk motion of the electron beam in the planar wiggler configuration. The distinctions between WIGGLIN and ARACHNE are 1) that ARACHNE deals with a helical wiggler/axial guide field with a cylindrical waveguide, while 2) WIGGLIN deals with a planar wiggler with parabolic pole faces and a rectangular waveguide, and 3) that the Gould–Trivelpiece space-charge modes are not included in WIGGLIN. As shall be shown later, this last distinction is no impediment as space-charge effects were not important to the single planar wiggler experiment under consideration. The four experiments under consideration deal with both helical and planar wiggler configurations; hence, ARACHNE has been used to analyze the experiments described in refs. [1,3,4] while WIGGLIN was used to analyze the experiment described in ref. [2].

The first experiment conducted [1] was an amplifier driven by a traveling wave tube. As shown in table 1, criterion (1) places this experiment in the Raman regime, as was also demonstrated by the observation that the gain scaled as the fourth root of the current [8]. Further, the wiggler length of ≈ 150 cm permitted 5–6 plasma oscillations over the course of the interaction. Finally, the low energy spread ($\Delta\gamma_z/\gamma_0 \approx 0.3\%$) minimized the effect of Landau damping. Note that at 4.1 A this experiment had the lowest current in the group. A comparison of the variation in the phase of the output signal with beam energy from the experiment and as determined with ARACHNE is shown in fig. 1. The phase measurement is equivalent to a tuning curve which is the most sensitive test of the space-charge effect (as opposed to absolute power measurements). It is evident in the figure that substantial agreement exists between the experiment and ARACHNE; hence, we conclude that the collective interaction is treated correctly in this formulation.

The second experiment is the ELF experiment [2] which operated as a 35 GHz amplifier driven by a 50 kW magnetron with a planar wiggler and a rectangular waveguide. As shown in table 1, this experiment is transitional between the Compton and Raman regimes on the basis of the idealized criterion (1), and it might be expected that space-charge effects play some role. However, the calculated linewidth [9] is ≈ 15 GHz which is much greater than the plasma frequency (≈ 2.2
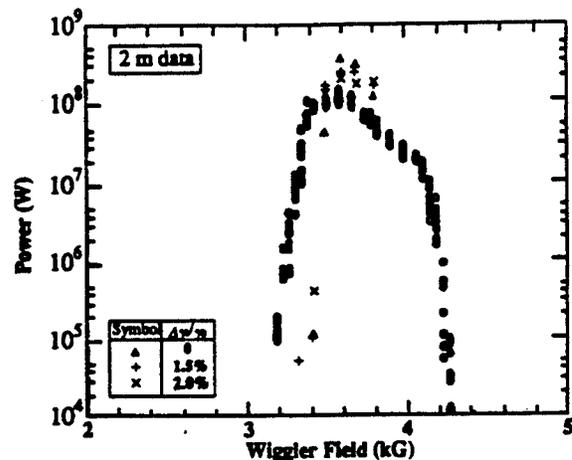

Fig. 2. Comparison of the tuning curves for the ELF experiment [2] shown as circles and WIGGLIN over a 2 m interaction length.

GHz). In addition, the axial energy spread ($\Delta\gamma_z/\gamma_0 \leq 2\%$) yields a Debye length of ≈ 0.8 cm. This is comparable to the space-charge wavelength of ≈ 0.8 cm; hence, the space-charge waves are strongly damped [10]. This issue, therefore, is not whether this experiment is in the Raman regime (it is not), but the extent to which space-charge effects were important. This question can be addressed by comparison of WIGGLIN with a detailed experimental spectrum.

Such a comparison is shown in fig. 2 where we plot output power after 2 m as calculated by WIGGLIN (for three choices of the axial energy spread) with an experimentally measured tuning curve [2]. Note that 1) since the experiment was a 34.6 GHz amplifier driven by a magnetron, the tuning is accomplished by varying the magnetic field, and 2) saturation was found to occur over a length of 1.4 m. In view of the latter point, a detailed comparison of the spectral width is not valid because sidebands are expected to result in spectral broadening after saturation, and WIGGLIN does not include sidebands in the formulation. Be that as it may, the agreement between the spectral peak predicted by WIGGLIN and found in the experiment is excellent and does not vary greatly with the choices of axial energy spread. The agreement between these peaks from WIGGLIN and the experiment is ≈ 30 G, which is within the experimental uncertainty. As a result, it is concluded that space-charge effects did not play a role in this experiment.

It should be remarked for comparison purposes that the FRED simulation code was also compared with this spectral data [11]. The principal differences between WIGGLIN and FRED are 1) that FRED uses a field solver rather than a modal superposition, 2) that a wiggler-averaged orbit approximation is made in

FRED, and 3) that the approximation for space-charge is treated differently than by the Gould-Trivelpiece superposition used in ARACHNE. The results of this comparison between FRED and the spectral data are that FRED is detuned from the experiment by $\approx 7\%$ without space-charge, and the inclusion of the space-charge is necessary for agreement with the data. Since this contrasts with WIGGLIN, it is of interest to consider the source of the discrepancy.

The use of a field solver as opposed to a modal superposition is not expected to result in a significant discrepancy between these formulations. Since WIG-GLIN is in agreement with the spectral data without the explicit inclusion of space-charge effects, it is reasonable to suppose that the principal source of the discrepancy lies in the wiggler-averaged orbit approximation used in FRED but not WIGGLIN, and not in the space-charge algorithm. Thus, consider the limits of accuracy imposed by the orbit average.

Since the axial velocity in a planar wiggler is oscillatory, the tuning will be sensitive to this average. This is typically done with a Bessel function correction factor that is derived under the assumption of a sinusoidal variation in v_z. However, the variation in v_z is given by an elliptic function for large displacements of the orbit from the symmetry plane of the wiggler. Furthermore, in a 3-dimensional analysis the magnitude of the wiggler varies over an electron orbit, which also acts to break the sinusoidal variation in v_z. Each of these effects limit the accuracy of the wiggler-averaged orbit approximation. In addition, the effect of a large amplitude electromagnetic wave (i.e., near saturation) is included in the transverse components of the electron trajectories in WIGGLIN (but not FRED), and is observed to modify the electron orbits. Hence, we assert that the discrepancy between the spectral data and FRED arises from the wiggler-averaged orbit approximation. This discrepancy is to within $\approx 7\%$ in B_w, which is equivalent to an $\approx 3.5\%$ error in v_z. For most purposes, this is a reasonable approximation, and agreement between FRED an the experimental data has been typically good. However, we conclude that the wiggler-averaged orbit approximation is not good enough to resolve the importance of space-charge effects in the ELF experiment.

The third experiment was a superradiant amplifier (i.e., the signal grew from noise) employing a helical wiggler without an axial field [3]. As shown in table 1, this experiment is expected to be in the Raman regime on the basis of the idealized criterion (1). However, the linewidth of 50 GHz was much greater than the plasma frequency. The beam energy spread of $\Delta\gamma_z/\gamma_0 \approx 0.25\%$ was consistent with an analysis of the gun geometry using the EGUN code and with gains predicted with ARACHNE. Hence, the Debye length here is ≈ 0.09 cm while the space-charge wavelength is ≈ 0.06 cm,
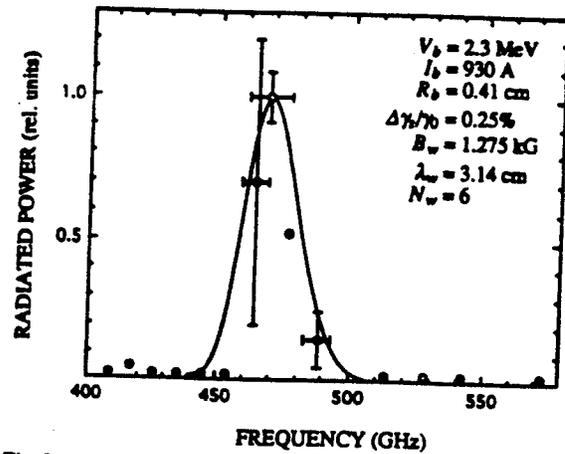

Fig. 3. Comparison of the experimental output spectrum [3] as represented by the dots with ARACHNE. TE_{11} and TM_{11} modes ($R_g = 0.8$ cm).

and we expect that space-charge waves will be damped, and that Raman effects will be unimportant. This conclusion is supported by ARACHNE. The output power versus frequency from ARACHNE and the experiment is shown in fig. 3. Evidently, ARACHNE accurately reproduces the observed spectrum. It should be noted that the space-charge waves can be disabled in ARACHNE, and that the predicted spectrum is unaffected by the inclusion of space-charge waves. We conclude that 3-dimensional affects (such as the plasma frequency reduction and realistic orbits) modify the idealized criterion (1).

The fourth experiment [4] operated as an amplifier. As shown in table 1, this experiment is also in the Raman regime based on criterion (1). In addition, the wiggler length of ≈ 150 cm permitted 28–29 plasma oscillations during the course of the interaction. Finally, the Debye length for this experiment was ≈ 0.14 cm while the wavelength of the space-charge waves was ≈ 0.80 cm. Hence, Landau damping of the space-charge waves is not important. Hence, we expect this experiment to be in the Raman regime, and this conclusion is supported by simulations with ARACHNE which shows good agreement with the experiment [12]. A maximum power of ≈ 61 MW was found for a reversed-guide field orientation. A comparison of the evolution of the power versus axial position as determined in the experiment and computed with ARACHNE is shown in fig. 4. Two curves from ARACHNE are shown corresponding to the nominal experimental parameters ($I_b = 300$ A, $B_w = 1.47$ kG, and $P_{in} = 8.5$ kW) as well as the upper limits due to experimental uncertainties. It is evident from the figure that ARACHNE is in agreement with the experiment to within the experimental uncertainty. Note that this agreement cannot be ob-
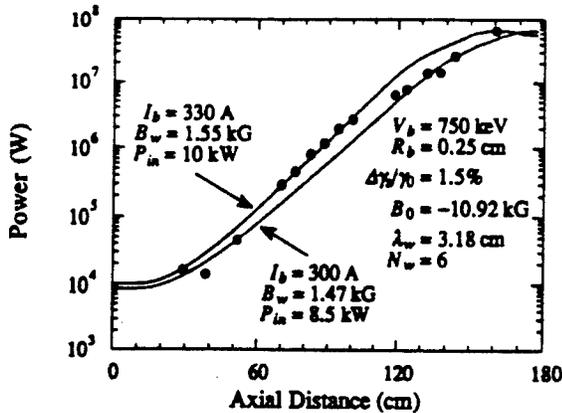
IX. RAMAN FEL THEORY

Fig. 4. The evolution of the power with axial position as determined with ARACHNE and from the experiment (dots) for a field-reversed configuration. TE_{11} mode ($R_g = 0.51$ cm; $f = 33.39$ GHz).

tained with ARACHNE if the space-charge modes are disabled.

In conclusion, we have examined the detailed effect of space-charge on four experiments with the purpose of determining criteria for the importance of Raman effects on the FEL interaction. In the first place, it is concluded that the wiggler-averaged orbit approximation can lead to a sufficiently large error in the bulk axial velocity that no reliable determination of the importance of space-charge effects can be made. It is also concluded that the idealized Raman criterion (1) must be used with caution since 3-dimensional effects alter the relationship between the ponderomotive and space-charge potentials. It should be pointed out here that improved models of the interaction in the linear regime have been developed which treat the Raman/Compton regime with more precision than is given in the one-dimensional Raman criterion (1). For example, a complete three-dimensional solution to the eigen-value problem posed by the propagation of a thin electron beam through a cylindrical waveguide in the presence of a helical wiggler and an axial guide field has been developed [13], and successfully applied to the analysis of a Raman FEL [8]. Similar analyses have also been conducted using a hybrid one-dimensional electron orbit/three-dimensional waveguide model [14]. Unfortunately, while such models are in good agreement with FEL experiments, they are often too complex to yield a simple Raman/Compton criterion. In addition, two other criteria must be considered as well. Specfically, 1) the Raman shift in the resonance condition must be greater than the FEL linewidth, and 2) Landau damping of the space-charge waves must be small in order for space-charge effects to be important.

It should be noted that an alternate approach to the development of a usable Raman/Compton criterion is to use an ad hoc model for such factors as the space-charge reduction factor for the plasma frequency or the filling-factor of the beam and radiation. However, these descriptions must be used with some caution. For example, it was shown that the beam space-charge wave itself can be driven unstable for helical wiggler/axial guide field configurations in the strong guide field regime [15]. Hence, the inclusion of the wiggler dynamics can have a significant dielectric effect on the space-charge wave which must be included in any self-consistent estimate of the effects of the plasma reduction factor. Further, attempts to include the effects of the filling-factor must also be approached with caution due to the optical guiding of the radiation. For these reasons, it was judged preferable to employ the simplified one-dimensional form for the Raman/Compton criterion in this work.

Acknowledgement

References

[1] J. Fajans et al., Phys. Rev. Lett. 57 (1986) 579.

[2] T.I. Orzechowski et al., Nucl. Instr. and Meth. A250 (1986) 144.

[3] D.A. Kirkpatrick et al., Phys. Fluids B1 (1989) 1511.

[4] M.E. Conde and G. Bekefi, Phys. Rev. Lett. 67 (1991) 3082.

[5] H.P. Freund and T.M. Antonsen, Jr., Principles of Free-Electron Lasers (Chapman and Hall, London, 1992) p. 106.

[6] A.K. Ganguly and H.P. Freund, Phys. Fluids 31 (1988) 387.

[7] H.P. Freund, Phys. Rev. A37 (1988) 3371.

[8] J. Fajans and G. Bekefi, IEEE J. Quantum Electron. QE-23 (1987) 1617.

[9] H.P. Freund, H. Bluem and C.L. Chang, Phys. Rev. A36 (1987) 2182.

[10] C.A. Brau, Free-Electron Lasers (Academic, Boston, 1990) p. 63.

[11] E.T. Scharlemann et al., Nucl. Instr. and Meth. A250 (1986) 150.

[12] H.P. Freund and A.K. Ganguly, IEEE Trans. Plasma Sci. PS-20 (1992) 245.

[13] H.P. Freund and A.K. Ganguly, Phys. Rev. A28 (1983) 3438.

[14] H.S. Uhm and R.C. Davidson, Phys. Fluids 26 (1983) 288.

[15] H.P. Freund and P. Sprangle, Phys. Rev. A28 (1983) 1835.

APPENDIX XII

The Coaxial Hybrid Iron (CHI) Wiggler

R.H. Jackson, H.P. Freund, D.E. pershing, and J.M. Taccetti

The coaxial hybrid iron (CHI) wiggler *

Robert H. Jackson **, Henry P. Freund [1], Dean E. Pershing [2], J.M. Taccetti [3]

Code 6840, Vacuum Electronics Branch, Naval Research Laboratory, Washington, DC 20375-5347, USA

A wiggler design has been developed which is scalable to small periods with high field amplitude, high beam current acceptance, and excellent transverse focusing and beam propagation properties. The coaxial hybrid iron (CHI) wiggler design consists of a coaxial arrangement of alternating ferromagnetic and non-ferromagnetic rings with the central portion of the coax shifted by one half period. The entire arrangement is immersed in a solenoidal field which results in a cylindrically symmetric periodic field. FEL configurations using this wiggler design have the potential for high power, high frequency coherent generation in relatively compact systems. Analytic and simulated characteristics of the CHI wiggler are discussed.

1. Introduction

Free-electron lasers (FELs) are attractive as tunable sources of coherent radiation. However, the voltages presently required for radiation are often beyond the desirable limit for many applications. Harmonic operation [1,2] and small period wigglers [3–10] are two approaches being tested for reduced voltage (or enhanced frequency) operation. Each has advantages and disadvantages depending on the parameters and performance requirements of the particular application or system. By utilizing micro-wigglers ($\lambda_w < 5$ mm), FEL operating voltages can be reduced ($\alpha \sqrt{\lambda_w}$) with resulting reductions in shielding, size, and cost. The difficulty with this approach lies in fabricating small period wigglers which will provide high field strength and uniformity with reasonable gap spacing and good beam focusing. Several micro-wiggler configurations have been proposed and investigated [3–10]. Each of these configurations has advantages and disadvantages in the areas of achievable field strength and uniformity, fabrication, control, tuning, cost, and beam acceptance and focusing. The coaxial hybrid iron (CHI) wiggler design presented in this paper has a number of

advantages in these areas for high power, high frequency FELs.

2. CHI wiggler configuration

Prior work [3,11] has shown that large wiggler fields can be generated by immersing a periodic array of ferromagnetic material in a solenoidal magnetic field. The maximum wiggler field attainable in this manner is set by geometric factors and saturation of the ferromagnetic material. The strengths of this arrangement are simplicity and the relative ease of generating large solenoidal fields. Disadvantages include a large periodic component in the axial field within the structure, large variation in the axial and transverse field amplitudes away from the symmetry axis, and potential beam propagation problems because of gyroresonant and field gradient effects. In addition, although the wiggler fields generated can be large they are still not high enough to lower operating voltages significantly without sacrificing gain and power.

The CHI wiggler design overcomes many of these shortcomings by employing a coaxial arrangement of alternating ferromagnetic and non-ferromagnetic rings with the central portion of the coax shifted relative to the outer by one half period, see Fig. 1. The entire arrangement is then immersed in a solenoidal field resulting in a periodic radial magnetic field and a reduced solenoidal field with a low amplitude ripple and alternating gradients. One period in the CHI wiggler structure consists of two adjacent rings or disks, one ferromagnetic and one not. This accounts for the ability of this wiggler structure to produce very small periods. Disks and rings of magnetic and non-magnetic

R.H. Jackson et al. / Nucl. Instr. and Meth. in Phys. Res. A 341 (1994) 454-458

455

materials only fractions of a millimeter thick can be fabricated with very high precision. Stacks of such disks can be brazed or otherwise formed into mechanically robust wigglers. The most obvious materials for the construction of the ferromagnetic disks are iron alloys. However, other materials which have beneficial magnetic properties (e.g. high saturation field at cryogenic temperatures) could be used. The non-ferromagnetic disks can be fabricated from a wide range of materials (or combinations of materials) including non-magnetic metals, ceramics, plastics, air, superconducting materials, etc. The two different rings which make up a period need not be identical in thickness, height, or shape. Also, it is possible to use different ring properties for the central element as long as the period remains the same. The key to the enhanced performance of the CHI wiggler is the addition of the central element. The reasons for this will be discussed below. (A linear wiggler system utilizing immersed shifted iron poles has been under investigation by a group at Stanford University, see ref. [12] for details.)

3. Analytic field approximation

An analytic representation for the CHI wiggler field can be obtained by the solution of Laplace's equation subject to the appropriate boundary conditions at the surfaces of the magnetic and non-magnetic rings. A complete derivation of this representation will be given in detail in a future work [13], and we merely state the result here. The CHI wiggler field is azimuthally symmetric. The radial and axial components of this field are given by

$$B_r(r, z) = 2B_0 \sum_{n=1}^{\infty} \frac{\sin k_n z}{G_0(k_n R_{out}, k_n R_{in})}$$
$$\times \left\{ \frac{\sin(k_n \Delta_{out}/2)}{(k_n \Delta_{out}/2)} [I_1(k_n r) K_0(k_n R_{in}) + K_1(k_n r) I_0(k_n R_{in})] \right.$$
$$-(-1)^n \frac{\sin(k_n \Delta_{in}/2)}{(k_n \Delta_{in}/2)}$$
$$\times [I_1(k_n r) K_0(k_n R_{out}) + K_1(k_n r) I_0(k_n R_{out})] \right\}, \quad (1)$$

and

$$B_z(r, z) = B_0 + 2B_0 \sum_{n=1}^{\infty} \frac{\cos k_n z}{G_0(k_n R_{out}, k_n R_{in})}$$
$$\times \left\{ \frac{\sin(k_n \Delta_{out}/2)}{(k_n \Delta_{out}/2)} G_0(k_n r, k_n R_{in}) \right.$$
$$-(-1)^n \frac{\sin(k_n \Delta_{in}/2)}{(k_n \Delta_{in}/2)} G_0(k_n r, k_n R_{out}) \right\}, \quad (2)$$

Fig. 1. Schematic of the Coaxial Hybrid iron (CHI) wiggler geometry.

where B_0 denotes the average magnitude of the axial field in the coaxial gap, $k_n = nk_w [= 2\pi n/\lambda_w]$, Δ_{in} and Δ_{out} denote the width of the rings on the inner rod and the outer ring respectively, I_n and K_n denote the modified Bessel functions of the first and second kind of order n, and

$$G_0(x_1, x_2) = I_0(x_1) K_0(x_2) - I_0(x_2) K_0(x_1). \quad (3)$$

Observe that for most applications $\Delta_{in} = \Delta_{out} = \lambda_w/2$; hence, the CHI wiggler field contains only the odd harmonics.

The predicted axial and radial fields according to Eqs. (1) and (2) for $n = 1, 3$ are shown in Figs. 2 and 3 where the field amplitudes within the coaxial gap are plotted over two periods for gap/λ_w and ring width/$\lambda_w = 0.5$. The plots show field component amplitudes within the gap of the coaxial structure with the "back" being the outer radius of the central piece, the "front" being the inner radius of the outer piece, and the axial direction running left to right. Note that both field components have good focusing properties at the inner and outer coaxial surfaces. Also, the axial field has alternating gradients which should provide even better beam focusing and transport characteristics. A relatively large section of the mid-gap region has a reasonably uniform radial and axial field strength. Thus, the beam will have less velocity spread induced by intrinsic wiggler field gradients. This is an important feature for high power FELs employing small period wigglers.

4. Performance characteristics

The POISSON codes were used to examine the nonlinear magnetic properties of the CHI wiggler (the internal $B-H$ table for low carbon steel was used). A configuration was used which allowed study of CHI wiggler end effects and variation of a number of parameters. A full discussion of all the calculation results is not possible in this paper, and details will be given elsewhere [13,14]. Both the radial and axial fields within
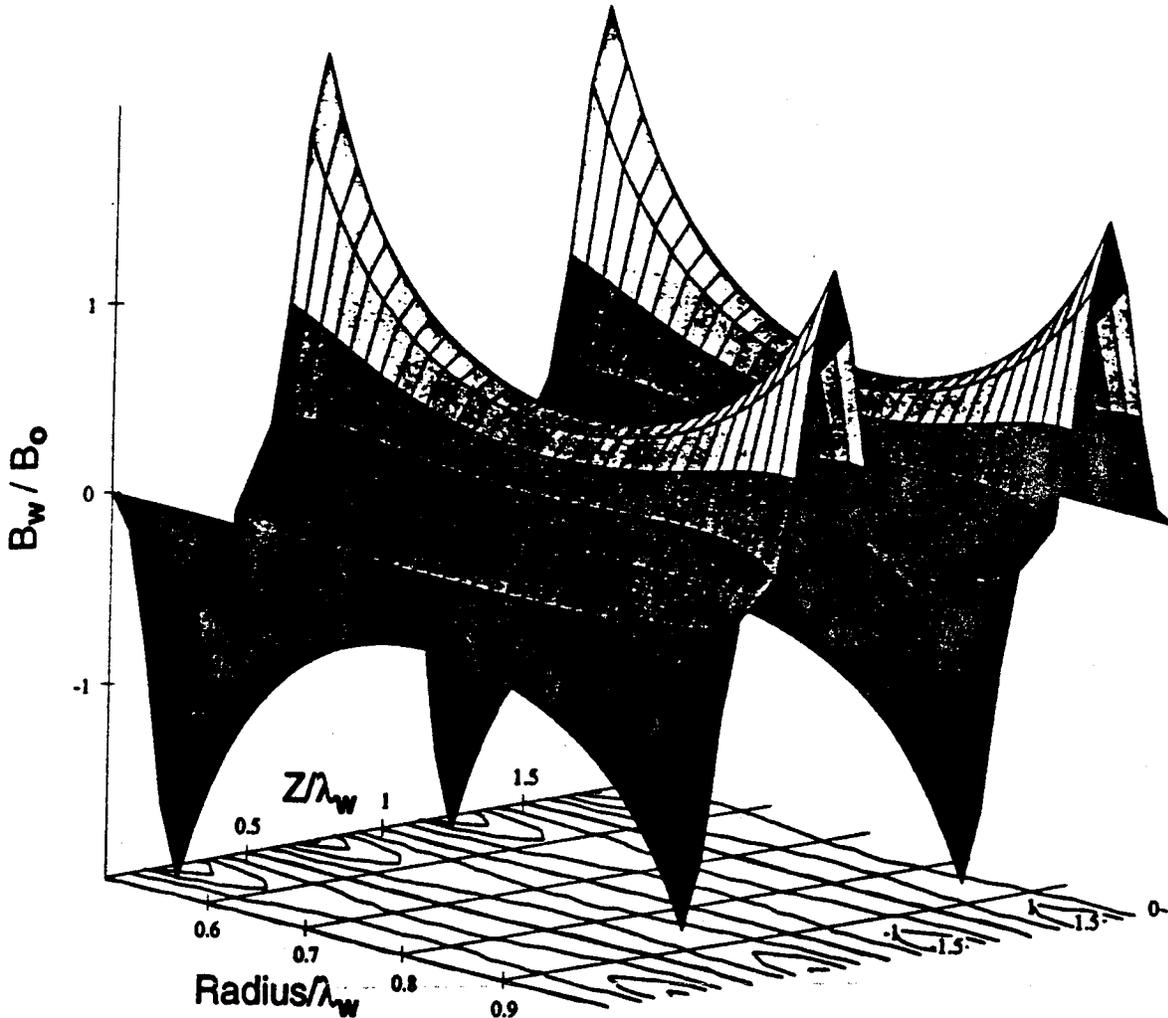
VIII. UNDULATORS

R.H. Jackson et al. / Nucl. Instr. and Meth. in Phys. Res. A 341 (1994) 454–458

457

Fig. 3. Surface plot of analytic radial magnetic field in the gap of a CHI wiggler (gap/λ_w = 0.5, ring width/λ_w = 0.5).
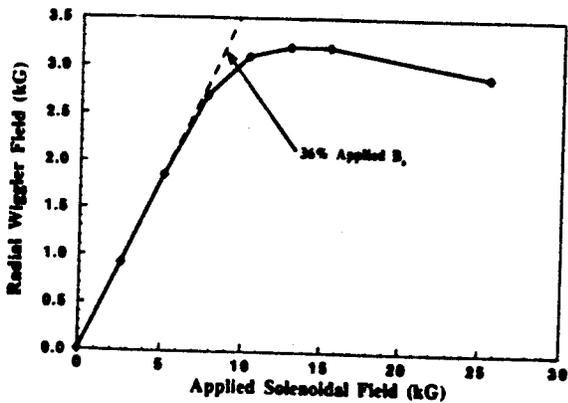

Fig. 4. Peak radial wiggler field as a function of applied solenoidal field (gap/λ_w = 0.5, ring width/λ_w = 0.5).
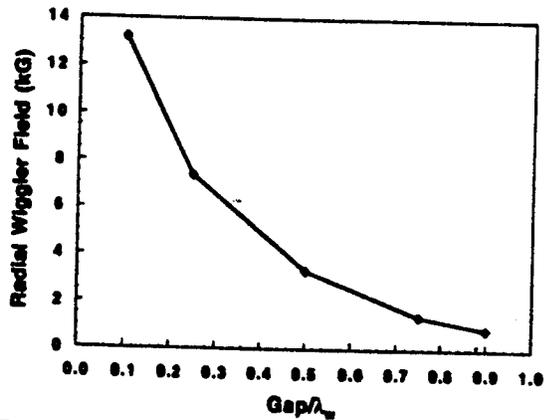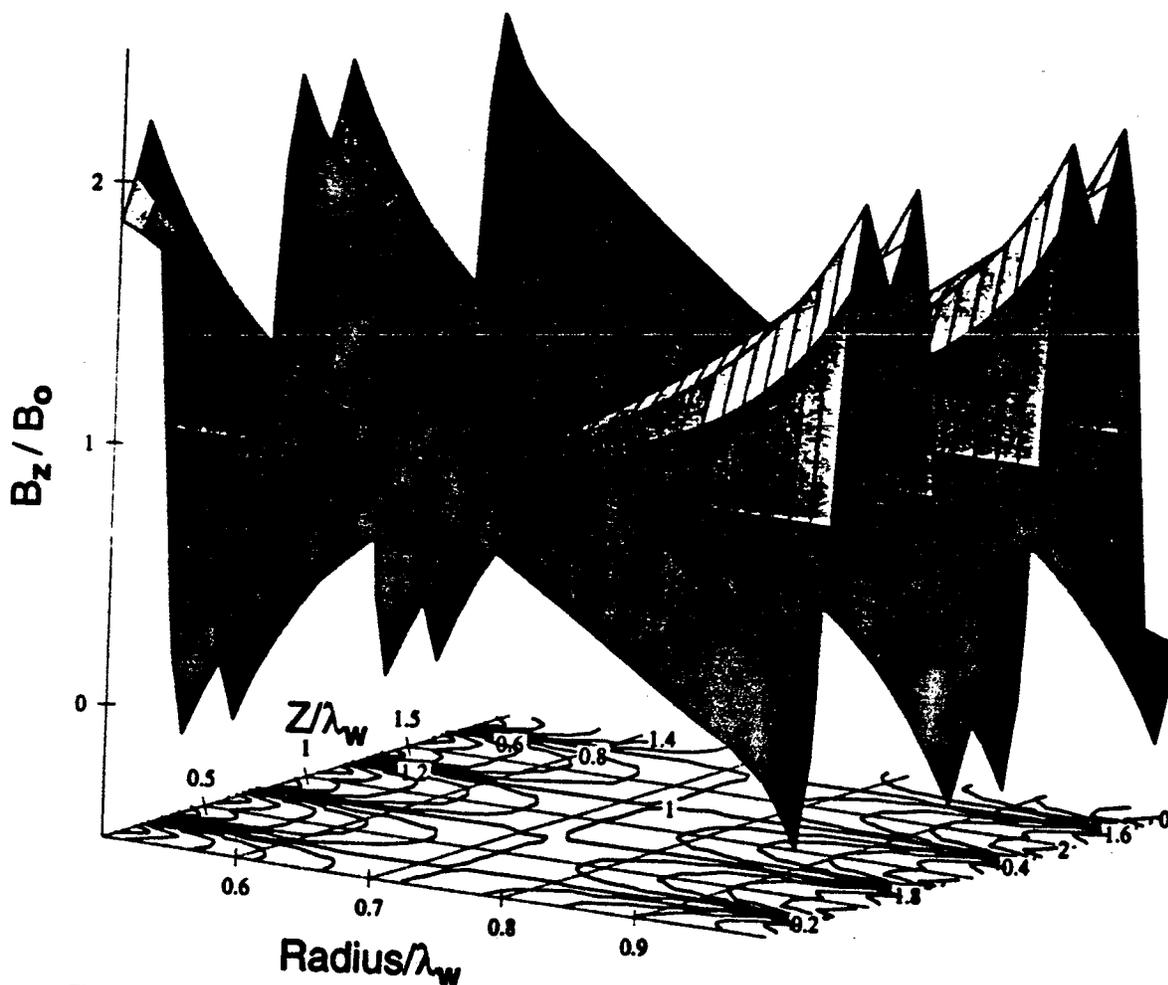
Fig. 5. Peak radial wiggler field as a function of normalized gap spacing (ring width/λ_w = 0.5, field measured in the middle of gap).

VIII. UNDULATORS

the gap were calculated and compared with the analytic results. Both qualitative and quantitative agreement is excellent, and the results are substantially the same as shown in Figs. 2 and 3. Magnetic flux line plots from simulations of the CHI wiggler show the enhancement caused by the center element. The central rings act to pull the flux lines down as the upper rings pull the flux lines up resulting in strong radial fields at the edges of the rings. These radial fields are two times larger than without the central rings when measured at the same radius. (The difference is even larger if the field is measured at the peak field radius of the TE_{01} waveguide mode where the electron beam would be placed.) In addition, field perturbations due to end effects are much lower in the CHI wiggler configuration.

The aspect of wiggler performance of most interest is the dependence of the peak radial field on various geometric and operational parameters. An operating curve for a CHI wiggler with a gap to period ratio of

0.5 is shown in Fig. 4. This figure plots radial field amplitude against applied solenoidal field, i.e. the solenoidal field which would exist in the absence of the CHI wiggler structure. The radial field increases linearly with the applied solenoidal field until the ring material begins to saturate around 8 kG. In this linear range, a substantial fraction, about 36%, of axial field is converted into radial field. As the applied field is further increased, the wiggler field amplitude levels off and then decreases slowly. The peak wiggler field generated is substantial, ≈ 3.2 kG, and, it should be noted, is fully compatible with dc operation. Numerous simulations have shown that the initial slope of the CHI wiggler performance curve is dependent on details, but the peak is mainly determined by the coaxial gap to period ratio and the saturation field of the ring material.

The variation of the peak field with respect to two CHI wiggler geometric parameters is shown in Figs. 5 and 6 for gap to period ratio and magnetic ring width

Fig. 2. Surface plot of analytic axial magnetic field in the gap of a CHI wiggler (gap/λ_w = 0.5, ring width/λ_w = 0.5).
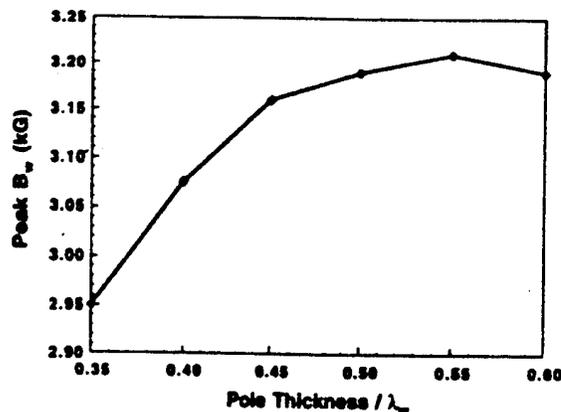
Fig. 6. Peak radial wiggler field as a function of normalized central element pole thickness (outter ring width/λ_w = 0.5, gap/λ_w = 0.5, field measured in the middle of gap).

to period ratio respectively. Fig. 5 shows the expected exponential drop in field strength as the gap/period ratio increases. A pole width/period ratio of 0.5 was assumed. For small gap values, corresponding to high beam energy or long wavelength radiation, extremely high fields are possible, approaching 14 kG. The effect of variation of the magnetic ring thickness, central ring elements only, is shown in Fig. 6 for a gap/period ratio of 0.5. A peak occurs when there is a small axial overlap of the outer and inner magnetic rings, i.e. the inner magnetic rings are slightly wider than one half period, ring-width/λ_w = 0.55. For smaller gaps, the peak field is achieved with greater pole overlap, e.g. at gap/λ_w = 0.25 peak field is achieved at ring-width/λ_w = 0.6. These results also apply to width variation of the outer rings or to simultaneous variation of both inner and outer rings. Other factors such as ring height, etc. have been varied with similar results.

Although the CHI parameters at which the peak field is achieved are highly dependent on particulars, the peak value is almost independent of any factors other than the relative gap size and ring material magnetic saturation characteristics. In all calculations performed to date, the peak field has fallen somewhere in the 3.2-3.3 kG range for low carbon steel rings with gap/λ_w = 0.5. Rings constructed from the best available iron alloys (Hiperco or Permendur) would increase the maximum wiggler field by up to 20%, i.e. to approximately 4 kG. Note that variations of the period, gap, material, ring height, applied axial field, etc. provide ample opportunities for tapering and tuning of CHI wiggler fields.

5. Summary and discussion

The CHI wiggler configuration has several advantages for applications in FEL systems. It is a simple,

low cost wiggler structure which is easy to fabricate and assemble, and is capable of producing multi-kilo-gauss fields even at millimeter wiggler periods. Because cooling considerations involve only the solenoid, CHI wigglers are compatible with dc, ac and pulsed operation. The "effective" wiggler field amplitude is tunable over a broad range in both the linear and saturated domains (in the latter due to gyroresonance effects, see ref. [14].) The CHI configuration also provides a number of parameters which can be axially tapered to control or enhance various FEL interaction characteristics. In addition, the coaxial nature of the CHI configuration greatly increases the level of beam current which can be propagated with sufficient quality for the FEL interaction.

To be sure, the CHI wiggler also has potential disadvantages such as mechanical support of the central element, increased mode competition and unconventional beam and resonator geometries. Although these details must be addressed, they do not appear to be insurmountable. With proper attention to details, CHI wigglers will enable the development of compact, low voltage FELs able to deliver high power at millimeter and IR wavelengths.

References

[1] H. Bluem, R.H. Jackson, H.P. Freund, D.E. Pershing and V.L. Granatstein, Phys. Rev. Lett. 67 (1991) 824.

[2] C.J. Elliot and M.J. Schmitt, IEEE Trans. Plasma Sci. PS-15 (1987) 319.

[3] R.M. Phillips, Nucl. Instr. and Meth. A 272 (1988) 1.

[4] V.L. Bratman, G.M. Genkin and V.V. Zil'berberg, Sov. Tech. Phys. Lett. 8 (1982) 419.

[5] R.M. White, Appl. Phys. Lett. 46 (1985) 194.

[6] G. Ramian, L. Elias and I. Kimel, Nucl. Instr. and Meth. A 250 (1986) 125.

[7] W.W. Destler, V.L. Granatstein, I.D. Mayergoyz and Z. Segalov, J. Appl. Phys. 60 (1986) 521.

[8] S.C. Chen, G. Bekefi, S. DiCecca and R. Temkin, Appl. Phys. Lett. 54 (1989) 1299.

[9] R.H. Jackson and H. Bluem, Conf. Digest of the 14th Int. Conf. on Infrared and Millimeter Waves, SPIE 1989 IR&MM Vol. 1240 (1989) 423.

[10] R.L. Sheffield, J.H. Booske, R.W. Warren, K. Halbach, B. Danly, R.H. Jackson, P. Walstrom, J. Slater and A. Toor, Digest of the 11th Int. Conf on Free-Electron Lasers, IEEE LEOS (1989) p. 100.

[11] J.M. Baird, S. Sensiper, K. Amboss and J.F. Heney, Rome Air Development Command Technical Report RADC-TR-77-133 (1977).

[12] Y.C. Huang, H.C. Wang, J. Feinstein and R.H. Pantell, Nucl. Instr. and Meth. A, to be published.

[13] H.P. Freund, R.H. Jackson and D.E. Pershing, Nonlinear theory of the free-electron laser based upon a coaxial hybrid iron wiggler, submitted to Phys. Fluids B.

[14] R.H. Jackson, H.P. Freund, D.E. Pershing and J.M. Taccetti, Coaxial hybrid iron (CHI) wiggler FEL design and performance characteristics, in preparation.

APPENDIX XIII

Nonlinear Theory of the Free-Electron Laser Based upon a Coaxial Hybrid Wiggler

H.P. Freund, R.H. Jackson, D.E. Pershing, and J.M. Taccetti

Nonlinear theory of the free-electron laser based upon a coaxial hybrid wiggler

H. P. Freund,[a] R. H. Jackson, D. E. Pershing,[b] and J. M. Taccetti[c]
Naval Research Laboratory, Washington, D.C. 20375

A three-dimensional nonlinear formulation of a free-electron laser based upon a coaxial hybrid iron (CHI) wiggler is described. The CHI wiggler is created by insertion of a central rod and an outer ring [composed of alternating ferrite and dielectric spacers in which the ferrite (dielectric) spacer on the central rod is opposite to the dielectric (ferrite) spacer on the outer ring] along the axis of a solenoidal. An analytic model of the CHI wiggler is developed which is in good agreement with the Poisson/Superfish group of codes. The free-electron laser (FEL) formulation is a slow-time-scale analysis of the interaction of an annular electron beam with the CHI wiggler in a coaxial waveguide. The electromagnetic field is represented as the superposition of the vacuum transverse electric (TE), transverse magnetic (TM), and transverse electromagnetic (TEM) modes of the waveguide, and a set of nonlinear second-order differential equations is derived for the amplitudes and phases of these modes. These equations are solved simultaneously with the three-dimensional Lorentz force equations for the combined magnetostatic and electromagnetic fields. An adiabatic taper is used to model the injection of the beam, and an amplitude taper is included for efficiency enhancement. Simulations are presented for K_a-, K_u- and W-band operation. Multimode operation is also studied. The results indicate that operation over a wide bandwidth is practical with the CHI wiggler, and that the bandwidth in the tapered-wiggler cases is comparable to that for a uniform wiggler. Therefore, relatively high field strengths can be achieved with the CHI wiggler at shorter wiggler periods than is possible in many other conventional wiggler designs.

I. INTRODUCTION

The free-electron laser (FEL) has demonstrated operation over virtually the entire electromagnetic spectrum.[1-5] The FEL operates by means of the beating of a periodic magnetostatic field (called a *wiggler*) and an electromagnetic field to produce a slowly varying ponderomotive wave in phase with the electron beam. The wavelength λ of the resonant electromagnetic wave depends both upon the beam energy and the wiggler parameters approximately as $\lambda \approx (1+a_w^2)\lambda_w/2\gamma_0^2$, where λ_w is the wiggler period, γ_0 is the bulk relativistic factor of the beam, and $a_w \approx 0.0934 B_w\lambda_w$ for a RMS wiggler amplitude B_w in kG and a wiggler period in cm. Further, in the exponential Compton regime in which the collective space-charge effects of the beam are negligible, both the gain and saturation efficiency scale as $a_w^{2/3}/\gamma_0$. Hence, the wavelength, gain, and efficiency of the interaction all decrease as the beam energy increases for fixed wiggler parameters. A great deal of effort has been devoted, therefore, to the design of short period wigglers in order to operate at short wavelengths with low beam energies. However, this is an ultimately self-defeating process, since reductions in the

wiggler period often result in a corresponding reduction in the wiggler amplitude as well with a deleterious impact on the efficiency and gain of the FEL.

It is our intention in this paper to analyze the performance of a FEL amplifier based upon a coaxial hybrid wiggler.[6] This novel wiggler design is based upon a configuration in which a central rod and a coaxial ring of alternating ferrite and dielectric spacers is inserted into a solenoidal magnetic field. Further, in this design the ferrite (dielectric) spacers on the central rod are aligned opposite to the dielectric (ferrite) spacers on the outer ring. For convenience, we refer to this design as the coaxial hybrid iron wiggler, or CHI wiggler for short. A schematic illustration of this configuration is shown in Fig. 1. The geometry of this design produces an azimuthally symmetric periodic field in which, for a fixed period, the amplitude can be increased by the relatively simple expedient of increasing the strength of the solenoid. Since solenoidal magnets are readily available with amplitudes of many tens of tesla, the CHI wiggler is capable of producing relatively high-amplitude but short period wiggler fields. It is important to observe that the radial component of the field in the CHI wiggler has a minimum at the center of the gap; hence, the field tends to focus the electron beam against the effects of self-field-induced spreading. In addition, the azimuthal symmetry of the field in the CHI wiggler results in a bulk wiggler-induced transverse velocity in the azimuthal direction; hence, the beam interaction is strongest for electromagnetic waves with an azimuthal component.

The organization of the paper is as follows. An analytical representation of the CHI wiggler is derived in Sec. II,

---
[a] Permanent address: Science Applications International Corp., McLean, Virginia 22102.
[b] Permanent address: Mission Research Corp., Newington, Virginia 22122.
[c] Permanent address: University of Maryland, College Park, Maryland 20742.
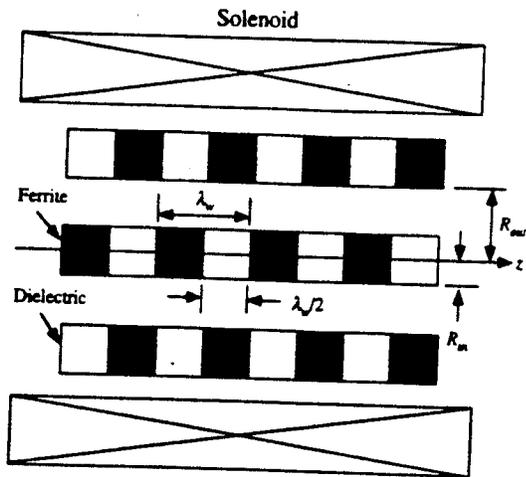
FIG. 1. Schematic illustration of the CHI wiggler configuration.

based upon a solution of Laplace's equation and boundary conditions appropriate to the coaxial geometry of the CHI wiggler. This analytic representation is in substantial agreement with results of a simulation of the CHI wiggler[6] using the Poisson/Superfish group of codes (see Ref. 7 for a discussion of the algorithm employed by these codes). A nonlinear formulation of the interaction of the beam and the CHI wiggler with the transverse electric (TE), transverse magnetic (TM), and transverse electric and magnetic (TEM) modes of a coaxial waveguide is derived in Sec. III. In this section a slow-time-scale formulation of the dynamical equations for the electromagnetic fields is derived for the coaxial waveguide geometry. These equations must be solved simultaneously with the Lorentz force equations for the electron trajectories in the combined fields of the CHI wiggler and the TE, TM, and/or TEM modes of the waveguide. A numerical analysis of the gain and saturation efficiency for various representative sets of parameters is described in Sec. IV, and a summary and discussion is given in Sec. V.

II. THE CHI WIGGLER

The CHI wiggler is formed by the insertion of a central rod and a coaxial ring of alternating ferrite and dielectric spacers within a solenoidal magnetic field. A schematic illustration of this configuration is shown in Fig. 1. The arrangement of the ferrite and dielectric spacers are such that the ferrite (dielectric) element on the central rod is opposed to the dielectric (ferrite) element on the outer ring. The magnetic field produced by this arrangement is azimuthally symmetric, and the radial component of the field has a minimum in the center of the gap. Hence, the field provides a focusing force on the electron beam. Additional focusing is provided by the bulk axial component of the field.

The ease of construction of this design permits the development of wigglers with extremely short periods by the simple expedient of using thin dielectric and ferrite spacers. The advantage of a short period wiggler is that relatively low beam energies are required for resonance at

a given frequency. However, in most wiggler designs this is offset by the fact that shorter wiggler periods typically result in lower wiggler amplitudes and increased wiggler field gradients. This is not necessarily the case for the CHI wiggler, since high wiggler amplitudes can be achieved by using a stronger solenoid. Also note that the gyroresonance between the periodic and axial components can enhance the FEL interaction as well.

In a source-free region the divergence and curl of the magnetic field vanish, and the field in coaxial gap of the CHI wiggler can be found by solution of Laplace's equation,

$$\nabla^2 \mathbf{B}(r,z) = 0, \tag{1}$$

for the appropriate boundary conditions. Since the geometry is azimuthally symmetric, we assume that

$$\mathbf{B}(r,z) = B_r(r,z)\hat{e}_r + B_z(r,z)\hat{e}_z, \tag{2}$$

where $B_r(r,z) = R_r(r)R_z(z)$, and $B_z(r,z) = Z_r(r)Z_z(z)$. Each wiggler period, denoted by λ_w, corresponds to the combined length of one ferrite and dielectric spacer, and we assume that the length of each spacer is $\lambda_w/2$. As a result, the wiggler field exhibits an axial periodicity of the form $\mathbf{B}(r,z) = \mathbf{B}(r,z+N\lambda_w)$, where N is an integer. Finally, we shall use R_{in} to denote the radius of the central rod, and R_{out} for the inner radius of the outer ring.

Substitution of this field into Laplace's equation yields two equations:

$$B_r(r,z)\left\{\left[\frac{1}{rR_r(r)}\frac{d}{dr}\left(r\frac{d}{dr}R_r(r)\right) - \frac{1}{r^2}\right] + \frac{1}{R_z(z)}\frac{d^2}{dz^2}R_z(z)\right\} = 0, \tag{3}$$

and

$$B_z(r,z)\left[\frac{1}{rZ_r(r)}\frac{d}{dr}\left(r\frac{d}{dr}Z_r(r)\right) + \frac{1}{Z_z(z)}\frac{d^2}{dz^2}Z_z(z)\right] = 0. \tag{4}$$

Since the radial and axial components of the fields should independently vanish, we use $nk_w(\equiv 2\pi n/\lambda_w)$ as the separation constant where n is an integer, and write

$$\left(\frac{d^2}{dz^2} + n^2 k_w^2\right)\begin{bmatrix} R_z(z) \\ Z_z(z) \end{bmatrix} = 0, \tag{5}$$

$$\left[\frac{d^2}{dr^2} + \frac{1}{r}\frac{d}{dr} - \left(n^2 k_w^2 + \frac{1}{r^2}\right)\right]R_r(r) = 0, \tag{6}$$

and

$$\left(\frac{d^2}{dr^2} + \frac{1}{r}\frac{d}{dr} - n^2 k_w^2\right)Z_r(r) = 0. \tag{7}$$

Equations (5)–(7) have the general solutions

$$Z_z(z) = A_{zn}\cos nk_w z + B_{zn}\sin nk_w z,$$

$$R_z(z) = A_{rn}\cos nk_w z + B_{rn}\sin nk_w z,$$

$$Z_r(r) = C_{zn}I_0(nk_w r) + D_{zn}K_0(nk_w r), \tag{8}$$

$$R_r(r) = C_{rn}I_1(nk_w r) + D_{rn}K_1(nk_w r).$$

Under the requirement that $\nabla \cdot B = 0$, the coefficients satisfy $A_m C_m + B_m C_{sn} = 0$, $B_m C_m - A_{sn} C_{sn} = 0$, $A_m D_m - B_{sn} D_{sn} = 0$, and $B_m D_m + A_{sn} D_{sn} = 0$. As a result, the field may be written as a sum over spatial harmonics,

$$B_z(r,z) = B_0 + \sum_{n=1}^{\infty} [B_n I_0(nk_w r) + C_n K_0(nk_w r)]$$
$$\times \cos[nk_w(z - z_n)] \qquad (9)$$

and

$$B_r(r,z) = \sum_{n=1}^{\infty} [B_n I_1(nk_w r) + C_n K_1(nk_w r)]$$
$$\times \sin[nk_w(z - z_n)]. \qquad (10)$$

The relations between the remaining coefficients can be determined by application of the boundary conditions. We now assume that the effect of the ferrite spacers results in a step function in the axial field at $r = R_{in}$ and R_{out}, such that $B_z(R_{in}, z) = B_{in}$ and $B_z(R_{out}, z) = B_{out}$ along the surface of the dielectric and zero along the surface of the ferrite. Therefore, for the $n = 0$ spatial harmonic,

$$\lambda_w B_0 = \int_0^{\lambda_w} dz \, B_z(R_{in}, z) = \frac{\lambda_w B_{in}}{2} \qquad (11)$$

and

$$\lambda_w B_0 = \int_0^{\lambda_w} dz \, B_z(R_{out}, z) = \frac{\lambda_w B_{out}}{2}. \qquad (12)$$

This implies that $B_{in} = B_{out} = 2B_0$. We can now Fourier decompose the $n > 1$ spatial harmonics. Under the assumption that the dielectric spacer along the surface of the central rod is found over the first half-period of the wiggler, we find that

$$B_n I_0(nk_w R_{in}) + C_n K_0(nk_w R_{in})$$
$$= \frac{4B_0}{\lambda_w} \int_{\lambda_w/4}^{3\lambda_w/4} dz \cos nk_w z = (-1)^n B_0 \left(\frac{4}{n\pi}\right) \sin\left(\frac{n\pi}{2}\right),$$
$$(13)$$

where we choose $z_n = 0$ under the assumption that the first spacers are half the typical length. This implies that the dielectric spacer is found over the second half-period of the wiggler along the outer ring; hence

$$B_n I_0(nk_w R_{out}) + C_n K_0(nk_w R_{out})$$
$$= \frac{4B_0}{\lambda_w} \left(\int_0^{\lambda_w/4} dz \cos nk_w z + \int_{3\lambda_w/4}^{\lambda_w} dz \cos nk_w z \right)$$
$$= B_0 \left(\frac{4}{n\pi}\right) \sin\left(\frac{n\pi}{2}\right). \qquad (14)$$

Using Eqs. (13) and (14), we can now write the field in the form
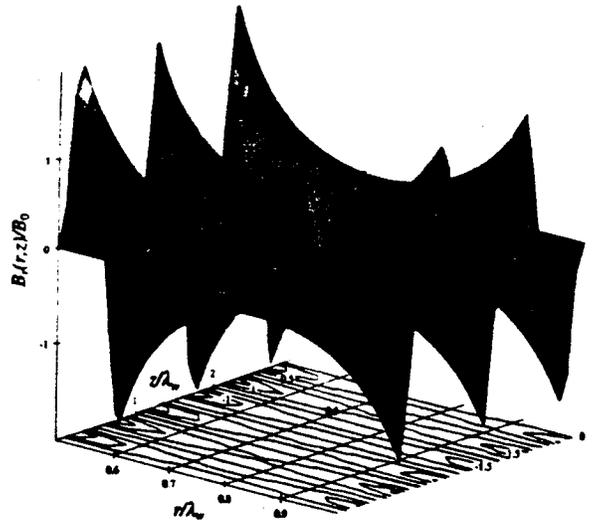
FIG. 2. Illustration of the radial component of the CHI wiggler.

$$B_z(r,z) = B_0 + B_w \sum_{n=1}^{\infty} \cos(nk_w z)$$
$$\times \frac{[S_n I_0(nk_w r) - T_n K_0(nk_w r)]}{G(nk_w R_{out}, nk_w R_{in})} \qquad (15)$$

and

$$B_r(r,z) = B_w \sum_{n=1}^{\infty} \sin(nk_w z)$$
$$\times \frac{[S_n I_1(nk_w r) + T_n K_1(nk_w r)]}{G(nk_w R_{out}, nk_w R_{in})}, \qquad (16)$$

where $B_w = 2B_0$,

$$G(\xi, \zeta) = I_0(\xi) K_0(\zeta) - I_0(\zeta) K_0(\xi), \qquad (17)$$

$$S_n = \left(\frac{2}{n\pi}\right) \sin\left(\frac{n\pi}{2}\right) [K_0(nk_w R_{in}) + K_0(nk_w R_{out})],$$
$$(18)$$

and

$$T_n = \left(\frac{2}{n\pi}\right) \sin\left(\frac{n\pi}{2}\right) [I_0(nk_w R_{in}) + I_0(nk_w R_{out})]. \qquad (19)$$

This field has the form of a superposition of an axial guide field and an azimuthally symmetric wiggler with a large number of odd spatial harmonics.

The CHI wiggler field described in Eqs. (15) and (16) represents a reasonable approximation to the realistic field within the limits of the assumptions made in solving Laplace's equation. The radial and axial components of the field normalized to B_0 are shown in Figs. 2 and 3 for $R_{out}/\lambda_w = 1.0$ and $R_{in}/\lambda_w = 0.5$ using the fundamental and third spatial harmonic components, and is in good agreement with the solution for the field obtained in this geometry using the Poisson/Superfish group of codes.[6] The ef-
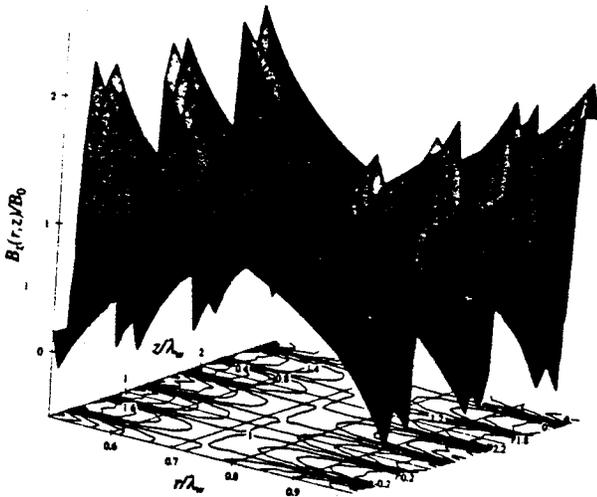
FIG. 3. Illustration of the axial component of the CHI wiggler.

fect of the third harmonic contribution is substantial, and results in a narrowing of the peaks in the radial field component and the double-peaked extrema in the axial field component.

III. THE NONLINEAR FORMULATION

We now consider the dynamical equations that govern the electromagnetic fields and the electron beam. We consider propagation within a coaxial waveguide with inner and outer radii a and b, respectively. Space-charge effects are neglected in the analysis. In general, this is valid as long as $\omega_b/ck_w < \gamma_z^3 v_w^2/8\gamma_0 c^2$, where ω_b denotes the ambient beam plasma frequency, v_w is the bulk transverse velocity imparted by the wiggler, γ_0 is the bulk relativistic factor of the beam, and $\gamma_z = (1 - v_\parallel^2/c^2)^{-1/2}$ for a bulk streaming velocity $v_\parallel$. Space-charge effects can also be neglected if (1) the wavelength is less than the Debye length and the space-charge waves are subject to strong Landau damping, or (2) the bandwidth of the interaction is greater than the plasma frequency. These conditions for the neglect of space-charge effects can be valid, even for relatively high-current electron beams.[8]

Within the context of the analysis, the boundary condition of the fields at the walls of the waveguide can be satisfied by an expansion of the electromagnetic field as the superposition of the TE, TM, and TEM modes of the waveguide. As such, the vector potential can be expressed in cylindrical coordinates as

$$\delta \mathbf{A}(\mathbf{x},t) = \sum_{\substack{l=0 \\ m=1}}^{\infty} \delta A_{lm}(z) \left(\frac{l}{\kappa_{lm}r} Z_l(\kappa_{lm}r) \hat{\mathbf{e}}_r \sin \alpha_{lm} \right.$$
$$\left. + Z_l'(\kappa_{lm}r) \hat{\mathbf{e}}_\theta \cos \alpha_{lm} \right), \qquad (20)$$

for the TE modes,

$$\delta \mathbf{A}(\mathbf{x},t) = \sum_{\substack{l=0 \\ m=1}}^{\infty} \delta A_{lm}(z) \left(Z_l'(\kappa_{lm}r) \hat{\mathbf{e}}_r \cos \alpha_{lm} \right.$$
$$- \frac{l}{\kappa_{lm}r} Z_l(\kappa_{lm}r) \hat{\mathbf{e}}_\theta \sin \alpha_{lm}$$
$$\left. + \frac{\kappa_{lm}}{k_{lm}} Z_l(\kappa_{lm}r) \hat{\mathbf{e}}_z \sin \alpha_{lm} \right), \qquad (21)$$

for the TM modes, where the phase for angular frequency ω and wave number k_{lm} is

$$\alpha_{lm} \equiv \int_0^z dz' \, k_{lm}(z') + l\theta - \omega t, \qquad (22)$$

and the dispersion of the modes is given by

$$\frac{\omega^2}{c^2} = k_{lm}^2 + \kappa_{lm}^2, \qquad (23)$$

for a given cutoff κ_{lm}. Observe that the amplitudes and wave numbers are assumed to vary slowly in z over a wavelength. The cutoffs are given by solution of the dispersion equations, which are

$$J_l'(\kappa_{lm}a) Y_l'(\kappa_{lm}b) - J_l'(\kappa_{lm}b) Y_l'(\kappa_{lm}a) = 0, \qquad (24)$$

for the TE modes, and

$$J_l(\kappa_{lm}a) Y_l(\kappa_{lm}b) - J_l(\kappa_{lm}b) Y_l(\kappa_{lm}a) = 0, \qquad (25)$$

for the TM modes, where J_l and Y_l denote the regular Bessel and Neumann functions of order l. The radial polarization functions are composed of linear combinations of the Bessel and Neumann functions,

$$Z_l(\kappa_{lm}r) \equiv J_l(\kappa_{lm}r) + \Delta_{lm} Y_l(\kappa_{lm}r), \qquad (26)$$

where

$$\Delta_{lm} \equiv \begin{cases} -\dfrac{J_l'(\kappa_{lm}b)}{Y_l'(\kappa_{lm}b)}; & \text{TE modes,} \\[2ex] -\dfrac{J_l(\kappa_{lm}b)}{Y_l(\kappa_{lm}b)}; & \text{TM modes.} \end{cases} \qquad (27)$$

The vector potential for the TEM mode is given simply by

$$\delta \mathbf{A}(\mathbf{x},t) = \delta A(z) \frac{a}{r} \hat{\mathbf{e}}_r \cos \alpha. \qquad (28)$$

Since the TEM mode is not cut off, the dispersion and phase are given by $\omega = ck$, and

$$\alpha = \int_0^z dz' \, k(z') - \omega t. \qquad (29)$$

As in the case of the TE and TM modes, the amplitude and wave number of the TEM mode is assumed to vary slowly in z over a wavelength.

The dynamical equations for the amplitudes and phases of each mode are obtained by substitution of the field representations into Maxwell's equations and then performing an orthogonalization in r and θ, as well as an average over the wave period. Derivations of these equa-

tions for cylindrical and rectangular waveguides have been described in detail,[9] and the derivation for the coaxial waveguide follows analogously. The dynamical equations that result are

$$\left[\frac{d^2}{dz^2}+\left(\frac{\omega^2}{c^2}-k_{lm}^2-\kappa_{lm}^2\right)\right]\delta a_{lm}$$

$$=\frac{\omega_b^2}{c^2}H_{lm}\left\langle\frac{v_r}{|v_z|}\frac{l}{\kappa_{lm}r}Z_l(\kappa_{lm}r)\sin\alpha_{lm}\right.$$

$$\left.+\frac{v_\theta}{|v_z|}Z_l'(\kappa_{lm}r)\cos\alpha_{lm}\right),\qquad(30)$$

$$2k_{lm}^{1/2}\frac{d}{dz}(k_{lm}^{1/2}\delta a_{lm})$$

$$=\frac{\omega_b^2}{c^2}H_{lm}\left\langle\frac{v_r}{|v_z|}\frac{l}{\kappa_{lm}r}Z_l(\kappa_{lm}r)\cos\alpha_{lm}\right.$$

$$\left.-\frac{v_\theta}{|v_z|}Z_l'(\kappa_{lm}r)\sin\alpha_{lm}\right),\qquad(31)$$

for the TE modes,

$$\left[\frac{d^2}{dz^2}+\left(1+\frac{\kappa_{lm}^2}{k_{lm}^2}\right)\left(\frac{\omega^2}{c^2}-k_{lm}^2-\kappa_{lm}^2\right)\right]\delta a_{lm}$$

$$=\frac{\omega_b^2}{c^2}H_{lm}\left\langle\frac{v_r}{|v_z|}Z_l'(\kappa_{lm}r)\cos\alpha_{lm}\right.$$

$$-\frac{v_\theta}{|v_z|}\frac{l}{\kappa_{lm}r}Z_l(\kappa_{lm}r)\sin\alpha_{lm}$$

$$\left.+\frac{\kappa_{lm}}{k_{lm}}Z_l(\kappa_{lm}r)\sin\alpha_{lm}\right),\qquad(32)$$

$$2\left(k_{lm}+\frac{\kappa_{lm}^2}{k_{lm}}\right)^{1/2}\frac{d}{dz}\left[\left(k_{lm}+\frac{\kappa_{lm}^2}{k_{lm}}\right)^{1/2}\delta a_{lm}\right]$$

$$=-\frac{\omega_b^2}{c^2}H_{lm}\left\langle\frac{v_r}{|v_z|}Z_l'(\kappa_{lm}r)\sin\alpha_{lm}\right.$$

$$+\frac{v_\theta}{|v_z|}\frac{l}{\kappa_{lm}r}Z_l(\kappa_{lm}r)\cos\alpha_{lm}$$

$$\left.-\frac{\kappa_{lm}}{k_{lm}}Z_l(\kappa_{lm}r)\cos\alpha_{lm}\right),\qquad(33)$$

for the TM modes, and

$$\left[\frac{d^2}{dz^2}+\left(\frac{\omega^2}{c^2}-k^2\right)\right]\delta a=\frac{\omega_b^2}{c^2}\frac{b^2-a^2}{b\ln(b/a)}\left\langle\frac{v_r}{r|v_z|}\cos\alpha\right\rangle,\qquad(34)$$

$$2k^{1/2}\frac{d}{dz}(k^{1/2}\delta a)=-\frac{\omega_b^2}{c^2}\frac{b^2-a^2}{b\ln(b/a)}\left\langle\frac{v_r}{r|v_z|}\sin\alpha\right\rangle,\qquad(35)$$

for the TEM mode. In Eqs. (30)–(33), $\delta a_{lm}\equiv e\,\delta A_{lm}/m_e c^2$ is the normalized amplitude of the modes, and we have defined the TE/TM mode coupling coefficients as

$$H_{lm}\equiv\begin{cases}\dfrac{2\kappa_{lm}^2(b^2-a^2)}{(\kappa_{lm}^2b^2-l^2)Z_l^2(\kappa_{lm}b)-(\kappa_{lm}^2a^2-l^2)Z_l^2(\kappa_{lm}a)};\\ \quad\text{TE modes,}\\[2mm]\dfrac{2\kappa_{lm}^2(b^2-a^2)}{\kappa_{lm}^2b^2Z_l'^2(\kappa_{lm}b)-\kappa_{lm}^2a^2Z_l'^2(\kappa_{lm}a)};\quad\text{TM modes.}\end{cases}$$

$$(36)$$

The electron beam is assumed to be monoenergetic with an axial energy spread determined by an initial (i.e., at $z=0$) pitch angle spread, and the averaging operator is defined over the initial beam parameters,

$$\langle(\cdots)\rangle\equiv\frac{A}{4\pi A_g}\int_0^{2\pi}d\phi_0\int_0^{p_0}dp_{z0}\beta_{z0}$$

$$\times\exp[-(p_{z0}-p_0)^2/\Delta p_z^2]$$

$$\times\iint_{A_g}dx_0\,dy_0\sigma_\perp(x_0,y_0)$$

$$\times\int_{-\pi}^{\pi}d\psi_0\sigma_\parallel(\psi_0)(\cdots),\qquad(37)$$

where $A_g\equiv\pi(b^2-a^2)$ is the cross-sectional area of the waveguide, $\beta_{z0}\equiv v_{z0}/c$ for the initial axial velocity v_{z0}, $\phi_0\equiv\tan^{-1}(p_{y0}/p_{x0})$, (p_{x0},p_{y0},p_{z0}) denote the initial beam momenta, p_0 and Δp_z denote the initial total momentum of the beam and the initial axial momentum spread, respectively, $\psi_0(\equiv-\omega t_0$, where t_0 is the time at which the particle crosses the $z=0$ plane) is the initial ponderomotive phase, $\sigma_\perp$ and $\sigma_\parallel$ are the initial distributions of the beam in cross section and phase, and

$$A\equiv\left[\pi\int_0^{p_0}dp_{z0}\exp\left(\frac{-(p_{z0}-p_0)^2}{\Delta p_z^2}\right)\right]^{-1},\qquad(38)$$

is a normalization constant. This results in an axial energy spread given by

$$\frac{\Delta\gamma_z}{\gamma_0}=1-\frac{1}{\sqrt{1+2(\gamma_0^2-1)(\Delta p_z/p_0)}}.\qquad(39)$$

The equations for the fields must be solved simultaneously with the orbit equations for an ensemble of electrons. Since this is an amplifier formulation, we integrate the complete three-dimensional Lorentz force equations,

$$v_z\frac{d}{dz}\mathbf{p}=-e\,\delta\mathbf{E}-\frac{e}{c}\mathbf{v}\times(\mathbf{B}_{ext}+\delta\mathbf{B}),\qquad(40)$$

for each electron, where $\mathbf{B}_{ext}$ is the magnetostatic field due to the CHI wiggler, and $\delta\mathbf{E}$ and $\delta\mathbf{B}$ denote the aggregate electromagnetic fields for all the wave modes,

$$\delta\mathbf{E}=-\frac{1}{c}\sum_{\text{all modes}}\frac{\partial}{\partial t}\delta\mathbf{A}_{lm},\qquad(41)$$

and

$$\delta\mathbf{B}=\sum_{\text{all modes}}\nabla\times\delta\mathbf{A}_{lm}.\qquad(42)$$

Further, the electron coordinates obey the equations

$$v_z \frac{d}{dz} r = v_r,$$ (43)

$$v_z \frac{d}{dz} \theta = \frac{1}{r} v_\theta,$$ (44)

and

$$v_z \frac{d}{dz} \psi = k + k_w - \frac{\omega}{v_z},$$ (45)

for the ponderomotive phase.

By specifying the initial beam conditions to the entrance of the wiggler and integrating the complete Lorentz force equations, we obtain the advantage of modeling the injection of the beam into the wiggler. This describes any increase in the effective beam emittance due to the injection mechanism in a self-consistent way. For this purpose, we model the adiabatic injection region by means of a tapered wiggler amplitude. In addition, we also consider amplitude tapering for the purpose of efficiency enhancement. In order to describe these effects within the CHI wiggler model in Eqs. (15) and (16) we assume that the overall coefficient of the periodic component of the magnetostatic field varies as

$$B_w = \begin{cases} 2B_0 \sin^2\left(\frac{k_w z}{4N_w}\right); & z < N_w \lambda_w, \\ 2B_0; & N_w \lambda_w < z < z_0, \\ 2B_0[1 + k_w \epsilon_w (z - z_0)]; & z > z_0, \end{cases}$$ (46)

where N_w denotes the number of wiggler periods in the entry taper region, and ϵ_w is the normalized slope of the taper for purposes of efficiency enhancement.

IV. NUMERICAL ANALYSIS

The dynamical equations for the particles and fields are solved for an amplifier configuration in which several modes may propagate at a fixed frequency ω. The numerical treatment involves the solution of $6N_T + 4N_M$ ordinary differential equations (where N_T is the total number of electrons and N_M is the total number of modes) as an initial value problem, and we use a Runge–Kutta–Gill algorithm for this purpose. The particle average is accomplished by the Nth-order Gaussian quadrature in each of the initial variables. This results in the use of 1000 particles in the absence of an initial axial energy spread, and 9600 particles when the axial energy spread is nonzero.

The initial conditions on the fields are chosen to model the injection of an arbitrary power level for each mode. We note here that the time-averaged Poynting flux in GW for each mode is given in terms of the mode amplitudes and wave numbers as

$$P \cong \begin{cases} 0.69 \frac{\omega k_{lm}}{c H_{lm}} A_\ell \, \delta a_{lm}^2; & \text{TE modes,} \\ 0.69 \frac{\omega k_{lm}}{c H_{lm}} A_\ell \left(1 + \frac{\kappa_{lm}^2}{k_{lm}^2}\right) \delta a_{lm}^2; & \text{TM modes,} \\ 2.18 \frac{\omega k b^2}{c^2} \delta a \ln\left(\frac{b}{a}\right); & \text{TEM mode.} \end{cases}$$ (47)

The initial wave numbers are chosen by the vacuum state, and the growth rates are initially zero, since the amplitude of the periodic component of the CHI wiggler is also initially zero. The initial state of the electron beam is chosen to model the injection of a continuous, axisymmetric beam with a uniform density and annular cross section, so that $\sigma_\parallel = 1$ for $-\pi < \psi_0 < \pi$ and $\sigma_\perp = 1$ for $R_{min} < r < R_{max}$.

For convenience, we also choose the inner and outer radii of the CHI wiggler to coincide with those of the waveguide; hence, $R_{in} = a$ and $R_{out} = b$. While we shall be concerned with the fundamental resonance [i.e., $\omega \approx (k + k_w) v_\parallel$] in this paper, both the first and third spatial harmonics of the CHI wiggler are included in the analysis. The third harmonic interaction will be treated separately in a future work.

A. K_u-band operation

The first case we consider deals with a 200 kV/100 A electron beam with inner and outer radii of $R_{min} = 1.9$ cm and $R_{max} = 2.3$ cm propagating through a coaxial waveguide, with $a = 1.4$ cm and $b = 2.8$ cm. The CHI wiggler is characterized by a solenoidal field of $B_0 = 1.6$ kG, a period $\lambda_w = 2.54$ cm, and an overall length of 35 wiggler periods with a five period entry taper region. This gives a wiggler field at the center of the gap of approximately 800 G, which, in turn, results in an average axial velocity of $\beta_z \approx 0.685$. For these parameters, $\omega_b/ck_w \approx 0.057$, which corresponds to a beam plasma frequency of approximately 0.68 GHz. As will be discussed, this is much lower than either the resonant frequency or bandwidth of the interaction, and we are fully justified in the neglect of the collective space-charge modes in the analysis.

The TE_{01} mode for this waveguide is resonant in the K_u band with frequencies in the range of 15–19 GHz. In all cases, we shall assume that the drive power is 1 kW. The variation in the TE_{01} mode gain as a function of frequency is shown in Fig. 4 for the case of an ideal beam with $\Delta\gamma_z = 0$. It is evident from the figure that the gain is relatively constant at approximately 30 dB from 13–17 GHz, and falls off rapidly at the edges of the band. We now examine the variation in the gain at the center of this band (i.e., at 15 GHz) in more detail.

The evolution of the power as a function of axial distance is shown in Fig. 5 for the case of the ideal beam. The power is seen in the figure to remain relatively constant over the initial ten wiggler periods, which includes the entry taper region, and to grow exponentially thereafter. A rapid oscillation is also found to occur with a period of $\lambda_w/2$, which corresponds to the lower beat wave interaction. Such an oscillation has also been found to occur in planar wiggler FEL's.[10] An output power of approximately
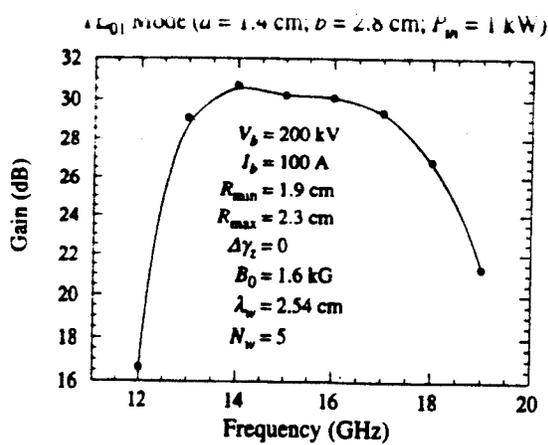
Phys. Plasmas, Vol. 1, No. 4, April 1994

Freund et al.   1051

TE$_{01}$ Mode ($a = 1.4$ cm; $b = 2.8$ cm; $P_{in} = 1$ kW)

FIG. 4. Plot of the gain as a function of frequency over a fixed length of 35 wiggler periods.

FIG. 6. Evolution of the average axial velocity of the beam.

1.05 MW is reached at the end of the interaction region for an overall efficiency of 5.3%, but saturation is not found and more power can still be extracted with a longer wiggler.

The variation in the average beam velocity over the interaction length is shown in Figs. 6–8. The evolution of the average axial velocity is shown in Fig. 6. The injection of the beam is clearly indicated by the initial decrease of the axial beam velocity over the first five wiggler periods, which corresponds to the increasing transverse components of the velocity due to the wiggler. The average velocity remains relatively constant thereafter until $z \approx 25\lambda_w$, after which the rapid decrease in the axial velocity is due to the extraction of energy from the beam. The bulk of the transverse motion due to the wiggler is in the azimuthal motion of the beam, which is shown in Fig. 7. Again, the "spin-up" of the beam in the entry taper region is clearly shown along with the primary oscillation at the wiggler period. The RMS component of the azimuthal velocity of approximately $\langle v_\theta \rangle / c \approx 0.1$. The average radial velocity is shown in Fig. 8, and is seen to be substantially smaller than the azimuthal component.

Figures 6–8 for the evolution of the average beam velocity show existence of velocity components at higher harmonics of the wiggler period. This is shown more clearly by taking fast Fourier transforms of the average velocity components. The Fourier transform of the average axial velocity is shown in Fig. 9 and indicates the existence of a second harmonic component, which is some 50 dB below the amplitude of the average velocity. This second harmonic component is due to the fact that, as in the case of planar wigglers, the magnitude of the transverse velocity is not constant. The Fourier transform of the azimuthal velocity is shown in Fig. 10, and the predominant oscillation is clearly at the fundamental wiggler period. However, smaller oscillatory components are also seen at the second harmonic and at the subharmonic, although these components are about 35 dB lower than the bulk wiggler oscillation. Similar behavior is seen for the average radial velocity, as shown in Fig. 11. In the case of the average radial velocity, however, the subharmonic is relatively larger than for the average azimuthal velocity.

As in the case of more conventional FEL designs, the interaction efficiency is very sensitive to the axial energy spread of the beam.[9] Observing that the resonance condition is $\omega \approx (k + k_w)v_z$, thermal effects become important when $\Delta v_z/v_z \approx \text{Im } k/(\text{Re } k + k_w)$. In the present case, $\langle \text{Im } k \rangle / k_w \approx 0.015$ and $\langle \text{Re } k \rangle / k_w \approx 0.88$; hence, we expect that thermal effects will be important when $\Delta v_z/v_z$
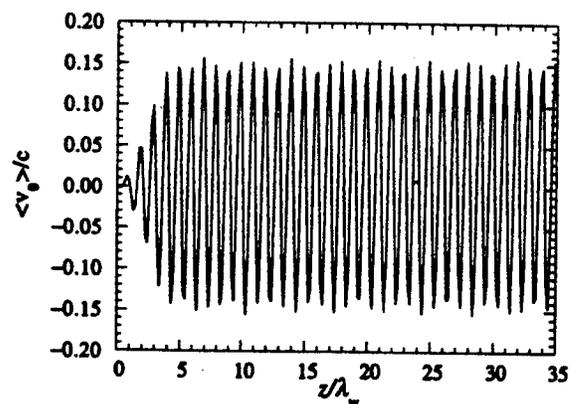
TE$_{01}$ Mode ($a = 1.4$ cm; $b = 2.8$ cm; $f = 15$ GHz)

FIG. 5. Evolution of the power as a function of axial distance for an ideal beam.

FIG. 7. Evolution of the average azimuthal velocity of the beam.

Freund et al.

FIG. 8. Evolution of the average radial velocity of the beam.

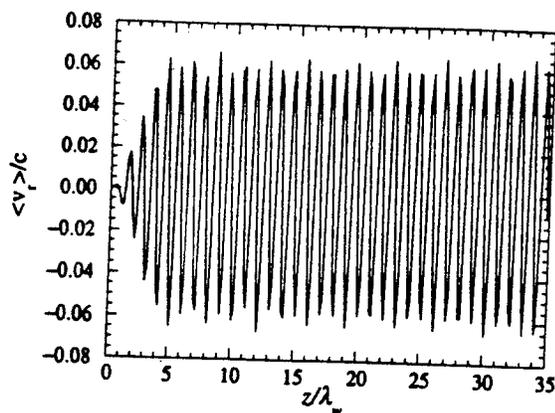FIG. 10. Fast Fourier transform of the average azimuthal velocity.

$\approx 0.80\%$ and $\Delta\gamma_z/\gamma_0\approx 0.74\%$. The variation in the output power as a function of the initial axial energy spread is shown in Fig. 12. It is evident in the figure that there is a rapid decrease in the output power as the axial energy spread increases from zero. This decrease remains relatively linear until thermal effects become important, after which the power decreases somewhat less rapidly. Overall, however, the output power decreases by more than an order of magnitude as the initial axial energy spread increases to 1.5%.

We now turn to the study of efficiency enhancement with a tapered field. Note that with a drive power of 1 kW and a configuration of 35 wiggler periods in length with a five wiggler period entry taper this system did not reach saturation at 15 GHz. Allowing for an arbitrary length, we find that saturation in the case of an ideal beam with $\Delta\gamma_z=0$ occurs at $z/\lambda_w\approx 40$ at a power level of 1.8 MW, which corresponds to an efficiency of $\eta\approx 9.0\%$. This saturation efficiency can be enhanced by tapering of the amplitudes of the bulk axial component of the CHI wiggler, or the amplitude and/or period of the periodic components of the CHI wiggler. This can be accomplished by tapering the solenoidal field or varying the thickness and width of the spacers. Of course, the specific design of the tapered components in any given system can result in a field tapering in which the amplitude of the bulk axial field as well as the amplitude and period of the periodic component of the

CHI wiggler vary in complicated ways. The description of any specific tapered configuration, therefore, requires the detailed description of each of these components. For simplicity, however, we shall assume that the solenoid and spacer dimensions are chosen in such a way that only the amplitude of the periodic component of the CHI wiggler varies, as given in Eq. (46).

The basic physical mechanism underlying the tapered–wiggler interaction depends upon the fact that the electrons decelerate in the axial direction as they lose energy to the wave. If the wiggler is tapered, it is possible to reaccelerate the electrons and so prolong the resonant interaction and extract more energy from the beam. The specific performance of a tapered wiggler configuration, however, depends upon numerous considerations. For example, the start-taper point must be chosen to correspond to the position at which the bulk of the beam becomes trapped in the ponderomotive well. A choice of the start-taper point that is either too early or too late results in a degraded performance. In addition, the slope of the taper must be chosen properly to counter the rate of deceleration of the beam. Finally, the magnitude of the efficiency enhancement depends upon the magnitude of the wiggler-induced transverse velocity.

As shown in Fig. 6, the average axial electron velocity begins to decrease rapidly for $z/\lambda_w\approx 25$, which corre-
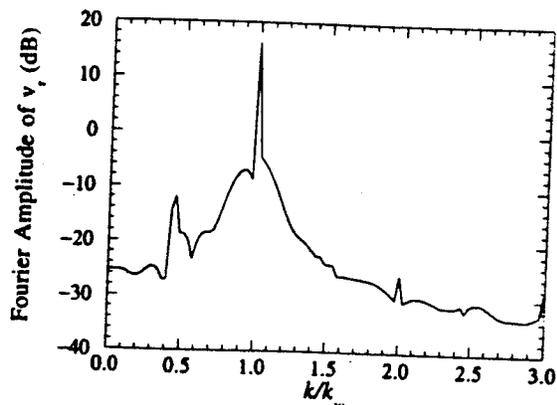

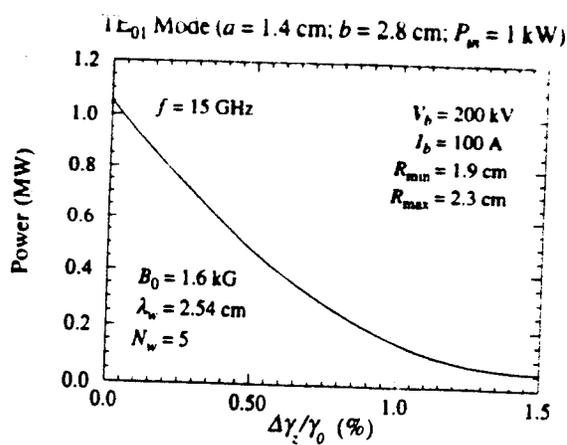FIG. 9. Fast Fourier transform of the average axial velocity.

FIG. 11. Fourier transform of the average radial velocity.

Phys. Plasmas, Vol. 1, No. 4, April 1994

Freund et al.   1053

FIG. 12. Variation in the output power as a function of the initial axial energy spread of the beam.

FIG. 14. Gains for the TE_{11}, TE_{21}, TE_{31}, and TE_{41} modes for the same beam, wiggler, and waveguide parameters as shown for the TE_{01} mode in Fig. 4.

sponds to the trapping of the beam in the ponderomotive potential, and we find that the optimal start-taper point for the TE_{01} mode interaction discussed above occurs for a start-taper point of $z_0/\lambda_w \approx 13$. Similarly, the optimal slope of the taper is found to be $\epsilon_w \approx -0.002$. A comparison of the evolution of the power with axial position for these tapered-wiggler parameters and for the uniform wiggler is shown in Fig. 13 for the case in which the wiggler amplitude is tapered to zero. The maximum efficiency found with the tapered wiggler in this case is $\eta \approx 10.3\%$. This corresponds to a $\Delta\eta \approx 1.3\%$ due to the tapered wiggler.

The reason for this relatively small efficiency enhancement is that the wiggler-induced transverse velocity is also small. The bulk transverse velocity for the CHI wiggler is directed in the azimuthal direction, and, as shown in Fig. 7, $\langle v_\theta \rangle_{RMS}/c \approx 0.1$. However, the efficiency enhancement predicted from an idealized one-dimensional model of the tapered-wiggler interaction is given by[9]

$$\Delta\eta \approx -\gamma_\parallel^2 \frac{v_\perp^2 {}_{,RMS}}{c^2} \frac{\Delta B_w}{B_w}. \qquad (48)$$

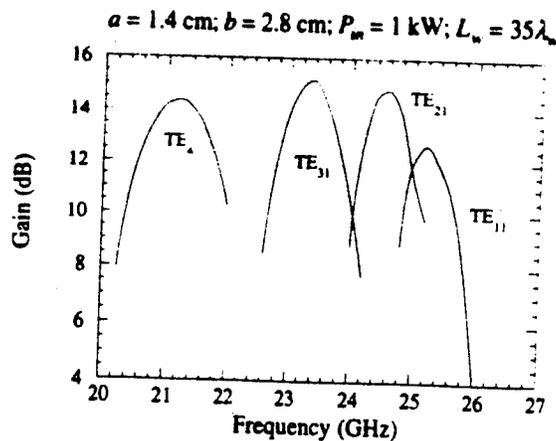FIG. 13. Evolution of the power for both uniform and tapered-wiggler configurations.

The maximum tapered-wiggler extraction efficiency is found for $\Delta B_w/B_w = -1$ and is $\Delta\eta_{max} \approx \gamma_\parallel^2 v_\perp^2 {}_{,RMS}/c^2$. For this specific example (see Fig. 6), $\langle v_z \rangle/c \approx 0.69$; hence $\gamma_\parallel^2 \approx 1.9$ and $\Delta\eta_{max} \approx 1.9\%$. This is in reasonable agreement with the simulation.

The TE_{01} mode is the dominant mode for the CHI wiggler interaction because it is polarized in the azimuthal direction, which corresponds to the predominant direction of the wiggler-induced transverse motion. However, the resonance condition can be satisfied for other modes as well. Of these, the TEM mode has a resonance at a frequency of approximately 26 GHz for these beam and wiggler parameters. However, the TEM mode couples to the radial component of the velocity, and, as indicated in Fig. 8, $\langle v_r \rangle_{RMS}/c \approx 0.04$, which is much less than the azimuthal velocity. Hence, the gain found in simulation for the TEM mode is negligible. The TM modes are also polarized predominantly in the radial direction, and these modes are also found to have negligible gain for these beam, wiggler, and waveguide parameters. However, the TE modes can result in gain at other frequencies.

We restrict the discussion to the high-frequency upper intersections between the TE mode dispersion curves and the beam resonance line. For the specific choice of parameters used to study the TE_{01} mode, there are four other TE modes that can interact resonantly with the beam. These are the TE_{11} mode, which has an intersection with the beam resonance line at a frequency of approximately 25.4 GHz, the TE_{21} mode at a frequency of approximately 24.8 GHz, the TE_{31} mode at a frequency of about 23.5 GHz, and the TE_{41} mode at a frequency of about 21.6 GHz. It should be remarked at this point that our single-mode analysis of the TE_{01} mode is valid, since the resonant frequencies for these modes are much higher that the 13–18 GHz found for the TE_{01} mode.

A summary of the variation of the gains of these modes with frequency is shown in Fig. 14, corresponding to the same beam, wiggler, and waveguide parameters used in Fig. 4. It is evident from the figure that the gain for each of these modes is in the neighborhood of 12–15 dB which is
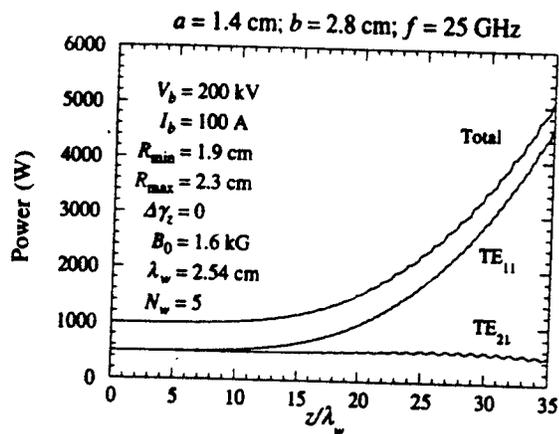
Freund *et al.*

FIG. 15. Evolution of the power for a multimode TE_{11}/TE_{21} case.

FIG. 17. Evolution of the power with axial position at 35 GHz.

much less than the 30 dB found for the TE_{01} mode. The reason for this is that while the TE_{01} mode is polarized entirely in the azimuthal direction, the TE_{1n} modes have a component in the radial direction and thus couple less strongly to the beam for a given set of wiggle parameters. Note that each mode was considered individually in the analysis in Fig. 14. However, there is some overlap between the TE_{11} and TE_{21} modes at approximately 25 GHz and between the TE_{21} and TE_{31} modes at approximately 24 GHz. In these frequency regions, therefore, a multimode analysis is required.

In order to examine the issue of multimode operation, we now consider the growth of the TE_{11} and TE_{21} modes at 25 GHz and the TE_{21} and TE_{31} modes at 24 GHz. The beam, wiggler, and waveguide parameters are the same as used previously, but we now initialize each mode at 500 W rather than the 1 kW used for the single-mode analyses. The results for the TE_{11} and TE_{21} modes at 25 GHz are shown in Fig. 15, and indicate that the TE_{11} mode suppresses the growth of the TE_{21} mode. A similar suppression of the higher-order mode is seen in Fig. 16 for the TE_{21} and TE_{31} modes at 24 GHz.
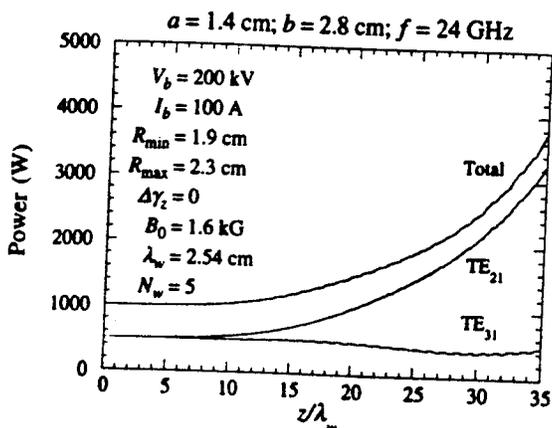

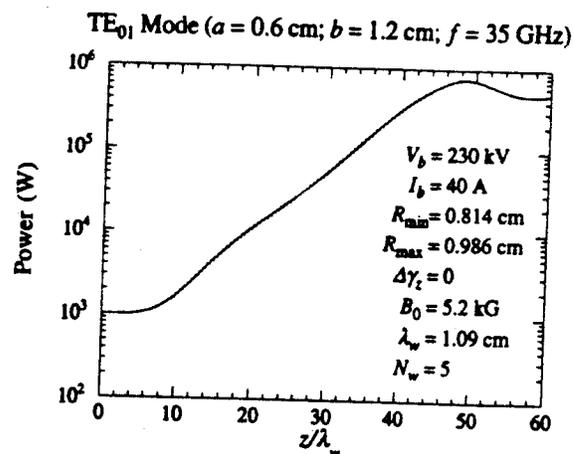FIG. 16. Evolution of the power for a multimode TE_{21}/TE_{31} case.

B. K_a-band operation

The second case we consider is that of operation in the K_a band. The electron beam parameters in this case are assumed to have an energy of 230 keV, a current of 40 A, and inner and outer radii of 0.814 and 0.986 cm, respectively. The CHI wiggler is characterized by a solenoidal field of 5.2 kG, a period of 1.09 cm, and an entry taper of five wiggler periods in length. The gain band is extremely broad and amplification is found for operation in the TE_{01} mode over the frequency range from 28 through 46 GHz with inner and outer radii of 0.6 and 1.2 cm, respectively. Further, we shall assume an input power level of 1 kW in all subsequent simulations.

The evolution of the power as a function of axial position is shown in Fig. 17 for the case of an ideal beam (i.e., $\Delta\gamma_z=0$) and operation at 35 GHz with an input power of 1 kW. As shown in the figure, saturation occurs at a power level of approximately 768 kW for an efficiency of 8.35%. The saturation point occurs at $z/\lambda_w\approx47.6$; hence, the average gain over the uniform wiggler region is approximately 0.62 dB/cm.

The 35 GHz example is near the center of the gain band and is close to the peak efficiency. The maximum efficiency (at varying axial distances) is plotted as a function of frequency in Fig. 18. As shown in the figure, amplification is found for frequencies ranging from 28 through 47 GHz, with the maximum efficiency of approximately 9.4% found at 33 GHz. This does not, however, correspond to the peak gain. The variation in the gain with frequency is illustrated in Fig. 19. Two peaks are clearly evident, corresponding to the high- and low-frequency intersections between the TE_{01} mode dispersion curve and the beam resonance line. The low-(high-) frequency maximum occurs at 30 GHz (43 GHz) with a gain of approximately 0.82 dB/cm (0.71 dB/cm). Clearly, this represents an extremely broadband interaction.

The sensitivity of the interaction to the axial energy spread is shown in Fig. 20 at a frequency of 35 GHz. It is clear from the figure that the efficiency decreases from the peak of 8.57% to approximately 2.84% for an axial energy spread of 1.0%. While this may seem to be a steep decline,
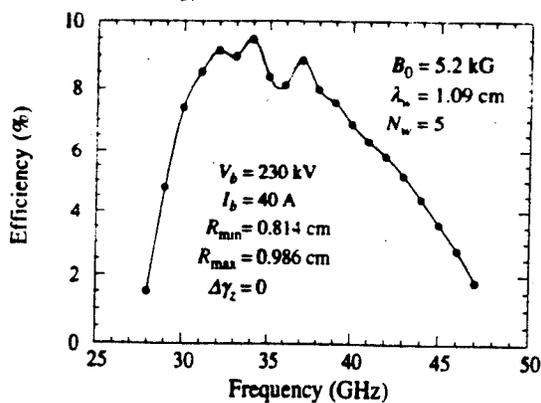
FIG. 18. Variation in the efficiency with frequency.

FIG. 20. Variation in the efficiency with an axial energy spread.

it should be recognized that designs of electron guns that produce axial energy spreads of less than 0.5% are fairly standard at these voltages and has been achieved in several experiments to date.[11-13] Therefore, the peak efficiencies predicted in simulation should be achievable in the laboratory.

We now turn to the question of efficiency enhancement with a tapered field. As discussed previously, the efficiency enhancement is sensitive to both the slope of the taper and to the start-taper point. In particular, the start-taper point must be chosen to correspond to a point after which the beam has become trapped in the ponderomotive potential but before the beam has had a chance to execute one-half of its oscillation within the potential well. This corresponds to a point before saturation is reached. In order to determine the optimal start-taper point, therefore, we consider the variation in the average axial velocity of the beam with axial position. This is shown in Fig. 21 for the case of the uniform wiggler interaction at 35 GHz. The figure illustrates the decrease in the axial velocity over the injection process during the first five periods of the entry taper region, as well as the decrease in the axial velocity after the beam becomes trapped at $z/\lambda_w \approx 30$. It is clear from the figure that saturation is found for $z/\lambda_w \approx 47$; hence the
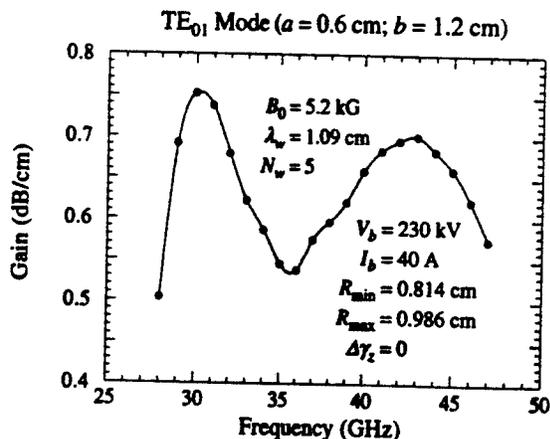
start-taper point must be chosen within the range $30 < z/\lambda_w < 47$. Note that the oscillations in the average axial velocity for $z/\lambda_w > 40$ correspond to the oscillations of the beam in the ponderomotive well. A more precise determination of the optimal start-taper point must be determined by simulations with a tapered wiggler.

We now consider operation at 35 GHz and assume that we have an ideal beam with a vanishing axial energy spread. The optimal start-taper point for this case is found to be $z/\lambda_w \approx 42.2$, and the optimum slope is $\epsilon_w \approx -0.0005$. The evolution of the power for this tapered wiggler field is shown in Fig. 22 along with the result for the untapered wiggler for comparison. As shown in the figure, the output power can be substantially enhanced for this example with a tapered wiggler, and the maximum output power rises to approximately 1.41 MW at $z/\lambda_w \approx 235$. This corresponds to a maximum efficiency of 15.3%. Thus, in contrast to the K_u band example, the higher wiggler field used in this case permits a larger efficiency enhancement.

As illustrated in Figs. 18 and 19, the uniform–wiggler interaction has an extremely broad bandwidth. In contrast, it is generally believed that the bandwidth for a tapered–wiggler interaction must be narrow, due to the sensitivity of the efficiency enhancement to the start-taper point and the slope of the taper. While this belief may hold in specific
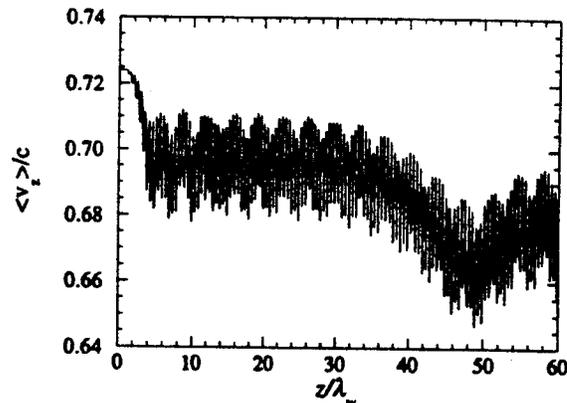

FIG. 19. Variation in the gain with frequency.

FIG. 21. Evolution of the average axial velocity of the beam.

Freund *et al.*

TE$_{01}$ Mode ($a = 0.6$ cm; $b = 1.2$ cm; $f = 35$ GHz)

$\varepsilon_w = -.0005$
$z_0/\lambda_w = 42$

$V_b = 230$ kV
$I_b = 40$ A
$R_{min} = 0.814$ cm
$R_{max} = 0.986$ cm
$\Delta\gamma_z = 0$
$B_0 = 5.2$ kG
$\lambda_w = 1.09$ cm
$N_w = 5$
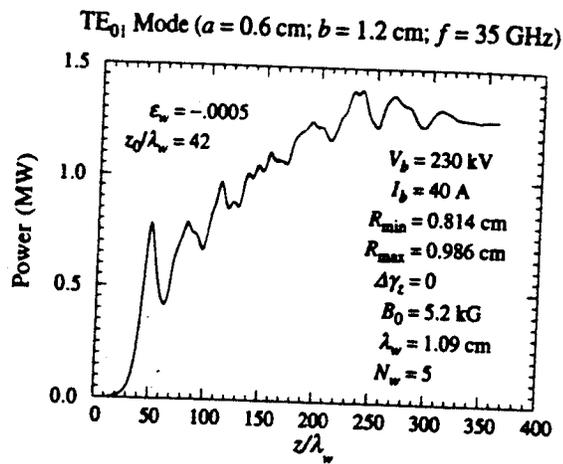
FIG. 22. Evolution of the power for a tapered wiggler.

TE$_{01}$ Mode ($a = 0.6$ cm; $b = 1.2$ cm; $P_{in} = 1$kW)

$\varepsilon_w = -.0005$
$z_0/\lambda_w = 42$
$z_{max}/\lambda_w = 235$

$V_b = 230$ kV
$I_b = 40$ A
$R_{min} = 0.814$ cm
$R_{max} = 0.986$ cm
$\Delta\gamma_z = 0$
$B_0 = 5.2$ kG
$\lambda_w = 1.09$ cm
$N_w = 5$
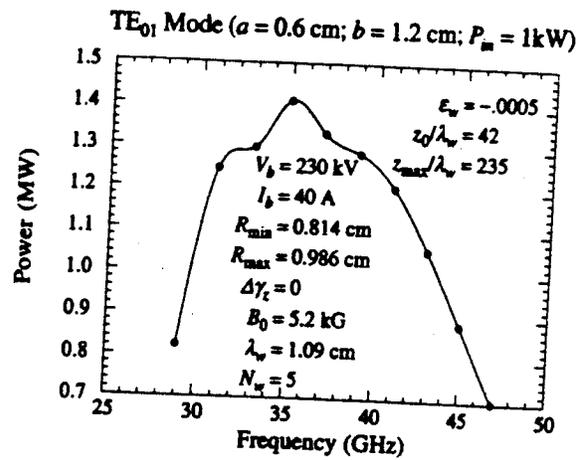
FIG. 23. Variation in the output power versus frequency for a tapered wiggler.

cases, it is not generally valid. Indeed, the tapered–wiggler interaction can exhibit a broad bandwidth. In order to illustrate this, we take the optimized tapered–wiggler interaction at 35 GHz, as shown in Fig. 22 as a starting point, and consider a tapered–wiggler amplifier with the same parameters and a length of $z/\lambda_w = 235$ (corresponding to the peak in the output power at 35 GHz). The essential purpose here is to consider a tapered–wiggler amplifier optimized for operation at 35 GHz, and to study the variation in the output power as the drive frequency is varied.

The variation in the output power with frequency for this example is shown in Fig. 23. It is clear from this figure that the bandwidth of the tapered–wiggler interaction for this example is comparable to the uniform-wiggler case. The power over this entire band varies between approximately 750 kW–1.4 MW. However, if the band is restricted slightly to between 31–41 GHz, then the output power varies over a much smaller range of from 1.2–1.4 MW. Thus, we conclude that using a tapered wiggler in this device will not compromise the bandwidth.

C. W-band operation

The third case under consideration is operation in the W band at frequencies between approximately 80 and 100 GHz. For this purpose, we assume the electron beam is characterized by an energy of 500 keV, a current of 50 A, and inner and outer radii of 0.4 and 0.5 cm, respectively. The CHI wiggler has $B_0 = 6.0$ kG and has a period of 0.9 cm with a five wiggler period entry taper and inner and outer radii of 0.311 and 0.622 cm, respectively. It should be remarked here that this produces a periodic wiggler field of approximately 3 kG at the center of the gap. While this constitutes a high-amplitude wiggler field, it should be noted that simulations with the Poisson code indicate that wiggler fields as high as 3.5 kG at the center of the gap are possible using standard low carbon steel. Hence, this represents a conservative choice for the wiggler field, which has been made to ensure that no beam intercepts the waveguide walls.

The mode of interest here is again the TE$_{01}$ mode, and we assume the drive power is 1 kW. Wave amplification is

found over a frequency band of from approximately 70 through 115 GHz, although the peak efficiencies are found in the W band from 80–100 GHz. This is illustrated in Fig. 24, in which we plot the variation in the saturation efficiency (over a variable interaction length) with frequency for an ideal beam with $\Delta\gamma_z = 0$. As is evident in the figure, the maximum efficiency for this choice of parameters is approximately 10.3% at a frequency of 85 GHz for an output power of almost 2.6 MW. However, the efficiency varies relatively little over the entire W band and the interaction exhibits a bandwidth of about 33%.

We now focus on the interaction at the peak efficiency at 85 GHz. The evolution of the power with axial distance in this case is shown in Fig. 25, and exponential growth is evident, starting at the end of the entry taper region and extending out to the saturation point at $z/\lambda_w \approx 56$. Note that this gives a total interaction length of only 50 cm. The decline in the efficiency with increases in the initial axial energy spread of the beam is much less severe in this case than in the two preceding examples due to the relatively larger wiggler strength. A plot of the decline in the interaction efficiency with increases in the axial energy spread is shown in Fig. 26. As shown in the figure, the efficiency
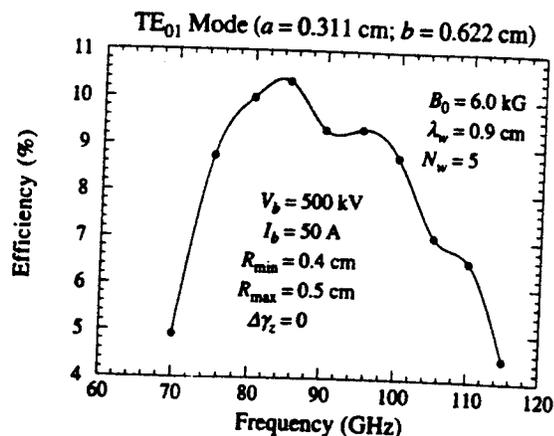
TE$_{01}$ Mode ($a = 0.311$ cm; $b = 0.622$ cm)

$B_0 = 6.0$ kG
$\lambda_w = 0.9$ cm
$N_w = 5$

$V_b = 500$ kV
$I_b = 50$ A
$R_{min} = 0.4$ cm
$R_{max} = 0.5$ cm
$\Delta\gamma_z = 0$

FIG. 24. Variation of the efficiency with frequency in the W band.
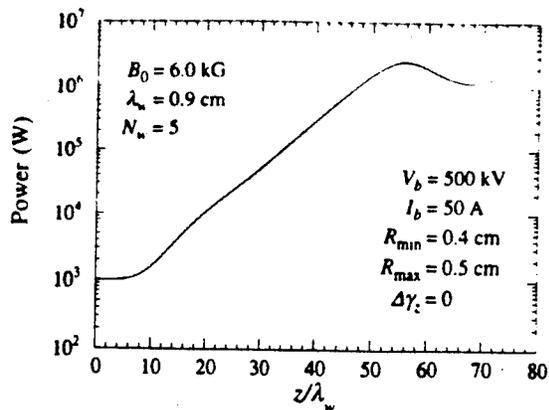
FIG. 25. Evolution of the power with axial position at 80 GHz.

FIG. 27. Evolution of the power with axial distance for an optimized taper at 85 GHz.

decreases by less than a factor of 2 as the axial energy spread increases to somewhat beyond $\Delta\gamma_z/\gamma_0 \approx 1.25\%$. Thus, good operational efficiencies are expected for axial energy spreads less than approximately 0.5%.

We now turn to the case of a tapered wiggler. As mentioned above, the performance of a tapered wiggler amplifier is sensitive to both the start-taper point and the slope of the taper. Optimization of the interaction efficiency for the case of operation at 80 GHz indicates that peak efficiency is found for a start-taper point at $z_0/\lambda_w \approx 52$ and a slope of $\epsilon_w \approx -0.003$. A plot of the evolution of the power with axial distance for this case is shown in Fig. 27. For this choice of parameters, it is evident that the output power peaks at approximately 4.2 MW over a total length of 88 wiggler periods. This translates into a total wiggler length of only 79 cm, including the five wiggler period entry taper region.

The variation in the output power as a function of frequency over the W band is shown in Fig. 28. The choice of parameters here is made to optimize the device for operation at 80 GHz. Hence, we have chosen a start-taper point of $z_0/\lambda_w = 52$, a slope of $\epsilon_w = -0.003$, and a total length of 88 wiggler periods. As shown in the figure, the
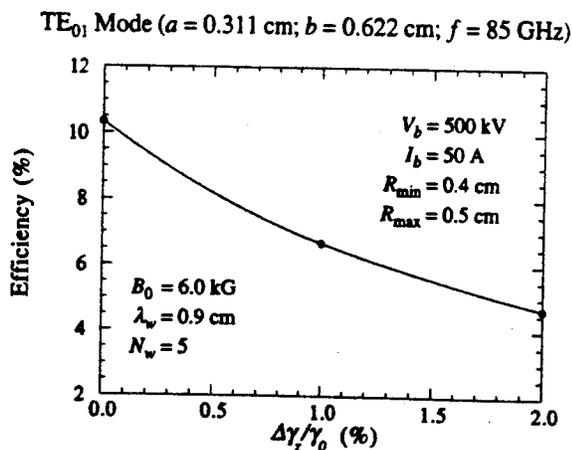
curve of the efficiency versus frequency is double peaked. The larger peak is, as might be expected, at 85 GHz and the secondary peak is at the upper end of the W band at 95 GHz, representing an output power of about 3.5 MW. Hence, we conclude that it is possible to design a W-band MW amplifier using the CHI wiggler.

V. SUMMARY AND DISCUSSION

In this paper, we have presented a complete analytical description of a FEL amplifier based upon the CHI wiggler. The nonlinear analysis makes use of an analytical representation for the CHI wiggler derived in Sec. II, which is, despite certain idealizations made in the interests of achieving an analytic representation, in close agreement with the results of nonlinear magnetics code calculations.[6] The nonlinear FEL simulation represents a slow-time-scale model for the self-consistent evolution of the TE, TM, and TEM modes of a coaxial waveguide along with the trajectories of an ensemble of electrons. It should be emphasized that no wiggler-period-averaging process is applied to
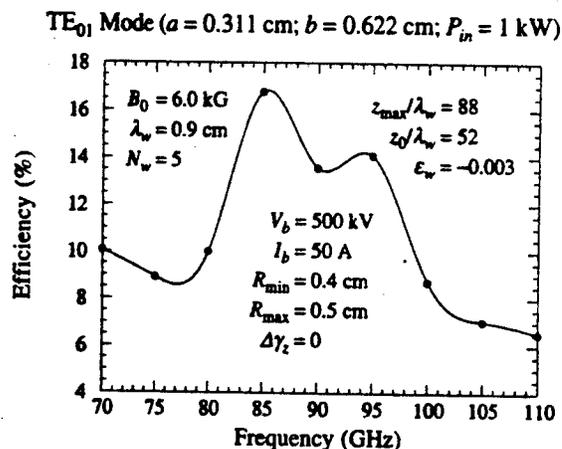

FIG. 26. Variation of the efficiency with axial energy spread at 85 GHz.

TE_{01} Mode ($a = 0.311$ cm; $b = 0.622$ cm; $P_{in} = 1$ kW)

FIG. 28. Variation in the efficiency as a function of frequency in the W band.

smooth the orbital dynamics. Hence, we treat the full particle dynamics and model the injection of the beam into the wiggler.

Three specific examples have been discussed corresponding to amplifier operation in the K_u, K_a, and W bands, with both uniform and tapered wigglers. The simulations have been performed primarily for cases in which the interaction is with the TE_{01} mode of the coaxial waveguide, although multimode operation in the K_u band is also studied. For multimode operation, it was found that the lower-order mode had the effect of suppressing the higher-order mode for each specific case studied. Operation over a wide bandwidth is found to be practical for the CHI wiggler-based FEL's for both the uniform and tapered-wiggler examples.

It is of particular interest to observe that the bandwidth of the interaction for a tapered wiggler is found to be comparable to that of the uniform wiggler. This is in contrast to the commonly accepted belief that the sensitivity of the tapered-wiggler interaction to the start-taper point and the slope of the taper would result in a narrow bandwidth. We note here that this conclusion that the tapered-wiggler interaction does not necessarily sacrifice bandwidth holds for other wiggler designs as well, and is not confined to the CHI wiggler. In support of this, we refer the interested reader to a paper by Levush et al.[14] dealing with the tunability of a tapered-wiggler FEL based upon a planar wiggler.

Our overall conclusion is that the CHI wiggler represents a design in which the limitations of conventional wigglers to reach high field strengths at short wiggler periods are overcome to some degree. The CHI wiggler, therefore, permits the construction of high-frequency FEL amplifiers at relatively low beam voltages. In addition, it should also be noted that the CHI wiggler contains substantial compo-nents at the odd harmonics; principally at the third harmonic. While this harmonic component was included in the simulation studies in this paper, we did not study the third harmonic FEL resonance with the beam. We expect that this will permit still further reductions in the beam voltage requirements for high-frequency operation; however, this issue is now under study.

ACKNOWLEDGMENT

[1] R. M. Phillips, IRE Trans. Electron. Devices 7, 231 (1960).
[2] D. A. G. Deacon, L. R. Elias, J. M. J. Madey, G. J. Ramian, H. A. Schwettmann, and T. I. Smith, Phys. Rev. Lett. 38, 892 (1977).
[3] R. K. Parker, R. H. Jackson, S. H. Gold, H. P. Freund, V. L. Granatstein, P. C. Efthimion, M. Herndon, and A. K. Kinkead, Phys. Rev. Lett. 48, 238 (1982).
[4] M. Billardon, P. Ellaume, J. M. Ortega, C. Bazin, M. Bergher, M. Velghe, and Y. Petroff, Phys. Rev. Lett. 51, 1652 (1983).
[5] R. W. Warren, B. E. Newnam, J. G. Winston, W. E. Stein, L. M. Young, and C. A. Brau, IEEE J. Quantum Electron. QE-19, 391 (1983).
[6] R. H. Jackson, H. P. Freund, D. E. Pershing, and J. M. Taccetti, Nucl. Instrum. Methods A 341, 454 (1994).
[7] A. M. Winslow, J. Comput. Phys. 2, 149 (1967).
[8] H. P. Freund, Nucl. Instrum. Methods A 331, 496 (1993).
[9] H. P. Freund and T. M. Antonsen, Jr., Principles of Free-Electron Lasers (Chapman & Hall, London, 1992), Chap. 5.
[10] H. P. Freund, Phys. Rev. A 37, 3371 (1988).
[11] G. Merdinian, G. Miram, R. Jackson, R. Parker, and D. Pershing, Technical Digest of the IEEE International Electron Devices Meeting, Washington, DC (Institute of Electrical and Electronic Engineers, Piscataway, NJ, 1985), p. 188.
[12] D. A. Kirkpatrick, G. Bekefi, A. C. DiRienzo, H. P. Freund, and A. K. Ganguly, Phys. Fluids B 1, 1511 (1989).
[13] H. Bluem, R. H. Jackson, H. P. Freund, D. E. Pershing, and V. L. Granatstein, Phys. Rev. Lett. 67, 824 (1991).
[14] B. Levush, H. P. Freund, and T. M. Antonsen, Jr., Nucl. Instrum. Methods A 341, 234 (1994).

APPENDIX XIV

A Free-Electron Laser for Cyclotron Resonant Heating in Magnetic Fusion Reactors

H.P. Freund, M.E. Read, R.H. Jackson, D.E. Pershing, and J.M. Taccetti

A FREE-ELECTRON LASER FOR CYCLOTRON RESONANT HEATING IN MAGNETIC FUSION REACTORS

H.P. Freund,[†] M.E. Read
Physical Sciences, Inc., Alexandria, VA 22314

and

R.H. Jackson, D.E. Pershing,[††] and J.M. Taccetti[§]
Naval Research Laboratory, Washington, D.C. 20375

ABSTRACT

A G-band free-electron laser designed for plasma heating is described using a coaxial hybrid iron (CHI) wiggler formed by insertion into a solenoid of a central rod and an outer ring of alternating ferrite and nonferrite spacers positioned so that the central ferrite (nonferrite) spacers are opposite the outer nonferrite (ferrite) spacers. The CHI wiggler provides for enhanced beam focusing and the ability to handle intense beams and high power CW radiation. Simulations indicate that a power/efficiency of 3.5 MW/13% are possible using a 690 kV/40 A beam. No beam loss was found in simulation.

[†]Permanent Address: Science Applications International Corp., McLean, VA 22102.
[††]Permanent Address: Mission Research Corp., Newington, VA 22122.
[§]Permanent Address: University of Maryland, College Park, MD 20742.

Sources of plasma heating for thermonuclear fusion reactors employ both ion and electron cyclotron schemes. Electron cyclotron heating requires approximately 20 MW of CW power at frequencies of 140-280 GHz depending upon whether the fundamental or second harmonic resonance is utilized.[1] No source currently under consideration, or even anticipated, is expected to produce the full power requirement in a single module, and a system composed of several sources is envisioned. In this paper, we describe the design of a G-band (140-150 GHz) free-electron laser (FEL) amplifier based upon a coaxial hybrid iron (CHI) wiggler[2,3] which can meet these requirements.
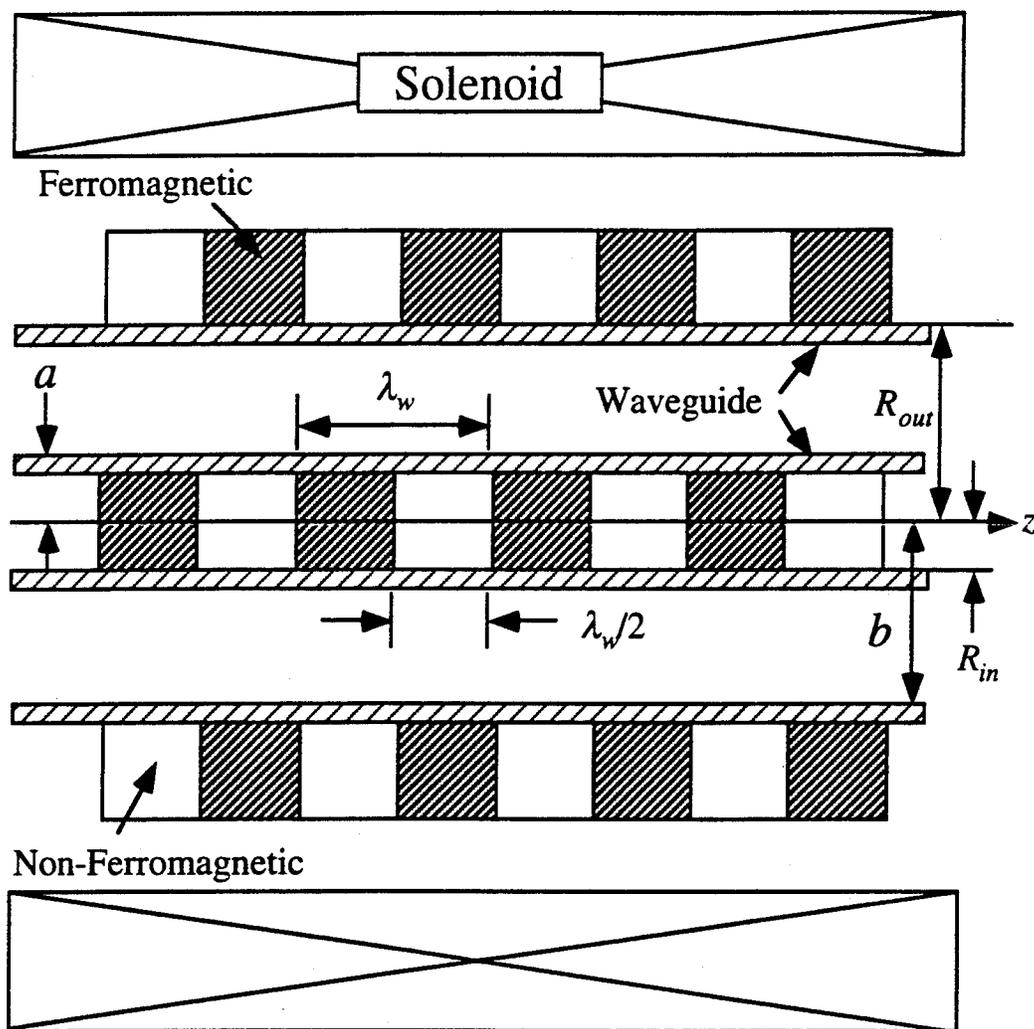

Fig. 1 Schematic illustration of the CHI wiggler configuration.

The CHI wiggler is produced by insertion into a solenoid of a central rod and an outer ring composed of alternating ferromagnetic and non-ferromagnetic (or dielectric) spacers. A schematic representation of the structure is shown in Fig. 1. The position of the spacers is such that the ferrite (nonferrite) spacers on the central rod are opposite the nonferrite (ferrite) spacers on the outer ring. The field is cylindrically symmetric and exhibits minima in the center of the gap providing for enhanced beam focusing.

The CHI wiggler has two major advantages for the application of interest. First, even a small amount of beam loss in a high power CW design can result in catastrophic failure. For example, the average beam power under discussion is ≈ 28 MW, and a beam loss of 1% implies that 28 kW is dissipated in the drift tube walls. This poses a difficult design problem. Hence, the favorable focusing properties of the CHI wiggler are ideally suited to high power CW applications. Indeed, no beam loss was observed in simulation. Second, short wiggler periods are desireable to minimize the required beam energy, while high wiggler fields are required for high gains. This is difficult to achieve in conventional wiggler designs. However, high fields at short wiggler periods can be achieved with the CHI wiggler by using narrow spacers and a ferrite with a high saturation level in a strong solenoid. Hence, a CHI wiggler-based FEL is capable of producing high power at the required wavelengths with a relatively low energy beam.

An analytic form for the CHI wiggler field can be found by solution of Laplace's equation $\nabla^2 \mathbf{B}(r,z) = 0$ for appropriate boundary conditions. The solution is cylindrically symmetric and has the form[2,3]

$$B_z(r,z) = B_0 + B_w \sum_{n=1}^{\infty} \cos(nk_w z) \frac{\left[S_n I_0(nk_w r) - T_n K_0(nk_w r) \right]}{G(nk_w R_{out}, nk_w R_{in})} , \qquad (1)$$

and

$$B_r(r,z) = B_w \sum_{n=1}^{\infty} \sin(nk_w z) \frac{\left[S_n I_1(nk_w r) + T_n K_1(nk_w r) \right]}{G(nk_w R_{out}, nk_w R_{in})} , \qquad (2)$$

where $B_w \equiv 2B_0$, $G(\xi,\zeta) \equiv I_0(\xi)K_0(\zeta) - I_0(\zeta)K_0(\xi)$,

$$S_n \equiv \left(\frac{2}{n\pi} \right) \sin \left(\frac{n\pi}{2} \right) \left[K_0(nk_w R_{in}) + K_0(nk_w R_{out}) \right] , \qquad (3)$$

and

$$T_n \equiv \left(\frac{2}{n\pi}\right) \sin\left(\frac{n\pi}{2}\right) \left[I_0(nk_wR_{in}) + I_0(nk_wR_{out})\right] . \tag{4}$$

This solution is in substantial agreement with the results of the Poisson/Superfish family of magnetics codes.[4]

We consider propagation within a coaxial waveguide with inner and outer radii a and b respectively. Space-charge effects are negligible as long as $\omega_b/ck_w < \gamma_z^3 v_w^2/8\gamma_0 c^2$, where ω_b denotes the beam plasma frequency, v_w is the bulk transverse wiggler velocity, γ_0 is the bulk relativistic factor of the beam, and $\gamma_z = (1 - v_\parallel^2/c^2)^{-1/2}$ for a bulk streaming velocity $v_\parallel$. Space-charge effects can also be neglected if (1) the wavelength is less than the Debye length and the space-charge waves are subject to strong Landau damping, or (2) the bandwidth of the interaction is greater than the plasma frequency. These conditions for the neglect of space-charge effects are valid even for relatively high-current electron beams.[5]

The boundary conditions of the fields at the coaxial waveguide walls (inner radius a and outer radius b) are satisfied by a superposition of the TE, TM, and TEM modes of the waveguide which constitute a complete and orthogonal set of basis vectors. The interaction strength depends both upon the wave-particle resonance and upon the polarization of the moeds. The CHI wiggler induces an oscillation which is predominantly in the aziumthal direction; hence, the modes with the highest gains are those which are largely polarized in that direction. For the present case, the predominant resonance is with an azimuthally polarized TE_{01} mode. The other modes are farther from resonance and have less favorable polarizations. Hence, we limit the discussion here to the case of the TE modes. As such, the vector potential can be expressed in cylindrical coordinates as[3]

$$\delta A(x,t) = \sum_{\substack{l=0 \\ m=1}}^{\infty} \delta A_{lm}(z)\left[\frac{l}{\kappa_{lm}r} Z_l(\kappa_{lm}r)\,\hat{e}_r \sin\alpha_{lm} + Z_l'(\kappa_{lm}r)\,\hat{e}_\theta \cos\alpha_{lm}\right], \tag{5}$$

where the phase for angular frequency ω and wavenumber k_{lm} is

$$\alpha_{lm} \equiv \int_0^z dz' k_{lm}(z') + l\theta - \omega t , \tag{6}$$

where $\omega^2 = c^2 k_{lm}^2 + c^2 \kappa_{lm}^2$ for a given cutoff κ_{lm}. The amplitudes and wavenumbers are assumed to vary slowly in z over a wavelength. The cutoffs are given by solution of the dispersion equation $J_l'(\kappa_{lm}a)Y_l'(\kappa_{lm}b) = J_l'(\kappa_{lm}b)Y_l'(\kappa_{lm}a)$, where J_l and Y_l denote the regular Bessel and Neumann functions, and $Z_l(\kappa_{lm}r) \equiv J_l(\kappa_{lm}r) + \Delta_{lm}Y_l(\kappa_{lm}r)$, where $\Delta_{lm} \equiv - J_l'(\kappa_{lm}b)/Y_l'(\kappa_{lm}b)$.

The dynamical equations for the modes in coaxial waveguides have been described in detail,[3] and the results for the TE modes are

$$\left[\frac{d^2}{dz^2} + \left(\frac{\omega^2}{c^2} - k_{lm}^2 - \kappa_{lm}^2 \right) \right] \delta a_{lm} =$$

$$= \frac{\omega_b^2}{c^2} H_{lm} \left\langle \frac{v_r}{|v_z|} \frac{l}{\kappa_{lm}r} Z_l(\kappa_{lm}r) \sin \alpha_{lm} + \frac{v_\theta}{|v_z|} Z_l'(\kappa_{lm}r) \cos \alpha_{lm} \right\rangle , \quad (7)$$

$$2k_{lm}^{1/2} \frac{d}{dz} \left(k_{lm}^{1/2} \delta a_{lm} \right) = \frac{\omega_b^2}{c^2} H_{lm} \left\langle \frac{v_r}{|v_z|} \frac{l}{\kappa_{lm}r} Z_l(\kappa_{lm}r) \cos \alpha_{lm} - \frac{v_\theta}{|v_z|} Z_l'(\kappa_{lm}r) \sin \alpha_{lm} \right\rangle , \quad (8)$$

where $\delta a_{lm} \equiv e\delta A_{lm}/m_e c^2$ is the normalized amplitude of the modes, and

$$H_{lm} \equiv \frac{2\kappa_{lm}^2(b^2 - a^2)}{(\kappa_{lm}^2 b^2 - l^2) Z_l^2(\kappa_{lm}b) - (\kappa_{lm}^2 a^2 - l^2) Z_l^2(\kappa_{lm}a)} . \quad (9)$$

The beam is assumed to be monoenergetic with an axial energy spread determined by an initial [i.e., at $z = 0$] pitch angle spread, and the averaging operator is defined over the initial beam parameters

$$\langle (\cdots) \rangle \equiv \frac{A}{4\pi A_g} \int_0^{2\pi} d\phi_0 \int_0^{p_0} dp_{z0}\beta_{z0} \exp[-(p_{z0} - p_0)^2/\Delta p_z^2]$$

$$\times \iint_{A_g} dx_0 dy_0 \sigma_\perp(x_0,y_0) \int_{-\pi}^{\pi} d\psi_0 \sigma_\parallel(\psi_0) (\cdots) , \quad (10)$$

where A_g is the cross-sectional area of the waveguide, $\beta_{z0} \equiv v_{z0}/c$ for an initial axial velocity v_{z0}, $\phi_0 \equiv \tan^{-1}(p_{y0}/p_{x0})$, (p_{x0},p_{y0},p_{z0}) denote the initial beam momenta, p_0 and Δp_z denote the initial total momentum of the beam and the initial axial momentum spread respectively, ψ_0 [$\equiv - \omega t_0$, where t_0 is the time at which the particle crosses the $z = 0$ plane] is the initial ponderomotive phase, $\sigma_\perp$ and $\sigma_\parallel$ are the initial distributions of the beam in cross-section and phase, and

$$A \equiv \left[\pi \int_0^{p_0} dp_{z0} \exp[-(p_{z0} - p_0)^2/\Delta p_z^2] \right]^{-1} , \qquad (11)$$

is a normalization constant.

The field equations must be solved simultaneously with the orbit equations for an ensemble of electrons. We integrate the complete 3D Lorentz force equations for each electron in the aggregate fields of the CHI wiggler and electromagnetic fields for all the wave modes. No orbit average is imposed, and we treat the injection of the beam into the wiggler. This describes any increase in the effective beam emittance due to the injection mechanism. For this purpose, we model the adiabatic injection region by means of a tapered wiggler amplitude. In addition, we also consider amplitude tapering for the purpose of efficiency enhancement. In order to describe these effects within the CHI wiggler model, we assume that the overall coefficient of the periodic component of the field varies as

$$B_w = \begin{cases} 2B_0\sin^2\left(\dfrac{k_w z}{4N_w}\right) & ; z \le N_w\lambda_w \\ 2B_0 & ; N_w\lambda_w < z \le z_0 \\ 2B_0\left[1 + k_w\varepsilon_w(z - z_0)\right] & ; z > z_0 \end{cases} \qquad (12)$$

where N_w denotes the number of wiggler periods in the entry taper region, and ε_w is the normalized slope of the taper for purposes of efficiency enhancement.

The wiggler amplitudes and periods which can be achieved are determined using the POISSON codes.[4] To this end, we specified vanadium permendur spacers and found that a 6 kG solenoid saturates the ferrite for spacers with inner and outer radii of $a = 0.7$ and $b = 1.5$ cm, and a wiggler period of $\lambda_w = 1.5$ cm. We also assume that a and b are the inner and outer radii of the waveguide. Using these dimensions, we operate with a 10 kG solenoid which provides a maximum periodic field of 4 kG and a uniform axial field component of ≈ 6 kG. Note that a magneto-resonant enhancement in the gain and efficiency is also present when the Larmor period associated with the uniform axial field component is

close to the wiggler period. We assume that $N_w = 5$ to preserve the initial beam quality through injection.

Since FEL performance is critically dependent upon beam quality, we must have an electron gun which produces an annular beam with a low energy spread. The design tool we used for this is the EGUN code.[6] Since operation in G-band is desired, we chose an electron beam voltage in the neighborhood of 690 kV and a current of 40 A. Assuming that the inner and outer radii of the beam at the exit of the gun were 1.05 cm and 1.15 cm respectively, it is possible to design a gun which produces an axial energy spread of substantially less than 0.1%. The results from the gun calculation were used as initial conditions in the FEL simulation.
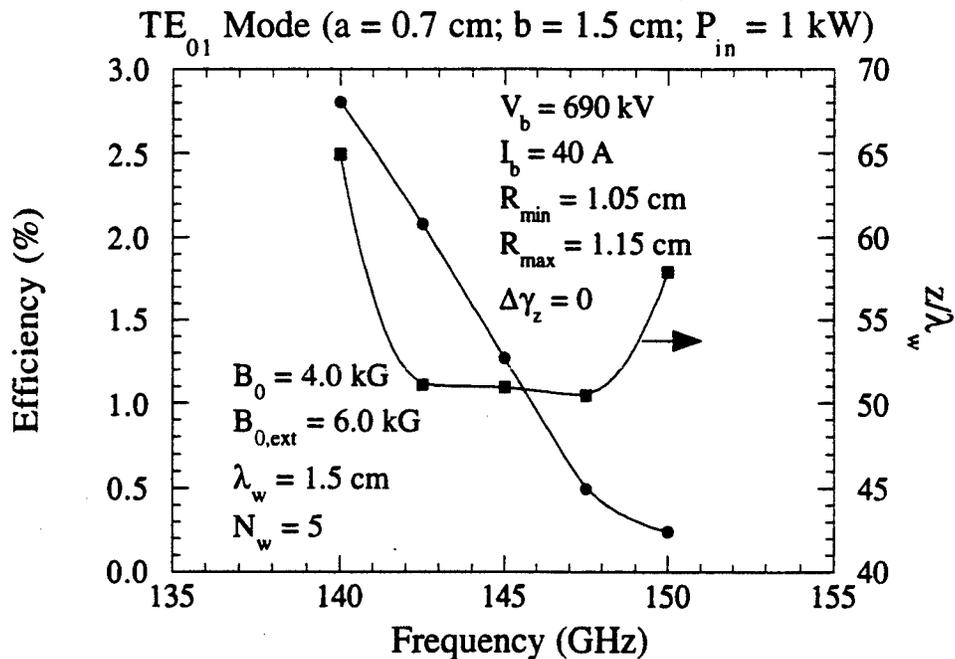
Fig. 2 Efficiency and saturation distance versus frequency at 690 kV.

We first address the interaction for a uniform wiggler, and consider the case of an ideal beam in which the axial energy spread $\Delta\gamma_z = 0$. We also deal with the TE_{01} mode at an injected power of 1 kW. The efficiency and saturation distance versus frequency are plotted in Fig. 2. It is clear that the efficiency decreases with frequency over the resonant

band from 140-150 GHz. Observe that the maximum efficiency occurs at the minimum minimum resonant frequency and does not correspond to the peak gain. This is a common feature of the interaction in FELs,[7] and stems from the fact that the efficiency varies with the difference between the beam velocity v_b and the phase velocity of the ponderomotive wave formed by the beating of the wiggler and radiation fields $[\Delta v = v_b - \omega/(k + k_w)]$. Since the saturation distance is relatively constant over the range of 142-147 GHz, the peak gain of ≈ 0.5 dB/cm occurs at ≈ 142 GHz for an efficiency of $\approx 2.2\%$. As such, we assume a frequency of 142.5 GHz in the remainder of the paper. It is possible, however, to retune to higher frequencies using higher voltages or shorter wiggler periods.

Before proceeding to the study of the tapered wiggler interaction, we turn to the effect of the axial beam energy spread. The variation in the efficiency as a function of $\Delta \gamma_z$ is shown in Fig. 3. Observe that the efficiency falls from about 2.24% to 2.10% as the axial energy spread increases to 0.10%. This is a relatively modest decrease in efficiency, and a beam quality within this range has been demonstrated in the gun design code.
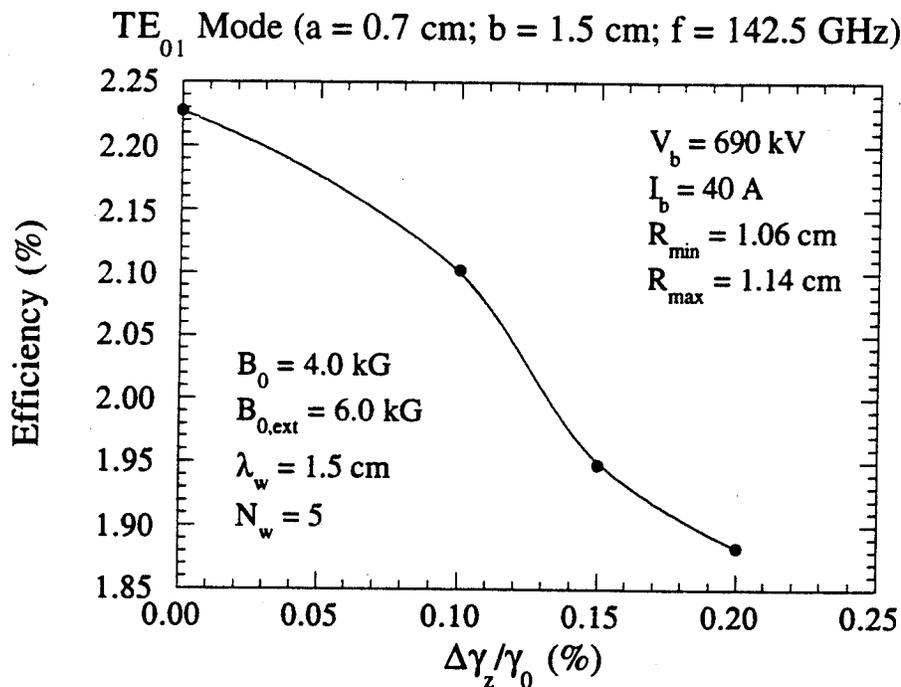

Fig. 3 Variation in the efficiency and saturation distance versus beam thickness.

Finally, it is important to note that no beam loss was found in the simulation prior to saturation for the uniform wiggler cases studied.

Turning to a tapered wiggler, it should be noted that there is an optimum both in the start-taper point and in the slope of the taper. Optimizing in both of these parameters, we find that for 1 kW input power the optimal start-taper point is $z_0/\lambda_w = 46$ and the optimal slope is $\varepsilon_w = -0.001$. The evolution of the power with axial distance for this choice is shown in Fig. 4 for the cases of an ideal beam [$\Delta\gamma_z = 0$] and for $\Delta\gamma_z/\gamma_0 = 0.2\%$. Note that the interaction length is $\approx 200\lambda_w$, which is the length required to taper the wiggler amplitude to zero [note that the uniform axial field component does not vanish]. It is clear that the efficiency does not change greatly with the decrease in beam quality over this range, and rises to over 13% for an output power of better than 3.5 MW.

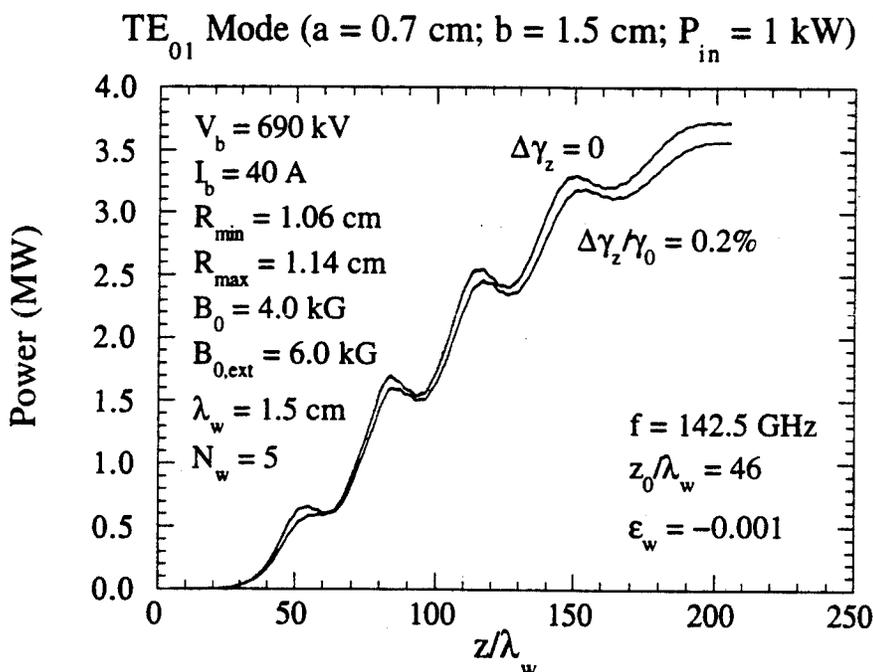TE_{01} Mode (a = 0.7 cm; b = 1.5 cm; P_{in} = 1 kW)

Fig. 4 Evolution of the power with axial position for two choices of the energy spread.

The bandwidth of the tapered wiggler interaction is quite large. Consider the case of the optimum parameters for the interaction at 142.5 GHz, including the total length of the system. The bandwidth is determined by the response of this system at different drive

frequencies. In Fig. 5 we plot the tapered efficiency versus frequency. It is evident that the efficiency remains high over a frequency range of $\approx$ 142.5-160 GHz, for a large instantaneous bandwidth. This agrees with an earlier study using a simpler FEL model.[8] Finally, note that despite the extended interaction length for the tapered wiggler cases shown, no beam loss was found in simulation for any of these parameters.
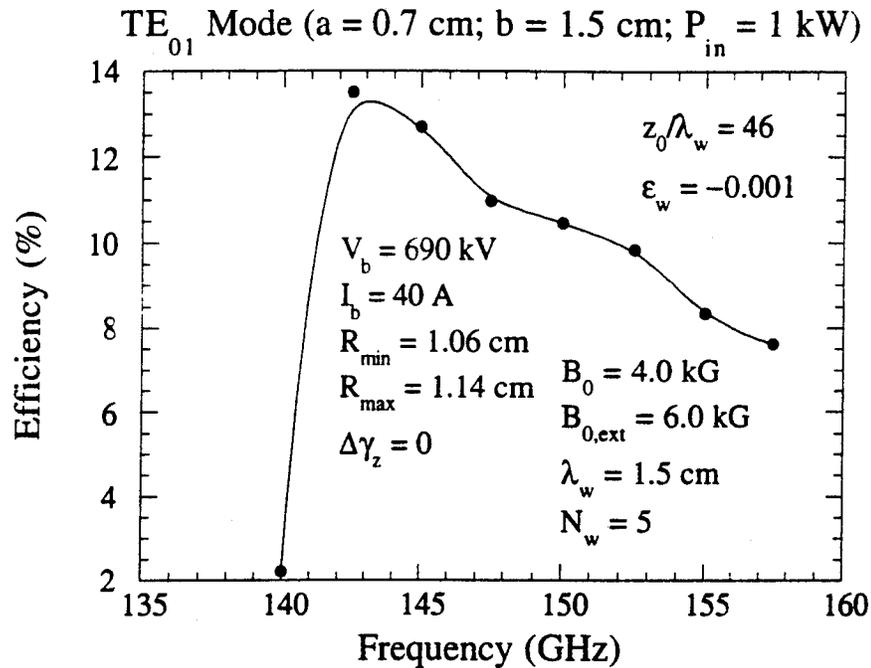
TE_{01} Mode (a = 0.7 cm; b = 1.5 cm; P_{in} = 1 kW)

$z_0/\lambda_w = 46$

$\varepsilon_w = -0.001$

$V_b = 690$ kV

$I_b = 40$ A

$R_{min} = 1.06$ cm

$R_{max} = 1.14$ cm

$\Delta\gamma_z = 0$

$B_0 = 4.0$ kG

$B_{0,ext} = 6.0$ kG

$\lambda_w = 1.5$ cm

$N_w = 5$

Fig. 5 The bandwidth for the tapered wiggler interaction.

Our results can be summarized rather simply. In the first place, no beam loss was found to occur for either the uniform or tapered wiggler runs. This is required for the design of a CW device. In the second place, the efficiencies were found to be fairly high. The tapered wiggler interaction produced efficiencies of 13-14%. These conclusions hold for both an ideal beam and for one with the more realistic beam energy spread of ≤ 0.2%. It should be remarked that such beams are quite reasonable with careful gun design.

The major source of concern is the length of the interaction. At 200 wiggler periods in length, the support of the central rod becomes a serious issue. However, we feel that it is not insurmountable, and can be addressed in several ways. Firstly, a vertical mount is

necessary in which the central rod is supported from the top by the collector. Secondly, it is not necessary to taper the wiggler to saturation. A shorter tapered wiggler would sacrifice some power but facilitate the support of the central rod. Lastly, this design is for an amplifier configuration; however, an oscillator can also be constructed which would be more compact without sacrifice of efficiency. The only drawback to an oscillator would be a narrower bandwidth. Tuning of an oscillator would have to be accomplished by varying the voltage, and whether the bandwidth would be sufficiently narrow to impair the device's usefulness depends upon the Q factor of the cavity. This is an area of future study. Note, however, that we do not expand the bandwidth to be less than that of the current generation of gyrotrons which are used for this purpose. It should be emphasized that this study represents an initial design only, and higher gains and shorter lengths are likely with proper optimization of parameters. Preliminary estimates of the efficiency and interaction length made on the basis of simple scaling laws[7] indicate that it should be possible to shrink the interaction length by $\approx 50\%$ with only a minor reduction in the efficiency using a somewhat shorter wiggler period and a beam with a lower voltage but a higher current. Operation closer to the magneto-resonance is also an attractive means of achieving this goal.

Cooling is not expected to be a major problem even for long pulse/CW operation since this is a low loss mode. Estimates indicate that loading on the central rod is ≈ 10 W/cm^2 at a power of 5 MW, and that the loading on the outer conductor is even less. As a result, cooling would be required only near the end of the interaction region using relatively narrow water passages in the rod.

In summary, the CHI wiggler based FEL is attractive for a high power CW radiation source. It is a robust design in which high efficiencies are possible over a wide parameter range, and the required beam quality is well within current gun technology. Finally, overall system efficency can be substantially increased by incorporation of depressed collectors for energy recovery.

REFERENCES

1. V.L. Granatstein and R. Colestock, eds., *Wave Heating in Plasmas* (Gordon & Breach, New York, 1986).

2. R.H. Jackson, H.P. Freund, D.E. Pershing, and J.M. Taccetti, Nucl. Instr. and Meth. **A341**, 454 (1994).

3. H.P. Freund, R.H. Jackson, D.E. Pershing, and J.M. Taccetti, Phys. Plasmas **1**, 1046 (1994).

4. A.M. Winslow, J. Comp. Phys. **2**, 149 (1967).

5. H.P. Freund, Nucl. Instrum. Meth. **A331**, 496 (1993).

6. W.B. Herrmannsfeldt, SLAC Report No. 226 (November 1979).

7. H.P. Freund and T.M. Antonsen, Jr., *Principles of Free-electron Lasers* (Chapman & Hall, London, 1992), Chap. 5.

8. B. Levush, H.P. Freund, and T.M. Antonsen, Jr., Nucl. Instr. and Meth. **A341**, 234 (1994).

APPENDIX XV

Design and Performance Calculations for a Ka-Band CHI Wiggler Ubitron Amplifier

J.M.Taccetti, R.H. Jackson, H.P. Freund, D.E. Pershing, and M. Blank

DESIGN AND PERFORMANCE CALCULATIONS FOR A Ka-BAND CHI WIGGLER UBITRON AMPLIFIER

J. M. Taccetti[†], R. H. Jackson, H. P. Freund[††], D. E. Pershing[§], M. Blank,
and V.L. Granatstein[†]
Naval Research Laboratory,
Washington, D.C. 20375

ABSTRACT

Design and performance calculations for a Coaxial Hybrid Iron (CHI) wiggler free-electron laser configuration are presented. The capability of generating high fields at short periods, as well as good beam focusing properties, make it a desirable configuration for high power coherent radiation sources in relatively compact systems. In addition to a description of the geometry, numerical calculations detailing the magnetostatic wiggler fields, the beam dynamics, and interaction of the beam with electromagnetic waves in K_a-band (26-40 GHz) will be presented. Key considerations for the experimental design will be outlined and discussed.

[†] Permanent address University of Maryland, College Park, MD 20742.
[††] Permanent address Science Applications International Corp., McLean, VA 22102.
[§] Permanent address Mission Research Corp., Newington, VA 22122.

INTRODUCTION

Fast-wave interaction devices, i.e. gyrotrons and FEL/ubitrons, have many attractive properties for the generation of high power, high frequency microwaves. However, practical devices have been elusive because of magnetic field, voltage, and size requirements. For FEL/ubitrons the disadvantage can be partially overcome by the utilization of short period ($\lambda_w < 5$ mm) magnetic wigglers. Several micro-wiggler configurations have been investigated, each having its own advantages and disadvantages in the areas of achievable field strength and uniformity, ease and cost of fabrication, control, tuning, and beam acceptance and focusing (see (1), (2), and references therein).

The coaxial hybrid iron (CHI) wiggler is a short-period compatible configuration which offers several advantages relative to the above issues. This paper will present design and performance calculations for a CHI wiggler based K_a-Band FEL amplifier under development at the Naval Research Laboratory. The goal is an output power of 100 kW at 35 GHz while reducing the voltage to approximately 150 kV.

CHI WIGGLER CONFIGURATION

The CHI wiggler consists of alternating rings of ferro- and nonferromagnetic materials, surrounding a central rod consisting of cylinders of the same materials as the rings but shifted axially by half a period. As shown in Fig. 1, a wiggler period consists of only two ferromagnetic pieces (an inner cylinder and an outer ring) along with their respective non-ferromagnetic *spacers*. The width of the two ferromagnetic pieces need not be the same, as long as the *combined* length is the same for both inner and outer sections. This entire structure is placed inside a solenoid (the axes of the solenoid and the wiggler are coincident) and causes a deformation of the solenoidal field into a combination of periodic radial and axial components. Having the magnetic field source external to the wiggler offers advantages for coil cooling and field tapering. Large wiggler fields are possible while maintaining a relatively simple and low-cost design.

2

The electron beam is annular and travels down the gap between the outer rings and the central piece. The radially undulating magnetic fields cause this annular beam to wiggle *azimuthally*. The electrons may then exchange energy with coaxial modes which contain an azimuthal electric field component, for example the TE_{01} mode.
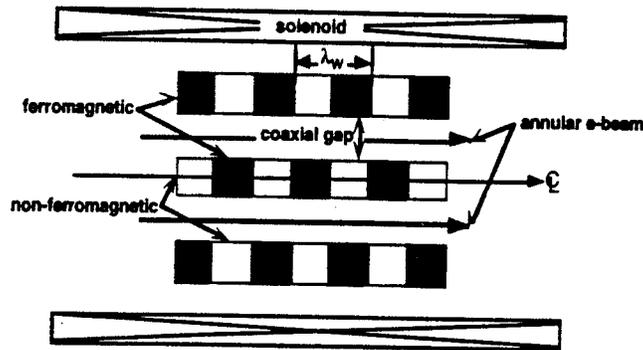
Fig. 1 CHI wiggler geometry.

The magnetic fields in the gap can be found analytically by solving Laplace's equation with the boundary conditions that the axial component of the magnetic field be zero along the faces of the ferromagnetic pieces and some constant value B_z along the faces of the non-ferromagnetic ones. The resulting equations for both the axial and radial components of the field (and accompanying figures) are described in earlier publications.[1,2] In essence, the radial component varies sinusoidally along the axial direction and has a minimum at the center of the gap. The axial component consists of a constant term and oscillating terms which are small at the gap center.

MAGNETOSTATIC WIGGLER ANALYSIS

The magnetic field profile of a CHI wiggler may be modified by changing or tapering several parameters of the basic configuration. Multiple variations of the basic CHI wiggler geometry were studied in a parametric search aimed primarily at finding the configuration which produced the highest periodic field. This search also detailed ways in which the magnetic fields may be tailored by varying the parameters of the geometry. These

parametric variations were performed by running computer simulations with the POISSON codes. The ferromagnetic material was assumed to be low-carbon steel, and the *B-H* table provided with the codes was used.

A schematic of the "standard" configuration used in the simulations is shown in Fig. 2. Only one quarter of the actual wiggler is input because the codes take advantage of its symmetry about the axis (bottom edge) and right edge. Notice that this configuration also allows study of the entrance fields. Parameters varied on the standard configuration include: gap height; inner pole height, width, taper angle; outer pole height, width, taper angle; and axial phase offset of inner and outer pieces.
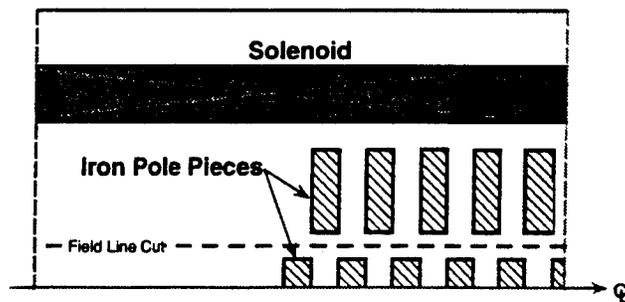
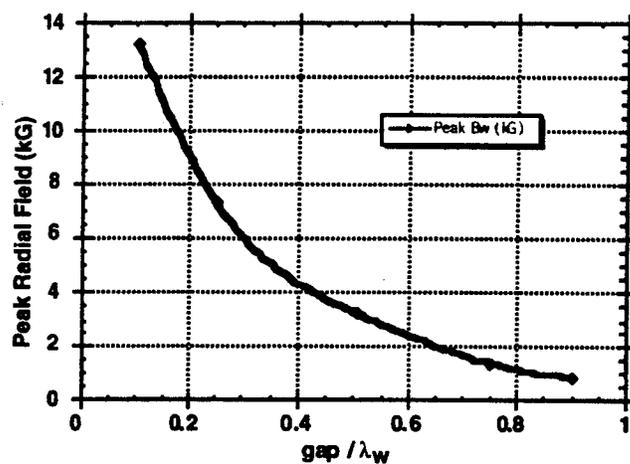Fig. 2 Standard POISSON input file for the magnetostatic field study.

Fig. 3 Peak radial magnetic field versus gap height.

4

Sample results are shown in Figs. 3-4. Fig.3 shows the dependence of the maximum radial magnetic field on the gap height, and Fig. 4 shows how varying the height of the outer rings can be used to change the value of the peak radial field. These and other results show that variations of pole shapes increased the peak radial field by only a few percent, and also show various ways to taper the field.
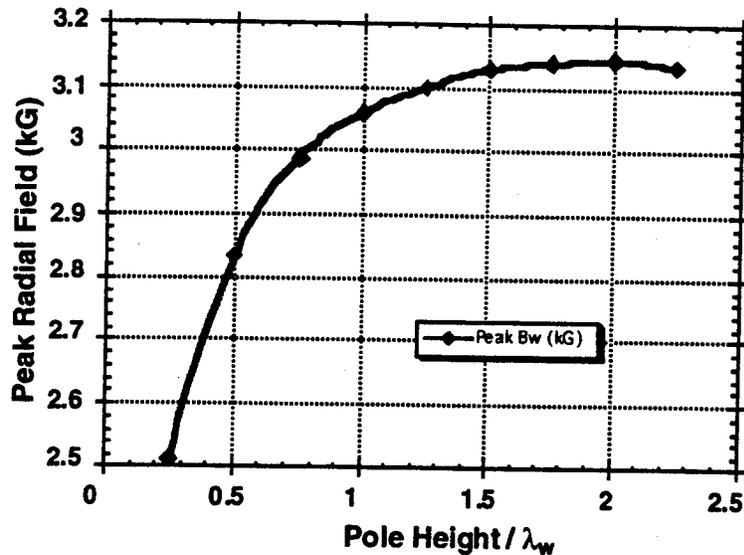

Fig. 4 Peak radial field versus the height of the outer rings.

BEAM DYNAMICS

The dynamics of electrons in the CHI fields were also studied both analytically and computationally. For the analytic solution, it was assumed that the particle did not stray far from the gap center-its original position (i.e. $\delta r \ll \lambda_w$). The simplified forms used for the fields were:

$$B_r = B_w \sin k_w z \ ,$$

$$B_z = B_0 \ ,$$

(1)

In the above equations $k_w = 2\pi/\lambda_w$ and B_w and B_0 are constants. Assuming a constant bulk axial velocity $v_{\parallel}$ and solving the equations of motion to lowest order in wiggler amplitude, one obtains the quasi-steady-state solutions:

$$v_\theta = \left[\frac{B_w(\beta_z/\beta_o)B_T}{B_o^2 - (\beta_z/\beta_o)^2 B_T^2} \right] v_{\parallel} \cos k_w z \ , \tag{2}$$

$$v_r = \left[\frac{B_o B_w}{B_o^2 - (\beta_z/\beta_o)^2 B_T^2} \right] v_{\parallel} \sin k_w z \ , \tag{3}$$

where $\beta_z = v_{\parallel}/c$, B_T is a constant field in the axial direction, called the transition field, and is given by:

$$B_T = \frac{mc^2}{e} \gamma \beta_o k_w \ , \tag{4}$$

where γ is the relativistic factor and β_0 is the magnitude of the total particle velocity (a constant) in units of c. The transition field is a constant value of the axial field which delineates the transition from group I orbits to group II orbits as B_z is increased. These equations describe an electron performing an elliptical orbit in the r-θ plane (with a period equal to the wiggler period) while streaming at a constant axial velocity. These results are analogous to those of a simplified planar wiggler field with a constant axial guide field.[3]

Using energy conservation and the quasi-steady state solutions for v_θ and v_r obtained above, one may obtain a quartic polynomial in $v_{\parallel}$, which may be solved numerically. The existence of a constant field in the axial direction causes the transverse velocities to increase about a certain resonant value of the axial field. The azimuthal component of the velocity (Eq. 2) (as well as the radial component) is seen to depend strongly on this gyroresonance effect, from the fact that the fields are squared in the denominator.

A figure of merit of the strength of the wiggler is α (the ratio of azimuthal to axial velocity). A plot of α against the applied field is given in Fig. 5 showing the *gyroresonant gap*. Fig. 5 shows the sensitivity to the applied field, as seen from the width of this gap. Notice that orbits below B_T (Group I) are more sensitive as B_z approaches B_T than those above B_T (Group II). This sensitivity indicates that tapering of parameters will be very

important for achieving maximum performance. It also shows the enhancement possible in the interaction due to the existence of the axial field. In preparing this figure, single and multi-particle three-dimensional orbits were simulated using TRACK-3, a trajectory integrator. The fields were calculated using the analytic solutions[1] with the field increasing adiabatically in the entrance into the wiggler. Results of the simulations agree very well with analytic values away from the gyroresonant gap, as the electron remains very near the wiggler gap center.
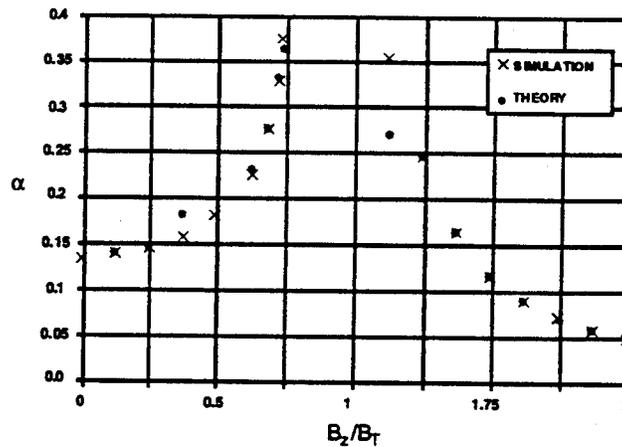

Fig. 5 Variation of α versus the applied field for $B_w/B_T = 0.135$ (comparison of theory and TRACK-3 simulation results).

An examination of the trajectories shows a drift in the θ-direction, but this is acceptable in the CHI FEL case since it remains in the interaction region due to the cylindrical geometry. Calculations have shown that this drift can be explained using Busch's theorem and depends on the entrance conditions used in the simulation. Actual CHI wiggler axial fields decrease in magnitude at the entrance into the wiggler (due to the iron pieces), and may partially cancel out this drift. Future plans include running simulations with PIC (particle in cell) codes utilizing 2-D simulations of the CHI wiggler field including entrance conditions.

THE EXPERIMENT

The experiment to be built at the Naval Research Lab will be a CHI wiggler FEL operating as an amplifier at a frequency of 35 GHz in K_a-Band. The principal goal of the experiment is to operate at lower voltages while still generating high power, high frequency microwaves. Current plans call for operation at approximately 150 kV with an output power of 100 kW.

The major components of the FEL are the gun, the wiggler section (including the solenoid and the waveguide), the beam collector, and the input and output couplers. The gun will operate at around 150 kV and produce a 10 A annular beam for the CHI wiggler. The wiggler assembly will be placed horizontally within the bore of an existing superconducting magnet. The central rod of the wiggler will be supported by radial struts located near the gun and the collector. The coaxial waveguide consists of the (electroplated) faces of the inner and outer pieces of the wiggler. This waveguide will contain a central sever to reduce rf reflections. The diameter of the wiggler, and therefore of the waveguide, is limited by the bore of the magnet, 6.4 cm, and places a lower bound on our operating frequency. The wiggler will have a period of about 1 cm and will be about 60 periods in length.

A SLAC klystron gun will be modified to produce the necessary annular beam. The superconducting magnet, with an axial field of up to 30 kG, will permit an extensive study of the full performance range of the CHI FEL. The bore size of the magnet is 6.4 cm and its total length is 78.3 cm .

Preliminary calculations using untapered configurations (using a previously described nonlinear three-dimensional slow-time-scale formulation[2]) have shown gains on the order of 0.3 dB/cm and efficiencies in excess of 10 % in this frequency range. Studies are currently under way to lower the voltage required while still retaining performance. Figure 6 shows the gain profile for a specific set of parameters, for which a saturated gain of about 30 dB (0.26 dB/cm) with a gain bandwidth of around 20% was achieved. In this

8

figure, R_{min} and R_{max} are the inner and outer radii of the coaxial waveguide (i.e. the wiggler gap), and N_w is the number of adiabatic entrance periods. It must again be stressed that these results are very preliminary since optimization of parameters was not performed.
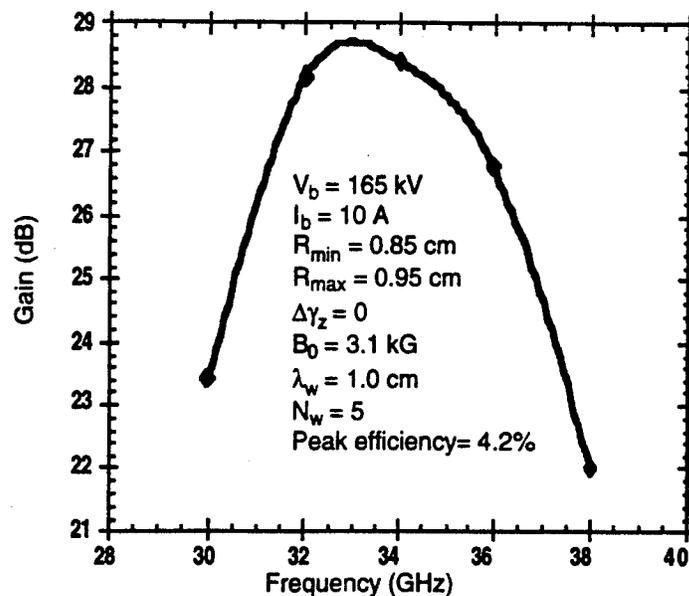

Fig. 6 Preliminary simulation results for a K_a-Band amplifier utilizing a coaxial TE_{01} mode.

SUMMARY AND CONCLUSIONS

The above results indicate interesting potential for high frequency amplifiers based on the CHI wiggler configuration. Work is in progress on the design of a CHI wiggler ubitron amplifier in K_a-band. A Pierce-type electron gun is being modified to produce a hollow beam for the device, which will have a period of about 1 cm and will consist of about sixty periods with a central sever. An existing superconducting magnet ($B_z \leq 30$ kG) will be used to produce the axial field in order to allow exploration of the full performance range of the CHI wiggler.

This work was supported by the Office of Naval Research.

REFERENCES

1. R. H. Jackson, H. P. Freund, D. E. Pershing, J. M. Taccetti, Nucl. Instrum. Methods Phys. Res. **A341**, 454 (1994).

2. H. P. Freund, R. H. Jackson, D. E. Pershing, J. M. Taccetti, Phys. Plasmas **1**, 1046 (1994) .

3. H. P. Freund and T. M. Antonsen, Jr., *Principles of Free Electron Lasers*, (Chapman & Hall, London, 1992).

APPENDIX XVI

Improved Amplifier Performance of the NRL Ubitron

D.E. Pershing, R.H. Jackson, H. Bluem, and H.P. Freund
Nucl. Instrum. Meth. **A304**, 127 (1991)

Improved amplifier performance of the NRL ubitron

D.E. Pershing [1], R.H. Jackson, H. Bluem [2] and H.P. Freund [3]

Vacuum Electronics Branch, Electronics Science and Technology Division, Naval Research Laboratory, Washington, DC 20375, USA

Improved amplifier performance of the NRL Ku-band ubitron is reported following several experimental modifications. The major modification is the substitution of a higher-current (100 A), higher-quality electron gun for the original modified SLAC klystron gun (250 kV, 37 A). The experimental configuration is otherwise unchanged: a solid, uniform-density electron beam propagating through a helical wiggler/axial guide field configuration, interacting with a co-propagating circularly polarized TE$_{11}$ rf wave. With these changes, small-signal gains of 23 dB have been observed in the 12.6–17.5 GHz frequency range. Good agreement between measured and calculated gain in the Raman regime has been obtained using a three-wiggler model in the 3D nonlinear FEL code ARACHNE.

1. Introduction

The Vacuum Electronics Branch of the Naval Research Laboratory has an ongoing program to evaluate the potential of the ubitron/FEL interaction as a high-gain, high-power, broad-bandwidth micro- or millimeter wave source. Moderate gain operation of the NRL ubitron has been previously reported using a modified SLAC klystron gun [1,2]. An improvement in the gain has been observed following the installation of a higher-current, higher-quality electron gun [3]. The maximum gain for a uniform axial field is 20 dB, and substantial gain has been measured over the 12.6 to 17.4 GHz frequency range. Gain is found to be limited by the onset of a high-power oscillation. The oscillation can reach high power levels ($\approx$ 700 kW) and is dependent

on the wiggler field. Power is also dependent on the axial field profile and trim coil current. In addition, it exhibits oscillation thresholds dependent upon both beam voltage and wiggle velocity. Both amplifier and oscillator experimental measurements are compared with a fully three-dimensional nonlinear simulation of this configuration using the code ARACHNE [4–7].

2. Experimental configuration

The present amplifier configuration is shown in fig. 1. The electron gun is on the left. All current emitted from the gun is magnetically focused and injected into the interaction region; no beam scraping is used. A solenoidal field, generated by 14 individual coils, is used for beam confinement and transport. Following the direction of beam propagation, the major components are: resistive injected-current monitor, modified four-port turnstile junction input coupler, double taper, fluid cooled bifilar helix (repetitively pulsed), resistive transmitted current monitor, beam collector, four-port output coupler, and a combination water load/calorimeter.
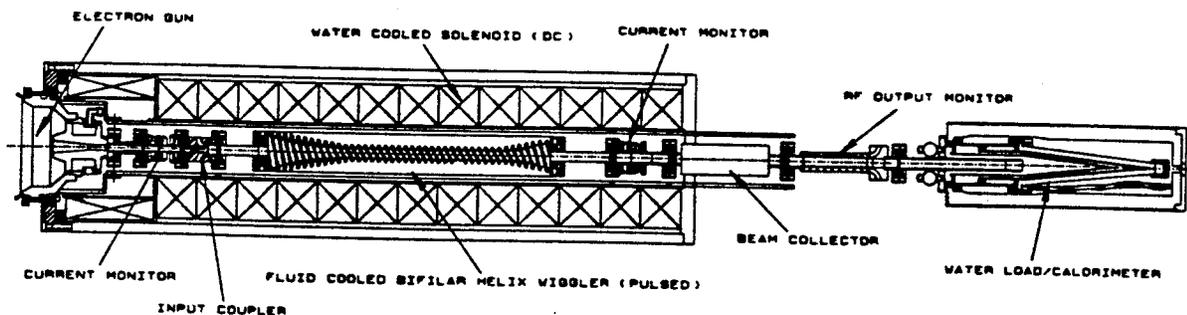
[1] Permanent address: Mission Research Corporation, 8560 Cinderbed Rd., Suite 700, Newington, VA 22122, USA.
[2] Permanent address: Laboratory for Plasma Research, University of Maryland, College Park, Maryland 20742, USA.
[3] Permanent address: Science Applications International Corp., McLean, Virginia 22102, USA.

Fig. 1. Schematic illustration of the NRL ubitron.

III. RAMAN EXPERIMENTS

The input coupler generally launches a LHCP TE$_{11}$ fundamental mode wave into the interaction region, although it can also launch a linearly polarized wave if desired. The output coupler employs both broadwall and narrow-wall ports for TE/TM mode selection purposes. Essentially all of the injected and amplified rf power is absorbed in the water load/calorimeter. The parameter range over which the ubitron has been operated is: $190 < V_b < 250$ kV, $65 < I_b < 94$ A, $1.8 < B_z < 2.9$ kG, $B_w < 575$ G, and $12.6 < f < 17.4$ GHz. The wiggler field has a 2.54 cm period with effectively 10 periods in the uniform region and 4 and 5 periods in the entrance and exit tapers, respectively. The device is typically repetitively pulsed in the 3–6 Hz range.

3. Experimental results and comparison with theory

Ubitron amplifier performance has been measured as a function of several independent variables: rf frequency, wiggler field, beam voltage, and axial field. Most measurements are in the small-signal regime; saturation was not reached. The major performance results discussed below are gain vs frequency and wiggler field.

The RHCP wiggler field is generated by a multiple-turn bifilar helix electromagnet with radially tapered entrance and exit sections which was wound on an aluminum form in anticipation of dc operation. However, due to cooling problems, the wiggler is operated in a repetitively pulsed mode to achieve high field

strengths. As shown in fig. 2, the resulting transverse field profile was measured only on-axis. Due principally to magnetic diffusion effects, the field profile departs considerably from the ideal profile, which would consist of a smooth adiabatic increase in transverse field followed by a constant transverse field region and then an adiabatically decreasing field.

In addition to the reduced performance that could be expected from this wiggler profile, comparison between experiment and theory is complicated due to the difficulty in modelling this field. Since only the on-axis transverse field profile was measured, insufficient data were obtained to directly incorporate the measured profile into the simulation. For simulation purposes, therefore, the wiggler field is approximated as the superposition of the fields of three ideal bifilar helices of different amplitude and period. The fit is also shown in fig. 2, and comes reasonably close to replicating the fine structure in the uniform field region.

The small-signal gain is shown in fig. 3 for the following parameters: $V_b = 232$ kV, $I_b = 85$ A, $B_z = 2.51$ kG, $B_w = 294$ G, and $P_{in} \approx 150$ W. The solid line represents simulation results in the Raman regime from the code ARACHNE for axial energy spreads of 0 and 0.25%. For this set of parameters, velocity spread has little effect on gain. The simulation results are in good agreement with the average measured gain, but are less accurate concerning the detailed profile. Contributing factors to this discrepancy are the wiggler field model, detailed beam characteristics not included in the code, and treatment of ac space charge in the code.
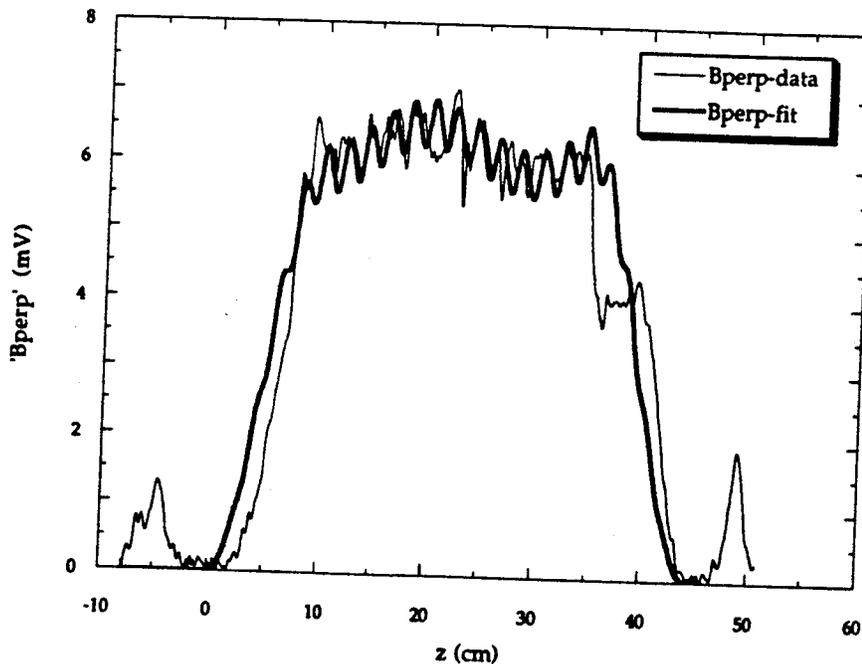

Fig. 2. Comparison of the measured transverse on-axis wiggler field and the three-wiggler model used in simulation.
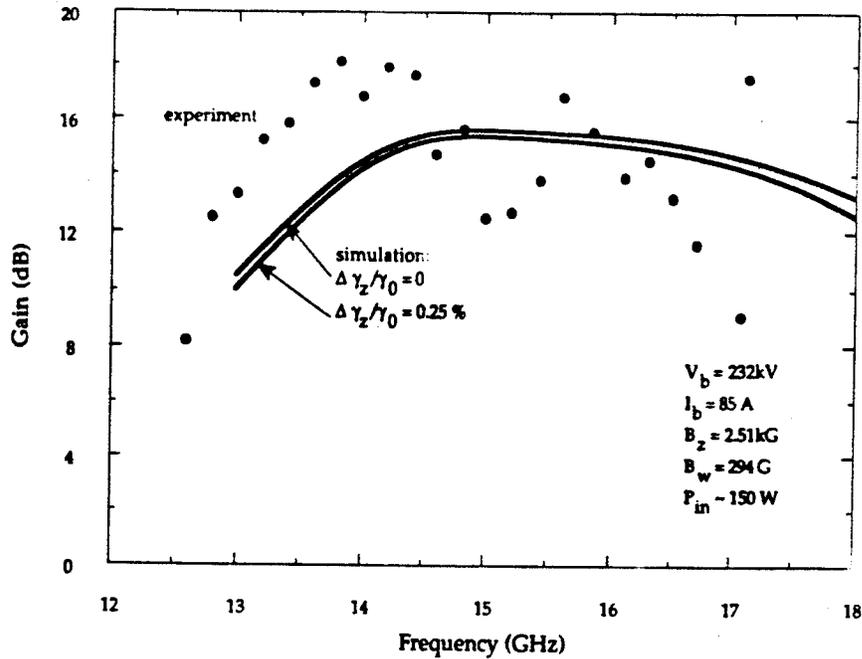
Fig. 3. Small-signal gain of the amplifier in the TE$_{11}$ mode.

The saturation behavior has not been measured due to an rf oscillation that limited the maximum gain to approximately 20 dB. This value was measured at 14.8 and 16.6 GHz for different combinations of V_b, B_z, and

B_w. Insufficient rf drive power was available to achieve saturation at this level of gain. The maximum power measured in the amplifier mode was 200–300 kW using a uniform B_z field. However, approximately 23 dB of
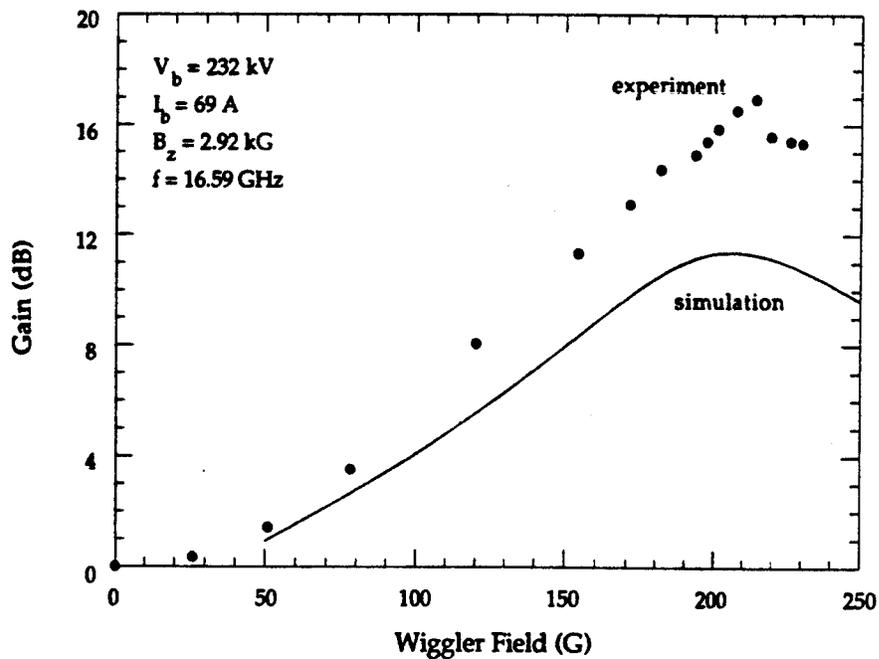

Fig. 4. Dependence of the TE$_{11}$ small-signal gain upon the wiggler field.

III. RAMAN EXPERIMENTS

gain has been measured using a nonuniform B_z field. Bandwidth in the small-signal regime exceeds 25%, and the calculated peak gain/wavelength is approximately 1.6 dB/λ.

To further characterize ubitron performance, the gain dependence on wiggler field was measured and calculated for a second set of parameters and is shown in fig. 4. In this case, the simulation and measurements are in good agreement for the wiggler field required to generate maximum gain. However, the values of that maximum gain differ significantly. Discrepancies between experiment and theory are due to the same factors listed above.

4. High power oscillation

In an attempt to increase amplifier gain by increasing the wiggler field, an oscillation was observed that limited maximum gain, and which reached power levels of approximately 700 kW (corresponding to an efficiency of 3%) at a frequency of approximately 17.4 GHz. Severe beam disruption also occurred at high power levels. Identification of the oscillation mechanism remains elusive at this time. Experimental evidence points to either a fundamental ubitron oscillation with the TE_{11} mode, or a second harmonic ubitron interaction with the TE_{21} mode. This ambiguity results from inadequate diagnostics to discriminate between TE modes. The principal characteristics of the oscillation are:

(1) The oscillation *requires* the wiggler field, and is not strongly dependent on the axial field; hence it is not a cyclotron maser. The oscillation would have to switch between the 2nd, 3rd and 4th gyrotron harmonics to maintain either a TE_{21}, or a TE_{11} intersection near 18 GHz for the parameters at which oscillation was observed.

(2) Oscillation power is dependent on the axial field profile, wiggler field amplitude, and on gun trim coil current. Measurements of oscillator power dependence on wiggler field is shown in fig. 5 for two axial field profiles. The compression B_z profile has the effect of slightly reducing the beam diameter in the wiggler region. The maximum power in this case is considerably reduced from the maximum power measured with a uniform B_z, for nominal values of trim current, although the oscillation will start at a lower wiggler field. Measurements of oscillator power vs trim coil current for both field profiles show a strong linear reduction in oscillator power with increasing trim current.

(3) High output power is possible. However, at high power levels, considerable pulse-to-pulse amplitude fluctuations were observed, not correlated to macroscopic parameter variations. Both output coupler/diode detector and calorimetric power measurements were made.
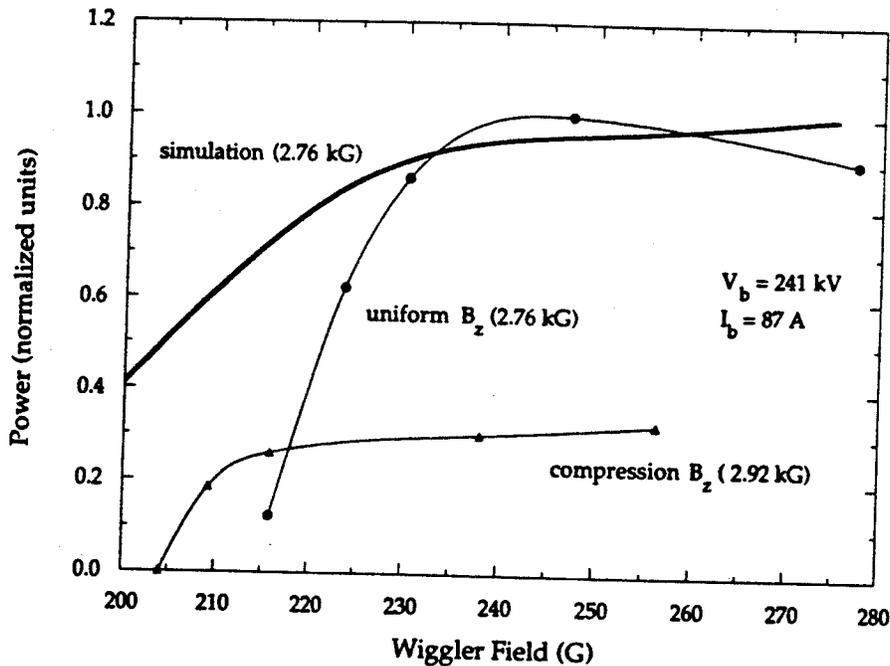

Fig. 5. Dependence of the oscillation power on wiggler field for two axial field profiles, and comparison with the TE_{21} mode second harmonic oscillation calculation.

(4) The oscillation frequency, which typically differs from the amplifier frequency, is near the TE_{21} mode cutoff. A wavemeter was used for this measurement. The oscillation does not appear to be a typical feedback oscillation at the driven frequency, but grows from noise on the beam at 17.4 GHz. Examination of uncoupled dispersion curves for both TE_{11} and TE_{21} combinations show possible intersections near 17.4 GHz.

(5) An oscillation threshold exists at an on-axis velocity ratio, independent of the axial field over the range of 1.9 to 2.9 kG. The wiggler field required to initiate the oscillation was measured for a variety of beam voltages and axial field values and/or profiles. Although the initiation wiggler field spans the range of 250 to 300 G, the on-axis $v_\perp/v_\parallel$ is found to be approximately 0.13, computed in each case for an ideal wiggler field and a uniform axial field of the measured values.

(6) No oscillation occurs for beam voltages below approximately 200 kV – independent of the wiggler field magnitude. At this voltage, the second harmonic TE_{21} interaction occurs at a frequency of 18.7 GHz which is considerably higher than observed. However, there is no TE_{11} mode intersection at all at this voltage.

(7) Output coupler characteristics eliminate the possibility of a TM interaction.

The amplifier code ARACHNE (including the three-wiggler model), was employed to model the interaction. In order to obtain a second harmonic ubitron interaction with the TE_{21} mode the waveguide radius was increased from 0.815 to 0.844 cm in order to lower the cutoff frequency below the measured 17.4 GHz oscillation frequency. Simulation results are presented in fig. 5, showing the computed oscillator power (saturated amplifier power) as a function of wiggler field for a uniform 2.76 kG axial field. The shape of the curve is in reasonable agreement with measured data, lending credence to the hypothesis that this is a second harmonic interaction with the TE_{21} mode. The maximum computed oscillator power (intracavity) is approximately 1.5 MW, also in reasonable agreement with the estimated maximum oscillator output power of 700 kW. Calculations of the saturated amplifier power for the TE_{11} mode using ARACHNE (with the nominal waveguide radius of 0.815 cm) are on the order of 4–5 MW. This is considerably higher than the measured value.

Factors favoring the TE_{11} interpretation are: (1) the measured frequency is consistent with a TE_{11} intersection for the nominal waveguide radius, (2) the voltage threshold is consistent with no TE_{11} intersection for those parameters, and (3) no mode conversion is required for the free propagation of the signal. Arguments against the TE_{11} interpretation are less well founded on explicit observations: (1) measurements of component return loss using linear polarization do not show large

reflections at 17.4 GHz, reflectivity is actually higher near 17.8 GHz, (2) the reason for the power sensitivity to trim coil current is not clear, and (3) the measured power level appears to be considerably lower than predicted by simulation.

The primary factors leading to a TE_{21} interpretation of the observed oscillation characteristics are: (1) The reflectivity is high near cutoff which facilitates oscillation, (2) the dispersion curve intersection frequency is fairly constant, not highly dependent on external parameters, (3) operation near cutoff is also consistent with pulse-to-pulse power fluctuations and power sensitivity to trim current, and (4) the observed power is consistent with the expected saturation level based on simulations. The primary factors against a TE_{21} interpretation are related. While it is possible that the dispersion curve is altered in such a manner to reduce the cutoff frequency from the vacuum value of 17.8 to 17.4 GHz in the interaction region, TE_{21} propagation beyond the beam collector is not possible without mode conversion, since 17.4 GHz is below the vacuum waveguide cutoff.

5. Summary

Amplifier performance of the NRL ubitron has improved following the installation of a higher-current, higher-quality electron gun. A gain of 20 dB has been measured, corresponding to a peak gain/wavelength of 1.6 dB/λ. The maximum output power is 200–300 kW. 3D nonlinear simulations of the ubitron configuration, including a three-wiggler model, are in reasonable agreement with measured data. Small-signal bandwidth has been measured to exceed 25%. However, saturation has not been achieved due to gain limitations caused by the onset of a high power oscillation. The oscillation can be fairly powerful; approximately 700 kW has been measured. The oscillation mechanism has not been conclusively identified at this time. A major component redesign is currently under way in order to improve the wiggler and to enhance the diagnostics available for distinguishing between TE modes.

References

[1] R.H. Jackson, D.E. Pershing and F. Wood, Nucl. Instr. and Meth. A259 (1987) 99.

[2] D.E. Pershing. R.H. Jackson. H.P. Freund and H. Bluem, Nucl. Instr. and Meth. A285 (1989) 56.

[3] G. Merdinian. G. Miram. R. Jackson. R. Parker, and D. Pershing, Techn. Digest Int. Electron. Devices Meeting, 1985, Washington, DC (IEEE Press, New York, 1985) p. 188.

[4] A.K. Ganguly and H.P. Freund, Phys. Rev. A32 (1985) 2275.

[5] H.P. Freund and A.K. Ganguly, Phys. Rev. A33 (1986) 1060.

[6] H.P. Freund and A.K. Ganguly, Phys. Rev. A34 (1986) 1242.

[7] A.K. Ganguly and H.P. Freund, Phys. Fluids 31 (1988) 387.

APPENDIX XVII

Amplifier Performance of the NRL Ubitron

D.E. Pershing, R.D. Seeley, R.H. Jackson, and H.P. Freund

AMPLIFIER PERFORMANCE OF THE NRL UBITRON

D. E. Pershing, [†] R. D. Seeley,[†] R. H. Jackson, and H. P. Freund[§]
Naval Research Laboratory
Washington, DC 20375

ABSTRACT

Operation of the Naval Research Laboratory K_u-band ubitron has successfully demonstrated a high power/efficiency and broad bandwidth capability. This device employs a helical wiggler/axial guide field configuration with a 212-255 kV/67-100 A electron beam and wiggler and guide magnetic fields of 175-320 G and 1.75-2.54 kG. Performance levels achieved at 16.6 GHz can be summarized as a peak power of 4.2 MW for an efficiency of 17.5% and a gain of 29 dB, and an instantaneous bandwidth of 22%. Substantial beam loss was observed. The specific loss rate was correlated with output power, and reached a level of 50% beam loss at the 4.2 MW level. Nonlinear simulations of the experiment are in good agreement with these observations.

[†]Permanent Address: Mission Research Corp., Newington, VA 22122.
[§]Permanent Address: Science Applications International Corp., McLean, VA 22102.

I. INTRODUCTION

With several modifications to the previous design,[1] the NRL ubitron has demonstrated operation as a high power, broad band, and efficient amplifier with a maximum output power of 4.2 MW for an efficiency of 18%, a 29 dB gain, and a large signal bandwidth (not saturated) greater than 22%. The experiement met the performance goals for the fundamental mode amplifier; specifically, an output power of 1-5 MW, an efficiency greater than 15%, a large-signal gain of 25-30 dB, and a large-signal bandwidth greater than 20%. Experimental results are in good agreement with theoretical predictions using the 3-D nonlinear code ARACHNE.[2-4] It is important to note in this regard that, in contrast to earlier devices operating in the Raman regime,[3] the DC self-fields of the beam played an important role in the interaction.

The fundamental mode amplifier reported here is only one of several experiments in the NRL ubitron program which includes integrated theory, simulation, design, fabrication, and testing whose objective is the determination of the potential of the ubitron/FEL as the basis for a new class of high-power, broad band, micro- and millimeter wave amplifiers. Experiments include the fundamental mode amplifier, a harmonic amplifier using rectangular waveguide and a linear wiggler,[5] and a reduced voltage ubitron using the CHI wiggler.[6,7] Three dimensional theories and simulation codes have been developed for these and other interaction geometries.

II. EXPERIMENTAL RESULTS

A summary of the basic parameters and recent alterations in the experiment is reported here. An extensive description of other experimental aspects is given in ref. 1. The wiggler is a pulsed bifilar helix with a period of 2.54 cm and an overall length 33 wiggler periods. Of this length, the first five and the last three wiggler periods represent an adiabatic entrance and exit. Amplification was measured over the following parameter ranges: wiggler amplitude ≈ 175-320 G, axial field ≈ 1.75-2.54 kG, beam voltage ≈ 212-

254 kV, and beam current ≈ 67-100 A. The beam radius upon wiggler entry is ≈ 0.4 cm and the waveguide radius is 0.815 cm. The FWHM of the beam pulse is ≈ 2.4 μs, with a flat top of ≈ 1 μs. Operation is largely in the TE_{11} mode at K_u band (12.4-18 GHz). The experimental configuration is shown in Fig. 1 with the major components identified. Note that the solenoid is split to accommodate a gate valve separating the gun and the interaction/diagnostics sections which necessitated additional solenoid coils to maintain the field profile. Vacuum pumping has been added to the calorimeter to accommodate any additional gas loading caused by beam loss in the interaction region.
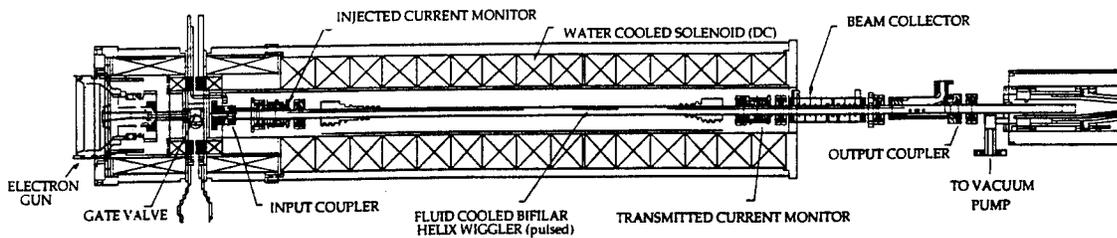

Fig. 1 Illustration of the experimental configuration.

Amplification has been measured over a wide parameter range. Although the nominal beam and axial field values are 250 kV/100 A and 2.2 kG, these do not necessarily represent the optimal parameter range, and equivalent output power has been obtained for several different parameter sets. The maximum power measured to date is 4.2-4.5 MW at a frequency of 16.6 GHz. Typical waveforms showing the essential characteristics of ubitron operation are given in Fig. 2. In this case, an output power of ≈ 4.5 MW (4.2 MW from calorimeter) was measured for a 245 kV/94 A beam, with axial guide field and wiggler field amplitudes of 2.47 kG and 270 G, respectively. This represents a gain of 29 dB and an efficiency 18%.
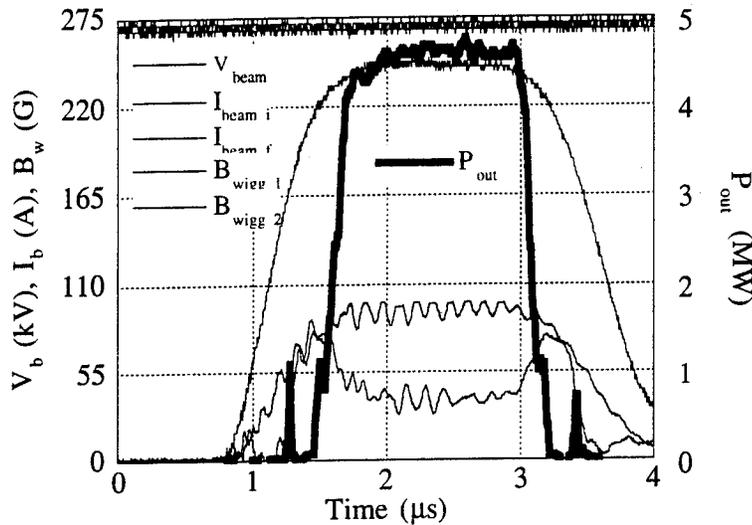
Fig. 2 Typical waveforms.

It is important to observe the presence of beam loss on the rising and falling edges of the voltage pulse as well as high beam loss during the interaction. This will be discussed later in more detail. Note that the ripples on the two beam current traces are not physical, but are due to current monitor ringing. It should also be noted that the output power shown in the figure does not represent saturation of the interaction. Indeed, for most parameters we have been unable to drive the system to saturation.

The ubitron has also demonstrated a wide instantaneous bandwidth. However, there are two factors which render this measurement difficult. Specifically (1) the modulator exhibits a slow time scale voltage drift, and (2) in order to accommodate high input power, the phase splitting circuitry utilizes two sets of short slot hybrids to cover most of K_u band and several hours are required switch between the them. Hence, the bandwidth measurements are not always made with the identical parameters; however, the measurements are indicative of ubitron bandwidth potential. Fig. 3 shows the bandwidth characteristics for a case in which the output power exceeds 600 kW. This represents a bandwidth in excess of 22%.
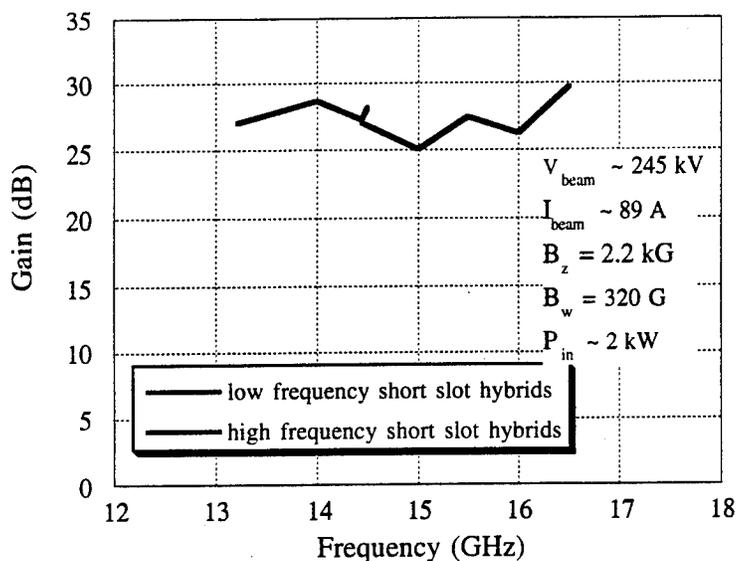
Fig. 3 Ubitron bandwidth characteristics.

The NRL ubitron exhibits a high degree of sensitivity to variations in the beam voltage and the axial and wiggler magnetic fields. An example of the sensitivity of the output power to beam voltage is shown in Fig. 4. Output power for this case is seen to reach a maximum in excess of 4 MW at a beam voltage of 245 kV, and to increase from 2-4 MW as the voltage increases about 4.5% from 234-245 kV. This sensitivity points to the need for very tight modulator voltage control. Similar sensitivity to variations in the axial and wiggler magnetic fields are also seen. In order to illustrate the sensitivity of the interaction to variations in the axial magnetic field, we consider a 250 kV/83 A beam with a wiggler field amplitude of 275 G. Experimentally, the output power is found to vary from 2-4.4 MW at 16.6 GHz as the axial magnetic field increases from 2.4-2.54 kG. Observe that the output power nearly doubles for an axial field increase of only about 5.5%. Somewhat less sensitivity is measured for wiggler field variations. With a 247 kV/83 A beam and an axial magnetic field of 7.6 kG, the output power increases from 0.4 to 2.6 MW at 16.6 GHz as the wiggler field increases from 160-280 G (i.e., a field increase of $\approx$ 25 % is required to double the output power). Part of the sensitivity to the

parameters arises because the system is not driven to saturation; hence, small changes in the growth rate can result in relatively large variations in the output power.
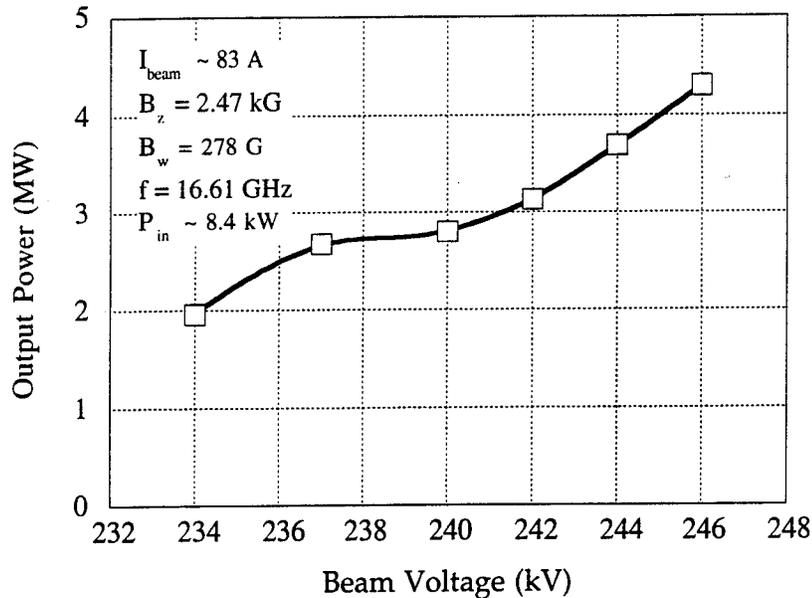

Fig. 4 Variation in the output power with beam voltage.

III. COMPARISON WITH THEORY

A key feature of the NRL ubitron program is the integration of theoretical, computational, and experimental efforts which leads to the development and validation of a detailed and precise design and simulation capability. To demonstrate this capability, we of course need to compare experimental measurements with theory. We use the 3-D nonlinear simulation code ARACHNE, which in its latest version[3,4] includes both RF and DC beam space charge effects, under the assumption of an initial axial energy spread of 1.5 %. It is also important to bear in mind that, as pointed out in ref. 3, the inclusion of the DC space-charge fields are important for the current experiment

In general, we find that experimental performance generally follows theoretical predictions as far as trends with wiggler field, axial field, beam voltage, and beam transmission are concerned. However, we usually measure somewhat higher power than predicted theoretically. Typically, we find that an approximately 5 % increase in both the

wiggler and axial magnetic fields in ARACHNE over the experimental calibration results in good agreement between theory and experiment. Note that this is slightly outside our estimated 2-3 % experimental uncertainty. Although this is not a large discrepancy, it is an issue that is still under investigation, and there are several possible factors which contribute to the discrepancy. On the theoretical side, possible reasons for the discrepancy include unavoidable differences between the experimental implementation and theoretical model, such as mechanical and field misalignments or actual injected beam conditions. Although these factors would normally have a deleterious affect on output power, we cannot rule these out as possible contributing factors. Experimentally, the presence of internal reflections could increase the effective input power, and thereby increase the output power over that expected for a single pass amplifier. In addition, although the solenoid and wiggler fields were carefully measured with calibrated diagnostics and compared with simulations prior to assembly, a final confirmation of the field calibrations must await the ultimate dismantling of the apparatus.

The first comparison between theory and experiment deals with the dependence of output power on input power. To this end, drive curves at 16.6 GHz are shown in Fig. 5 from the experiment and from ARACHNE for a 244 kV/82 A electron beam and for wiggler and axial guide magnetic fields of 231 G and 2.47 kG, respectively. Power measurements are higher than predicted by ARACHNE for single pass amplification, but the system is not driven to saturation. In order to explain the discrepancy, we first assume the presence of a small amount of internal reflections which can increase the output power over that computed for single pass amplification. Note that the beam flat top is about 1 μs wide and the distance from the input coupler to the calorimeter is $\approx$ 125 cm. Hence, more than 100 round trip bounces of the radiation are possible during the beam pulse and even a small degree of reflection can substantially alter the output power. In the case shown, an assumed total reflection coefficient of 0.65% resulted in good agreement between the simulation and the experiment. However, based on cold tests and some

reflected power during operation, we expect the round trip reflections of the order of 0.1-0.3% at 16.6 GHz. Therefore, we expect that other factors must be involved.
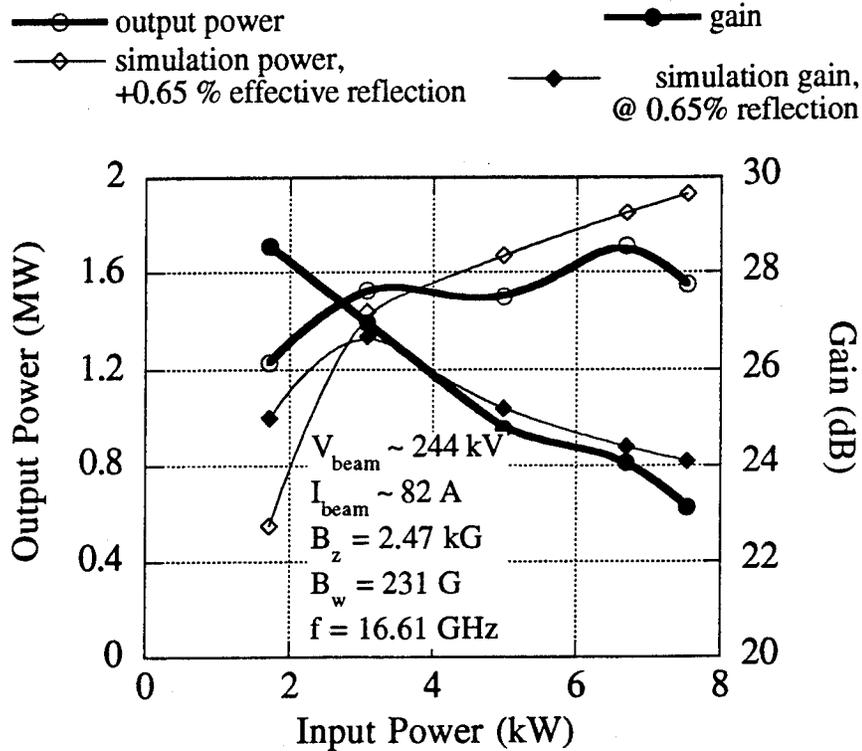

Fig. 5 Drive curve showing the output power and gain as a function of the input power.
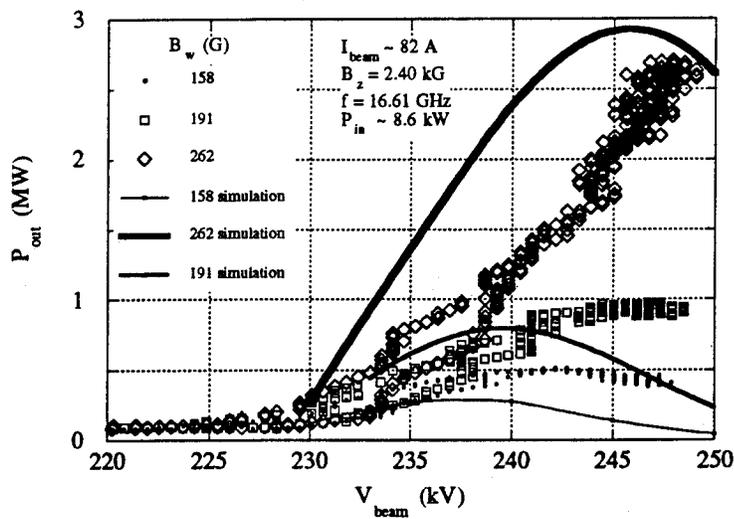

Fig. 6 Variation in the output power with beam voltage for several values of wiggler amplitude.

The dependence of the output power on beam voltage for several values of the wiggler field is shown in Fig. 6. The data for this figure are unfolded from a series of acquired waveforms and presented as output power vs. beam voltage, where each point represents a digitized value. The simulation results from ARACHNE are shown with the solid curves, with the curve thickness matching the corresponding point thickness of the experimental measurement for a given wiggler field. Good agreement is shown in the voltage at which the peak output power occurs and in the overall voltage dependence. However, as mentioned above, both the wiggler and axial magnetic field values used in the simulation were 5 % higher than the experimental values.

In view of these two comparisons, it is our expectation that the discrepancy between theory and experiment can, in many case, be accounted for by the assumptions of (1) a small degree of internal reflections, and (2) a recalibration in the magnetic field levels.
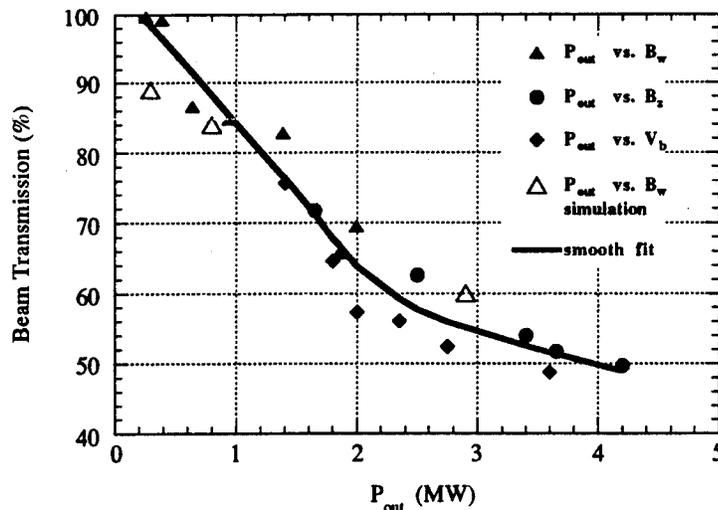

Fig. 7 Variation in beam loss with output power.

One final issue which is important in a production device is the beam loss. Both simulation and experiment have shown high beam loss in the interaction region at multimegawatt power levels. This is demonstrated in Fig. 7 in which we plot the variation

in beam loss with output power for a variety of different beam, wiggler and axial field parameters. The solid triangles in the figure represent data collected from experimental runs in which the variation in output power versus wiggler amplitude was studied. Similarly, the solid circles (diamonds) represent data collected from studies of the variation in the output power versus the axial guide field (beam voltage). The hollow triangles represent ARACHNE simulations of output power dependencies on wiggler and axial guide fields. The solid line is simply a smooth fit to all of these points. It is evident that the fraction of transmitted beam falls fairly uniformly with output power and reaches about 50% transmission at a 4 MW power level. Observe that all the points from both the experiment and the simulation cluster fairly closely about the fitted curve, and represents good agreement between the theory and the experiment.

Although this degree of beam loss is clearly undesirable for high duty factor operation, it does not necessarily result in tube damage. The NRL ubitron was disassembled after many hours of operation at 6 pps and examined for damage in the wiggler region. None was found. This not to say that the current loss is not a potential problem; rather, that the beam loss is sufficiently distributed axially to result in little or no tube damage. This effect could probably be reduced by simply reducing the initial beam diameter, or operation further from gyroresonance.

IV. SUMMARY

In conclusion, results from the NRL ubitron experiment demonstrate that the performance potential of the ubitron/FEL has been realized. A configuration using a fundamental mode circularly polarized rf wave and a helical wiggler results in a relatively compact, high power, and efficient amplifier with wide instantaneous bandwidth and without the necessity of wiggler field tapering. Performance levels compare quite favorably with those from other pulsed, high power microwave amplifier designs.

In general, there is good agreement between theory and experiment considering output power dependence on beam voltage, wiggler field, and axial field. Both theory and experiment show a high degree of output power sensitivity to beam voltage and axial magnetic field. Some differences exist, with the experimental power levels typically higher than predicted. Work is underway to determine the source of this discrepancy. At the present time, we are examining the questions of internal reflections, magnetic field calibrations, and beam modelling as sources of the discrepancy. Further attention to the beam loss issue is required for higher duty factor operation. Future work will include more extensive measurements of noise and phase characteristics, as well as utilization of our theory/design capability for designs at higher frequency and lower voltage regimes.

ACKNOWLEDGMENTS

REFERENCES

1. D. E. Pershing, R. H. Jackson, H. Bluem, and H. P. Freund, Nucl. Instr. and Meth. **A304**, 127 (1991).

2. A. K. Ganguly and H. P. Freund, Phys. Fluids **31**, 387 (1988).

3. H.P. Freund, R.H. Jackson, and D.E. Pershing, Phys. Fluids B **5**, 2318 (1993).

4. H.P. Freund and T.M. Antonsen, Jr., Principles of Free-electron Lasers (Chapman & Hall, London, 1992), Chap. 5.

5. H. Bluem, R. H. Jackson, H. P. Freund, D. E. Pershing, and V. L. Granatstein, Phys. Rev. Lett. **67**, 824 (1991).

6. R.H. Jackson, H.P. Freund, D.E. Pershing, and J.M. Taccetti, Nucl. Instr. and Meth. **A341**, 454 (1994).

7. H.P. Freund, R.H. Jackson, D.E. Pershing, and J.M. Taccetti, Phys. Plasmas **1**, 1046 (1994).

APPENDIX XVIII

Demonstration of a New Free-Electron Laser Harmonic Interaction

H. Bluem, R.H. Jackson, H.P. Freund , D.E. Pershing, and
V.L. Granatstein

Demonstration of a New Free-Electron-Laser Harmonic Interaction

H. Bluem,[a] R. H. Jackson, H. P. Freund,[b] D. E. Pershing,[c] and V. L. Granatstein[d]

Naval Research Laboratory, Washington, D.C. 20375

(Received 15 April 1991)

The first experimental demonstration of a harmonic free-electron-laser amplifier utilizing a periodic position instability is described for a planar wiggler configuration. The interaction occurs at the even harmonics of the fundamental. A maximum gain of 7 dB was observed over a frequency band ranging from 14 to 15 GHz. The experimental results are compared with predictions from the three-dimensional simulation code WIGGLIN with excellent agreement. Improvements due to a tapered wiggler for this interaction are discussed.

The free-electron laser (FEL) dates back over three decades [1,2], and has been intensively studied for over a decade. Recently, harmonic generation has become an important topic for either extending the frequency range of fixed-voltage facilities or reducing the beam voltage required at a given frequency. Reduced beam voltage would have a significant impact on potential applications. This paper describes the first measurement of even-harmonic amplification utilizing a periodic position instability [2,3].

For conventional planar-wiggler FELs the interaction occurs at the fundamental and the odd harmonics [4–11], due to the velocity harmonics present in the unperturbed undulations of the electrons. These harmonics are present even for ideal wigglers with perfect beam injection, and give rise to the periodic velocity instability of the FEL. The even-harmonic interaction considered here, however, requires no higher velocity harmonics. Rather, it depends on a synchronism in the electron position with respect to an antisymmetric radiation field. The interaction can occur with either a transverse or axial electric field. The transverse field must be odd in the direction of the wiggle motion, and the axial field must be even for the respective interactions to occur. For a second-harmonic interaction, the radiation goes through two cycles as the electron beam traverses one wiggler period λ_w.

For the transverse interaction, the on-axis electric field is zero, and the field peaks off axis. Considering only the central part of the beam, the essentials of the transverse interaction are shown in Fig. 1(a) where the electron motion is greatly exaggerated and the transverse profile of the field is included (in this case, the TE_{11} rectangular waveguide mode). As seen in the figure, the electron will always be in either a decelerating or a zero electric field. Although a particle displaced from the horizontal center of the beam will be in an accelerating field a portion of the time, the bulk of the beam will be in a decelerating field most of the time, leading to a net amplification. The axial interaction is shown in Fig. 1(b), again for the central part of an on-axis beam. The transverse profile in this case represents the axial field of the TM_{11} mode. Here, even the central particle sees both an accelerating and a decelerating field. The electron is in a decelerating

field on axis where the field is at its maximum and the axial velocity at a minimum, and in an accelerating field off axis where the field is reduced and the axial velocity is maximum. However, the transverse variation of the electric field is greater than the transverse variation of the axial velocity. This results in a stronger interaction on axis which, again, leads to net amplification.

Although the axial and transverse interactions have been considered separately in the preceding paragraph, it is difficult to completely separate the two interactions. In fact, computer simulations indicate that the overall performance at the second harmonic is improved when the two interactions are combined. Simulation also shows that the second-harmonic periodic position interaction

Transverse Interaction

electron beam transverse position (direction of velocity is indicated by arrows)
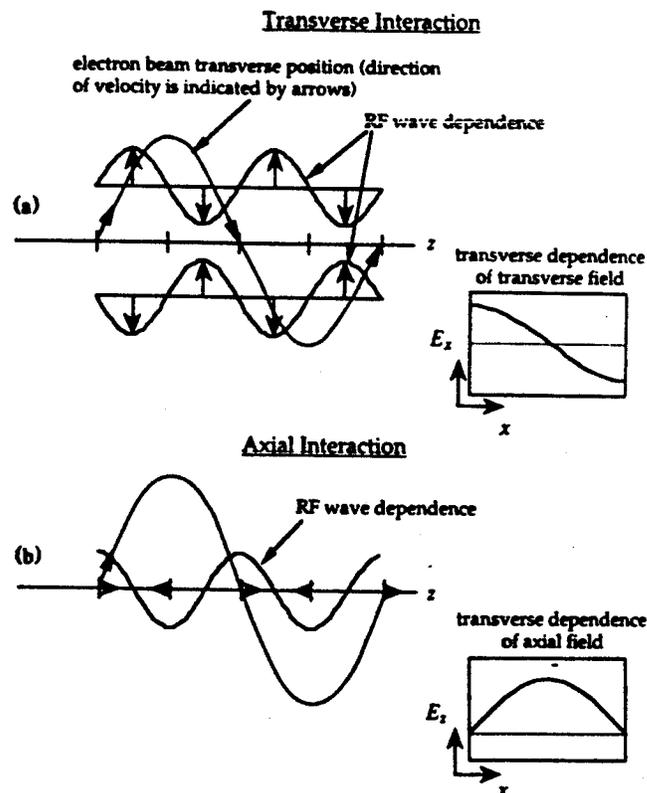

FIG. 1. Physical representation of the periodic position interaction.

can have a stronger growth rate than the fundamental interaction, and is a significantly stronger interaction than the third-harmonic FEL interaction for the current range of experimental parameters. The remainder of this paper includes a description of the experiment, as well as a comparison with simulation results using the three-dimensional nonlinear FEL amplifier code WIGGLIN [10,12,13].

The experimental configuration is described in Ref. [9]. The drive frequency was between 12 and 18 GHz. The experiment used a cylindrical electron beam tunable in voltage from about 30 to 250 kV, with a 100-kV nominal operating voltage for the second-harmonic interaction. The beam voltage was measured as the output voltage of the modulator using a capacitive voltage divider. The current was measured at the gun with a current transformer, and at two downstream locations with resistive current monitors. One measurement was taken before the input coupler region and the other just after the interaction region. The wiggler consisted of a permanent-magnet-assisted electromagnet with a period of 3 cm and an amplitude variable over 670–1300 G. This corresponds to a large perturbation of the electron motion at these low voltages, and the ratio of transverse to axial velocity is in the range of 0.23–0.43. The pole pieces extended partially down the sides of the waveguide to provide wiggle-plane focusing, and resulted in a very flat profile near the center of the waveguide with the field rising sharply near the wall.

The experiment operated as an amplifier in an oversized waveguide (3.485×1.58 cm) with the input signal injected using a novel coupler capable of launching the TE_{01} and TE/TM_{11} modes. These are the lowest-order modes with the odd transverse symmetry necessary for the periodic position interaction. Simulations of this coupler suggest there was a 9 to 1 split between the TE_{11} and TM_{11} modes with very little power in other modes. The output radiation was analyzed via mode-selective output couplers, and the microwave power was measured with calibrated detectors at each of the output coupler ports. By comparing the signals from the output couplers and by utilizing the uncoupled dispersion curves, the interaction was positively identified as a second-harmonic interaction with the 1,1 modes. The input coupler was also switched to launch the TE_{01} mode (the lowest-order mode for the FEL interaction) to verify that no interaction occurred at these parameters.

Gain due to the second-harmonic periodic position interaction was measured at beam voltages of 78–106 kV and currents of 6–10 A (measured downstream from the interaction region). This contrasts with voltages in the range of 200–250 kV required for the fundamental interaction at the same frequency. Operation at frequencies of 12.5–16.5 GHz was achieved by both voltage and wiggler-field tuning. The maximum observed gain was approximately 7 dB. The measured gain spectrum will be presented later in comparison with the theoretical analysis. The interaction could not be saturated at this value of gain with the available drive power, but the maximum unsaturated efficiency obtained was 1.1%.

An oscillation also occurred at beam voltages of 115–130 kV (depending on the wiggler strength) which had a significant effect on the transported beam current, reducing it by as much as 12% and indicating a strong interaction. The measured frequency was 10.4 GHz, corresponding to the cutoff frequency of the 1,1 modes. An uncoupled dispersion analysis indicated the oscillation was a backward-wave second-harmonic periodic position instability. This was supported by the observation of a higher power exiting the input coupler than was measured at the output couplers. The measured power exiting from the input coupler was 41.5 kW, corresponding to an efficiency of over 3%. The actual power inside the device was uncertain due to the unknown response of the input and output couplers at 10.4 GHz for the TE_{11} and TM_{11} modes. Although the fraction of the total power that was actually coupled out from the input coupler is unknown, the apparent strength of this oscillation indicates the potential of the periodic position interaction.

The experiment was not optimized for the second-harmonic periodic position interaction. The primary limitations were electron-beam generation and injection. The electron gun was designed for a different experiment, and new focusing and transport systems were devised to match the beam to the wiggler. A good match was difficult to achieve as the beam was transported from a solenoidal field into the planar wiggler, and a significant portion of the beam was lost in the transition. The problems in the transition region also resulted in a larger than desired beam diameter. Because of the nature of the interaction, an increasing portion of the beam becomes essentially noninteracting as the beam diameter increases, thus limiting the gain. In addition, a large diameter also gives rise to a large wiggler-induced velocity spread which limits the operating efficiency.

The experimental observations were compared with simulations using WIGGLIN, which includes the simultaneous integration of a slow-time-scale formulation of Maxwell's equations as well as the complete Lorentz-force equations for an ensemble of electrons. No average of the orbit equations is performed. As such, WIGGLIN implicitly includes both the well-known odd harmonic interaction in a planar wiggler and the periodic position interaction. No further fundamental modification is required to model the experiment. In this formulation, the electrons are assumed to be initially monoenergetic but with a pitch-angle spread that describes an axial energy spread [12,13].

The wiggler model describes an inhomogeneity in the wiggle direction (i.e., the x axis). The measured field was quite uniform about the symmetry axis, and rose sharply toward the edges of the interaction region. As such, we

employ the following wiggler model [14]:

$$B_{w,x}(x) = \left[\left\{ \sin k_w z - \frac{\cos k_w z}{k_w} \frac{d}{dz} \right\} B_w(z) \right] \left[\sinh k_w y - \frac{Y(k_w y)}{2k_w^2} \frac{d^2}{dx^2} \right] \frac{1}{k_w} \frac{d}{dx} X(x) , \tag{1}$$

$$B_{w,y}(x) = \left[\left\{ \sin k_w z - \frac{\cos k_w z}{k_w} \frac{d}{dz} \right\} B_w(z) \right] \left[\cosh k_w y - \frac{k_w y \sinh k_w y}{2k_w^2} \frac{d^2}{dx^2} \right] X(x) , \tag{2}$$

$$B_{w,z}(x) = B_w(z) \cos k_w z \left[\sinh k_w y - \frac{Y(k_w y)}{2k_w^2} \left\{ 1 + \frac{1}{k_w^2} \frac{d^2}{dx^2} \right\} \frac{d^2}{dx^2} \right] X(x) , \tag{3}$$

where $B_w(z)$ describes the axial variation, $k_w \equiv 2\pi/\lambda_w$, $X(x)$ denotes the variation in the wiggle plane, and $Y(k_w y) \equiv k_w y \cosh k_w y - \sinh k_w y$. This field is not self-consistent in that it is divergence-free but not curl-free. However, the approximation is good as long as $B_w(z)$ and $X(x)$ vary slowly compared with λ_w.

We choose $B_w(z)$ to describe both the adiabatic injection of the beam into the wiggler over N_w wiggler periods and the downstream taper of the wiggler for efficiency enhancement. Hence,

$$B_w(z) = \begin{cases} B_w \sin^2(k_w z/4N_w), & 0 \le z \le N_w \lambda_w , \\ B_w, & N_w \lambda_w < z \le z_0 , \\ B_w[1 + k_w \varepsilon_w (z - z_0)], & z_0 < z , \end{cases} \tag{4}$$

where B_w is the wiggler magnitude in the uniform region, and ε_w denotes the normalized taper. The variation in x is described for the general case by a polynomial

$$X(x) = 1 + \tfrac{1}{2}(x/a_x)^{2m} , \tag{5}$$

where a_x denotes the scale length for variation of the field, and m is an integer. As $a_x \to \infty$ this reduces to a wiggler with flat pole faces. A comparison of the actual field with $X(x)$ as used in the code (a quartic with $m=2$ and $a_x = 1.4938$) is shown in Fig. 2, and it is clear that the approximation gives a reasonable fit to the data.

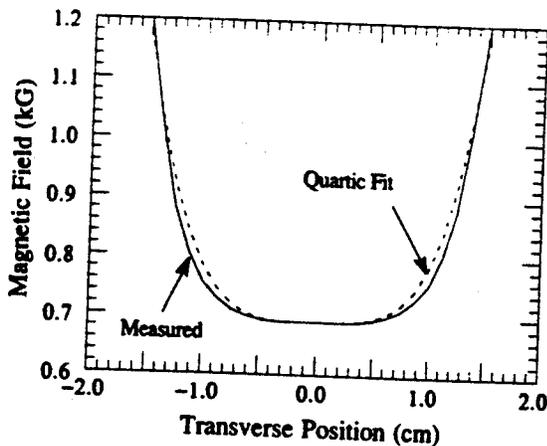The specific parameters used for comparison are a voltage and current of 99.4 kV and 6.6 A with a beam radius

of 0.4 cm. The wiggler was characterized by $B_w = 1.295$ kG, $\lambda_w = 3$ cm, an input taper of $N_w = 3$, and a total length of $34\lambda_w$. Both the TE_{11} and TM_{11} modes are included (at a ratio of 9 to 1) with a total input power of 300 W. Figure 3 contains a comparison of the observations with results from WIGGLIN over the unstable band for $\Delta\gamma_z/\gamma_0 = 0.0\%$, 0.025%, and 0.05%. The experimental points over the frequency band fall, for the most part, between the curves representing energy spreads of 0.025% and 0.05%. This is in good agreement with the estimated energy spread based upon trajectory calculations of the gun geometry. Observe that the power has not saturated in any of these cases. At 14.4 GHz, the saturated gain is about 10 dB over $40\lambda_w$ for $\Delta\gamma_z/\gamma_0 = 0$, which falls to about 8 dB over a distance of approximately $50\lambda_w$ for $\Delta\gamma_z/\gamma_0 = 0.025\%$.

The effect of a tapered wiggler is shown in Fig. 4 for the case of $\Delta\gamma_z = 0$ and $\varepsilon_w = -0.00083$. The efficiency enhancement is sensitive to the start-taper position, which must be close to the point at which the beam becomes trapped in the ponderomotive potential formed by the beating of the wiggler and radiation fields. For this example, the optimal start-taper point is $z_0 \approx 30.2$ cm. Only the total signal and the TE_{11} mode are shown in the figure, and the large oscillations in the total power are caused by the TM_{11} mode. It is evident that the saturat-
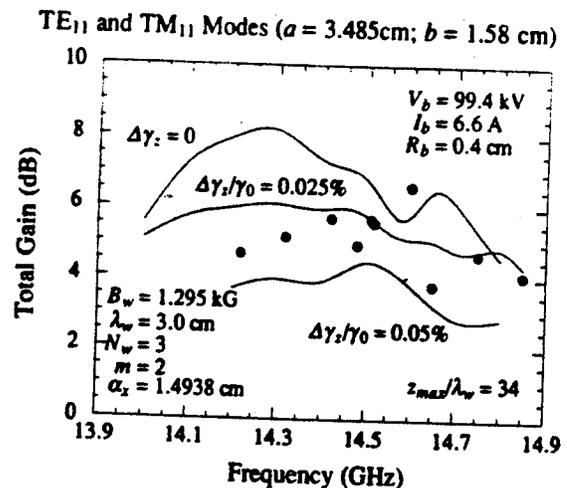

FIG. 2. Comparison of the measured transverse wiggler variation and the quartic representation used in WIGGLIN.

FIG. 3. Comparison of the observed output spectrum and the calculations with WIGGLIN.

TE$_{11}$ and TM$_{11}$ Modes ($a = 3.485$ cm; $b = 1.58$ cm)

$B_w = 1.295$ kG
$\lambda_w = 3.0$ cm
$N_w = 3$
$m = 2$
$\alpha_x = 1.4938$ cm

$z_0/\lambda_w = 30.2$

$\varepsilon_w = -0.00083$

Total

TE$_{11}$ Mode

$V_b = 99.4$ kV
$I_b = 6.6$ A
$R_b = 0.4$ cm
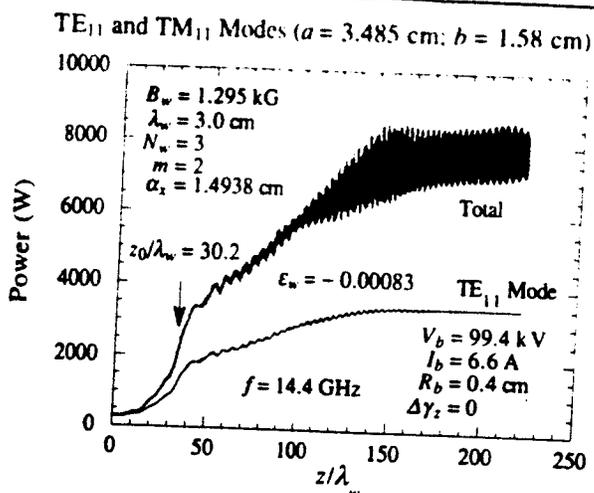$\Delta\gamma_z = 0$

$f = 14.4$ GHz

FIG. 4. Simulation of the power vs axial distance for a tapered-wiggler interaction.

ed efficiency can be increased relative to that of the uniform-wiggler case for the present parameters by almost threefold through the use of a tapered wiggler.

In summary, the first experimental demonstration of a harmonic periodic position amplifier has been achieved. The interaction occurs at the even harmonics of the fundamental FEL interaction frequency in planar-wiggler-rectangular-waveguide geometry where modes exist with an odd symmetry about the wiggler symmetry plane. The experiment permitted positive identification of the interacting modes, and the experiment was seen to be in close agreement with predictions from the WIGGLIN simulation code. Improvements in the interaction efficiency by means of a tapered-wiggler interaction have been demonstrated in simulation; however, these results are far from optimized, and we expect that substantial improvements in performance are possible. It is important to note that the harmonic periodic position interaction is operative for other wiggler-waveguide geometries and for optical-resonator modes with a similar odd symmetry.

(a)Permanent address: Louisiana State University, Baton Rouge, LA 70803.

(b)Permanent address: Science Applications International Corp., McLean, VA 22102.

(c)Permanent address: Mission Research Corp., Newington, VA 22122.

(d)Permanent address: University of Maryland, College Park, MD 20742.

[1] H. Motz, W. Thon, and R. N. Whitehurst, J. Appl. Phys. 24, 826 (1953).

[2] R. M. Phillips, IRE Trans. Electron Devices 7, 231 (1960).

[3] R. B. Dyott and M. C. Davies, IEEE Trans. Electron Devices 13, 374 (1966).

[4] W. B. Colson, IEEE J. Quantum Electron. 17, 1417 (1981).

[5] B. Girard, Y. Lapierre, J. M. Ortega, C. Bazin, M. Billardon, P. Ellaume, M. Bergher, M. Velghe, and Y. Petroff, Phys. Rev. Lett. 53, 2405 (1984).

[6] D. J. Bamford and D. A. G. Deacon, Phys. Rev. Lett. 62, 1106 (1989).

[7] S. V. Benson and J. M. J. Madey, Phys. Rev. A 39, 1579 (1989).

[8] R. W. Warren, L. C. Haynes, D. W. Feldman, W. E. Stein, and S. J. Gitomer, Nucl. Instrum. Methods Phys. Res., Sect. A 296, 84 (1990).

[9] H. Bluem, R. H. Jackson, D. E. Pershing, J. H. Booske, and V. L. Granatstein, Nucl. Instrum. Methods Phys. Res., Sect. A 296, 37 (1990).

[10] H. P. Freund, C. L. Chang, and H. Bluem, Phys. Rev. A 36, 3218 (1987).

[11] P. E. Latham, B. Levush, T. M. Antonsen, Jr., and N. Metzler, Phys. Rev. Lett. 66, 1442 (1991).

[12] H. P. Freund, H. Bluem, and C. L. Chang, Phys. Rev. A 36, 2182 (1987).

[13] H. P. Freund, Phys. Rev. A 37, 3371 (1988).

[14] T. M. Antonsen, Jr. (private communication).